DFT Studies on Heterobimetallic Complexes of Ru with Zn, Ga and In

Nasir Ahmad Rajabi

Submitted for the degree of Doctor of Philosophy

Heriot-Watt University

School of Engineering and Physical Sciences

August 2018

Abstract

Density Functional Theory (DFT) was used to study a series of heterobimetallic complexes of ruthenium with zinc, gallium and indium. In this thesis, **Chapter 1** presents an introductory discussion on the fundamental computational approaches and **Chapter 2** describes a literature survey of transition metal complexes featuring Zn, Ga and In moieties. Chapters **3**, **4** and **5** look at the mechanisms of the reactions of the Ru-H species **67**, $[Ru(IPr)_2(CO)(H)]^+$, with $ZnEt_2$, $InMe_3$ and $GaMe_3$, respectively, as well as the reactivities of the resultant heterobimetallic complexes with small molecules. Bonding analyses of the heterobimetallic complexes are also reported. In **Chapter 3**, the formation of $[Ru(IPr)_2(CO)ZnEt]^+$, **68**, is modelled and shown to involve Et transfer from Zn to Ru followed by the reductive elimination of ethane. **68** is shown to be a Ru(0)-Zn(II) species. H_2 activation at **68** occurs homolytically to produce $[Ru(IPr)_2(CO)(\eta^2–H_2)(H)_2(ZnEt)]^+$, **69**. Mechanisms for H_2 loss from **69** to give $[Ru(IPr)_2(CO)(H)_2(ZnEt)]^+$, **70**, and H/H exchange in **69** and **70** were also characterised. **Chapter 4** presents the computed mechanism for the formation of **71**, $[Ru(IPr)_2(CO)(Me)InMe]^+$. As with the Ru-Zn chemistry, this involves alkyl transfer along with a reductive elimination step. A second alkyl group then transfers to Ru to give **71** which is characterised as a Ru(II)-In(I) species. H_2 activation at **71** occurs via a σ-CAM mechanism which releases methane to form $[Ru(IPr)_2(CO)(\eta^2–H_2)(H)(InMe)]^+$, **72**. A computed mechanism for the reaction of **71** with CO shows that addition of the first CO to Ru transfers the Me group back to In with a low energy barrier to give a Ru-indyl species which can then be trapped by the addition of the second CO to give **74**, $[Ru(IPr)_2(CO)_3(InMe_2)]^+$. In **Chapter 5**, reaction of **68** with $GaMe_3$ to give **77**, $[Ru(IPr)(CO)(GaMe_2IPr)]^+$, is modelled. In this process, instead of transferring a second Me from Ga to Ru, an IPr ligand transfers from Ru to Ga to give the **77** which is shown to be a Ru(0)-Ga(III) species. Discrepancies between the stability of **77** and the Ga congener of **71** were found but could not be resolved. **Chapter 6** focuses on two new Cu complexes, $[(6\text{-Mes})Cu(HBR_3)]$ (R = Et and C_6F_5), that are characterised as Cu-borate complexes. Modelling the isolated species in the gas phase shows that the geometry of the $\{CuHBR_3\}$ unit is sensitive to the functional choice and dispersion correction, with M06 and ωB97xD giving the best overall results. Calculations in the extended solid state using periodic DFT showed the geometries are still sensitive to the functional choice but now dispersion is well balanced by the inter-molecular interactions. The PBE functional gives the best overall results.

Acknowledgments

I would like to thank to my supervisor, Professor Stuart Macgregor, for his help and patience throughout my PhD.

I would like to express my gratitude to my experimental collaborator, Professor Michael Whittlesey and his group at the University of Bath including, Ian, Lee and Mateusz for the great experimental work. Thanks to Doctor Rowan Young and his group at National University of Singapore for collaboration. I would also thank to the referees, Professor Alan Welch (Heriot-Watt University) and Doctor Mark Crimmin (Imperial College), for their reviews and useful comments.

I am also deeply thankful to the all the members of “Inorganic Computational Chemistry” research group, including Tobi, Claire M, Dave J, Nick, Sam, Bengt and Kevin for their help.

Finally, I would like to thank my parents Ali and Deljan, my sisters and brothers for their support and encouragement. I would not have come this far without your support.

Table of Contents

Publication List

I. M. Riddlestone, N. A. Rajabi, S. A. Macgregor, M. F. Mahon, M. K. Whittlesey, "Well-Defined Heterobimetallic Reactivity at Unsupported Ruthenium-Indium Bonds", *Chem. Eur. J.*, **2018**, *7*, 1732-1738.

S. Sung, J. K. Boon, J. J. C. Lee, N. A. Rajabi, S. A. Macgregor, T. Krämer, R. D. Young, "Convergent (De)Hydrogenative Pathways via a Rhodium α-Hydroxylalkyl Complex", *Organometallics*, **2017**, *36*, 1609-1617.

I. M. Riddlestone, N. A. Rajabi, J. P. Lowe, M. F. Mahon, S. A. Macgregor, M. K. Whittlesey, "Activation of H_2 over the Ru-Zn Bond in the Transition Metal-Lewis Acid Heterobimetallic Species $[Ru(IPr)_2(CO)ZnEt]^+$", *J. Am. Chem. Soc.*, **2016**, *138*, 11081.

L. R. Collins, N. A. Rajabi, S. A. Macgregor, M. F. Mahon, M. K. Whittlesey, "Experimental and Computational Studies of the Copper Borate Complexes [(NHC)Cu($HBEt_3$)] and [(NHC)Cu($HB(C_6F_5)_3$)]", *Angew. Chem. Int. Ed.*, **2016**, *50*, 15539-15543.

Chapter 1 – Theoretical Background

This chapter provides a brief overview of computational methods most often employed in this thesis. The first sections of this chapter briefly reviews the fundamental concepts in quantum mechanics and continues with an overview of the Hartree-Fock (HF) and Density Functional Theory (DFT). The next sections then describe different computational techniques to analyse the bonding situations of molecular systems.

1.1 The Schrödinger Equation

Central to computational chemistry is the solution of the Schrödinger equation:[1]

$$\hat{H}\psi = E\psi$$

Eq. 1-1

This equation describes a system with the wave function, ψ, and involves the Hamiltonian ($\hat{H}$) operator which represents the total energy (E) of the system. For a molecular system with N electrons and M nuclei, the Hamiltonian operator can be constructed by the equation below:

$$\hat{H} = -\frac{1}{2}\sum_{i=1}^{N}\nabla_i^2 - \frac{1}{2}\sum_{A=1}^{M}\frac{1}{M_A}\nabla_A^2 - \sum_{i=1}^{N}\sum_{A=1}^{M}\frac{Z_A}{r_{iA}} + \sum_{i=1}^{N}\sum_{j>i}^{N}\frac{1}{r_{ij}} + \sum_{A=1}^{M}\sum_{B>A}^{M}\frac{Z_A Z_B}{R_{AB}}$$
$$= \hat{T}_e + \hat{T}_N + \hat{V}_{Ne} + \hat{V}_{ee} + \hat{V}_{NN}$$

Eq. 1-2

In Eq. 1-2, the first two terms represent the summations of kinetic energy ($\hat{T}$) of the N and M particles, respectively. The Laplacian operator, ∇_q^2, is the second derivative of the position of the particle q with respect to the three Cartesian coordinates. M_A is the mass of the nuclei in atomic units.

$$\nabla_q^2 = \frac{\partial^2}{\partial x_q^2} + \frac{\partial^2}{\partial y_q^2} + \frac{\partial^2}{\partial z_q^2}$$

Eq. 1-3

The third term describes the interaction between the nuclei and electrons ($\hat{V}_{Ne}$). This term is always attractive and therefore, it is always stabilising. The degree of stabilisation depends on the nucleus charge, Z_A and the distance between the nucleus and electron, r_{iA}.

The last two terms represent the potential energy related to the electron-electron ($\widehat{V}_{ee}$) and nuclear-nuclear ($\widehat{V}_{NN}$) interactions, respectively. These types of interactions are always repulsive and therefore, they destabilise the system.

For hydrogenic systems (i.e. systems with one electron), the Schrödinger equation can be solved exactly. However, for systems with more than one electron, it is necessary to make approximations. In this regard, the Schrödinger equation can be simplified if we pay attention to the fact that the nuclear mass of hydrogen nucleus (i.e. a proton) is roughly 1800 times larger than the mass of an electron. This allows us to consider that the nucleus moves significantly more slowly than the electron. In this case, the motion of the nucleus can be decoupled from the electron and the nucleus position can be treated as fixed in the space. The consequence of this approach is the setting of the kinetic energy of the nuclei to zero. This approximation is called the Born-Oppenheimer (BO) approximation. The BO approximation simplifies the Hamiltonian to give the electronic Hamiltonian, $\widehat{H}_{elec}$:

$$\widehat{H}_{elec} = -\frac{1}{2}\sum_{i=1}^{N}\nabla_i^2 - \sum_{i=1}^{N}\sum_{A=1}^{M}\frac{Z_A}{r_{iA}} + \sum_{i=1}^{N}\sum_{j>i}^{N}\frac{1}{r_{ij}}$$
$$= \widehat{T}_e + \widehat{V}_{Ne} + \widehat{V}_{ee}$$

Eq. 1-4

The Schrödinger equation under the BO approximation is:

$$\widehat{H}_{elec}\,\psi_{elec} = E_{elec}\,\psi_{elec}$$

Eq. 1-5

where the action of the electronic Hamiltonian operator, $\widehat{H}_{elec}$, upon the electronic wave function, ψ_{elec}, gives the electronic energy, E_{elec}. Summation of the nuclear-nuclear potential energy, E_{nuc}, with the electronic energy then gives the total energy, E_{tot}.

$$E_{tot} = E_{elec} + E_{nuc}$$

Eq. 1-6

In the Hamiltonian operator, the electron-electron interaction is composed of three different terms; the Coulomb, exchange and correlation interactions. These terms will be discussed in detail in the following sections.

1.2 The Variational Principle

For N-electron systems (N>1), the exact form of the wave function is unknown. Therefore, in order to solve Schrödinger equation under the BO approximation, the wave function of the system must also be approximated. In this line, a trial wave function (ψ_{trial}) can be constructed based on an initial guess. This trial wave function then can give the trial energy (E_{trial}):

$$\hat{H}\,\psi_{trial} = E_{trial}\,\psi_{trial}$$

Eq. 1-7

$\hat{E}_{trial}$ can be equal to the actual ground state energy (E_0) if the trial wave function is equal to the exact wave function (ψ_{exact}).

$$E_{trial} = E_0 \qquad \text{if} \qquad \psi_{trial} = \psi_{exact}$$

Eq. 1-8

Otherwise, it results an energy which is always greater than E_0.

$$E_{trial} > E_0$$

Eq. 1-9

This principle can be used to improve the quality of the trial wave function. In this regard, any variation in the wave function which lowers the trial energy can be viewed as a better wave function than the former one. Therefore, the lowest trial energy corresponds to the best approximated wave function. Application of this principle, which is known as the variational principle, can be used to find the best approximated wave function and hence, the closest energy to the exact energy.

1.3 Spin Orbitals

In the approximated wave function of an N-electron system, each electron wave function has two different components. First, the spatial part which is a function of the electron coordinates denoted by $\psi(r)$ and provides the electron probability distribution. Second, the spin part (ω) which denotes the spin of electrons and can be spin up ($\alpha(\omega)\uparrow$) or spin down ($\beta(\omega)\downarrow$). These two components can be combined to give a spin orbital function ($\chi(\mathbf{x})$).

1.4 Hartree-Fock Theory

1.4.1 Hartree Method

As outlined above, for an N-electron system, approximations are required to solve the Schrödinger equation and a first step is to make an initial guess for the wave function. In this regard, in 1928, Hartree proposed a method to construct the many-body wave function. The basis of this idea was to treat an N-electron system as N individual particles. In this regime, electrons can be treated independently from each other, and the Hamiltonian can be constructed for each single electron. The resultant total wave function can be described as below:

$$\psi^{HP}(r_1, r_2 \dots, r_N) = \psi_1(\mathbf{r_1})\,\psi_2(\mathbf{r_2}) \dots \psi_N(\mathbf{r_N})$$

Eq. 1-10

where ψ^{HP} is the Hartree-product wave function and composed of individual electron wave functions. By considering each electron as an independent particle, there are some major shortcomings. Firstly, this approach allocates specific positions for particular electrons. However, as electrons are not distinguishable, they cannot be labelled. Secondly, as electrons are fermions, when their positions are swapped, the sign of the wave function must change.

$$\psi(X_1, X_2) = -\psi(X_2, X_1)$$

Eq. 1-11

Thus, the Hartree approach does not satisfy the antisymmetry condition of the wave function.

1.4.2 Slater Determinants

In an N-electron system, the indistinguishability of electrons can be addressed by distributing all N electrons across all possible positions. Interestingly, this can be captured by the determinant which is known as Slater determinant:

$$\psi(X_1, X_2 \dots, X_N) = (N!)^{-\frac{1}{2}} \begin{vmatrix} \chi_i(x_1) & \chi_j(x_1) & \dots & \chi_k(x_1) \\ \chi_i(x_2) & \chi_j(x_2) & \dots & \chi_k(x_2) \\ & \vdots & \vdots & \vdots \\ \chi_i(x_N) & \chi_j(x_N) & \dots & \chi_k(x_N) \end{vmatrix}$$

Eq. 1-12

The Slater determinant specifies the number of permutations which is all the possible ways to assign electrons to different spin-orbitals. According to this, there are N! ways to

distribute N electrons to N spin-orbitals. Each of these ways corresponds to one product of spin-orbitals. Therefore, by using the Slater determinant, electrons are no longer distinguishable.

In the Slater determinant, electrons are in the columns and orbitals are in the rows. The interchange of any two rows or columns gives a minus sign behind the resultant wave function. Interestingly, this is the antisymmetry property of the wave function which is now captured and generalised to an N-electron system by the Slater determinant.

For a two-electron system with same spin but in different orbitals, the Slater determinant can be constructed:

$$\psi(X_1, X_2) = 2^{-\frac{1}{2}} \begin{vmatrix} \chi_1(x_1) & \chi_2(x_1) \\ \chi_1(x_2) & \chi_2(x_2) \end{vmatrix}$$

Eq. 1-13

The expansion of the determinant for this system is:

$$\psi(X_1, X_2) = \frac{1}{\sqrt{2}} [\chi_1(x_1)\, \chi_2(x_2) \; - \; \chi_2(x_1)\chi_1(x_2)]$$

Eq. 1-14

The product of the Slater determinant for this system involves two permutations. One permutation is related to the condition where electron 1 and 2 occupy χ_1 and χ_2, respectively. The other one is related to the condition where electron 1 and 2 swap their positions and occupy χ_2 and χ_1, respectively. In the latter case changes the sign of the overall wave function and this can capture the antisymmetric properties of the wave function.

Interestingly, the product of the Slater determinant excludes the possibility that two electrons with the same spin occupy the same orbital. Therefore, the Slater determinant explicitly manifests the Pauli Exclusion Principle, since the determinant would vanish if any two rows are equal.

1.4.3 Hartree-Fock Equations

To address the shortcomings of the Hartree approach, Fock adopted the Hartree approach with the Slater determinantal wave function. This has been known as the Hartree-Fock (HF) theory. In the HF approach, each electron features a Fock operator ($\hat{f}$) which acts on the Slater determinantal wave function (ψ_i) and gives the orbital energy (ε_i).

$$\hat{f}\psi_i = \varepsilon_i \psi_i$$

Eq. 1-15

Summation of the orbital energies then gives the HF energy (E_{HF}) as defined:

$$E_{HF} = \sum_{i=1}^{N} \hat{f}\,\psi_i = \sum_{i=1}^{N} \varepsilon_i\,\psi_i$$

Eq. 1-16

The Fock operator involves three terms:

$$\hat{f}_i = -\frac{1}{2}\nabla_i^2 - \frac{1}{2}\sum_{A}^{M} \frac{Z_A}{r_{iA}} + \hat{V}_{HF}(i)$$

Eq. 1-17

where the first and second terms are the kinetic and the nuclear-electron potential energies, respectively. The last term, $\hat{V}_{HF}$, is related to the potential energy that electron i experiences due to the average charge distribution of the other electrons. This term is composed of two components, the Coulomb ($\hat{J}$) and the exchange operators ($\hat{K}$):

$$\hat{V}_{HF}(\vec{x}_1) = \sum_{j}^{N} \left(\hat{J}_j(\vec{x}_1) - \hat{K}_j(\vec{x}_1)\right)$$

Eq. 1-18

In the context of two-electron system, the Coulomb operator is defined as:

$$\hat{J}_j(\vec{x}_1) = \int \left|\chi_j(\vec{x}_2)\right|^2 r_{12}^{-1} d\vec{x}_2$$

Eq. 1-19

The Coulomb interaction is always repulsive and hence, it destabilises the system.
The exchange interaction ($\hat{K}$) is a property which arises from the interchanging of two electrons between two spin orbitals which is captured by the Slater determinant. This operator can be defined by:

$$\hat{K}_j(\vec{x}_1)\chi_i(\vec{x}_1) = \left[\int \chi_j^*(\vec{x}_2) r_{12}^{-1} \chi_i(\vec{x}_2)\, d\vec{x}_2\right]\chi_j(\vec{x}_1)$$

Eq. 1-20

Since there is no classical definition for the exchange operator, it can only be described by its effect on spin orbitals. In the case of electrons with parallel spins (i.e. either spins up or spins down), the exchange interaction results in the electrons being on average further apart from each other than a pair of electrons of opposite spin. This reduces the Coulomb interaction and therefore, it results in the reduction of destabilisation of the system. For electrons with anti-parallel spins (i.e. spins up and down), the integral becomes zero due to the orthonormality of spin orbitals. Therefore, no exchange contribution can be seen for such electrons with anti-parallel spin electrons.
There is an unphysical phenomenon which reveals itself when there is no exchange operator. This unreal phenomenon is called self-interaction. The self-interaction is the interaction of one electron with its own average charge distribution. In the absence of the exchange operator, self-interaction destabilises the system due to the unreal self-Coulomb interaction. However, cancelation of the self-Coulomb interaction of an electron happens when an equivalent term called self-exchange interaction is taken into account. This causes no self-interaction error to be seen in the HF theory.

1.4.4 Self-Consistent Field

In the one-electron Fock operator ($\hat{f}$) (Eq. 1-17) the repulsive interaction ($\hat{V}_{HF}(i)$) of electron i with the charge density of other electrons (ρ_j) can be expressed by:

$$\hat{V}_{HF}(i) = \sum_{j \neq i} \int \frac{\rho_j}{r_{ij}} dr$$

Eq. 1-21

However, in order to determine $\hat{V}_{HF}$ and solve the one-electron Fock operator, the wave function should be determined first. Therefore, the solution of the equation is required to find its solution. This can be solved by an iterative procedure known as the self-consistent field (SCF) method. In this method, firstly, an initial set of orbitals (ψ) is used to generate the electron charge density. The electron charge density is then implemented to obtain $\hat{V}_{HF}(i)$, solve the one-electron Fock operator and the HF equation. The solution of the Schrödinger equation then gives a new set of orbitals which can be presumably more accurate than the initial one. The new set of orbitals then again provides a new electron charge density and hence, a new set of orbitals. This procedure continues until the last set of the orbitals makes a very little change on the electron density and falls below a threshold criterion. The final set of orbitals can be referred to as the 'converged' SCF orbitals.

1.4.5 Electron Correlation in HF Theory

As outlined above, HF theory employs an approximate wave function to obtain the energy of a system. This energy (E_{HF}) is always associated with a discrepancy from the exact (E_0) energy:[2]

$$E_{corr} = E_0 - E_{HF}$$

Eq. 1-22

where E_{corr} is the correlation energy. There are two types of electron correlations; dynamical correlation and non-dynamical correlation. The former corresponds to instantaneous electron-electron interactions which minimise the Coulombic interaction

and hence, it reduces the electron-electron repulsive interaction. The latter can be seen in situations where there are more than one Slater determinant to approximate the ground state wave function. For instance in systems with two degenerate frontier orbitals and two electrons available, each electron must occupy one of the degenerate orbitals to give the lowest energy state (i.e. triplet ground state). However, in the absence of non-dynamical correlation, both electrons can occupy only one of the degenerate orbitals to give one doubly occupied orbital and one empty orbital (i.e. singlet state). This therefore can result in a large discrepancy from the exact ground state energy. In this regard, one example is the homolytic cleavage of H_2. This process should result in two hydrogen atoms in which each atom should have one electron (i.e. the first and second terms in Eq. 1-23). However, increasing the H···H distance until the complete dissociation of H–H bond also gives two hydrogen atoms in which one atom has two electrons while the other hydrogen atom has no electron (the third and fourth terms in Eq. 1-23).

$$(H^{\uparrow} \cdots H^{\downarrow}) + (H^{\downarrow} \cdots H^{\uparrow}) + (H^{\uparrow\downarrow} \cdots H) + (H \cdots H^{\uparrow\downarrow})$$

Eq. 1-23

This therefore adds two ionic electron configurations, resulting in a significant error in the ground state energy.

It should be noted that non-dynamical correlation can be seen in long-range distances where the dynamic correlation is negligible. However, in short-range distances, the dynamic correlation is more dominant over the non-dynamic one.

1.5 Density Functional Theory

1.5.1 Electron Density

Electron density is a physical observable property which can be determined practically by X-ray crystallography experiments. This property can also be generated computationally. For an N-electron system, the electron density ($\rho(\vec{r})$) can be described as the probability of finding any of the N electrons with the arbitrary spin ($d\vec{s}_1$) in a particular point ($d\vec{r}_1$):

$$\rho(\vec{r}) = N \int \dots \int |\psi(\vec{x}_1, \vec{x}_2, \dots, \vec{x}_N)|^2 d\vec{s}_1 d\vec{x}_2 \dots d\vec{x}_N$$

Eq. 1-24

while the other N-1 electrons are elsewhere in space and can be described by the given wave function, ψ.

1.5.2 The Hohenberg-Kohn Theorems

Modern DFT originates from two fundamental theorems by Hohenberg and Kohn (HK). The first theorem states that the external potential, V_{ext}, and hence the ground state energy, E_0, is a unique function of the ground state electron density, ρ_0.

$$E_0(\rho_0) = \int \rho_0(\vec{r}) V_{ext} d\vec{r} + T[\rho_0(\vec{r})] + V_{ee}[\rho_0(\vec{r})]$$

Eq. 1-25

where V_{ext} is the attractive interaction between nucleai and electrons. The last two terms represent the kinetic energy ($T(\rho_0)$) and the electron-electron potential energy ($V_{ee}(\rho_0)$). The latter contains the Coulomb interaction and the non-classical terms including exchange, correlation and self-interaction.

The first theorem outlined above can be proved by a *reductio ad absurdum* approach. In this approach, it is assumed that two different external potentials, V_{ext} and V'_{ext}, would give a same $\rho(\vec{r})$. However, with that, there are two different Hamiltonians ($\hat{H}$ and $\hat{H}'$) and therefore, two different ground state energies (E_0 and E_0') and two different wave functions (Ψ and Ψ'):

$$\hat{H} = \hat{T} + \hat{V}_{ee} + \hat{V}_{ext} \neq \hat{H} = \hat{T} + \hat{V}_{ee} + \hat{V}'_{ext}$$

Eq. 1-26

The primed wave function, Ψ', can be used as the trial wave function for the unprimed Hamiltonian, $\widehat{H}$:

$$E_0 < \langle \Psi' | \widehat{H} | \Psi' \rangle = \langle \Psi' | \widehat{H}' | \Psi' \rangle + \langle \Psi' | \widehat{H} - \widehat{H}' | \Psi' \rangle$$

Eq. 1-27

Based on the variational principle, this would give a trial energy, E_0', which is greater than the exact ground state energy, E_0:

$$E_0 < E_0' + \langle \Psi' | \widehat{T} + \widehat{V}_{ee} + \widehat{V}_{ext} - \widehat{T} - \widehat{V}_{ee} - \widehat{V}'_{ext} | \Psi' \rangle$$

Eq. 1-28

Cancelation of $\widehat{T}$ and $\widehat{V}_{ee}$ terms then gives:

$$E_0 < E_0' + \int \rho(\vec{r}) \{\widehat{V}_{ext} - \widehat{V}'_{ext}\} d\vec{r}$$

Eq. 1-29

A similar procedure can be repeated for the unprimed wave function, Ψ. In this regard, the primed Hamiltonian acting on the unprimed wave function Ψ gives:

$$E_0' < E_0 + \int \rho(\vec{r}) \{\widehat{V}'_{ext} - \widehat{V}_{ext}\} d\vec{r}$$

Eq. 1-30

The combination of equations Eq. 1-29 and Eq. 1-30 gives the following contradiction:

$$E_0 + E_0' < E_0 + E_0'$$

Eq. 1-31

This contradiction proves the first HK theorem and indicates that two different external potentials cannot give the same electron density, Hamiltonian and hence, ground state energy.

The second HK theorem is about the application of the variational theorem. This theorem states that a trial electron density will always give an upper bound energy to the exact ground state energy. In this case, the lower bound energy to the ground state energy will be achieved if the trial electron density is closer to the exact ground state electron density.

1.5.3 Kohn-Sham Approach

According to the HK theorems, there must be a practical way to produce the ground state energy from the ground state electron density. In this regard, Kohn and Sham (KS) proposed a method to produce the electron density of a fully interacting system from a fictitious non-interacting system by the consideration of the exchange and correlation terms.

According to the KS approach, the total Hamiltonian ($\widehat{H}_{KS}$) of the fictitious system is composed of single one-electron Hamiltonians:

$$\widehat{H}_{KS} = -\frac{1}{2}\sum_{i}^{N}\nabla_i^2 + \sum_{i}^{N} V_s\,(\vec{r_i})$$

Eq. 1-32

The first term is the kinetic energy of non-interacting system. Since in the non-interacting system, the motion of each single electron is independent of the motion of other electrons, the kinetic energy term ($T_s[\rho_0(\vec{r})]$) must be corrected by the additional term, T_c.

$$T[\rho_0(\vec{r})] = T_s[\rho_0(\vec{r})] + T_c[\rho_0(\vec{r})]$$

Eq. 1-33

The second term in the total Hamiltonian is the total potential energy due to the interaction of each single electron with the average charge of other electrons (V_s). Since V_s does not contain any exchange energy, it also requires to be corrected by the additional term, V_X.

$$V[\rho_0(\vec{r})] = V_s[\rho_0(\vec{r})] + V_X[\rho_0(\vec{r})]$$

Eq. 1-34

In this case, the total energy of the system can be obtained:

$$E[\rho_0(\vec{r})] = (T_s[\rho_0(\vec{r})] + T_c[\rho_0(\vec{r})]) + (V_s[\rho_0(\vec{r})] + V_X[\rho_0(\vec{r})]) + V_{ext}[\rho_0(\vec{r})]$$

Eq. 1-35

Both the T_C and V_X components can be addressed by the same term called exchange-correlation, V_{XC}. In this case, the total energy of the system can be rewritten as:

$$E[\rho_0(\vec{r})] = T_s[\rho_0(\vec{r})] + V_s[\rho_0(\vec{r})] + V_{XC}[\rho_0(\vec{r})] + V_{ext}[\rho_0(\vec{r})]$$

Eq. 1-36

This equation is known as the Kohn-Sham energy equation. Based on the KS equation, the Schrödinger equation for one electron of an N-electron system can be written as:

$$(T_i(\vec{r}) + V_i(\vec{r}) + V_{ext}(\vec{r}) + V_{XC}[\rho_0(\vec{r})])\varphi_i = \varepsilon_i\varphi_i$$

Eq. 1-37

where φ_i are the Kohn-Sham (KS) orbitals from which the electron density can be constructed:

$$\rho_0(\vec{r}) = \sum_i^N |\varphi_i(\vec{r})|^2$$

Eq. 1-38

Therefore, starting from an initial electron density, a new electron density can be obtained which can be more accurate than the initial one. This procedure can be performed by a self-consistent procedure which minimises the KS orbitals iteratively until it fulfils the convergence criterion.

The exact exchange-correlation functional is unknown and can only be obtained by approximation. Thus, the quality of the model describing an N-electron system depends on the quality of the exchange-correlation functional. It should be noted that the cancelation of the self-interaction error also relies on the approximated exchange-correlation functional.

1.5.4 Local Density Approximation (LDA)

The LDA is an approximation to the exchange–correlation (XC) energy functional which is based on the uniform electron gas (UEG) model. In the UEG, electrons are distributed uniformly in the system volume, moving in the external potential such that the total charge of the system remains neutral. With the LDA, the exchange-correlation energy functional can be computed by:

$$E_{XC}^{LDA}[\rho(\vec{r})] = \int \rho(\vec{r})\varepsilon_{XC}(\rho(\vec{r}))d\vec{r}$$

Eq. 1-39

where ε_{XC} is the exchange-correlation energy of a single electron of the UEG system with the electron density of $\rho(\vec{r})$. ε_{XC} can be decomposed into the exchange (ε_X) and correlation (ε_C) parts:

$$\varepsilon_{XC}(\rho(\vec{r})) = \varepsilon_X(\rho(\vec{r})) + \varepsilon_C(\rho(\vec{r}))$$

Eq. 1-40

The exchange function can be obtained by:

$$\varepsilon_X\left(\rho(\vec{r})\right) = -\frac{3}{4}\sqrt[3]{\frac{3\rho(\vec{r})}{\pi}}$$

Eq. 1-41

The exchange component of the LDA can be obtained exactly and the correlation component can be computed numerically to a high degree of precision. The LDA performs well for systems in which the electron density is constant or changes slowly as in solids like metals. However, for non-homogenous systems in which electron density changes more rapidly, such as molecules, the LDA gives a large error and hence, does not perform well. For example, LDA tends to overestimate bonding interactions and hence, bonds are too short.

1.5.5 Generalized Gradient Approximation

In molecular systems, the electron density has gradient which changes. Thus, the LDA can be improved by inclusion of the gradient of the electron density. Functionals which implement the gradient of the electron density as well as the electron density are called Generalised Gradient Approximation (GGA) functionals. In this approximation, the exchange-correlation functional energy (E_{XC}^{GGA}) can be obtained by:

$$E_{XC}^{GGA}[\rho_a, \rho_\beta] = \int f(\rho_a, \rho_\beta, \nabla\rho_a, \nabla\rho_\beta)d\vec{r}$$

Eq. 1-42

where ρ_α and ρ_β are electron densities with alpha and beta spin states while $\nabla\rho_a$ and $\nabla\rho_\beta$ are the reduced gradients, respectively. The E_{XC}^{GGA}can be decomposed into the exchange (E_X^{GGA}) and correlation (E_C^{GGA}) functionals:

$$E_{XC}^{GGA} = E_X^{GGA} + E_C^{GGA}$$

Eq. 1-43

There are different approaches to approximate the exchange and correlation energies. For instance, in 1988, Becke (B) and Perdew developed the GGA correlation functional (P86). The exchange and correlation functionals can be combined with each other. For example, combining the exchange (B) and correlation (P86) functionals gives the pure GGA functional known as BP86.[3] Alternatively, the exchange (B) can accompany other GGA correlation functionals such as LYP (developed by Lee, Yang and Parr) to give the BLYP functional.[4]

1.5.6 Meta GGA Functionals

As discussed above, GGA functionals use the electron density along with the first derivative of electron density ($\nabla\rho(\vec{r})$) to compute the exchange-correlation energy. Another class of DFT functional are the meta-GGA (MGGA) functionals which include additional terms to the GGA functionals, the second derivative of electron density ($\nabla^2\rho(\vec{r})$) and (or) the kinetic energy of electron density. The kinetic energy density (τ^{KS}) can be represented by:

$$\tau^{KS}(r) = \sum_{i=1}^{N} |\nabla\varphi_i(r)|^2$$

Eq. 1-44

in which summation of the kinetic energy of the occupied KS orbitals gives τ^{KS}. An example of MGGA functional is the Tao-Perdew-Staroverov-Scuseria functional (TPSS).[5]

1.5.7 Hybrid GGA Functionals

As discussed in the HF section, the exchange energy can be treated exactly under the HF approximation. Thus, an improvement to the DFT approximation can be achieved if some portions of the HF exchange were combined with approximated exchange-correlation functionals such as GGAs. Such functionals are termed hybrid GGA functionals (HGGA).

$$E_{XC}^{HGGA} = E_X^{HF} + E_{XC}^{GGA}$$

Eq. 1-45

HGGA functionals are based on adiabatic connection approximation which converts a non-interacting system to a fully interacting system to obtain the exchange-correlation energy:

$$E_{XC} = \int_0^1 < \psi(\lambda)|V_{XC}|\psi(\lambda) > d\lambda$$

Eq. 1-46

where λ describes the extent of inter-electronic interaction (V_{XC}). When $\lambda = 0$, there is a non-interacting system which only features the exact exchange energy component as in HF theory. With $\lambda = 1$, that system converts to a real, fully interacting system which features both exchange and correlation components. Therefore, different percentages of the HF exchange energy can be added to compute the DFT exchange-correlation energy:

$$E_{XC} = (1 - a)E_{XC}^{DFT} + aE_X^{HF}$$

Eq. 1-47

where a is the fraction of HF exchange and $(1 - a)$ is the term to avoid double counting of the HF exchange. In the case of $a = 0.5$, 50% of DFT exchange-correlation energy is replaced with 50% HF exchange energy. This is called the half-and-half method (HH). A very well-known example of a HGGA functional is B3LYP.[6] This implements three parameters to determine the composition of the exchange and correlation functional which is determined by parameterisation against experimental data sets. The exchange functional involves the LDA exchange (E_X^{LDA}), the B88 exchange (E_X^{B88}) and the exact HF exchange ($E_{XC}^{\lambda=0}$) functionals, while the correlation functional includes the LYP (E_C^{LYP}) and LDA (E_C^{LDA}) correlation functionals.

$$E_{XC}^{B3LYP} = (1 - a)E_X^{LDA} + a\,E_{XC}^{\lambda=0} + b\,E_X^{B88} + c\,E_C^{LYP} + (1 - c)E_C^{LDA}$$

Eq. 1-48

For B3LYP, the three parameters a, b and c are set to be 0.20, 0.72 and 0.81, respectively.

1.6 Basis Sets

Basis sets are generated to construct the approximated wave functions and hence, atomic (AOs) or molecular (MOs) orbitals. In this regard, the former (AOs) can be constructed by a mathematical function called a basis function while the latter (MOs) can be constructed by the combination of basis functions which is called basis set. The AOs for the hydrogenic systems can be accurately described by so-called Slater Type Orbitals (STOs). For example, the H 1s orbital is constructed by:

$$\phi_{1s}^{STO}(r) = \left(\frac{\zeta^3}{\pi}\right)^{\frac{1}{2}} e^{-\zeta r}$$

Eq. 1-49

where r is the distance from the nucleus and ζ is the Slater orbital exponent which controls the radial extent of basis function. STOs can give an accurate representation of hydrogenic atomic orbitals.

The e^{-r} term in STOs can be replaced by e^{-r^2} term to reduce the computational cost. This forms another type of basis functions termed as a Gaussian Type Orbital (GTO). With GTOs, the H 1s orbital takes the form of:

$$\phi_{1s}^{GTO}(r) = \left(\frac{2\alpha}{\pi}\right)^{\frac{3}{4}} e^{-\alpha r^2}$$

Eq. 1-50

where α acts similar to ζ and is the Gaussian orbital exponent. The representation of MOs with GTOs becomes computationally more accessible. However, GTOs change the shape of the wave function. For example, as shown in Figure 1-1**,** with an STO, the H 1s wave function features a cusp at r = 0 while with the GTO, there can be seen that the gradient at the point r = 0 becomes zero. In addition, the GTO wave function decays faster than the STO at longer distances. Therefore, GTOs provide a less accurate representation of wave functions than STOs.

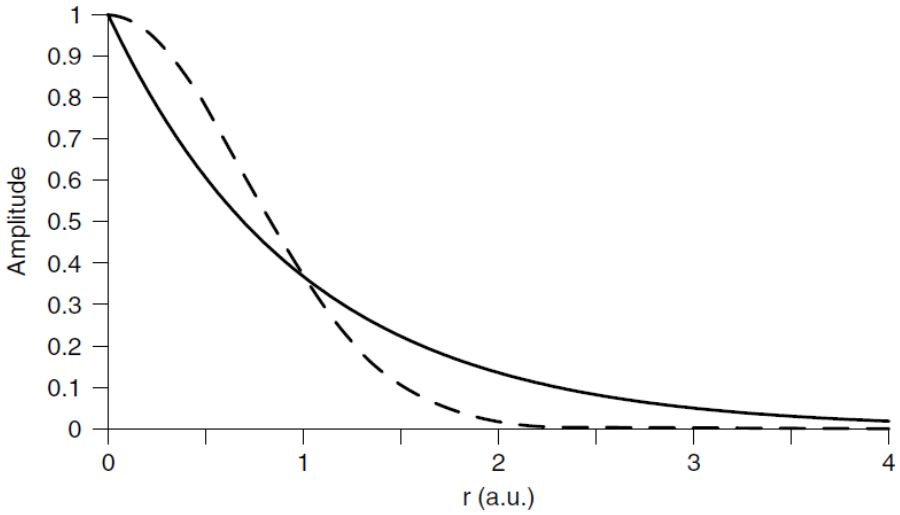

Figure 1-1. STO (solid line) vs GTO (dashed line) basis sets to describe the H 1s orbital.

In this regard, linear combination of GTOs can be used to increase the accuracy of GTOs, mimicking STOs. This combination forms so-called Contracted Gaussian Functions (CGFs). The individual components of a CGF are now termed primitive GTOs. The minimal example of CGFs is the STO-nG basis sets in which n is the number of primitive GTOs. The STO-1G basis set is the simplest example in which each atomic orbital is represented by one primitive GTO. For example, for a H_2 molecule, each 1s atomic orbital of the H atom is represented by one primitive GTO, giving two GTOs for the H_2 molecule. Increasing the number of basis functions can give more accuracy and flexibility to basis functions. This can be achieved by the linear combination of multiple CGFs. Such basis sets are called multiple ζ basis sets. For example, in double ζ basis sets, each AO is constructed based on two sets of CGFs.

1.6.1 Split-Valance Basis Sets

Due to the fact that core electrons do not participate in bonding interactions, some basis sets are developed based on the separation of core electrons from valence electrons. This type of basis sets are called split-valence basis sets. In this type of basis set core orbitals can be constructed by a single CGF while multiple CGFs can be used to construct the valence orbitals. Popular examples of split-valance basis sets are Pople basis sets such as 3-21G, 6-21G, 6-311G basis sets are valence-multiple-ζ basis sets. In such basis sets, the

first number denotes the number of GTOs used in a single CGF describing the core electrons while the second set shows the number of GTOs implemented in a multiple CGF to represent the valence electrons. For example, 6-311G basis set implements a single CGF to represent core orbitals and composed of 6 primitive GTOs while the valence electrons are constructed by a triple CGFs composed of 3, 1 and 1 primitive GTOs, respectively.

1.6.2 Polarisation Functions

When two atoms interact with each other to form a bond, their electron clouds are polarised toward each other. Therefore, the basis function which represents the AOs should be adequately flexible to capture the electron cloud distortion. This can be achieved by addition of so-called polarisation function to the basis set.[7] Polarisation function adds a p-function to the s orbital of the first row elements (H and He) and a d-function to the p-orbitals of p-block elements. This results in a further improvement in the flexibility of the basis set. One of the common examples of such basis sets is 6-311G** in which the first and second stars denote d- and p-polarisation functions, respectively.

1.6.3 Diffuse Functions

Electron density can be localised far from the valence region.[8] This situation can specifically be seen in anions. Thus, for greater accuracy to describe the diffuse electron density, standard basis sets can be augmented with s and p functions. For the Pople basis sets, diffuse functions are represented by sign '+' (plus). Addition of one + denotes the diffuse p-function for non-hydrogenic atoms and double ++ shows an extra s-function for H and He atoms.[9] For example, adding diffuse p- and s-functions to 6-311G basis set gives the augmented basis set, the 6-311++G basis set.

1.6.4 Pseudopotentials

The split-valence basis sets implement more primitives for core electrons than valence electrons. However, when going to heavier atoms, the explicit treatment of all electrons

becomes extremely expensive. Since core electrons do not participate in bonding interactions, they can be described by further approximations to reduce the computational cost. An example of such an approximation is to replace the core electrons of atoms with an effective core potential (ECP). Such an approach is called the pseudopotential approximation in which the core electrons are implicitly treated whereas the valence electrons are described explicitly.

Two commonly used examples are the Stuttgart-Dresden (SDD)[10] and Hay-Watt (known as Los Alamos National Laboratory (LANL))[11] pseudopotentials.

1.7 Solvent Effects

Since the majority of chemical reactions occur in condensed phases such as solution, it is crucial to consider the solvent effect on the electronic structure. In this regard, one way to represent the solvent effect is to explicitly represent the solvent molecules.[12] In this model, layer(s) of the solvent molecules surrounds the solute molecules explicitly to give a cluster-like structure. Due to the large number of the solvent molecules, many conformations for this cluster can be expected. This leads to a large number of local minima on the cluster potential energy surface (PES). Therefore, extensive statistical sampling is required to determine the most stable conformation and this is computationally very demanding.

Another method to describe solvent is the implicit treatment of solvent molecules. In this model, the solvent molecules can be displaced with a homogenous dielectric medium such that the main features of the solvent are approximated. This indeed demands particular attention to the physical properties of solvent and solute, before and after their interactions with each other (i.e. solvation process). The main contributing components in the solvation process are the cavitation process and the electrostatic (repulsive and attractive) interactions.[13]

In the first step of solvation process, when a solute molecule enters from gas phase to solution phase, it creates a cavity in the medium to accommodate the solute. This process comes with some energetic cost called cavitation energy as it changes the bulk structure of the medium. In the next step, due to the electrostatic interaction between the cavity surface and the medium, both can undergo charge distribution rearrangement. The charge polarisation of the solute is such that it induces an instantaneous dipole moment in the medium. The dipole moments of the solvent and solute then orient in a way to oppose

each other. This therefore forms a favourable electrostatic interaction between the medium and solute.

Two frequently used continuum models are the conductor-like PCM (C-PCM) and dielectric PCM (DPCM).[14]

1.8 Treatment of Dispersion Interactions in DFT

Dispersion interaction is the stabilising component of van der Waals interactions.[15] This interaction arises from long-range electron correlation which can be described by the r^{-6} term in the Lennard-Jones (LJ) model:[16, 17]

$$V_{LJ} = \varepsilon \left[\left(\frac{r_m}{r} \right)^{12} - 2 \left(\frac{r_m}{r} \right)^{6} \right]$$

Eq. 1-51

where ε represents the van der Waals depth which is the strength of the van der Waals interaction, r is the interatomic distance and r_m is the distance at which the potential passes through a minimum. The r^{-12} term is related to the short range interactions and represents the repulsive component due to interaction of the electron clouds of two atoms; while the r^{-6} term shows the attractive interaction in middle-range distances. As shown in Figure 1-2, at long-range distances, as the interatomic distance reduces, the potential energy of system decreases. This is mainly due to the fact that at the shorter distances, an instantaneous dipole on one atom induces a complementary dipole on a neighbouring one. This results in an attractive interaction between two atoms which stabilises the system.

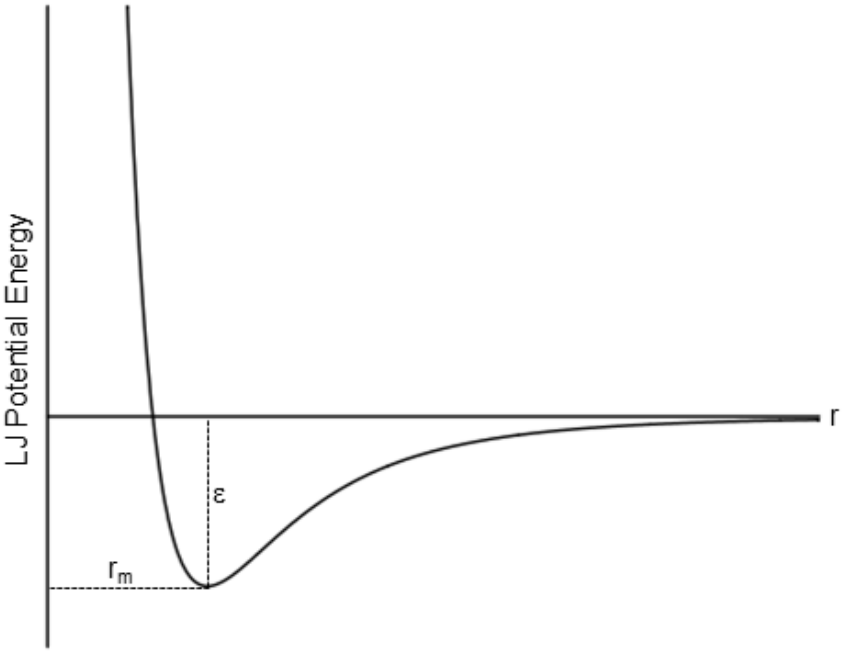

Figure 1-2. The LJ potential energy of a diatomic system with respect to the interatomic distance.

The contribution of such interactions in the total energy can be significant.[18, 19] Therefore, to obtain more accurate results, dispersion should be taken into account. However, long-range electron correlation is not accurately described by DFT functionals.[20] Therefore, one approach has been to incorporate some empirical terms into density functionals.[21] In this regard, Grimme and co-workers developed empirical dispersion terms such as D3.[22-24]

In order to avoid double counting of the short and middle range correlation, a damping function is required for D3 correction to switch off the r^{-6} function. In this regard, a finite-damping function has been proposed by Becke and Johnson[24] (D3BJ). As shown in Figure 1-3, with the zero-damping function, the dispersion energy tends to infinity at short distances (i.e. $R \rightarrow 0$). On the other hand with D3, the dispersion energy goes to zero at short distances. However, the contribution of the dispersion energy should be almost constant in short distances. This issue is addressed in the finite-damping function of D3BJ dispersion correction.

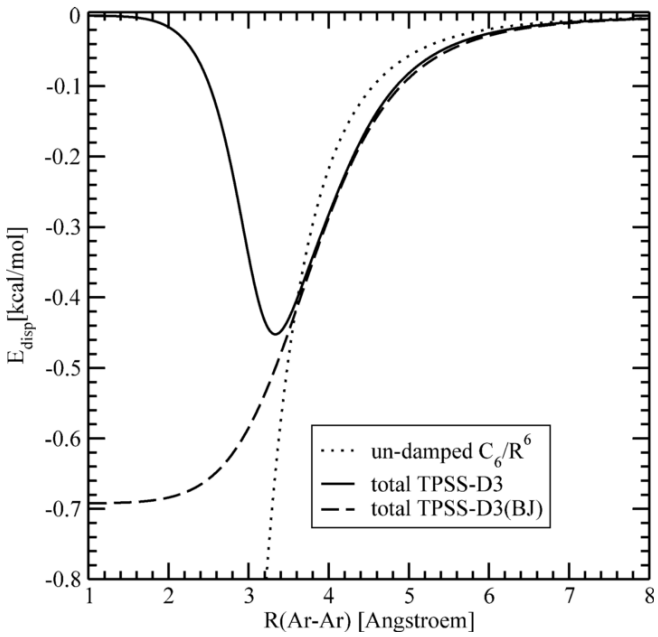

Figure 1-3. Effect of damping function on dispersion energy at short and middle range distances.

1.9 Quantum Theory of Atoms in Molecules

The quantum theory of atoms in molecules (QTAIM) was developed by Bader and co-workers to assess the electron density ($\rho(r)$) topology and provide a bonding scheme. This methodology implements the first (i.e. the gradients) and second derivatives of electron density (i.e. the curvatures).[25] The former vanishes in some certain points of the electron density called critical points (CPs). The latter can identify the properties of CPs. This can be obtained by the Hessian matrix of the electron density:

$$A(r_c) = \begin{pmatrix} \frac{\partial^2\rho}{\partial x^2} & \frac{\partial^2\rho}{\partial x\,\partial y} & \frac{\partial^2\rho}{\partial x\,\partial z} \\ \frac{\partial^2\rho}{\partial y\,\partial x} & \frac{\partial^2\rho}{\partial y^2} & \frac{\partial^2\rho}{\partial y\,\partial x} \\ \frac{\partial^2\rho}{\partial z\,\partial x} & \frac{\partial^2\rho}{\partial z\,\partial y} & \frac{\partial^2\rho}{\partial z^2} \end{pmatrix}$$

Eq. 1-52

Diagonalisation of the Hessian matrix then transforms it into:

$$\Lambda = \begin{pmatrix} \frac{\partial^2 \rho}{\partial x^2} & 0 & 0 \\ 0 & \frac{\partial^2 \rho}{\partial y^2} & 0 \\ 0 & 0 & \frac{\partial^2 \rho}{\partial z^2} \end{pmatrix} = \begin{pmatrix} \lambda_1 & 0 & 0 \\ 0 & \lambda_2 & 0 \\ 0 & 0 & \lambda_3 \end{pmatrix}$$

Eq. 1-53

where λ_1, λ_2 and λ_3 are the curvatures of the electron density with respect to the x, y and z coordinates. For a CP, the number of non-zero curvatures, denoted by the rank (ω), is three. However, the curvatures can be either positive (local minima) or negative (local maxima). The algebraic sum of the eigenvalues, denoted by the signature (σ), determines the type of CP. According to the rank and signature of the curvatures (ω, σ), CPs can be classified into four types: (3, -3) nuclear critical points (NCPs), (3, -1) bond critical points (BCPs), (3, +1) ring critical points (RCPs) and (3, +3) cage critical points (CCPs). An example which features all four types of CPs is cubane (Figure 1-4). Cubane features a BCP between C and H atoms, an RCP in the centre of the four-membered ring and a CCP situated in the centre of the cage composed of six rings.

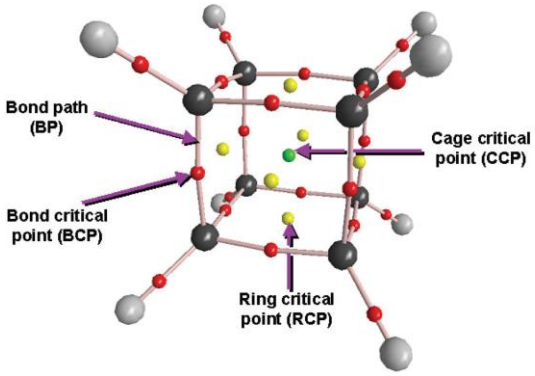

Figure 1-4. The molecular graph of cubane; CPs are shown with different colours: NCP (color-coded by element: C = black, H = grey), BCP (red dots), RCP (yellow), and CCP (green).[25]

In the context of a diatomic system featuring a BCP, there is a line which connects the locally maximum electron density at the nuclei through the minimum electron density, the BCP. The characteristics of BCPs can be assessed by the sum of the second derivatives

of the electron density with respect to three coordinates (i.e. the Laplacian of the electron density, $\nabla^2\rho(r)$):

$$\nabla^2\rho(r) = \lambda_1 + \lambda_2 + \lambda_3$$

Eq. 1-54

A positive Laplacian is indicative of charge density depletion while a negative Laplacian shows the accumulation of charge density.

Another parameter which can help to identify the nature of the interaction between two atoms is the total energy density, H(r). This element is composed of two elements: the kinetic energy density G(r) and the potential energy density, V(r). G(r) is always positive while V(r) is always negative. Summation of G(r) and V(r) gives the total energy density H(r). If G(r) dominates over V(r), it gives a positive H(r) while the dominance of V(r) over G(r) gives a negative H(r) value.

Based on the value of $\rho(r)$ and the sign of $\nabla^2\rho(r)$ and H(r) associated with a BCP, the nature of the interaction between two atoms can mainly be classified into shared and closed shell interactions.[26] As shown in Scheme 1-1, in shared interactions such as covalent bonds, BCPs feature a large $\rho(r)$, a negative $\nabla^2\rho(r)$ and a large negative $H(r)$. In the case of closed shell interactions such as ionic interactions, BCPs exhibit small $\rho(r)$, a positive $\nabla^2\rho(r)$ and a positive $H(r)$. Between these two extremes, there is also another type of classification called transit closed shell interactions which are less clear-cut than the two other types.[27] In transit closed shell interactions such as dative bonds, BCPs feature small $\rho(r)$, positive $\nabla^2\rho(r)$ but a negative small $H(r)$ close to zero.

Scheme 1-1. Classification of atomic interactions [26, 27]

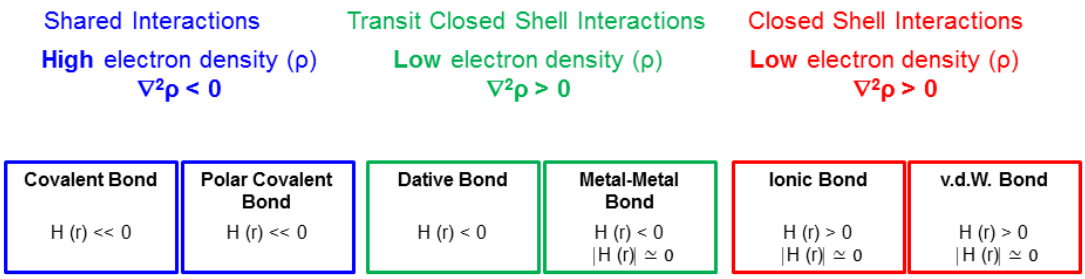

Both ρ(r) and H(r) values can be used to probe the strength of interaction between two atom centres. Higher values of ρ(r) and $|H(r)|$ are indicative of stronger interactions. However, in some cases, BCPs feature very small ρ(r) values. In particular, this situation can be seen when hydrogen atoms are connected to heavy atoms such as transition metals. In this case, using the H(r) values provide more reliable results than the ρ(r) values.[28] It is worth mentioning that in some cases, the BCPs along the TM–H bond paths can be situated in the region of charge density depletion (i.e. $\nabla^2\rho(r) > 0$).[28-29] Thus, the H(r) values also can give a better description of the nature of the TM–H bonding.

There is another element called bond ellipticity (ε) which shows the preferential accumulation of electron density in a given plane and can be obtained by:

$$\varepsilon = \frac{|\lambda_1|}{|\lambda_2|} - 1$$

Eq. 1-55

Ellipticities equal to zero ($\lambda_1 \cong \lambda_2$) show a spherically symmetric bond while non-zero ellipticities ($\lambda_1 > \lambda_2$) determines a cylindrically symmetric bond. This parameter can be used to assess the σ or π character of an interaction between two atom centre. However, in some cases, the bond ellipticity is ambiguously high.[30] Such situation specifically can be seen when a BCP features a very small electron density.

1.10 Bonding Analysis by Natural Bonding Orbital Approach

The idea of Natural Bond Orbital (NBO) approach was developed by Weinhold and co-workers to represent the Lewis structure of many-electron systems.[31] This methodology exploits single-detrimental wave function of a many-electron system to produce localised orbitals called natural atomic orbitals (NAOs).

Once NAOs are constructed, the NBO algorithms provide a set of NBOs which represent the filled and vacant orbitals. This is determined by the electron occupancy of the NBOs. NBOs with significant occupancies are expected to be seen in 1-centre regions (e.g. core electrons) and 2-centre regions (e.g. bonding orbitals). There are also some situations where the electron occupancy is significant in 3-centre regions. The unoccupied or partially occupied 1- or 2-centre regions account for vacant or anti-bonding orbitals. Collection of these orbitals then produces the best set of NBOs to accurately describe the wave function and hence, the total electron density of a many-electron system to represent the Lewis structure. This is achieved by a systematic procedure which tries to fulfil the NBO criteria from which a large fraction of electron density (%-ρ_L) can be captured by the given Lewis structure. The Lewis structure often accounts for more than 99% of the total electron density. The residual non-included electron density is referred as the non-Lewis NBOs (%-ρ_{NL}).

The NBO program can also compute donor-acceptor type interactions between two NBOs. Such interactions represent dative interactions where one NBO is an electron-donor (*i*) (e.g. a bonding orbital) and the other NBO is electron-acceptor (*j*) (e.g. an electron acceptor). The strength of this interaction can be assessed by stabilisation energy (E(2)) between two NBOs.

Chapter 2 – Introduction to Transition Metal Complexes Featuring Supported or Unsupported Metal-Metal Bonds with Zn, Ga and In

Transition metal (TM) complexes featuring main group metal moieties have received increasing attention due to a variety of applications in synthesis[32], catalysis[33] and materials[34] chemistry. Such species can be synthesised based on the concept of Lewis acid-Lewis base theory.[35, 36] For example, group 12 elements such as Zn can act as Lewis acidic moiety and hence bind to Lewis basic TM centres.[37-41] This has been extensively used in catalysis such as C–C coupling reactions.[42-44] However, examples of isolated heterobimetallic species featuring a TM–Zn bond are rare. In contrast, TM complexes containing group 13 metal elements have attracted considerable attention in TM coordination chemistry. This is due to the versatile bonding and coordination modes of group 13 elements which can tune the reactivity at TM centres and hence, bring interesting reactivities at TM centers such as H_2 and CO_2 activation.[45-49]

Herein, the first part of this chapter briefly summarizes the experimental and computational findings reported for heterobimetallic complexes of TMs with Zn. The second section then describes the experimental and computational findings for complexes that combine TMs with group 13 moieties.

2.1 Heterobimetallic Complexes of TMs with Group 12 Fragments

It is postulated that TM-Zn species can be formed as an intermediate in transmetalation step of Negishi cross-coupling reactions.[50-53] Thus, isolation and characterization of these species can give useful information about the understanding of the transmetalation step and subsequently, help to modify and develop C–C coupling reactions. In this regard, Bergman, Tilley and co-workers reported the reaction of [(phen)PtAr$_2$] (phen = 5,6-dihydro-1,10-phenanthroline, Ar = 4-tert-butylphenyl), **1**, with Zn(C_6F_5)$_2$ (Figure 2-1).[54] This reaction results in the formation of the heterobimetallic species **2**. The X-ray crystal structure of **2** shows that the divalent Zn moiety is situated in the apical position of the square pyramidal geometry of Pt, acting as a Z-type ligand. The Pt–Zn bond distance is 2.5526(5) Å which is shorter than sum of the covalent radii of Zn and Pt, consistent with a Pt→Zn bond.

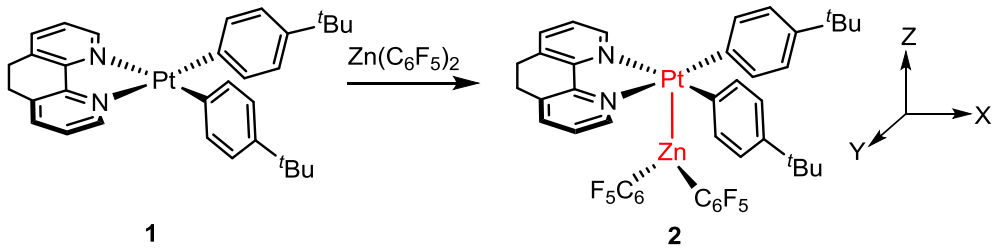

*Figure 2-1. Formation of the heterobimetallic species **2** by reaction of **1** with Zn(C_6F_5)$_2$.*

The authors then studied the effect of the chelating ancillary ligands on the coordination mode of the divalent Zn ligand. They used the dmpe (1,2-bis(dimethylphosphino)ethane) analogue of **1**, complex **3**. As shown in Figure 2-2, reaction of **3** with Zn(C_6F_5)$_2$ produces **4** in which the Zn moiety is situated in the coordination plane of the Pt complex. **4** exhibits a Pt–Zn distance of 2.7368(4) Å which is significantly longer than the Pt–Zn bond in **2** (2.5526(5) Å). However, the Pt–Zn distance in **4** is still shorter than sum of the covalent radii of Pt and Zn centres. This shows that **4** exhibits a Pt–Zn bond which is weaker than that in **2**.

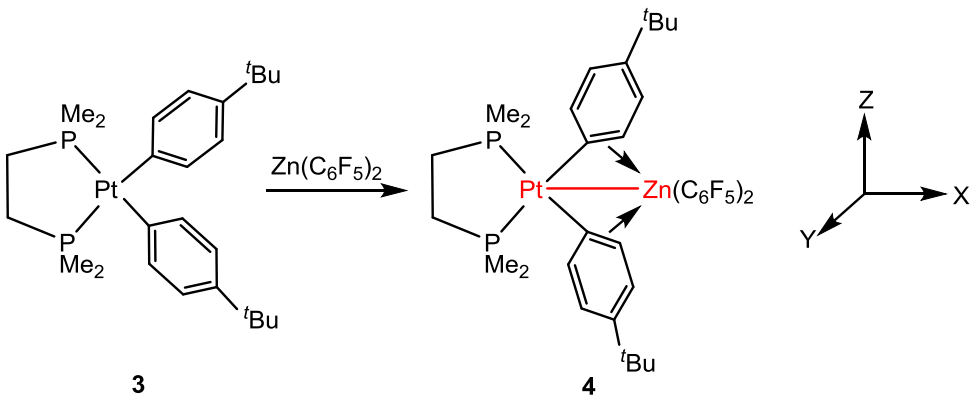

3 4

*Figure 2-2. Reaction of **3** with the divalent Zn precursor to give Pt-Zn complex **4**.*

Energy decomposition analysis (EDA) on the apical and aryl-bridged isomers of **2** and **4** shows that **2** is +7.7 kcal/mol more stable than the aryl-bridged isomer whereas **4** is +1.1 kcal/mol more stable than the apical isomer. The authors attributed this to the nature of the backbone ligands and postulated that the phen-supported species **2** has a higher electron density at the Pt centre compared with that in the phosphorus-supported species **4**. This results in the apical coordination of the divalent Zn moiety in the former while in the latter, coordination of the Zn moiety is more favoured in the equatorial plane of the Pt complex, probably due to interaction with the aryl groups.

Charge transfer analysis based on the complementary occupied–virtual pairs (COVPs) method shows that **4** has charge density flow from the Pt d_z^2 orbital to the Zn p_z orbital, indicating a Pt→Zn bond. It also shows that C_{ipso}–C π-bonds donate electron density to the Zn moiety while there is a small interaction between one of the d orbitals of the Zn to the Pt–C_{ipso} anti-bonding orbitals.

It is interesting to note that withdrawal of electron density from the Pt centre by the divalent Zn moiety makes the Pt(II) centre more electron deficient. This therefore increases the Pt propensity to undergo C–C reductive coupling reaction to form biaryl products. In **2**, the donor-acceptor interaction between the Pt and Zn moiety is stronger than that in **4**. Thus, the Zn moiety withdraws more electron density from the Pt centre in the former. As a result, the C–C coupling process to form the biaryl product is faster in **2**.

Chen and co-workers also reported the formation of the heterobimetallic species **6** by the reaction of the Pd(II) complex **5** with $Zn(C_6F_5)_2$ (Figure 2-3).[37] The molecular structure of **6** derived from the X-ray crystal structure exhibits an unsupported Pd–Zn bond in

which the Pd centre acts as a Lewis base moiety and the divalent Zn moiety acts as the Lewis acid moiety. It can also be seen than the Zn centre is slightly oriented toward the C_{ipso} position of the benzoquinoline ligand to give a short Zn–C_{ipso} distance of 2.47 Å. EDA-NOCV analysis (Energy Decomposition Analysis combined with the Natural Orbitals for Chemical Valence) of **6** identifies a Pd–Zn bonding orbital composed of the Pt d_z^2 orbital and the Zn p_z orbital. A QTAIM (Quantum Theory of Atoms in Molecules) analysis of **6** shows no BCP (Bond Critical Point) between the Zn and C_{ipso} centres, showing no interaction between these atoms; suggesting the heterobimetallic species is mainly stablised by the metal–metal covalent interaction.

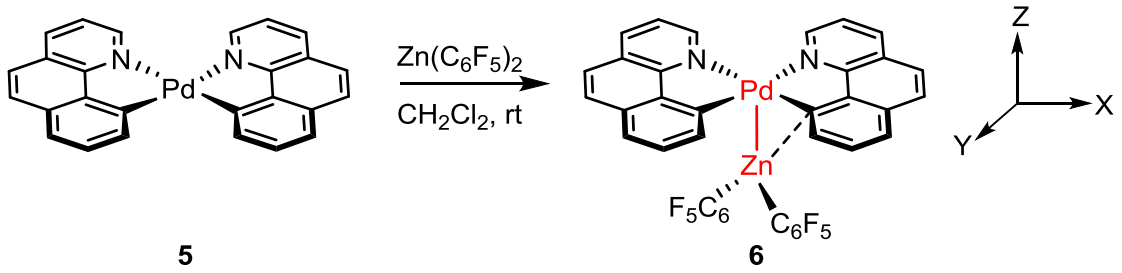

*Figure 2-3. Formation of the heterobimetallic species **6** by the reaction of **5** with the Zn precursor.*

Stasch, Jones and co-workers investigated the reactivity of divalent group 12 precursors at $Pt(PCy_3)_2$ (Cy = cyclohexyl).[55] As shown in Figure 2-4, with $ZnBr_2$ and CdI_2, this reaction generates the LB-LA adduct **8**, $[Pt(PCy_3)_2(MX_2)]$. However, with HgI_2, Hg–I bond activation occurs at the Pt centre via an oxidative addition mechanism and forms trans-$[(Cy_3P)_2(I)Pt(HgI)]$, **9**. One might expect the formation of a LB–LA adduct with the Hg reagent rather than the Cd reagent as the former is a stronger Lewis acid. It should be however noted that the Hg–I bond is weaker than the Cd–I bond. Thus, activation of the former is more feasible as observed experimentally. Thus, the different reactivities of the group 12 precursors at the Pt(0) species can be related to a set of factors including the Lewis acidity of the group 12 metal centre and the M–halide bond strength.

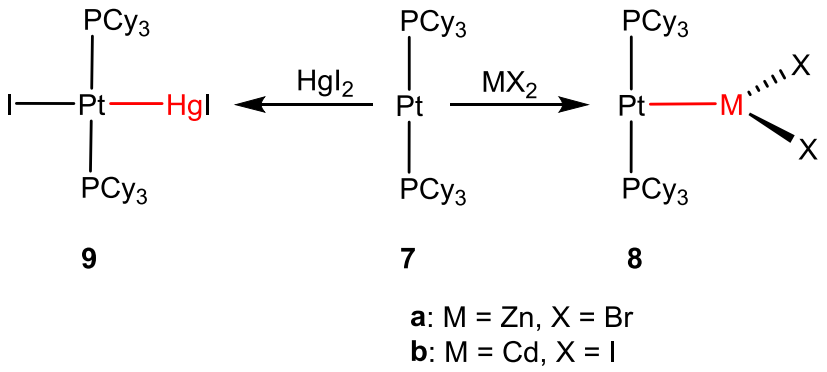

*Figure 2-4. Formation of the LA–LB adduct **8** with $ZnBr_2$ and CdI_2 and the oxidative addition product **9** with HgI_2.*

Ozerov and co-workers reported Zn–Ph bond activation at the Rh(I) complex **10** (Figure 2-5).[42] In this process, dissociation of TBE (tertbutylethylene) from the Rh centre paves the way for the insertion of the Rh(I) centre into the Zn–Ph bond to yield the pentacoordinated Rh(III) species **11**.

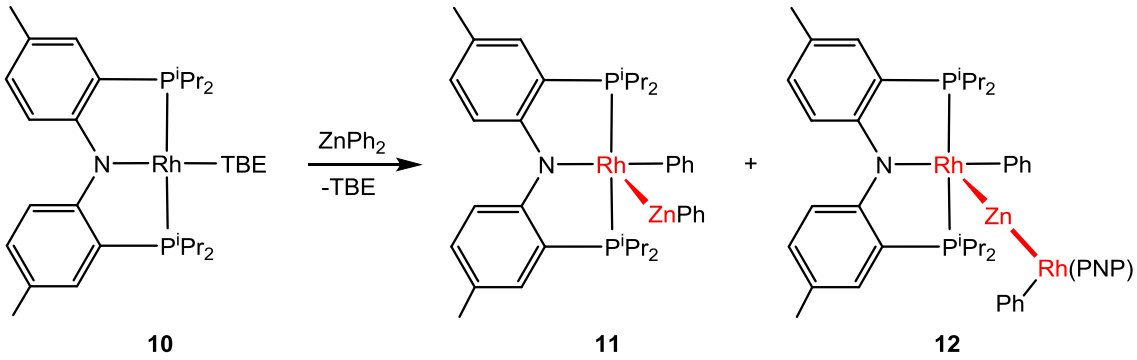

*Figure 2-5. Formation of the pentacoordinated Rh(III) species **11** and **12** by activation of Zn–Ph bond at **10**.*

Interestingly, **11** can undergo Zn–Ph bond activation at the Rh centre of a second molecule of **10** to give **12**. In both **11** and **12**, the Zn moiety is trans to a vacant site and as stated by the authors, this implies that the divalent Zn moiety displays a high trans influence.

Heterobimetallic species featuring mono-substituted group 12 moieties were also reported by other researchers. Zhivotovskii, Apeloig and co-workers investigated the activation of M–Si bonds (M = Zn and Hg) at Pt species **13** (Figure 2-6).[56] They showed that Pt(0) can activate the M–R bond of two molecules of MR_2 to yield a mixture of hexacoordinate complexes **14** and **15**. In **14**, the two MR moieties are situated in the equatorial position, cis to each other. In **15**, one of the MR moieties is in the axial position, trans to the R ligand and the other MR moiety is in the equatorial plane trans to the phosphine ligand. Interestingly, with the Zn precursor, isomer **14** is the major product (**14**:**15** = 63%:37%) while with the Hg precursor, isomer **15** is the major product (**14**:**15** = 26%:74%).

A DFT study on models of Pt-M species **14** and **15** (R = $SiMe_3$, B3LYP/ TZVP basis set) shows that for Zn, isomer **14** is +1.2 kcal/mol more stable than **15** and for Hg, isomer **15** is +1.5 kcal/mol more stable than **14**. This suggests that the higher yield of one isomer versus the other isomer can be controlled thermodynamically.

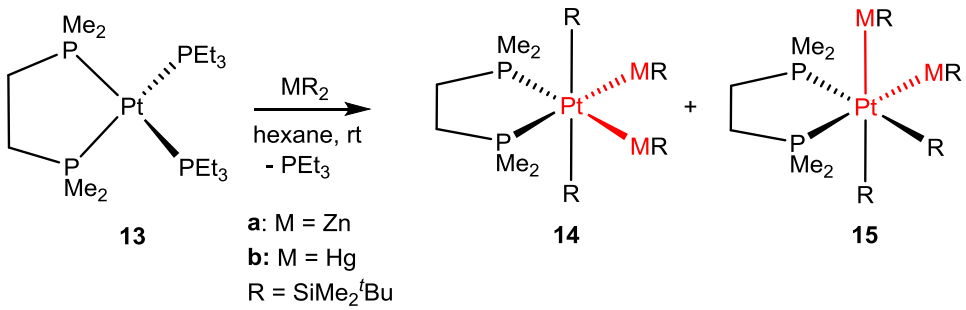

*Figure 2-6. Formation of heterobimetallic Pt-M species **14** and **15** by the reaction of **13** with MR_2 precursors.*

Interestingly, reaction of **13** with metal precursors featuring sterically bulkier silyl substituents than $SiMe_2{}^tBu$ ($SiMe{}^tBu_2$) involves only one molecule of the metal precursor (Figure 2-7). In this reaction, insertion of the Pt centre into the M–R bond generates the tetracoordinate Pt(II) complex **16**.

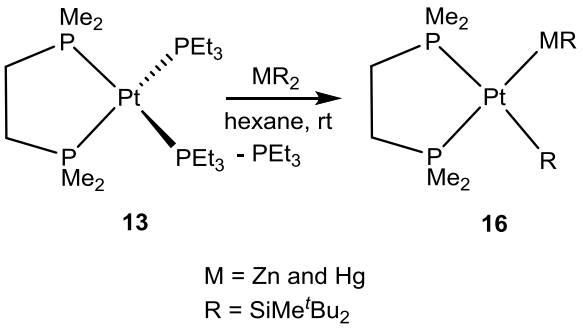

*Figure 2-7. Activation of one molecule of MR_2 at the Pt complex **13** to yield the heterobimetallic species **16**.*

Fischer and co-workers investigated the reactivity of $ZnMe_2$ with $[Ru(PCy_3)_2(\eta^2\text{–}H_2)_2(H)_2]$, **17** (Figure 2-8).[41] Interestingly, the electron deficiency of Ru along with the presence of the Ru-H moieties in **17** causes the activation of the Zn–Me bond to be followed by the elimination of methane to produce **18**. The X-ray crystal structure of **18** exhibits two {ZnMe} moieties situated in the equatorial plane, trans to each other with the Ru···Zn motifs bridged by two hydride ligands (Ru···Zn = 2.436(1) Å).

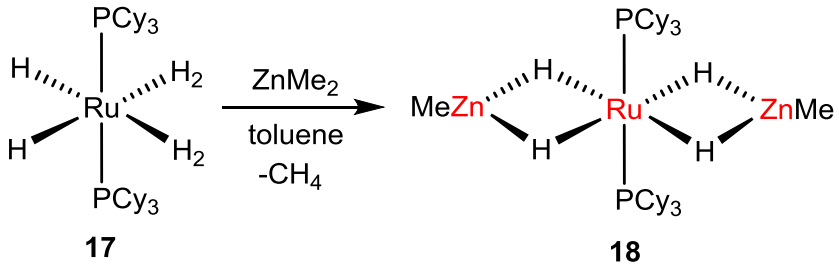

*Figure 2-8. Formation of the Ru-Zn complex **18** and methane by reaction of $ZnMe_2$ with **17**.*

As outlined above, Zn–R bonds can be activated at TM centres to form TM–Zn and TM–R bonds. However, this also depends on the nature of the TM centre. For example, Crimmin and co-workers investigated the reaction of the β-diketiminato (nacnac)-stabilized Zn–H precursor **19** with different TM species (Figure 2-9).[57] Reaction of **19** with $[Cr(CO)_6]$ produces the σ-zincane species **20**. In **20**, the terminal Zn–H bond donates electron density to the TM centre via a three-centre two-electron interaction (3c-2e). With $[Co(CO)_2(Cp)]$ which is more electron rich than $[Cr(CO)_6]$, **21** is formed in which the

hydride is more evenly shared between the metal centres. Going to an even more electron-rich complex, $[Rh(H)_2(SiEt_3)_2(Cp^*)]$, oxidative addition of the Zn–H bond occurs at the Rh centre to produce **22**. **22** exhibits a terminal Rh–H which donates electron density to the Zn moiety.

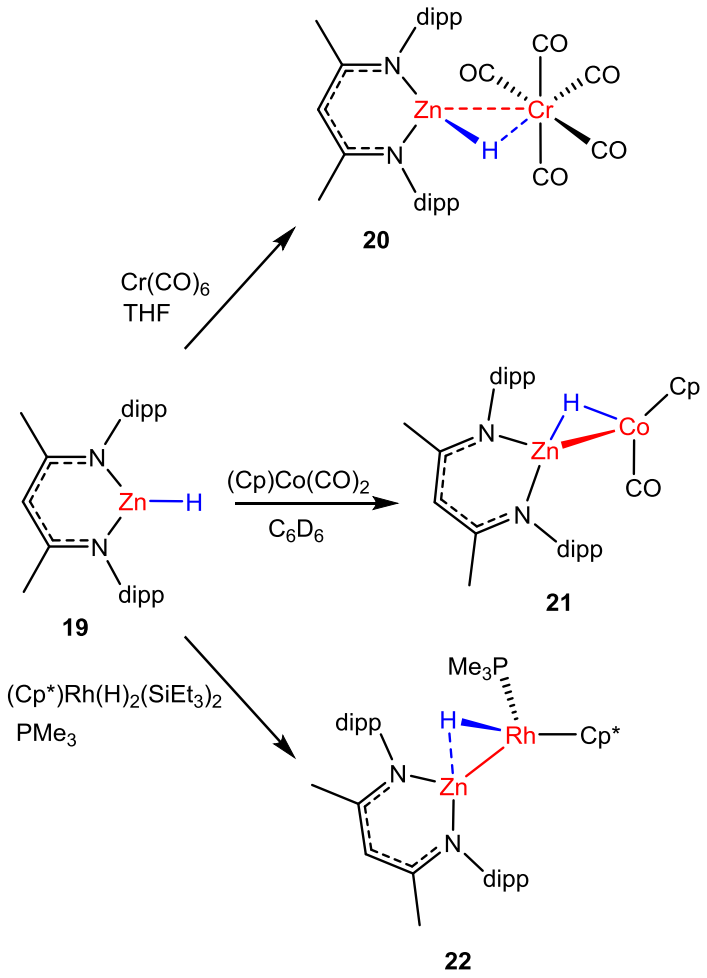

Figure 2-9. Trajectory of Zn–H bond activation at TM centres.

Natural Bond Orbital Wiberg bond index (NBO WBI) analysis of the TM–Zn bond in **20**, **21** and **22** shows that **22** has the highest value of WBI (WBI; **20** = 0.08, **21** = 0.21 and **22** = 0.39) and hence, features the strongest metal–metal interaction. It can also be seen that going from **20** to **21** and **22**, the NBO charge of the Zn centre becomes less positive (**20** = +1.51, **21** = +1.42 and **22** = +1.26). The decreasing trend of positive charge of the Zn centre shows that **22** accepts the greatest electron density from the TM moiety.

As outlined above, formation of σ-zincane species is more likely with more electron-deficient TM species. Using group 6 TM complexes (TM = Cr, Mo, W), Crimmin and co-workers reported the first examples of bis(σ-zincane) species.[58] As shown in Figure 2-10, reaction of the Zn–H precursor **19** with [TM(CO)$_6$] produces the bis(σ-zincane) species **23** where the Zn–H moieties are situated cis to each other with a Zn–H···H–Zn arrangement. With Mo and W precursors, the trans-isomer species **24** is also observed in solution. However, on the basis of NMR results, the cis isomer is found to be more stable than the trans isomer. The preference of the Zn–H···H–Zn arrangement over the Zn–H···Zn–H or Zn–Zn···Zn–H arrangements is due to less steric hindrance in the first arrangement. This also allows the interaction of the Zn moiety with the equatorial CO ligands which gives stability to the system.

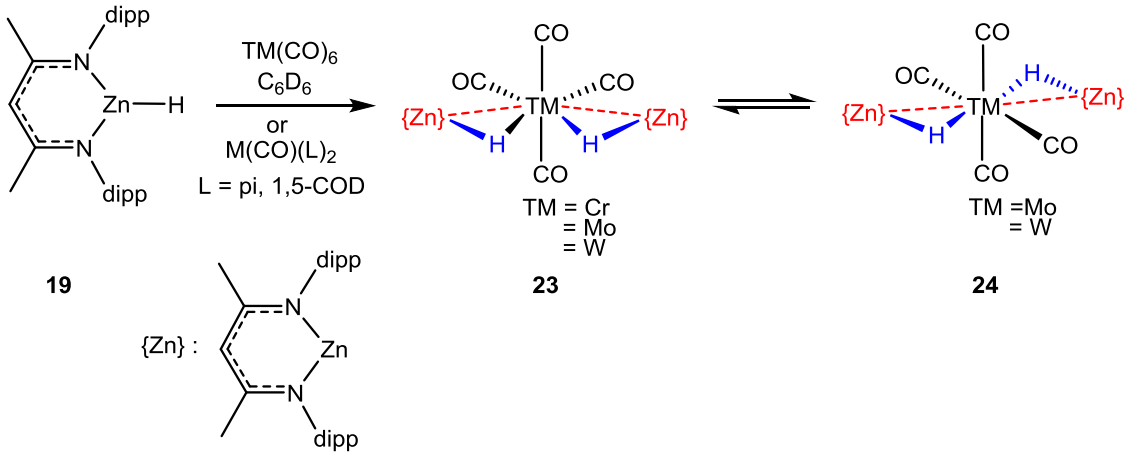

*Figure 2-10. Formation of the bis(σ-zincane) isomers **23** and **24** by the reaction of Zn–H precursor **19** with the TM precursor.*

TM complexes featuring more than two Zn moieties were also reported by Fischer and co-workers. The authors reported [TM(Cp*)(ZnCp*)$_3$] (TM = Ni and Pt), **25**.[59] **25** is formed by the reaction of [TM(COD)$_2$] (TM = Ni and Pt) with $Zn_2Cp^*_2$ (Figure 2-11). This reaction also results in the formation metallic Zn(0). Formation of **25** and metallic Zn(0) is postulated to involve a sequence of processes. Initially, dissociation of COD ligands from the TM centre provides a vacant site for the homolytic cleavage of Cp*Zn–ZnCp* bond to form two TM–Zn bonds. Activation of the second Cp*Zn–ZnCp* bond

forms another TM–Zn bond and a {Zn(I)Cp*} fragment. Transfer of Cp* from {Zn(I)Cp*} to the TM centre then forms a TM-Cp* bond and reduces Zn(I) to Zn(0).

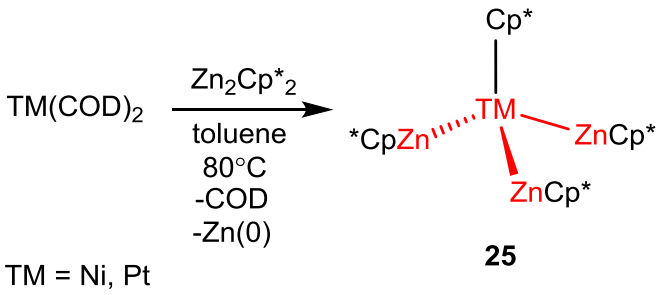

*Figure 2-11. Formation of Ru-Zn species **25** and metallic Zn(0) by the reaction of Zn precursor with [TM(COD)$_2$].*

The heterobimetallic species outlined above exhibit an unsupported TM–Zn bond. There are also a few examples of heterobimetallic species featuring a supported TM–Zn bond. For instance, Chen and co-worker reported the synthesis of the Ru-Zn species **27** (Figure 2-12).[39] The X-ray crystal structure analysis of **27** shows that the Ru–Zn interaction is supported by two bidentate ligands (diphenyl-2-pyridylphosphine). Comparison of the CO stretching frequencies of **27** with **26** shows that the latter has a lower CO stretching frequency (**26**: 1897 cm^{-1}; **27**: 2041 cm^{-1}, 1981 cm^{-1} and 1966 cm^{-1}). This indicates electron density flow from the Ru centre to the Zn moiety, i.e. a Ru→Zn interaction. **27** features a Ru–Zn distance of 2.659(1) Å which is slightly longer than the sum of the covalent radii of the Ru and Zn centres (2.50 Å). With respect to this and also the fact that **27** is a Ru(0) complex with a divalent Zn moiety, **27** exhibits a weak Ru→Zn interaction.

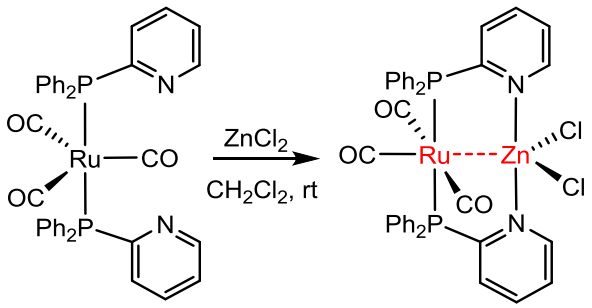

26 **27**

*Figure 2-12. Incorporation of $ZnCl_2$ into the ligand scaffold of the bidentate ligand of **26** to give the Ru-Zn species **27**.*

The cadmium congener of **27** (**27_Cd**) was also isolated by the authors. **27_Cd** has a Ru–Cd distance of 2.705(1) Å which similar to the Zn congener, is slightly shorter than sum of the covalent radii of the Ru and Cd centre (2.73 Å). This is suggestive of a slightly stronger metal–metal dative interaction in the Cd congener than the Zn congener.

Doerrer and co-workers also reported the synthesis of the heterobimetallic Pt-Zn species **28** and **29**. They showed that the strength of the Pt–Zn interaction can strongly be affected by the axial ligand at the Pt centre.[60] The former has a considerably shorter Pt–Zn bond (Pt–Zn: **28** = 2.5313(7) Å and **29** = 2.6180(5) Å). The authors investigated a series of Pt-M complexes (M = Co, Ni and Zn) and found a correlation between the Pt–M and Pt–L distances. This shows that as the Pt–L distance becomes shorter, the Pt–M distance decreases. In both **28** and **29**, the Zn centre is supported by electron-withdrawing groups which make it a significantly electropositive centre. On the other hand, the presence of the axial ligand at the Pt centre results in a more electron-rich Pt centre. This therefore gives a stronger Pt→Zn interaction due to probably an increase of attractive interaction between the metal centres and hence shortens the Pt–Zn bond in **28**.

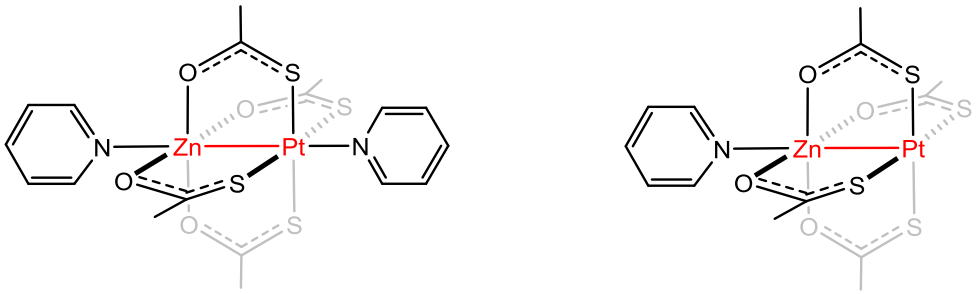

28 **29**

*Figure 2-13. Structures of the Pt-Zn species **28** and **29** featuring a supported metal–metal bond.*

2.2 Heterobimetallic Complexes of TMs with Group 13 (E) Fragments

2.2.1 Heterobimetallic Complexes with Unsupported TM–E Bonds

Classic examples of LA–LB adducts can also be formed by the reaction of electron-rich TM species with trivalent group 13 precursors (ER_3). In this regard, numerous LA–LB adducts have been reported for TMs containing boron.[61-69] However, more recently, heterobimetallic species containing heavier group 13 elements than B (E = Al, Ga and In) have attracted an increasing attention.[47, 70-74] Braunschweig reported the first example of a platinum alane complex **30** featuring an unsupported Pt→Al dative bond, formed by the reaction of electron-rich Pt species, [Pt(L)(PCy_3)], with $AlCl_3$ (Figure 2-14).[71, 75] Braunschweig and co-workers used a similar synthetic strategy to generate the first platinum gallane complex, **31**.[47] Subsequently, Nakazawa reported the first ruthenium indane complex **32**, featuring an unsupported Ru→In bond.[72] Nakazawa showed that in **32** the MeCN ligand trans to the InX_3 moiety can be selectively displaced by PPh_3 while the MeCN ligand trans to CO ligand remains intact. It should be noted that no PPh_3-InX_3 compound was formed in this reaction, implying that the Ru centre in **32** has a higher Lewis basicity than PPh_3.

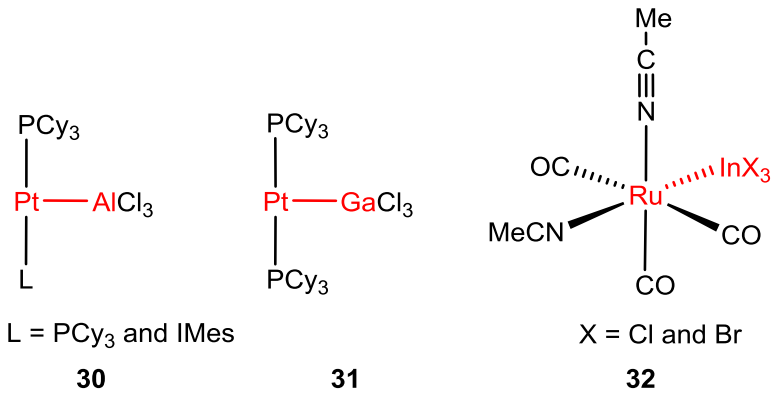

Figure 2-14. LA-LB adducts of TM species with trivalent group 13 elements.

A DFT study on a series of Pt-Al species shows that Pt complexes supported by NHC ligands exhibit stronger Pt–Al dative bonds than thoese with phosphine ligands.[75] This is mainly due to the fact that NHC ligands are stronger electron donors than phosphine ligands. Thus, they can increase the electron denisty at the Pt centre more than phosphine ligands, and hence give a stronger Pt→Al dative bond.

It is well established that in the reactions of ER_3 precursors with TM complexes, E–R bond activation can occur at the TM centre. [76-79] For instance, as shown in Figure 2-15, treatment of [(Mes)BBr_2] (Mes = mesityl) with [Pt(PCy_3)$_2$] results in the breaking of the B–Br bond via an oxidative addition mechanism and produces the Pt-boryl species **33**.

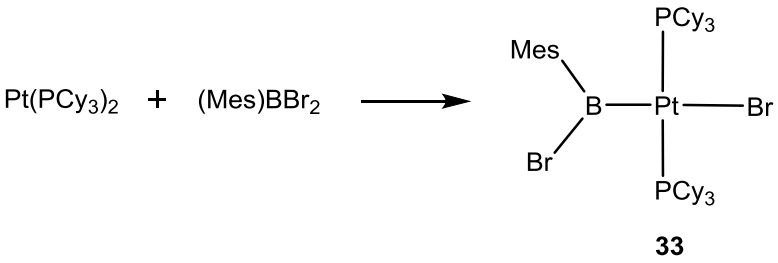

*Figure 2-15. Oxidative addition of (Mes)BBr_2 to Pt(PCy_3)$_2$ to give **33**.*

As shown in Figure 2-14, while the reaction of $GaCl_3$ with [Pt(PCy_3)$_2$] results in the formation of the LA–LB product, Pt-$GaCl_3$ species **31**, reaction of the Pt complex with $GaBr_3$ and GaI_3 results in the oxidative addition product where the cleavage of the Ga–Br and Ga–I bonds at the Pt centre produces the Pt-gallyl species **34** (Figure 2-16).[47]

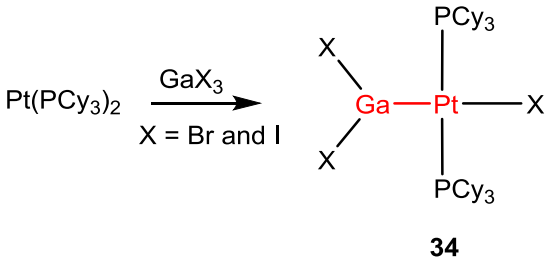

*Figure 2-16. Oxidative addition of GaX_3 to Pt centre to give the Pt-gallyl species **34**.*

This highlights the nature of the halide substituents of the trivalent Ga precursors. In this regard, the Ga centre in $GaCl_3$ is relatively more electron-deficient than that in $GaBr_3$ and GaI_3 as the Cl withdraws more electron density from the Ga centre than Br. Thus the LA-LB product **31** is more stable than the oxidative addition product **34**.

Fischer and Frenking reported the oxidative addition of a series of ER_3 precursors to the Pt complex **35**.[80] As shown in Figure 2-17, reductive elimination of alkane produces intermediate **36**. The highly reactive Pt(0) species can trapped by reaction with ER_3. This process cleaves the E–R bond at the Pt centre via an oxidative addition mechanism and yields the tetracoordinate Pt species **37**.

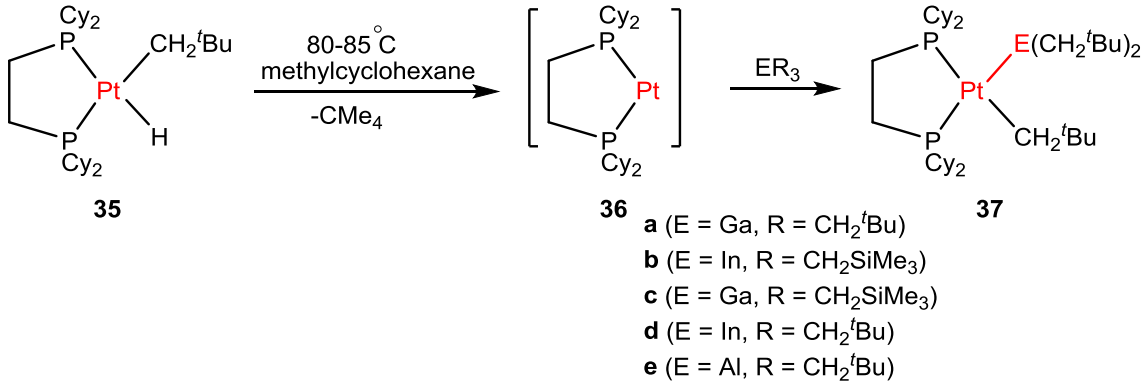

*Figure 2-17. Formation of the Pt(0) intermediate **36** and subsequent reaction with ER_3 precursors to give the tetracoordinate Pt(II) species **37**.*

A DFT study using EDA and NBO analysis performed by Pandey, Braunschweig and Aldridge on TM-GaX_2 species **38** (TM = Ni, Pd and Pt; X = Cl, Br and I) shows that the

TM–Ga interaction is mainly dominated by electrostatic interactions (Figure 2-18).[81] This interaction is heavily dependent on the nature of the halide substituent. In this regard, going from Cl to Br and I, the Ga centre becomes less electropositive. This shows a decrease in the Lewis acidity of Ga and hence, a decrease in the attractive interaction between the metal centres. It should be also noted that the TM–Ga interaction has a neglegible π-character. The TM–Ga σ-bonding orbital has a significant Ga s character which becomes greater as the TM–Ga interaction becomes stronger. A similar result was also obtained by the same authors for heterobimetallic species of group 8 TMs featuring a gallyl ligand, **39**.[82, 83]

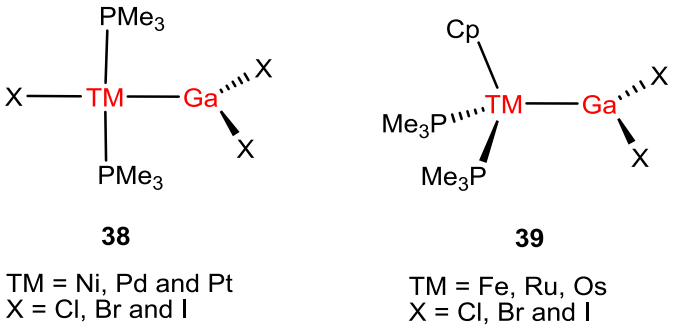

Figure 2-18. Heterobimetallic complexes of group 6 and 10 TMs with Ga halide.

Braunschweig and co-workers reported the reactivity of $[Pt(PCy_3)_2]$ (**7**) with InX_3 (X = Cl, Br and I) in Et_2O solvent. This reaction leads to the formation of a mixture of the LA–LB adduct **40** and the oxidative addition product **41** (Figure 2-19).[84]

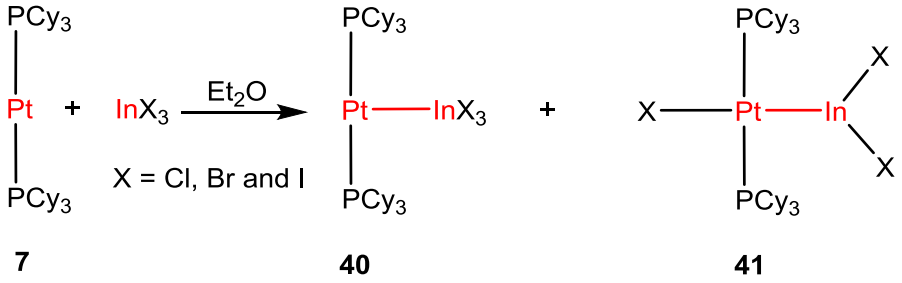

*Figure 2-19. Formation of LA–LB adduct **40** and oxidative addition product **41** by the reaction of Pt(0) species **7** and trihalide In precursors.*

NMR spectroscopy of the CH_2Cl_2 and THF solutions of **40** and **41** shows that, in most cases, both species are present in equilibrium. As shown in Table 2-1, in the case of X = Cl, the CH_2Cl_2 solution favours the formation of the LA–LB species **40a** over the formation of **41a** whereas in THF, **41a** is the dominant species. A similar trend can also be seen when X = Br (**40b** vs **41b**). For X = I, in both CH_2Cl_2 and THF solutions, the only product is the oxidative addition species **41c**. Thus, the equilibrium between **40** and **41** heavily depends on the type of solvent. In THF, the equilibrium is always more toward the formation of the oxidative addition product **41**. The authors attributed this to the coordination ability of THF to In in **41** while CH_2Cl_2 does not have this ability. The former can induce the X-group transfer from In onto the Pt centre.

*Table 2-1. Dependence of the equilibrium between the LA–LB adduct **40** and the oxidative addition product **41** to the nature of the halide and solvent.*

Entry	X	Solvent	40	41
a	Cl	CH_2Cl_2	100%	0%
		THF	9%	91%
b	Br	CH_2Cl_2	52%	48%
		THF	8%	92%
c	I	CH_2Cl_2	0%	100%
		THF	0%	100%

The other factor which also affects the equilibrium between **40** and **41** is the nature of the halide substituent. In this regard, Cl is smaller and features a higher electronegativity compared with Br and I. Thus, Cl withdraws more electron density from In than Br and I. This enhances the Lewis acidity of the In centre and results in a more stable Pt→In dative bond. In contrast, in the case of I, the In centre exhibits a significantly lower Lewis acidity due to lower electronegativity and also the greater size of I.

It is established that the Lewis acid fragment in the LA-LB adducts can be exchanged between TM centres (i.e. Lewis base).[47, 71, 85, 86] For instance, treatment of a mixture of **40b** and **41b** with [Pt(IMes)(PCy_3)] (**7'**) results in the complete transfer of the In moiety to **7'** to give **40b'** and **41b'**.[84] This is mainly due to the higher electron donicity of IMes ligand in **7'** which gives a higher Lewis basicity to the Pt centre than PCy_3 ligands in **7**.

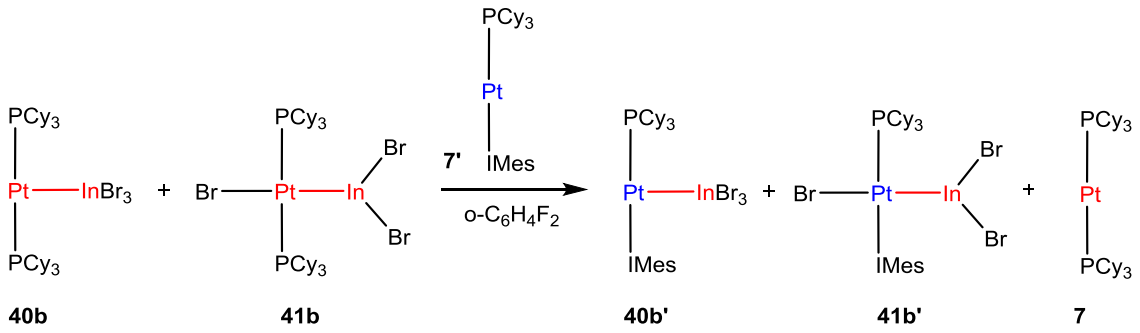

*Figure 2-20. Transfer of the In moiety (LA fragment) from **7** to **7'**.*

While the trivalent group 13 elements acts as Z-type ligands, monovalent group 13 compounds can act as a L-type ligand in the coordination chemistry of TM complexes.[87-101] In this context, Uhl showed the displacement of COD ligands, in [Ni(COD)$_2$], by [Ga{C(SiMe$_3$)$_3$}] to give [Ni(Ga{C(SiMe$_3$)$_3$})$_4$].[102, 103] A similar strategy was used by Fischer to produce [TM(GaCp*)$_4$] (TM = Pd and Pt).[97] Fischer then reported the coordination of ECp* (E = Ga and In) ligands to [TM{N(SiMe$_3$)$_2$}$_2$] (TM = Fe, Co) to form [TM(ECp*){N(SiMe$_3$)$_2$}$_2$].[93] Fischer and Frenking used the L-type nature of the monovalent group 13 compounds to trap the highly reactive Pt(0) intermediate **36** (Figure 2-21). In this regard, treatment of **35** with a series of monovalent ECp* species (E = Al, Ga and In) results in the formation of **42**.[104, 105]

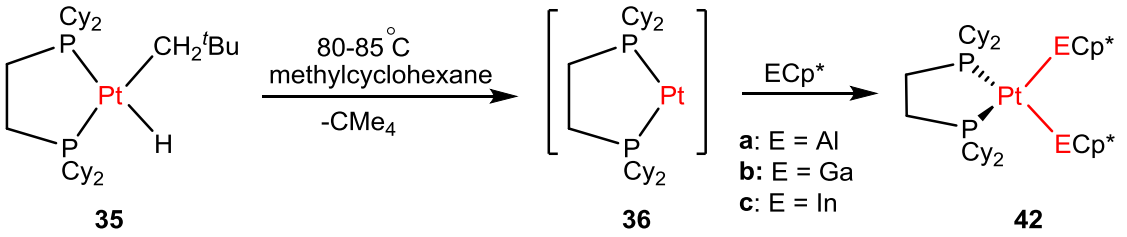

*Figure 2-21. Trapping of the dicoordinated Pt complex **36** by ECp* precursor to produce the tetracoordinate species **42**.*

Monovalent ER ligands are considered to be isolobal with CO.[106] However, their electronic properties vary with respect to the nature of the R substituents.[107] For instance, a detailed analysis of Pt–ER (E = Al and Ga) bonding performed by Fischer and Frenking shows that weak π-donor R substituents increase π-back bonding from Pt to the E centre.[104] However, the extent of π-back donation also reflects the nature of the supporting ligands at the TM centre. In this regard, π-acceptor ligands increase the Lewis acidity of the TM centre and hence, increase the strength of the TM←E σ-interaction. In addition, strong σ-donor R substituents can increase the Lewis basicity of the E centre and hence strengthen the TM←E σ-interaction.[101, 104] It is worth noting that summation of both σ- and π- characters of TM–E interaction gives a Wiberg bond order less than 1.

Trivalent group 13 compounds can bind to TMs via a 3c-2e interaction. For example, as shown in Figure 2-22, Aldridge and co-workers reported that the reaction of the NHC-stablised EH_3 compounds (**43**) (NHC = 6-Mes, 6-Dipp and IDipp, E = Al and Ga) with $[TM(CO)_4(COD)]$ (TM = Cr and Mo) results in the formation of κ^2–H_2E species **44**.[108]

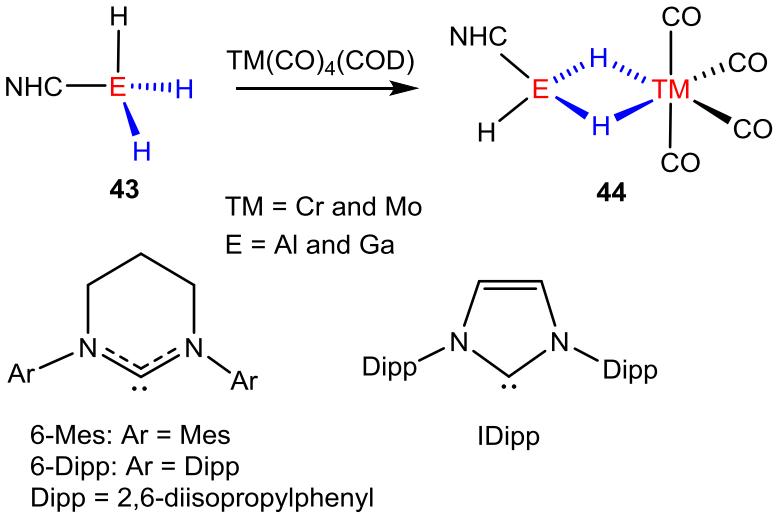

*Figure 2-22. Coordination of the trivalent group 13 precursor **43** to the TM(CO)$_4$(COD) to give **44**.*

Formation of the σ-alane and gallane species **44** shows a potential ability of the E centre to transfer hydride to TM centre. As shown in Figure 2-23, compared with **43**, treatment of the nacnac-stabilized AlH_2 species **45** with [TM(CO)$_4$(COD)] produces a mixture of κ^2–H_2Al species **46** and κ^1–H_2Al species **47**. Formation of the latter suggests a facile displacement of one of the bridging hydrides of **46** with a CO ligand.

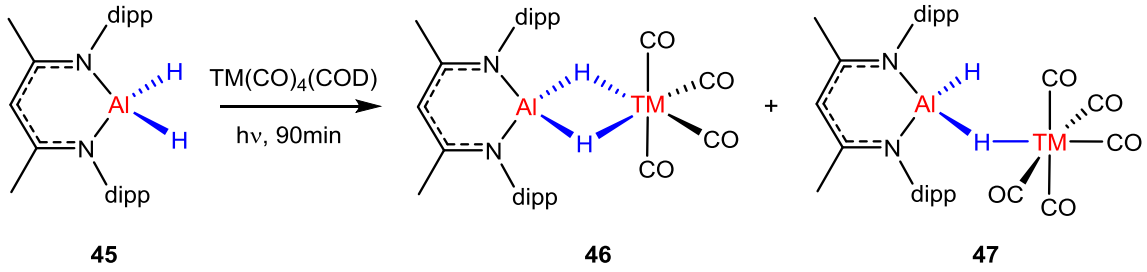

*Figure 2-23. Formation of κ^2-H_2Al species **46** and κ^1-H_2Al species **47** by the reaction of **45** with [TM(CO)$_4$(COD)].*

Interestingly, similar to the reaction of nacnac-AlH_2 with [Cr(CO)$_4$(COD)], reaction of the nacnac-Ga precursor with [Cr(CO)$_4$(COD)] yields the κ^2–H_2 product **49** (Figure 2-24).[108-111] However, with the Ga precursor, double Ga–H bond activation also occurs at the TM centre to yield **50** and H_2. Formation of **50** highlights the weaker strength of Ga–H bond relative to the Al–H bond.

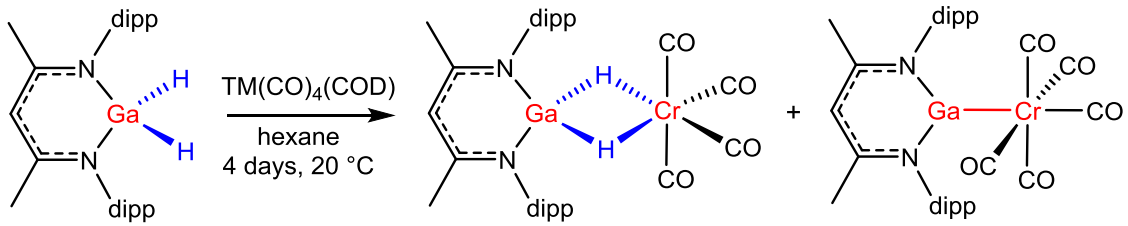

48 **49** **50**

*Figure 2-24. Formation of the heterobimetallic Cr-Ga species **49** and **50** by the reaction of the nacnac-GaH_2 (**48**) with $[Cr(CO)_4(COD)]$.*

Treatment of **48** with transition metal carbonyl reagents of the type $[TM(CO)_n]$ (Fe (n = 5), Mo (n = 6) and W (n = 6)) under photolytic conditions elliminates one H_2 and one CO to produce $[TM(CO)_{n-1}$(Ga-nacnac)], i.e. the analogue of **50**.[111] A DFT study on the reactivity of the photolytically generated $[Fe(CO)_4]$ with a small model of **48** (**48**') shows formation of the κ^2–H_2 analogue (**49**) is not possible (Figure 2-25).[111] Instead, oxidative addition of one Ga–H bond to the Fe centre occurs via a barrierless process and gives the Fe-H species **I(48'-50)1** at -30.4 kcal/mol. **I(48'-50)1** then isomerises to **I(48'-50)2** via **TS(48'-50)1** at -28.7 kcal/mol. This rotates the {HFeGaH} unit about the Fe–Ga bond and places the hydrides in a syn position relative to each other. H–H coupling then occurs across the Fe–Ga bond via **TS(48'-50)2** at the high energy of +4.8 kcal/mol. This produces H_2 and **50'-Fe** at -46.7 kcal/mol. The overall energy barrier for this process is computed to be 35.2 kcal/mol which is accessible under photolytic conditions.

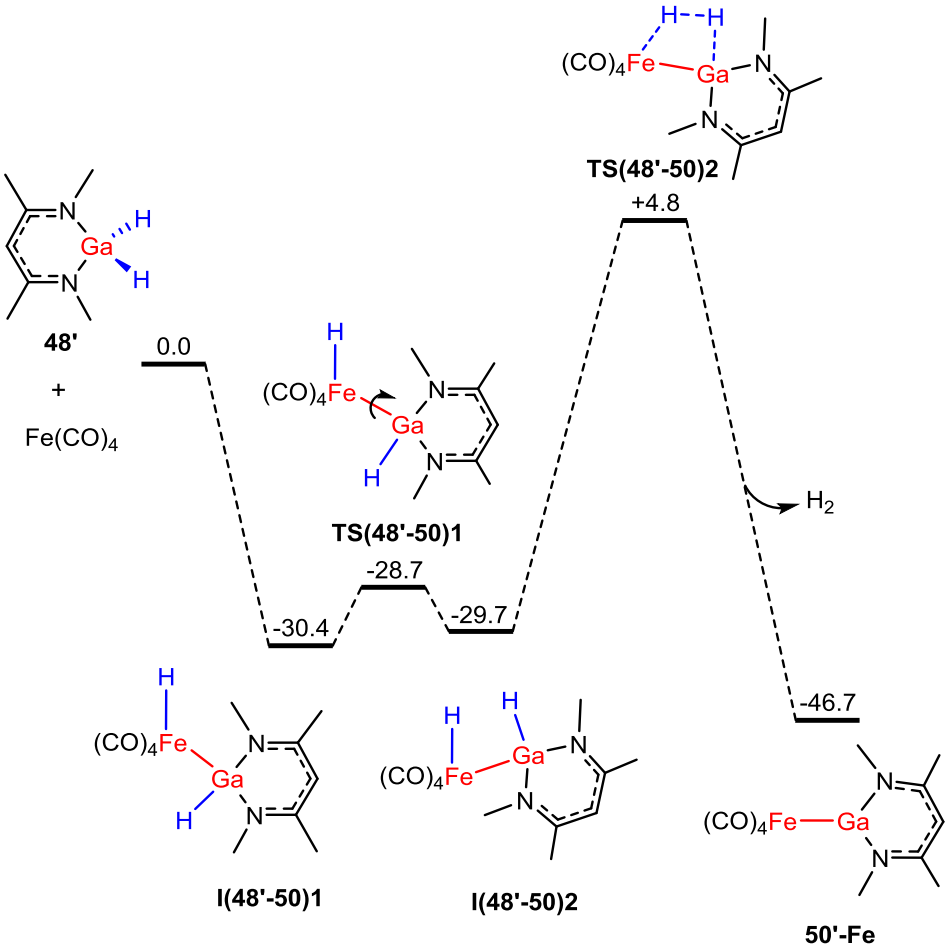

*Figure 2-25. Computed energy profile (BP86/TZVP) for the reaction of Ga-H_2 species **48'** with photolytically generated [$Fe(CO)_4$] to give the Fe-Ga species **50'-Fe** and H_2. Energies are in kcal/mol.*

Aldridge and co-workers studied the details of the Ga–H bond activation at TMs of the type $(TM)_2(CO)_{2n}$ (TM = Mn, n = 5 and Co , n = 4). As shown in Figure 2-26, with dihydride-gallane precursor **48_H** and TM = Co, activation of the Ga–H bonds is accompanied with the spontaneous reductive elimination of H_2 to produce the Co-gallyl species **51_H**. Formation of **51_H** and H_2 suggest the formation of **I(48_X)1** as an intermediate after the first Ga–H bond activation. Interestingly, such an intermediate can be formed when TM = Mn. In this case, double Ga–H bond activation also occurs. However, this process does not eliminate H_2 but instead, it eliminates a molecule of $[HMn(CO)_5]$. This is also accompanied with the transfer of the second hydride to the Mn centre to produce **52_H**. Formation of $[HMn(CO)_5]$ suggests the formation of intermediate **I(48_X)2** along the reaction coordinate.

With Ga-Cl precursor **48_Cl** and TM = Co, the first Ga–H bond activation occurs at the Co centre and gives **I(48_X)1**. However, this process does not eliminate HX. Instead, similar to the Mn-reaction, this process eliminates a [$HCo(CO)_5$] complex and hence, it gives **I(48_X)2**. This can be due to the stronger Ga–Cl bond relative to the Ga–H bond in **I(48_X)2** which disfavours transfer of Cl to the Co centre and hence does not give a Co analogue of **52_H**. Thus, addition of one CO to the Co centre traps **I(48_X)2** and gives **53_Cl**.

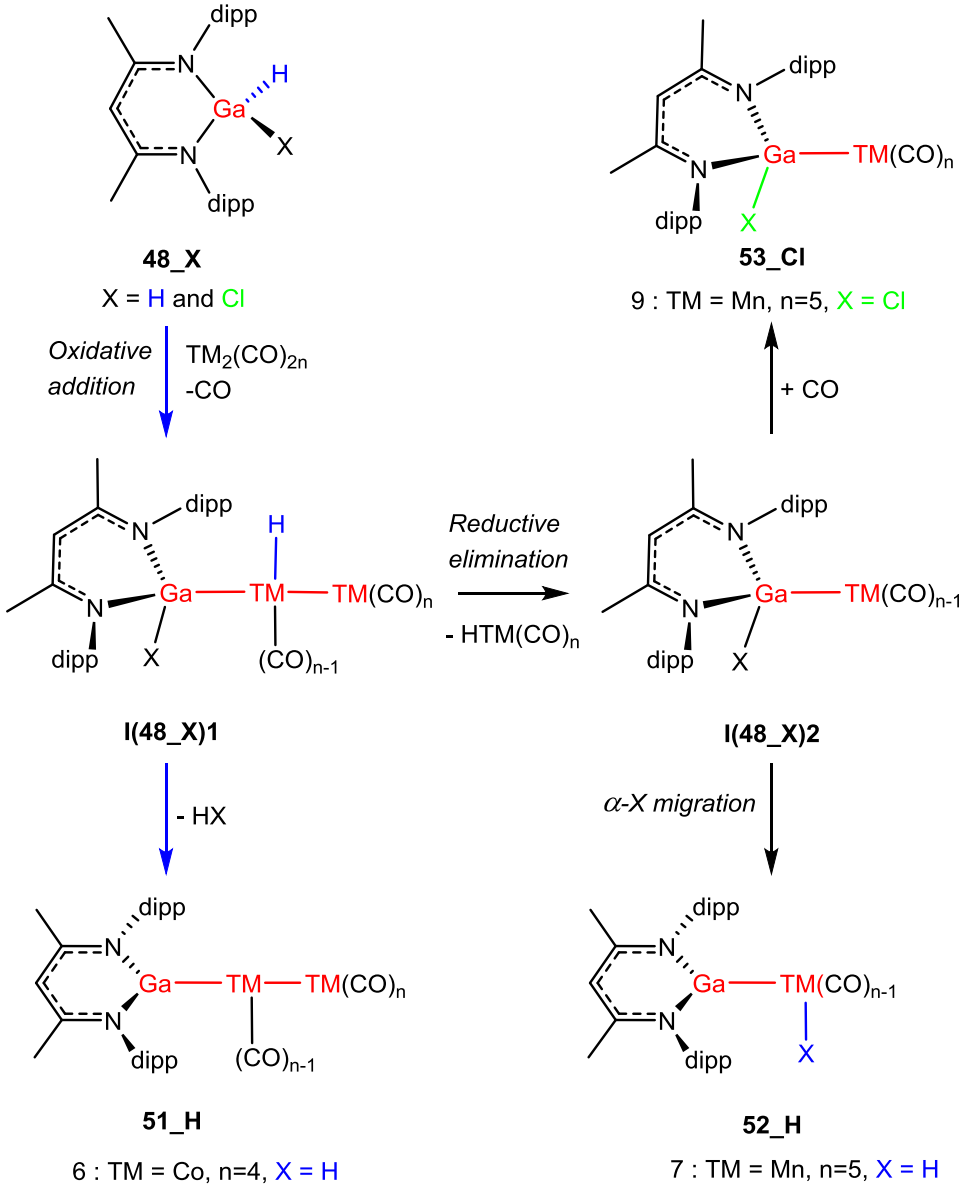

*Figure 2-26. Formation of TM-Ga species featuring an unsupported metal-metal bond by reaction of Ga precursor **48_X** and [$TM_2(CO)_{2n}$].*

Aldridge and co-workers investigated details of the Ga–H bond activation process at $[(L_2)Rh(COD)]^+$ (L_2 = 2-dppp, 2-dcype and 2-dcypp, Figure 2-27).[112] In this regard, when L_2 = 2-dppp, reaction of the Rh precursor with **48** forms **54** in which the Ga–H bonds donate electron density to the Rh(I) moiety. However, when L_2 = 2-dcype and 2-dcypp, double Ga–H bond activation occurs at the Rh centre and produces the Rh(III) dihydride complex **55**, featuring a monovalent Ga moiety. In **55**, the Rh–H bonds donate electron density to the Ga moiety via 3c-2e interactions and the Ga(I) moiety donates electron density to the Rh(III) moiety via a dative bond. The different reactivities of the Rh precursor with the Ga-H precursor **48** can be described by the electronic properties of the phosphine ligands. In this regard, when the phosphine ligand is a weaker electron-donor ligand, i.e. L_2 = 2-dppp, a κ^2–H_2 complex (**54**) is formed. However, the stronger electron-donor phosphine ligand, i.e. L_2 = 2-dcype and 2-dcypp, allows double Ga–H bonds activation at the Rh centre by stabilisation of a higher oxidation state of the Rh centre.

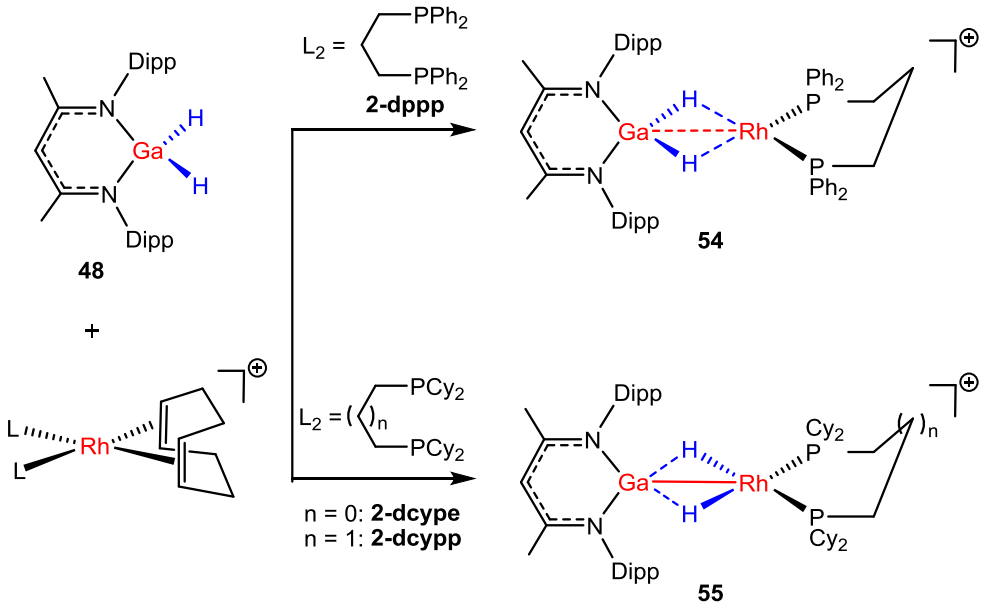

Figure 2-27. Dependency of the Ga–H bond activation on the nature of the ligands coordinated to the Rh centre.

2.2.2 Incorporation of Group 13 Elements into Ligand Scaffolds

Trivalent group 13 moieties can be combined with multidentate ligands to form so-called ambiphilic ligands.[113-115] Coordination of ambiphilic ligands to TM centres can form a

constrained TM→E geometry supported by the ligand scaffold.[116-122] This can stablise the lower oxidation state and tune the reactivity at the TM centre. For instance, it has been reported that Ni(0) species cannot undergo H_2 oxidative addition probably due to the instability of the consequent Ni (II)-dihydride species.[123] Peters and co-workers showed that reaction of the ambiphilic ligand **56** ([^{Mes}DPB^{Ph}]) with [Ni(COD)$_2$] yields the Ni-B species **57** which features a supported Ni-B bond (Figure 2-28). Treatment of **57** with H_2 results in a facile and reversible H_2 activation which forms **58**, [HNi(μ-H)B].[119] **58** is characterised as an intermediate in situ and demonstrated to be the active catalyst in the hydrogenation of alkenes. The precatalyst **57** then can be regenerated after the hydrogenation process.

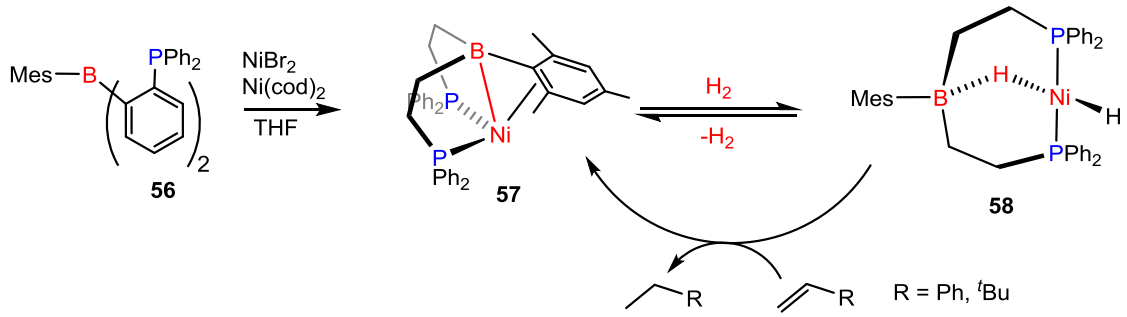

*Figure 2-28. Formation of the precatalyst Ni-B species **57** and its reaction with H_2 to form the active catalyst species **58** in hydrogenation of alkenes.*

A DFT study by Sakaki and co-workers shows that in **58,** the B centre acts as a Z-type ligand, withdraws electron density from the Ni centre and hence, reduces the electron density of Ni.[124] This favours the coordination of H_2 to the Ni centre in an η^2 fashion and forms a Ni–H_2 intermediate. H_2 activation then occurs via the cooperation of the Ni and B centres in a polarized manner. The borane moiety then accepts one of the hydrides to give a Ni–H–B bridge and stablises intermediate **58**.

Peters and co-workers then reported the Co-B species **60** formed by the reaction of the borane precursor **59** and $CoBr_2$ (Figure 2-29).[125] Exposure of **60** with amine−borane results in the formation of the Co-H-B species **61**. **61** is an active catalyst in the hydrogenation of alkenes and it is now stable enough to be isolated experimentally.

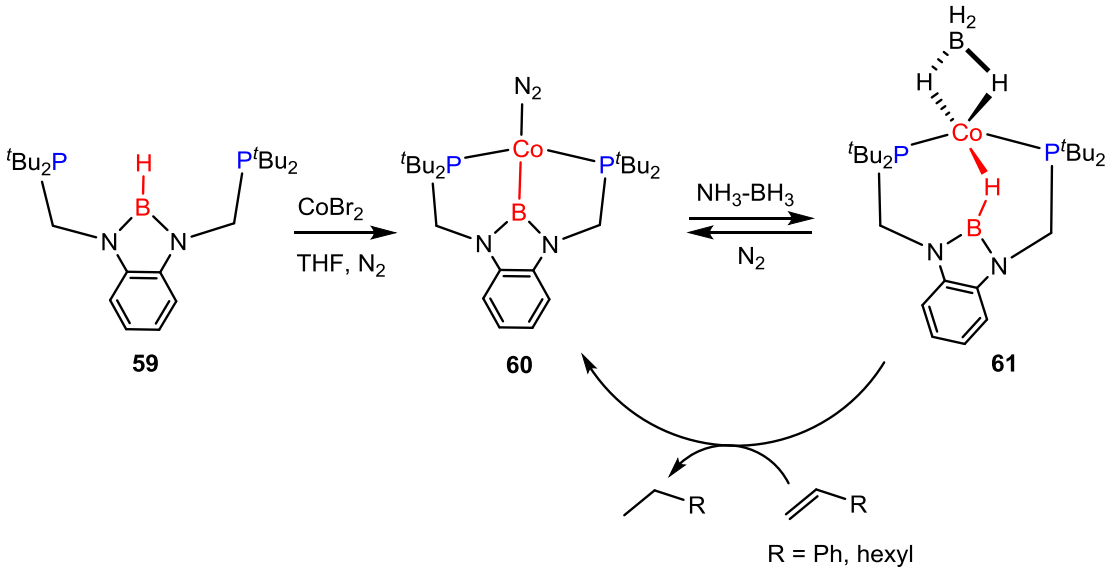

*Figure 2-29. Formation of the precatalyst **60** and its exposure with amine−borane to give **61** as the active catalyst in hydrogenation of olefins.*

Heavier group 13 elements than B (E = Al, Ga and In) can also be incorporated into the ligand scaffold.[126-128] In this regard, Lu and co-workers synthesised the ambiphilic ligand **62**, featuring a group 13 metal (Figure 2-30). Reaction of **62** with [Ni(COD)$_2$] generates the Ni-E complex **63** in which the Ni→E bond is supported by the ligand scaffold.[127]

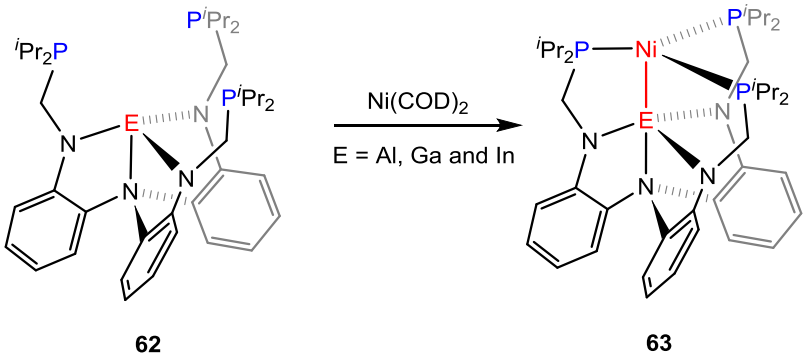

*Figure 2-30. Formation of the heterobimetallic Ni-E complex **63** featuring a supported Ni→E bond.*

As shown in Figure 2-31, reaction of **63_Ga** with H_2 does not yield the η^2–H_2 complex.[129] However, in the presence of a base, the H_2 at the Ni centre can be deprotonated to produce

the anionic Ni-H complex **64**. This suggests that the η^2–H_2 complex can be formed as an intermediate. Interestingly, the Ni-H species **64** is stable enough to be isolated experimentally. This is due to withdrawal of electron density by the Ga centre from the Ni centre which can stablise the Ni–H bond. **64** is a highly reactive Ni-H complex and hence, it can be used in as a reducing agent to hydrogenate for example CO_2.

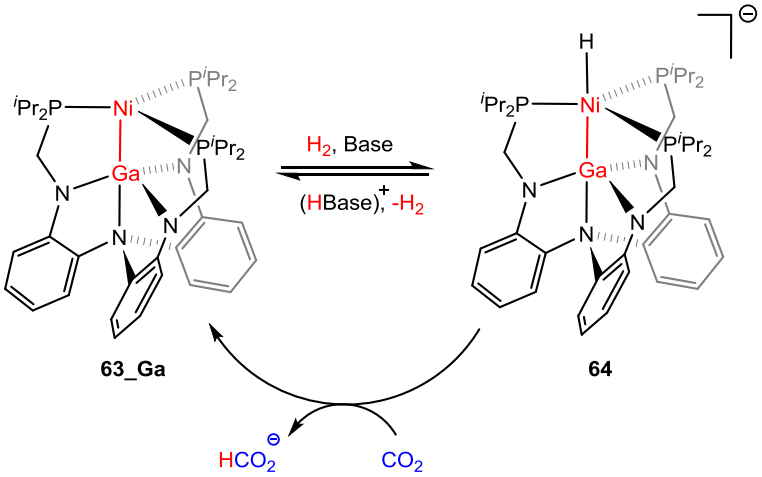

*Figure 2-31. Formation of the anionic Ni-H species **64** and its reaction with CO_2.*

Intrestingly, Lu and co-workers showed that while the reaction of Ni-Ga complex **63_Ga** with H_2 cannot produce a stable η^2–H_2 complex, reaction of the Ni-In complex (**63_In**) with H_2 results in an stable η^2–H_2 complex **66**, isolated experimentally. This is mainly due to the fact that In is a stronger Lewis acid compared with Ga. Therefore, it withdraws more electron density from the Ni centre and hence, it can stablise the η^2–H_2 species more than Ga.

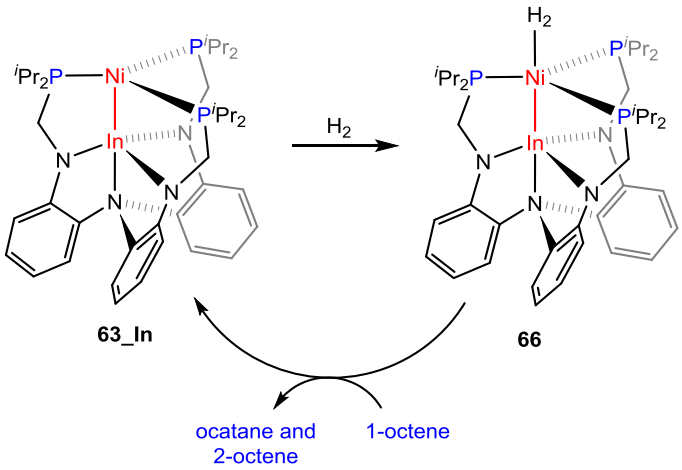

*Figure 2-32. Stabilisation of the Ni-H_2 complex **63_In** by the high Lewis acidity of In and the hydrogenation process by **66**.*

As outlined above, reaction of TM speices with metal precursor can produce heterobimetallic complexes featuring either supported or unsupported metal-metal bond. Such species can exhibit unusual reactivities with small molecules and hence, can be employed in synthesis and catalysis. In this regard, as part of a joint research program with the experimental group of Prof. Whittlesey at the University of Bath, computational studies have been conducted to study a new class of heterobimetallic complexes featuring unusual reactivites. Herein, the next three chapters describe the experimental and computational results of the heterobimetallic complexes of Ru with Zn, Ga and In.

Chapter 3 – DFT Studies on the Characterisation, Formation and Reactivity of the Heterobimetallic Ru-Zn Species 68, $[Ru(IPr)_2(CO)(ZnEt)]^+$

Recently, there has been a substantial increase in the study of transition metal-main group elements (TM-E) species featuring supported TM–E bonds as they exhibit interesting reactivities toward the activation of the small molecules.[35, 36, 114] However, little attention has been paid to the reactivity of heterobimetallic systems with unsupported TM–E bonds (E = group 12 and 13 metals).[126, 130, 131] In this regard, Whittlesey and co-workers, isolated the Ru–Zn species **68** featuring an unsupported metal–metal bond and investigated its reactivity with H_2 to form species **69** and **70**.[132]

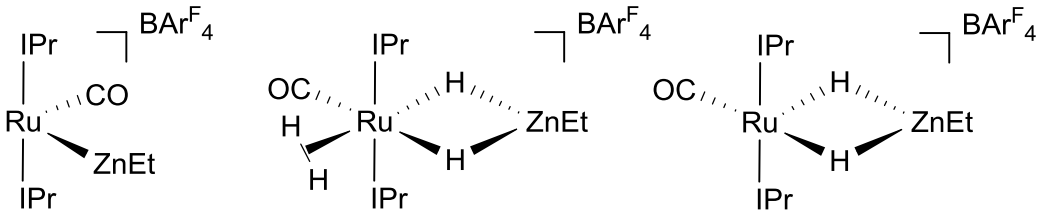

Herein, the first section of this chapter introduces the experimental results related to the synthesis and reactivity of the Ru-Zn species **68**. In the next section, computational results are described to elucidate the nature of the Ru–Zn interaction in **68**, **69** and **70** and the character of the hydride ligands in **69** and **70**. The final sections then focus on the mechanism of the formation and reactivity of the Ru-Zn species.

3.1 Experimental Background

3.1.1 Formation of the Ru-Zn Species

Whittlesey and co-workers isolated the 16-electron Ru-H species **67**, $[Ru(IPr)_2(CO)H]BAr^F{}_4$ (IPr = 1,3-bis(2,6-diisopropylphenyl)imidazol-2-ylidene, $BAr^F{}_4$ = Tetrakis(3,5-bis(trifluoromethyl)phenyl)borate)) (Figure 3-1).[133] They showed that the reaction of **67** with $ZnEt_2$ in fluorobenzene at room temperature generates the Ru-Zn species **68**, $[Ru(IPr)_2(CO)(ZnEt)]BAr^F{}_4$, while gaseous ethane is released.[132] Treatment of **68** with H_2 at room temperature in fluorobenzene binds an η^2–H_2 ligand to the Ru centre and adds two hydride ligands across the Ru–Zn vector to give $[Ru(IPr)_2(CO)(\eta^2\text{–}H_2)(H)_2(ZnEt)]BAr^F{}_4$, **69**. **69** can lose the η^2–H_2 at the elevated temperature of 50 °C under vacuum to produce $[Ru(IPr)_2(CO)(H)_2(ZnEt)]BAr^F{}_4$, **70**.

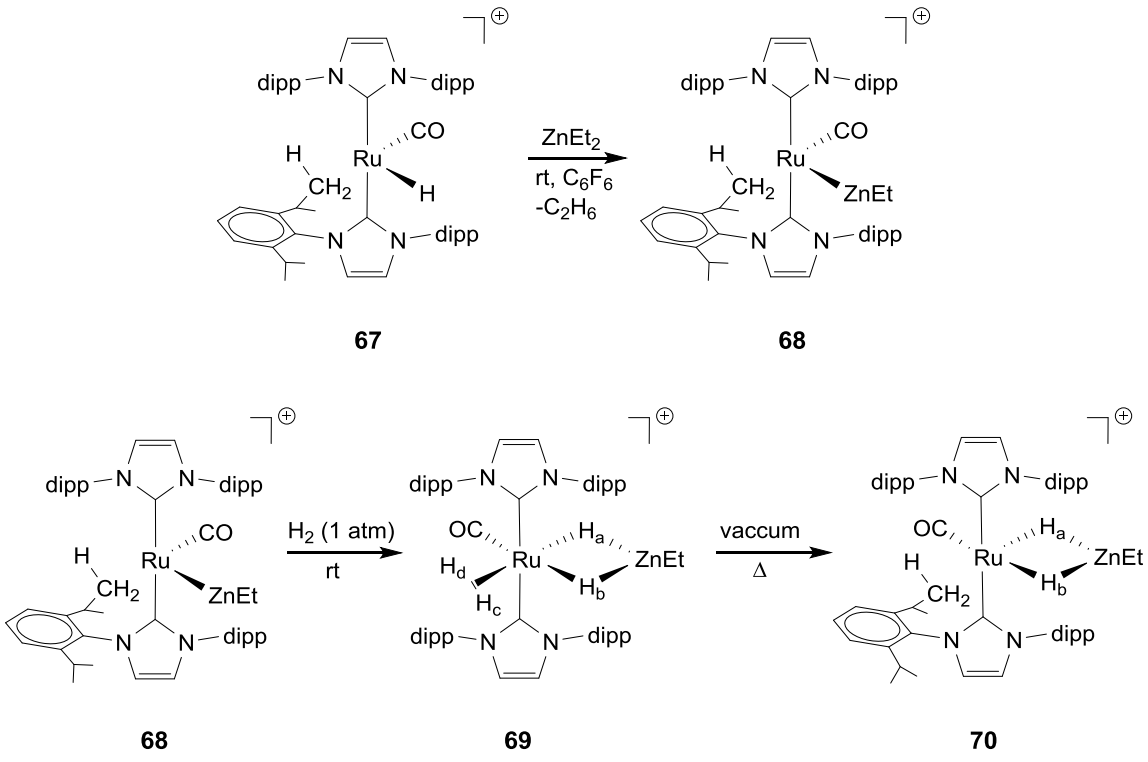

*Figure 3-1. Reaction of **67** with $ZnEt_2$ to form the Ru-Zn species **68** (top) and reactivity of **68** with H_2 (bottom) to form **69** and **70**.*

The X-ray crystal structure analysis of the Ru-Zn species shows that **68**, **69** and **70** exhibit Ru–Zn distances of 2.4069(7) Å, 2.5125(3) Å and 2.4896(4) Å, respectively. These

distances are shorter than the sum of the covalent radii of Ru and Zn atoms (2.68 Å).[134] This therefore suggests the presence of a bonding interaction between the metal centres. **67** features C–H agostic interactions involving one of the isopropyl substituents of the IPr ligand oriented toward the Ru centre.[133] Similar to **67**, the X-ray molecular structure of **68** and **70** exhibits a C–H bond in close geometrical proximity to the Ru atom (Ru···C, **68**: 2.58 Å and **70**: 2.90 Å). This therefore suggests the presence of a C–H agostic interaction in **68** and **70** as well.

3.1.2 H/H Exchange in the Ru-Zn Species 69 and 70

^{1}H NMR spectroscopy studies on **69** reveal an H/H exchange process between the hydrogens of the η^2–H_2 ligand and the cis hydride, H_b, at room temperature on the NMR timescale (Figure 3-2). However, no exchange was observed between the hydride trans to CO (H_a) and the hydride cis to CO (H_b). On the other hand, upon the treatment of **69** with D_2, all four hydrogen positions were seen to exhibit H/D exchange. Similar H/D exchange was also observed between the hydrides H_a and H_b in **70**. This indicates that the exchange process between the hydrogens of the η^2–H_2 ligand and the cis hydride H_a is a fast process as it occurs on the NMR timescale, whereas the exchange process between the hydrides H_a and H_b is a slower process.

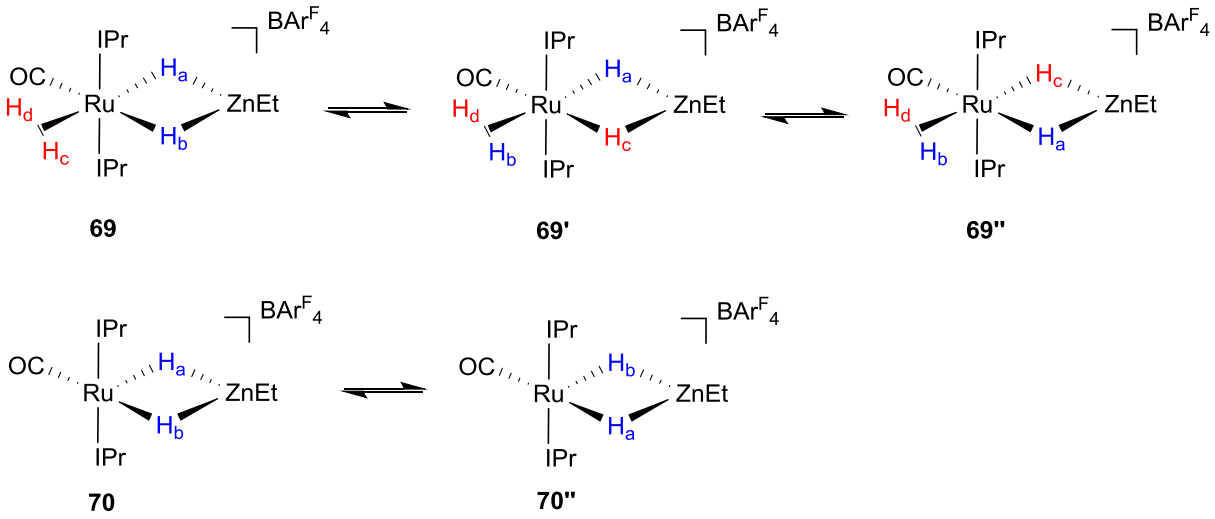

Figure 3-2. H/H exchange processes in **69** and **70**.

3.2 Aims

Herein, DFT calculations were performed to explore the nature of the Ru–Zn interactions in **68**, **69** and **70** as well as the character of the M–H interactions in **69** and **70**. In addition, with the aid of DFT, the mechanism of the formation of the Ru-Zn species **68** and its reactivity with H_2 to form **69** and **70** along with the H/H exchange process in the **69** and **70** were investigated.

3.3 Computational Details

DFT calculations have been performed with Gaussian 09 (Revision D.01)[135] at the BP86[136] level of density functional theory. For Ru and Zn atoms, the Stuttgart RECPs[137] and associated basis sets were used while other atoms were described with the 6-31g**[138] basis set. This basis set combination is referred to as BS1. Frequency calculations have been performed with Gaussian 09 to characterize all stationary points as either minima (all positive eigenvalues) or transition states (one negative eigenvalue). Intrinsic reaction coordinate (IRC) calculations were used to confirm the connectivity between transition structures and minima. To correct free energies, solvent and dispersion calculations have been performed on the fully optimized geometries using the same level of theory and basis sets with Gaussian 09. Solvent calculations in fluorobenzene ($\varepsilon = 5.42$) with the PCM[14] model and dispersion corrections with Grimme's D3[22] parameter set were used. To have a further insight into the bonding of all species **68**, **69** and **70**, QTAIM[30] and NBO[139] (version 6.0) calculations were performed with AIMAll[140] and Gaussian 09, respectively. Pipek-Mezey localized molecular orbitals (LMOs) were also computed with ORCA[141] (Version 4.0.0.2) using def2-TZVP[142] basis for Ru and Zn atoms and def2-SVP[143, 144] for other atoms.

3.4 Results and Discussion

3.4.1 Optimisation of the Molecular Species of 68, 69 and 70

The cationic molecular species **68**, **69** and **70** were fully optimised using the X-ray molecular geometries. Selected structural parameters of the experimental and computed

geometries of **68**, **69** and **70** are summarised in Table 3-1 (See Figure 3-3 for the labelling scheme).

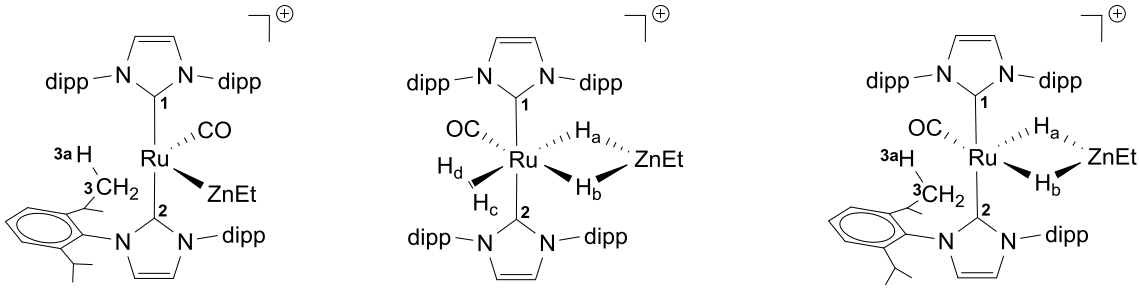

*Figure 3-3. The Ru-Zn species **68**, **69** and **70** with labelling scheme on selected atoms.*

*Table 3-1. Comparison of the selected structural parameters of the experimental Ru-Zn species **68**, **69** and **70** with the BP86-computed geometries. Selected bond lengths and angles are reported with Å and degrees, respectively.*

	68		**69**		**70**	
	Exp.	Comp.	Exp.	Comp.	Exp.	Comp.
Ru–Zn	2.4069(7)	2.421	2.5125(3)	2.550	2.4896(4)	2.535
Ru–CO	1.800(5)	1.803	1.907(2)	1.889	1.894(2)	1.879
Ru···C(3)	2.58	2.621	–	–	2.90	2.961
Ru···H(3a)	2.13(3)	2.113	–	–	2.048(18)	2.022
C(3)–H(3a)	0.99(2)	1.129	–	–	1.075(15)	1.132
C(3)–H(3b)	0.99(2)	1.111	–	–	1.075(15)	1.099
C(3)–H(3c)	0.99(2)	1.101	–	–	1.075(15)	1.103
Ru–H_a	–	–	1.52(3)	1.653	1.58(2)	1.592
Ru–H_b	–	–	1.77(3)	1.735	1.58(2)	1.758

$Ru–H_c$	–	–	1.78(2)	1.759	–	–
$Ru–H_d$	–	–	1.80(2)	1.766	–	–
$Zn–H_a$	–	–	1.78(3)	1.815	1.90(2)	1.786
$Zn–H_b$	–	–	1.85(3)	1.930	1.90(2)	2.020
∠C(1)–Ru–C(2)	177.31(18)	177.314	177.07(8)	176.694	175.70(8)	174.732

As illustrated in Table 3-1, compared with the experimental structures, the computed Ru–Zn distances in species **68**, **69** and **70** are slightly overestimated by 0.014 Å, 0.038 Å and 0.045 Å, respectively. However, they show the right trend in lengthening of the Ru–Zn distance in the **68**→**69**→**70** process. In **68**, the C(3)–H(3a) bond oriented toward the Ru atom is computed to be slightly longer than the two other C(3)–H bonds to give a short Ru···H(3a) contact. A similar trend can be seen in **70**. However, compared with **68**, **70** exhibits a shorter Ru···H(3a) distance and slightly longer C–H(3a) distance. This may suggest a stronger C–H agostic interaction in **70** than that in **68**.

The geometry of the {RuH_aH_bZn} unit in **69** and **70** displays different Ru–H bond distances. In **69**, the $Ru–H_a$ bond is shorter than the $Ru–H_b$ bond distance ($Ru–H_a$ = 1.653 Å and $Ru–H_b$ = 1.735 Å). A similar trend can also be seen in **70** ($Ru–H_a$ = 1.592 Å and $Ru–H_b$ = 1.758 Å). From **69** to **70** however, the $Ru–H_a$ distance is slightly shorter by 0.061 Å. This shows the dependency of the Ru–H distance on the trans influence of the ligand trans to the hydride ligands. In other words, as the trans influence of the ligand trans to the hydride ligand increases in the order of C–H agostic interaction < η^2–H_2 < CO, the Ru–H distance gets longer.

It is also worth noting that the computed geometries of the Ru-Zn species **68**, **69** and **70** exhibit a reasonable agreement with the experimental geometries.

3.4.2 Study of the Ru–Zn Interaction in 68, 69 and 70 and the Character of the Hydrides in 69 and 70

3.4.2.1 Characterisation of the Ru–Zn Interaction in 68, 69 and 70

In order to characterise the nature of the Ru–Zn interaction, the topological assessment of the electron density (with QTAIM), bonding analysis (with NBO and LMOs) along with the analysis of the observed CO stretching frequencies were carried out

Figure 3-4 depicts the topology of the electron density ($\rho(r)/eÅ^{-3}$) in the {Ru/Zn/C(O)} plane of **68**, **69** and **70**. Consistent with the covalent radii of the Ru and Zn atoms, the molecular graphs of all three Ru-Zn species exhibit a bond path between the Ru and Zn centres, suggesting the presence of an interaction between the metal centres. These interactions are characterised by a small ρ(r), a positive Laplacian of the electron density ($\nabla^2\rho(r)/eÅ^{-5}$) and small but negative total energy densities (H(r)/a.u.). Small ρ(r) and positive $\nabla^2\rho(r)$ values are indicative of closed shell interactions (e.g. ionic bonding). However, a small negative H(r) value is indicative of some degree of shared interaction. Such topological features of the electron density place the Ru–Zn interactions into the transit closed shell interactions classification,[27,145] exhibiting dative interactions.[26]

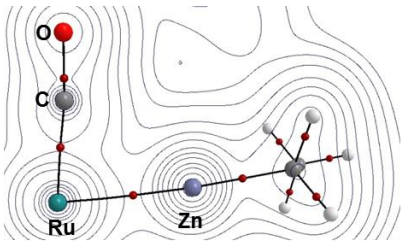

68

BCP	ρ(r)/eÅ^{-3}	$\nabla^2\rho(r)$/eÅ^{-5}	ε	H(r)/a.u.
Ru–Zn	0.071	0.106	0.018	-0.022

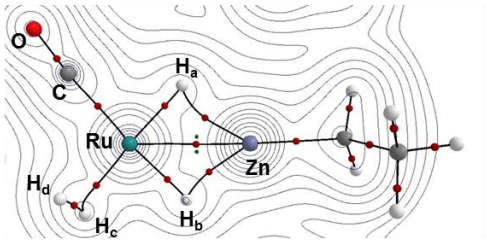

69

BCP	ρ(r)/eÅ^{-3}	$\nabla^2\rho(r)$/eÅ^{-5}	ε	H(r)/a.u.
Ru–Zn	0.057	0.089	4.512	-0.017

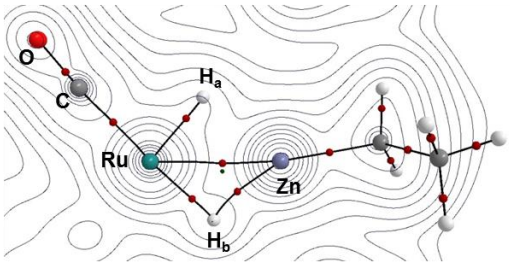

70

BCP	ρ(r)/eÅ^{-3}	$\nabla^2\rho(r)$/eÅ^{-5}	ε	H(r)/a.u.
Ru–Zn	0.059	0.095	2.374	-0.017

*Figure 3-4. Details of the QTAIM molecular graphs of **68**, **69** and **70** showing the electron density contours in the {Ru/Zn/C(O)} plane. Bond critical points (BCPs) and ring critical points (RCPs) are indicated as red and green spheres, respectively.*

In **68**, the BCP along the Ru–Zn bond path has a small electron density. This is even smaller in **69** and **70**. The $|H(r)|$ values also follow a similar trend as the ρ(r) values. Based on the larger ρ(r) and $|H(r)|$, the Ru–Zn interaction in **68** is stronger relative to that in **69** and **70**. It can also be seen that in **68**, the Ru–Zn ellipticity (ε) has a very small value of 0.018. However, in **69**, it becomes significantly larger to 4.512 and then decreases to 2.374 in **70**. This might be due to the small ρ(r) at the Ru–Zn interactions which in **69** and **70** are delocalised in the {RuH_aH_bZn} planes and hence results in a flat ρ(r) at the Ru–Zn BCP (i.e. higher ellipticity) while in the absence of hydride ligands (i.e. in **68**), there is only a single and direct Ru–Zn interaction and hence the ellipticity is low.

The nature of the Ru–Zn dative interaction can also be assessed based on the donor-acceptor interaction derived from an NBO analysis. Figure 3-5 depicts the donor-acceptor orbitals associated with the Ru–Zn interactions.

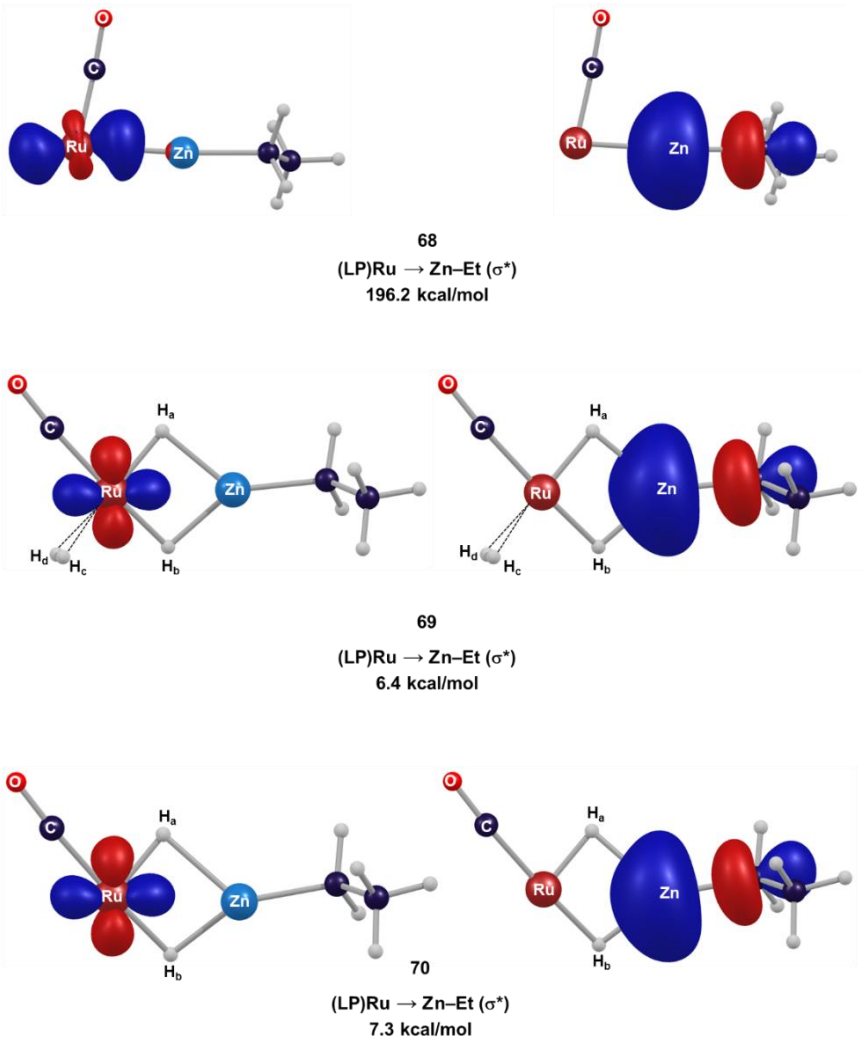

*Figure 3-5. NBO donor-acceptor interaction energy (E(2)) between one of the lone pairs (LPs) of the Ru atom and the Zn–Et anti-bonding orbital. The IPr ligands in **68**, **69** and **70** and the agostic interaction in **68** and **70** are omitted for clarity. Isosurfaces plotted with Chemcraft with a contour value of 0.1.*

NBO analysis of **68**, **69** and **70** identifies a donor-acceptor interaction between one of the lone pairs (LPs) of the Ru centre and the Zn–Et anti-bonding orbital. This therefore indicates in the Ru–Zn interaction of all three Ru-Zn complexes, the Ru centre is the

electron-donor centre and the Zn is the electron-acceptor moiety. This therefore supports a Ru→Zn dative interaction. The stabilisation energies (E(2)) associated with the Ru→Zn interactions obtained by the second-order perturbation theory are shown in Figure 3-5. In **68**, the E(2) value is computed to be 196.2 kcal/mol. However, when going to **69** and **70**, it becomes significantly smaller, to 6.4 kcal/mol and 7.3 kcal/mol, respectively. This therefore indicates a notably stronger Ru–Zn interaction in **68** than **69** and **70**.

The magnitudes of E(2) in the Ru–Zn interactions may reflect the electronic properties of the Ru centre, i.e. the oxidation state of the Ru centre. In this regard, the substantially larger E(2) in **68** relative to that in **69** and **70** is consistent with a Ru(0) species in the former and a Ru(II) species for the latter. The validity of this statement can be probed with the analysis of the observed CO stretching frequencies of the Ru-Zn species. As shown in Figure 3-6, the experimental CO stretching frequencies of **69** and **70** are higher than that in **67** which formally exhibits a Ru(II) centre. This therefore indicates that in both **69** and **70** the Ru centre lies more toward a Ru(II) species. Conversely, the CO stretching frequency of **68** is substantially lower than that in **67**, **69** and **70** which indeed supports the presence of a Ru(0) centre in **68**.

It should be noted that a small deviation can be seen between the computed CO stretching frequencies and the experimental CO stretching frequencies of the Ru complexes. However, the computed CO stretching frequencies show the right trend relative to the experimental CO stretching frequencies in the **67→68→69→70** process.

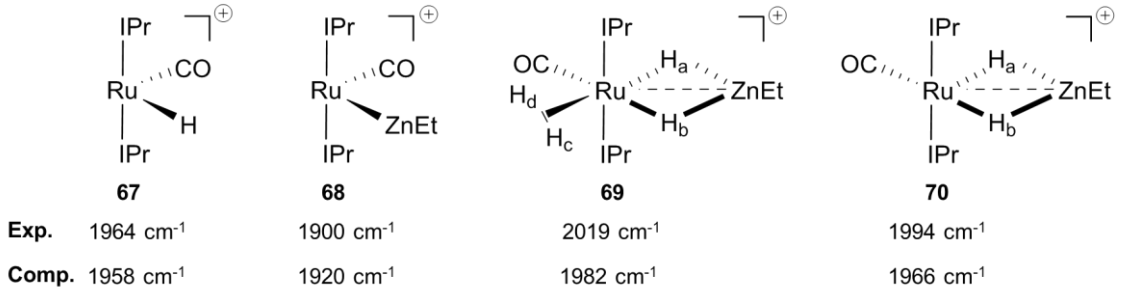

*Figure 3-6. The experimental and computed CO stretching frequencies of the Ru species. The Ru···H–C interactions in **67**, **68** and **70** are omitted for clarity.*

The proposal outlined above shows a Ru(0)-Zn(II) formulation in **68** and a Ru(II)-Zn(II) formulation in **69** and **70**. This can be further examined by the LMO analysis shown in Figure 3-7. In **68**, the LMO analysis identifies a σ-bonding orbital between the metal centres which is heavily polarised toward the Ru centre (75%(Ru), 13%(Zn), Figure 3-7(a)). The LMO analysis also characterises a negligible π-interaction between the metal centres (89%(Ru) and 2%(Zn), see Figure 3-7(b)). For species **69** and **70** however, no such σ- or π-interactions were found between the metal centres. Accordingly, the presence of the σ-interaction in **68** and the absence of that in **69** and **70** are indeed consistent with the Ru(0)–Zn(II) formulation in **68** and the Ru(II)–Zn(II) formulation in **69** and **70**.

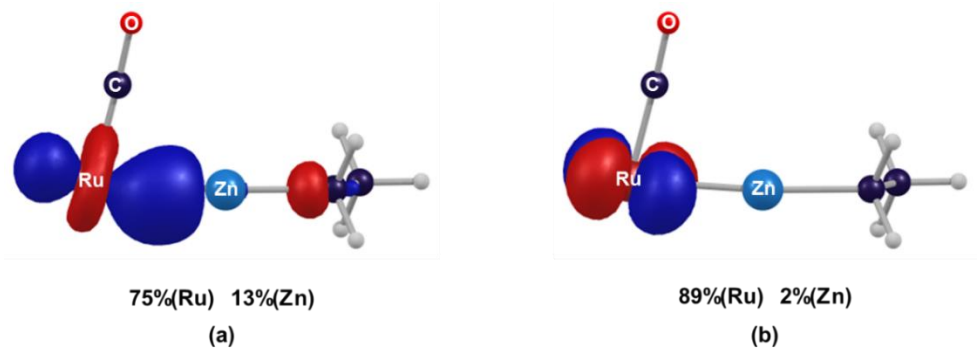

*Figure 3-7. LMO analysis of **68** showing the Ru-Zn σ-interaction (a) and negligible π-interaction (b). The IPr ligands and the agostic interaction are omitted for clarity. Isosurfaces plotted with Chemcraft with a contour value of 0.1.*

From the findings outlined above it can be seen that **68** exhibits a Ru–Zn bond. In comparison to **68**, the Ru–Zn interactions in **69** and **70** are significantly weaker and no sigma bonding interaction can be seen between the metal centres. This can be due the fact that the Ru centre in **68** is significantly more electron rich (i.e. higher basicity) than that in **69** and **70**. In other words, in **68**, the Ru centre has a d^8 electron configuration while in **69** and **70**, it has a d^6 electron configuration. Thus, in the remainder of this chapter, an organisational principal has been defined to distinguish a Ru–Zn bond from a weak Ru–Zn interaction. In this regard, in those structures featuring a Ru(0)-Zn(II) formulation, the strong metal–metal interaction will be shown by the "Ru–Zn" representation. For

structures with the Ru(II)–Zn(II) formulation, the weak metal-metal interaction will be shown by the "Ru···Zn" representation.

1.1.1 Study of the Ru···H–C Interactions in 68 and 70

As outlined above, **68** and **70** exhibit short Ru···C(3) contacts. Accordingly, as shown in Figure 3-8, the QTAIM molecular graphs of **68** and **70** exhibit a bond path between the Ru centre and the H(3a) atom based on the C(3) position of the IPr ligand. The BCPs associated with these bond paths feature similar electron densities of 0.041 and 0.040, respectively.

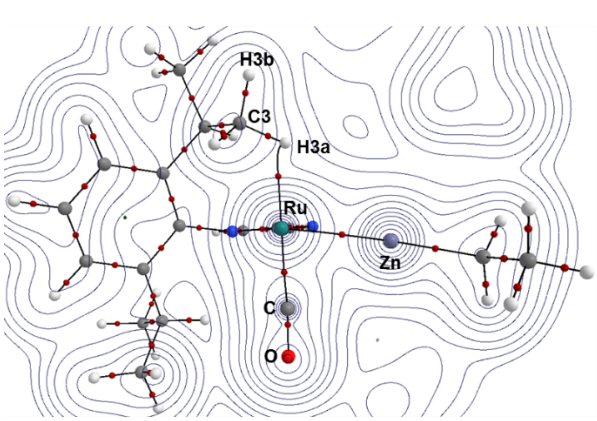

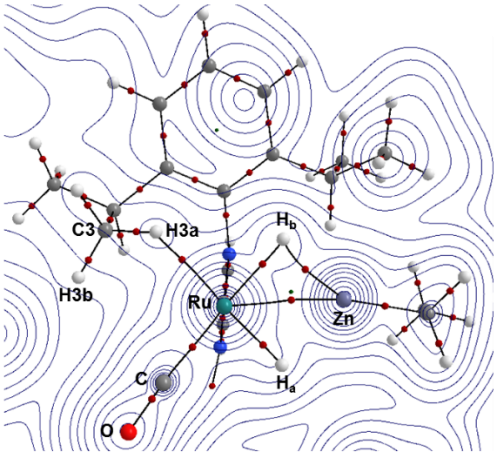

68

BCP	ρ(r)/eÅ^{-3}	∇^{2}ρ(r)/eÅ^{-5}	ε	H(r)/a.u.
Ru···H(3a)	0.041	0.154	0.986	-0.003
C(3)–H(3a)	0.249	-0.732	0.033	-0.231
C(3)–H(3b)	0.264	-0.846	0.025	-0.257

70

BCP	ρ(r)/eÅ^{-3}	∇^{2}ρ(r)/eÅ^{-5}	ε	H(r)/a.u.
Ru···H(3a)	0.040	0.154	0.187	-0.005
C(3)–H(3a)	0.241	-0.680	0.026	-0.219
C(3)–H(3b)	0.274	-0.931	0.014	-0.275

*Figure 3-8. Details of the QTAIM molecular graphs of **68** and **70** showing the electron density contours in the {Ru/Zn/C(O)} plane to characterise the Ru···H(3a) interaction. One of the IPr ligand and the aryl group connected to the N centre in the other IPr ligand are omitted for clarity.*

Both **68** and **70** exhibit small negative total energy densities at the Ru···H(3a) BCPs (**68**: H(r) = -0.003 and **70**: H(r) = -0.005). This is accompanied by the reduced ρ(r) of the C(3)–H(3a) BCP relative to the two other C(3)–H BCPs, indicating the donation of electron density from the C(3)–H(3a) bond to the Ru moiety, i.e. C–H agostic interactions. This can be further supported by the NBO analysis that shows a donor-acceptor interaction between the C(3)–H(3a) σ-bonding orbital and the Ru–X anti-bonding orbital (**68**: X = CO and **70**: X = H). In **68**, the E(2) value corresponding to this interaction is

13.8 kcal/mol. In **70**, it slightly increases to 15.4 kcal/mol. This shows a stronger C–H agostic interaction in **70** than in **68**, consistent with the shorter Ru···C(3) distance in **70** than that in **69**.

3.4.2.2 Study of the Character of the Hydride Ligands in 69 and 70

As outlined above, the Ru–H distance is a function of the trans influence of the ligand trans to the hydride ligand. Herein, QTAIM and NBO analyses were performed on **69** and **70** to quantify the effect of the trans influence on the M–H_a and M–H_b interactions. Figure 3-9 shows the topology of the ρ(r) in the {Ru/Zn/C(O)} plane in **69** and **70**.

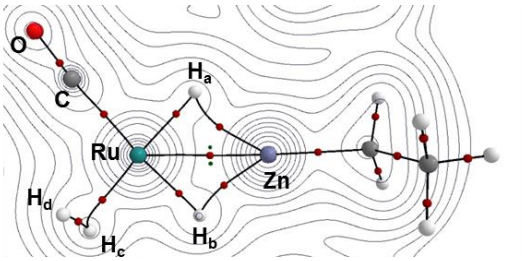

69

BCP	ρ(r)/eÅ^{-3}	∇^2ρ(r)/eÅ^{-5}	ε	H(r)/a.u.
Ru–H_a	0.118	0.174	0.071	-0.051
Ru–H_b	0.099	0.184	0.107	-0.037
Ru–H_c	0.094	0.363	6.022	-0.025
Zn–H_a	0.058	0.100	1.332	-0.014
Zn–H_b	0.064	0.110	0.522	-0.017

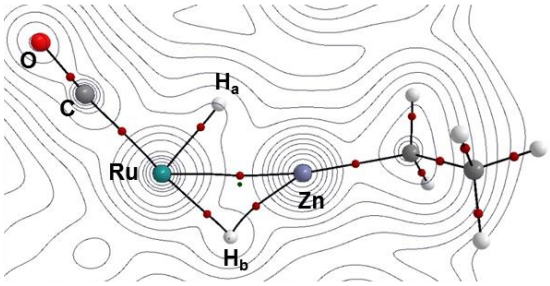

70

BCP	ρ(r)/eÅ^{-3}	∇^2ρ(r)/eÅ^{-5}	ε	H(r)/a.u.
Ru–H_a	0.137	0.134	0.018	-0.068
Ru–H_b	0.094	0.190	0.139	-0.033
Zn–H_b	0.067	0.114	0.448	-0.018

*Figure 3-9. Details of the QTAIM molecular graphs of **69** and **70** showing the electron density contours in the {Ru/Zn/C(O)} plane.*

In **69**, the {Ru$H_a$$H_b$Zn} unit features bond paths between the hydride ligands and the metal atom centres, enclosing two ring critical points (RCPs). The Ru–H_a and Ru–H_b BCPs feature larger ρ(r) values than the Zn–H_a and Zn–H_b BCPs, respectively. This indicates that both hydrides H_a and H_b interact more strongly with the Ru centre than the Zn centre. The Ru–H_a BCP exhibits a slightly higher ρ(r) than the Ru–H_b BCP indicating the Ru centre has a stronger interaction with the H_a centre than the H_b centre. The positive

values of $\nabla^2\rho(r)$ of the Ru–H BCPs suggest an ionic interaction between the corresponding atom centres. However, this situation is related to the close proximity of the hydrogen centres with metal centres.[146] In this case, the H(r) parameter is a reliable criterion to assess the nature of M–H interactions. In this regard, the negative H(r) values of the Ru–H BCPs support a covalent Ru–H interaction. The larger $|H(r)|$ value of the Ru–H_a BCP relative to the Ru–H_b BCP shows a slightly stronger interaction in the former compared with the latter, consistent with the trend of $\rho(r)$ values. This therefore does confirm that the strength of the Ru–H interaction varies depending on the trans influence of the ligand trans to the hydride centre. Thus, the high trans influence of CO weakens the Ru–H_b interaction and as a result, the Zn–H_b interaction is strengthened. In contrast, the Ru–H_a interaction becomes stronger trans to the lower trans influence η^2–H_2 ligand. Going to **70**, the Ru–H_a interaction is trans to a very low trans influence agostic interaction. As a result, no BCP is found between the Zn and H_a atom centres. This therefore shows that the hydrides H_a and H_b in **69** are bridging in character. However, in **70**, the hydride H_a has terminal character.

Assessment of the Ru–H ellipticities shows that in **69**, the Ru–H_a BCP has a lower ellipticity than the Ru–H_b interaction. A similar trend can also be seen in **70**. However, going from **69** to **70**, the ellipticity of the Ru–H_a interaction becomes significantly lower. This is consistent with the lower ellipticity of terminal hydride bond (0.01) relative to the bridging hydride (0.11) in complex $[\{Rh(H)(PPh_3)_2\}_2(\mu\text{–}Cl)_2(\mu\text{–}H)]^+$ reported by Macgregor**,** Weller and co-workers.[147]

NBO analysis can give further information about the nature of bonding in the $\{RuH_aH_bZn\}$ moieties of **69** and **70**. On the basis of the Wiberg bond indices (WBI) shown in Figure 3-10, the Ru centre interacts more strongly with H_a rather than H_b while the Zn centre interacts more strongly with H_b rather than H_a, consistent with the QTAIM results.

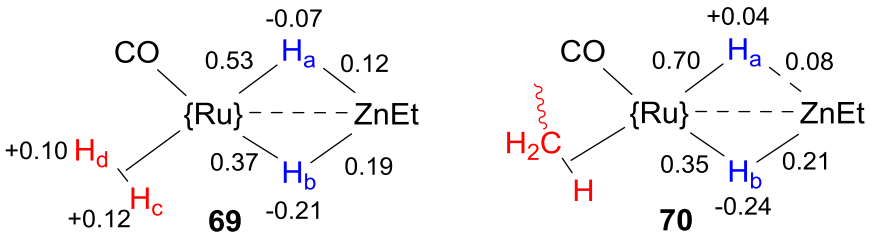

*Figure 3-10. WBI of the M–H interactions and the NBO charge of the hydride atoms in **69** and **70**. {Ru} = $Ru(IPr)_2^+$.*

Comparison of the NBO charge distribution of the H_a and H_b centres shows that in **69**, H_b has a more negative charge than H_a (Figure 3-10). From **69** to **70**, the charge of H_a reduces and becomes positive. For comparison, the terminal Ru–H bond in **1** features the charge of +0.15. This therefore does confirm that the H_a centre in **70** has a terminal character, consistent with the QTAIM results. In addition, it indicates that H_a is an electron deficient hydride while H_b is an electron rich hydride.

NBO analysis identifies a donor-acceptor interaction between the Ru–H_a bonding orbital and the Zn–Et anti-bonding orbital. In **69**, the E(2) energy associated with this interaction is computed to be 43.3 kcal/mol which lowers to 33.4 kcal/mol in **70**. The decrease in the E(2) of the donor-acceptor interaction is consistent with the lower trans influence of the agostic interaction relative to η^2–H_2 ligand. Interestingly, NBO identifies a lone pair of electron at the H_b centre in both **69** and **70**. This shows that the H_b ligand can be described as a hydride, consistent with the NBO charge distribution analysis. The second order perturbation analysis shows that the H_b centre in **69** and **70** interacts with the Ru–CO and Zn–Et anti-bonding orbitals. In **69**, the E(2) value associated with the interaction of the hydride H_b with Ru–CO anti-bonding orbital is stronger than with Zn–Et anti-bonding orbital (200.3 kcal/mol and 105.8) kcal/mol, respectively). A similar trend can be seen in **70** (161.0 kcal/mol and 93.9 kcal/mol. This shows that the hydride H_b interacts more strongly with the Ru moiety than the Zn moiety, presumably due to the lower energy of the Ru–CO anti-bonding orbital versus Zn–Et anti-bonding orbital.

Taken all the findings together, it can be seen that the character of the hydride ligands in **69** and **70** sits on a continuum between two clear-cut types (terminal or bridging hydride) which is a function of the trans influence of the ligand trans to the hydride. In this regard, the hydride H_b in **69** and **70** is trans to CO and hence has a bridging character. The hydride

H_a in **69** is trans to a H_2 ligand and is more toward a bridging hydride. However, in **70**, the hydride H_a is trans to an agostic interaction and hence it has a terminal character.

In the remainder of this chapter, another organisation principle was defined to distinguish a terminal hydride character from a bridging hydride character. In this regard, for hydride ligand trans to a low trans influence moiety such as an agostic interaction, the terminal character will be described by the "Ru–H" representation (i.e. no bond between the H and Zn centres). For hydride ligands trans to strong trans influence moieties such as CO, the bridging character will be shown by the "Ru–H–Zn" representation.

3.4.3 Mechanism of Formation of the Ru-Zn Species

3.4.3.1 Reaction Mechanism for the Formation of $[Ru(IPr)_2(CO)(ZnEt)]^+$, 68

DFT calculations to investigate the mechanism of the formation of **68** located the two possible adducts **I(67-68)** and **I(67-68)1** formed between **67** and $ZnEt_2$ with the latter being significantly more stable than the former by 11.9 kcal/mol. Figure 3-11 displays the structural details of **I(67-68)** and **I(67-68)1** in the {Ru/H/C(O)/Zn} plane.

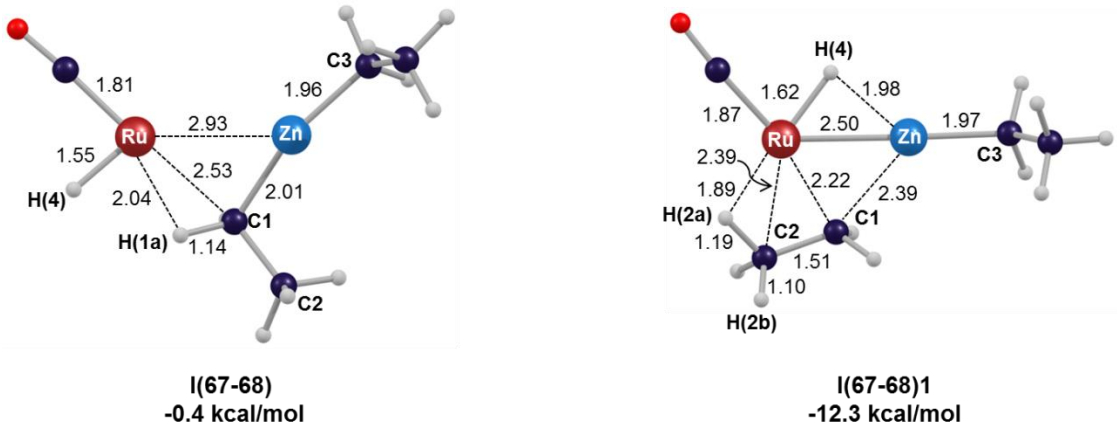

*Figure 3-11. Representation of adduct **I(67-68)** and the adduct **I(67-68)1** within the equatorial plane with the labelling scheme for selected atoms. Selected distances are shown in Å. The IPr ligands are omitted for clarity. The energies are relative to separate species **67** and $ZnEt_2$.*

In **I(67-68)**, the Ru···Zn distance is significantly longer than sum of the covalent radii of the Ru and Zn atoms, suggesting no covalent interaction between the metal centres. However, it exhibits a terminal ethyl on the Zn centre which has a short Ru···C(1) distance to give an α-C–H agostic interaction, showing **I(67-68)** is a sigma-complex.

In **I(67-68)1**, the Ru···Zn distance is shorter than the covalent radii of the Ru and Zn atoms, showing a covalent interaction between the metal centres. **I(67-68)1** possesses a bridging ethyl situated between the metal centres with the short Ru···C(2) and long C(2)–H(2a) distances to give the β-C–H agostic interaction. It is worth noting that the H(4) centre is trans to a C–H agostic interaction and hence, it displays terminal hydride character.

In **I(67-68)**, the H(4) centre is cis to the Zn–C(1) bond. Thus, the shortening of the C(1)···H(4) distance can promote the C–H bond formation. This process is assessed by the computed pathway shown in Figure 3-12. In this regard, elongation of the Zn–C(1) bond distance transfers the ethyl moiety to the hydride across the Ru–Zn bond to form the C–H bond. However, the transition structure (**TS(67-68)**) for this process lies at the high energy of +29.2 kcal/mol to generate the ethane complex of **68**, **I(67-68)3**, at -17.9 kcal/mol. It can be seen that upon the formation of the ethane complex, the Ru–Zn distance significantly shortens from 2.93 Å in **I(67-68)** to 2.44 Å in **I(67-68)3**, showing a substantial increase in the strength of the Ru–Zn interaction. This suggests the reduction of the Ru centre by two units upon the formation of the ethane complex **I(67-68)3**. Once ethane dissociates from the Ru centre, it produces the Ru-Zn species **68**. This process is computed to be exergonic by 30.4 kcal/mol. However, due to the very high energy barrier, this process is not in agreement with the facile formation of **68** seen experimentally.

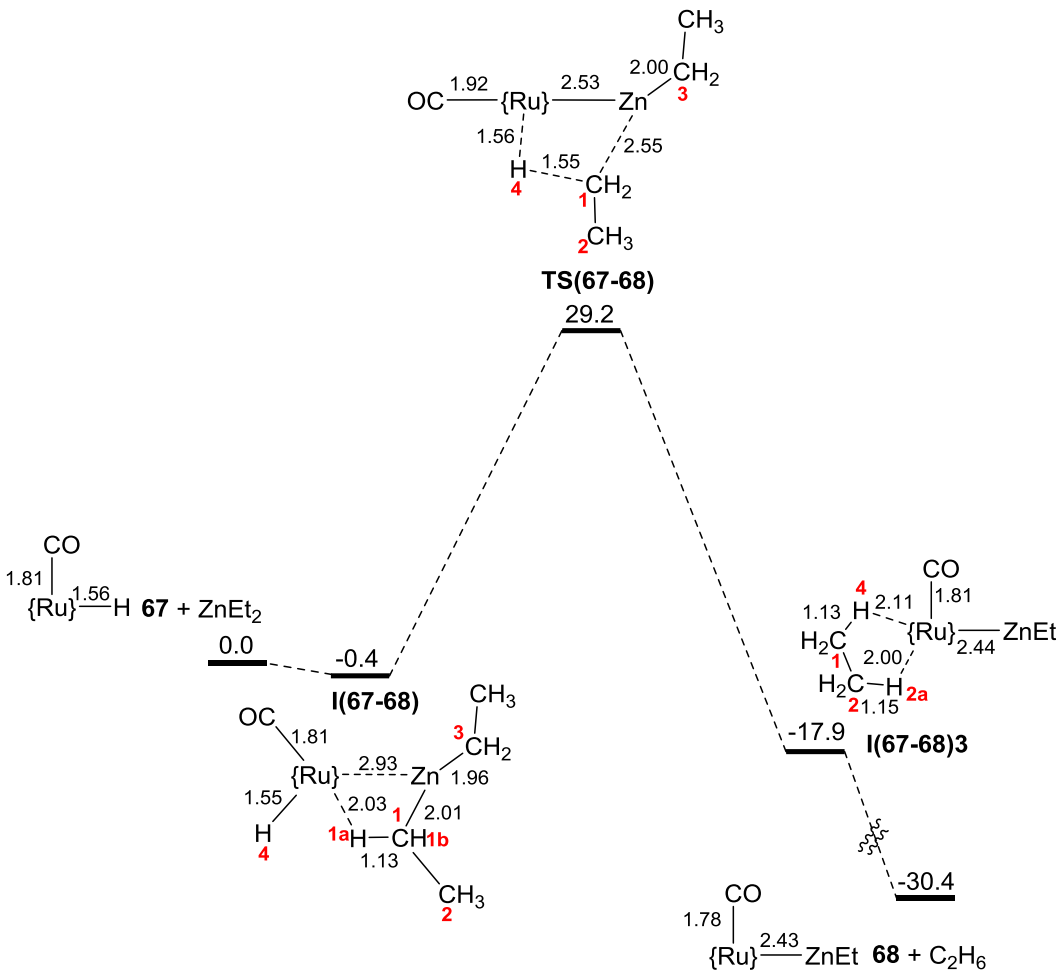

*Figure 3-12. Reaction profile (free energy, kcal/mol) for the formation of **68** and C_2H_6 from **67** and $ZnEt_2$; schematic structures show key distances (Å) within the equatorial plane; {Ru} = $Ru(IPr)_2^+$.*

The C–H coupling process was also investigated from **I(67-68)1**. In this regard, one possibility to form the ethane complex is the transfer of the hydride to the ethyl group situated in the cis position to the H(4) centre (i.e. the C(3) centre) via **TS(67-68)1'** (Figure 3-13). In contrast to **TS(67-68)** in which the C–H coupling process occurs across the Ru–Zn bond, in **TS(67-68)1'**, the C–H coupling process occurs at the Zn centre. However, similar to **TS(67-68)**, it is a high-energy process which requires an energy barrier of 42.5 kcal/mol to form the ethane complex **I(67-68)3**. Therefore, this process is again inconsistent with the reaction conditions. It should be noted that the IRC calculations corresponding to the reverse pathway to form **I(67-68)1** led to the formation of the separate reactants instead (**67** + $ZnEt_2$).

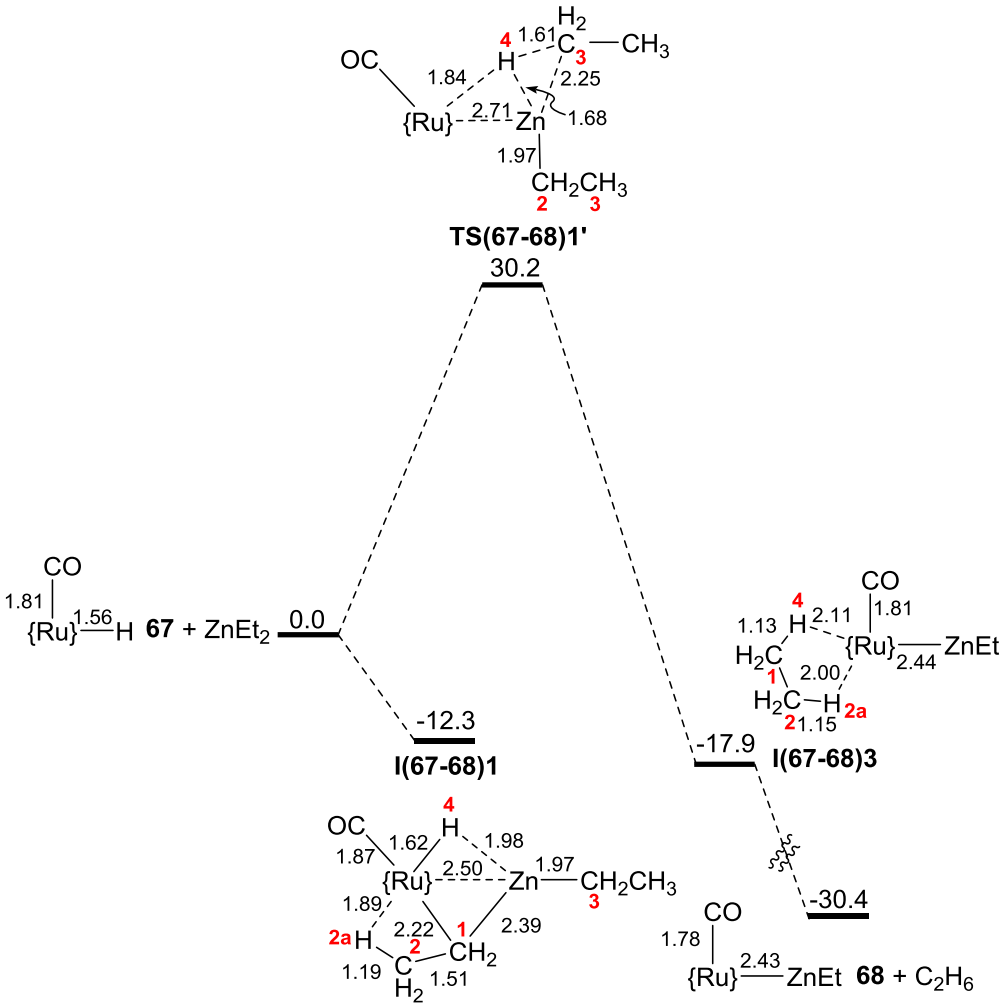

*Figure 3-13. Reaction profile (free energy, kcal/mol) for the formation of **68** and C_2H_6 from **67** and $ZnEt_2$; schematic structures show key distances (Å) within the equatorial plane; {Ru} = $Ru(IPr)_2^+$.*

Alternatively, transfer of the bridging ethyl to the hydride in **I(67-68)1** can form the ethane-complex. However, the ethyl and hydride should be firstly in the cis position relative to each other. Interestingly, the Ru–Zn interaction can accommodate the movement of the hydride around the Ru-Zn vector. This transfers the ethyl group onto the Ru centre and places the hydride in the cis position to the ethyl moiety while at the same time the CO ligand moves into the site vacated by the hydride. This process occurs via the single transition structure **TS(67-68)1** depicted in Figure 3-14. The energy barrier for this process is very low and computed to be 11.1 kcal/mol (relative to **I(67-68)1**) and forms **I(67-68)2** at -13.7 kcal/mol (Figure 3-15).

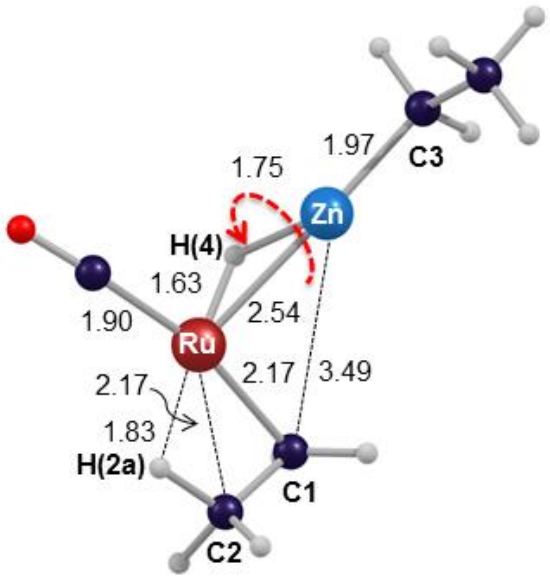

*Figure 3-14. Representation of **TS(67-68)1** within the equatorial plane with the labelling scheme for selected atoms. Selected distances are shown in Å. The IPr ligands are omitted for clarity.*

In **I(67-68)2**, the H(4) centre is still trans to a β-agostic interaction and hence shows a short Ru–H distance of 1.64 Å consistent with a terminal hydride character. **I(67-68)2** can then undergo a facile reductive coupling of ethane via **TS(67-68)2** at low energy barrier of 6.8 kcal/mol (relative to **I(67-68)2**) to give **I(67-68)3**.

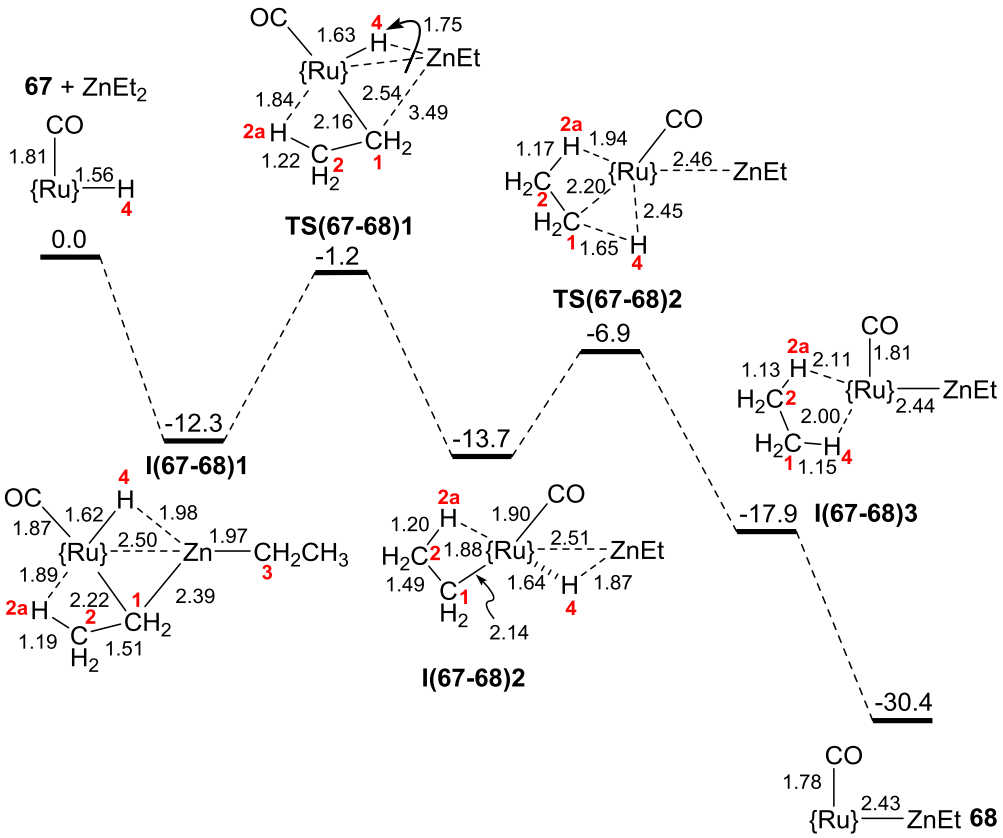

*Figure 3-15. Computed reaction profile (free energy, kcal/mol) for the formation of **68** and C_2H_6 from the reaction of **67** with $ZnEt_2$. Schematic structures show key distances (Å) within the equatorial plane; {Ru} = $Ru(IPr)_2^+$.*

On the basis of the computed pathways to form **68**, the two-step process shown in Figure 3-15 is significantly more kinetically feasible than the one-step processes shown in Figure 3-12 and Figure 3-13 and is consistent with the facile formation of **68** at room temperature. This is mainly due to the feasible rotation of the {Ru/H/Zn} unit about the Ru–Zn vector which transfers the ethyl group from the Zn centre onto the Ru centre and places the hydride cis to the ethyl. It is worth noting that in this pathway, the C–H coupling process occurs at the Ru centre while in the one-step process it either happens at the Zn centre or across the Ru–Zn bond.

3.4.3.2 Reaction of 68 with H_2 to Form $[Ru(IPr)_2(CO)(\eta^2\text{–}H_2)(H_2)(ZnEt)]^+$ (69)

Addition of the first molecule of H_2 to the unsaturated Ru(0)–Zn(II) species **68** can take place either in the position trans or cis to the {ZnEt} moiety (Figure 3-16). The former gives **I(68-69)** at -30.3 kcal/mol while the latter gives the slightly less stable species **I(68-**

69)' at -26.5 kcal/mol. Addition of the second molecule of H_2 gives the bis–η^2–H_2 species **I(68-69)1** at -32.1 kcal/mol which is slightly more stable than **I(68-69)** and **I(68-69)'**. It is worth noting that attempts to locate the transition states corresponding to the addition of H_2 to the Ru centre trans or cis to CO were inconclusive due to a very flat potential energy surface.

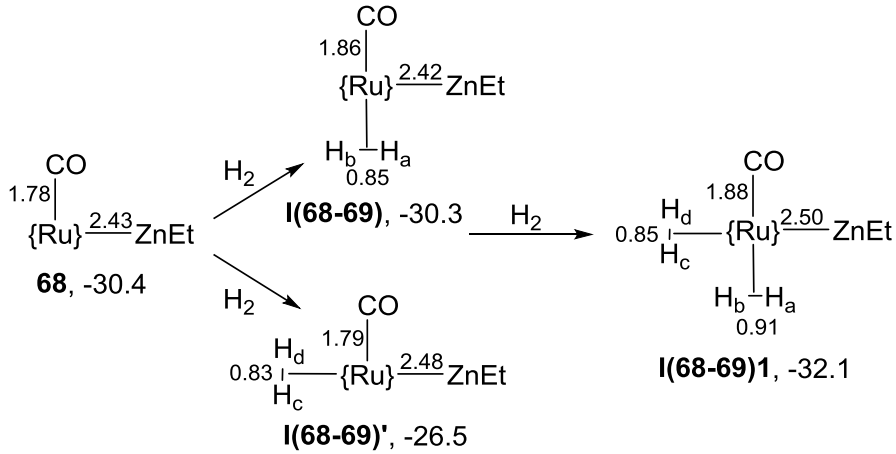

*Figure 3-16. Addition of H_2 to **68** to form the mono– and bis–η^2–H_2 species. Schematic structures show key distances (Å) within the equatorial plane; {Ru} = Ru(IPr)$_2^+$. Free energies are reported relative to **67** and other small molecules (H_2 and C_2H_6) in kcal/mol.*

H_2 activation in **I(68-69)1** can occur via two pathways depending on whether the reacting H_2 is cis or trans to the Zn. As shown in Figure 3-17, in Pathway **I**, the cleavage of the H_2 cis to the Zn occurs via **TS(68-69)4**. This transition state lies slightly lower in energy than **I(68-69)1** at -32.3 kcal/mol. This is mainly due to the zero point energy correction of the free energy which destabilises **TS(68-69)4** slightly less than **I(68-69)1**. H_a–H_b bond cleavage transfers H_a into a bridging position to give **I(68-69)4** at -34.8 kcal/mol.

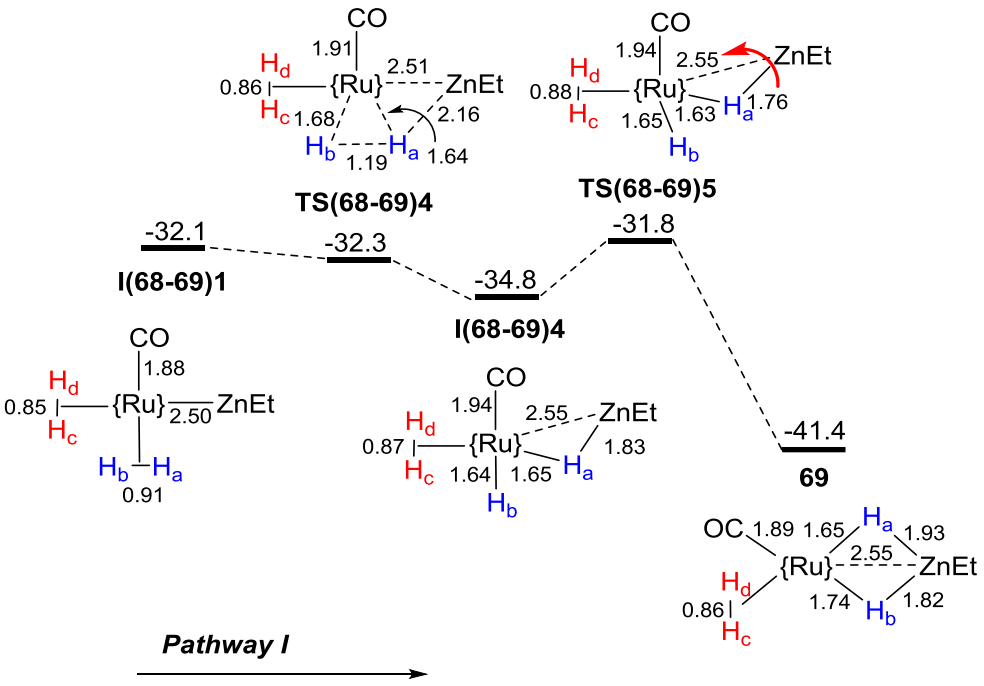

*Figure 3-17. The computed energy profile for formation of **69** from **I(68-69)1** via Pathway **I**. Free energies are in kcal/mol. Schematic structures show key distances (Å) within the equatorial plane, as well as the labelling scheme for the H atoms; {Ru} = $Ru(IPr)_2^+$.*

Since the H_b centre is cis to H_a in a bridging position, its transfer into the bridging position requires H_a to move cis to the CO. Interestingly, rotation of the {RuH_aZn} moiety about the Ru–Zn vector would achieve this. The transition structure corresponding to this process is **TS(68-69)5** at -31.8 kcal/mol which is shown in Figure 3-18. In **TS(68-69)5**, rotation of the {RuH_aZn} moiety places the H_a centre into the bridging position cis to the CO ligand and transfers the H_b centre into the bridging position trans to the CO ligand. Interestingly, **TS(68-69)5** performs a very similar process as the transition structure **TS(67-68)1**. However, in the former, the rotation process transfers an X-type ligand (H_b) from the Ru centre into the bridging position while in the latter, an X-type ligand (ethyl) transfers from the bridging position onto the Ru centre. Once H_b has transferred into the bridging position, it produces **69** at -41.4 kcal/mol.

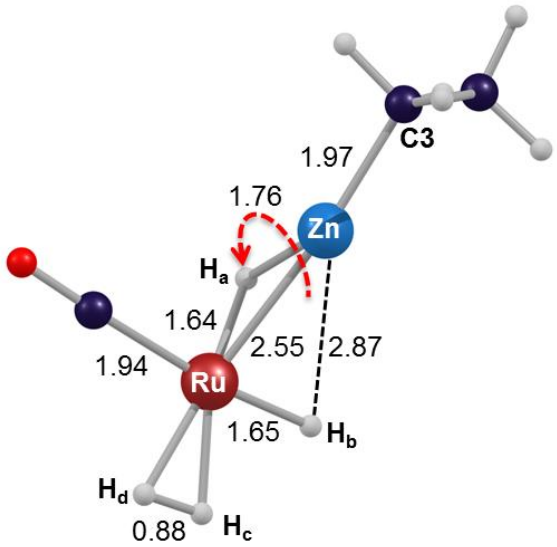

*Figure 3-18. Representation of **TS(68-69)2** within the equatorial plane with the labelling scheme for selected atoms. Selected distances are shown in Å. The IPr ligands are omitted for clarity.*

In Pathway **II**, the oxidative cleavage of the H_c–H_d bond at the Ru centre takes place via **TS(68-69)1** at -28.6 kcal/mol (Figure 3-19). In contrast to the first step of Pathway **I**, Pathway **II** does not transfer either of the hydrogen centres into a bridging position and instead forms the classical dihydride species **I(68-69)1** at -28.0 kcal/mol. In the next step of the process, H_c can transfer to the H_b centre to give an η^2–H_c–H_b ligand. This breaks the H_a–H_b bond and transfers the H_a into a bridging position which then induces {RuH_aZn} rotation about the Ru–Zn vector and places H_a cis to the CO. These processes occur via the single transition state **TS(68-69)2** at -28.1 kcal/mol and forms **I(68-69)2** at -35.0 kcal/mol. In **I(68-69)2**, the H_c–H_b moiety is cis to a vacant bridging position. Therefore, transfer of H_b into that vacant position would form **69**. This occurs by H_d transfer to H_c which breaks the H_c–H_b bond and transfers the H_b into the bridging position.

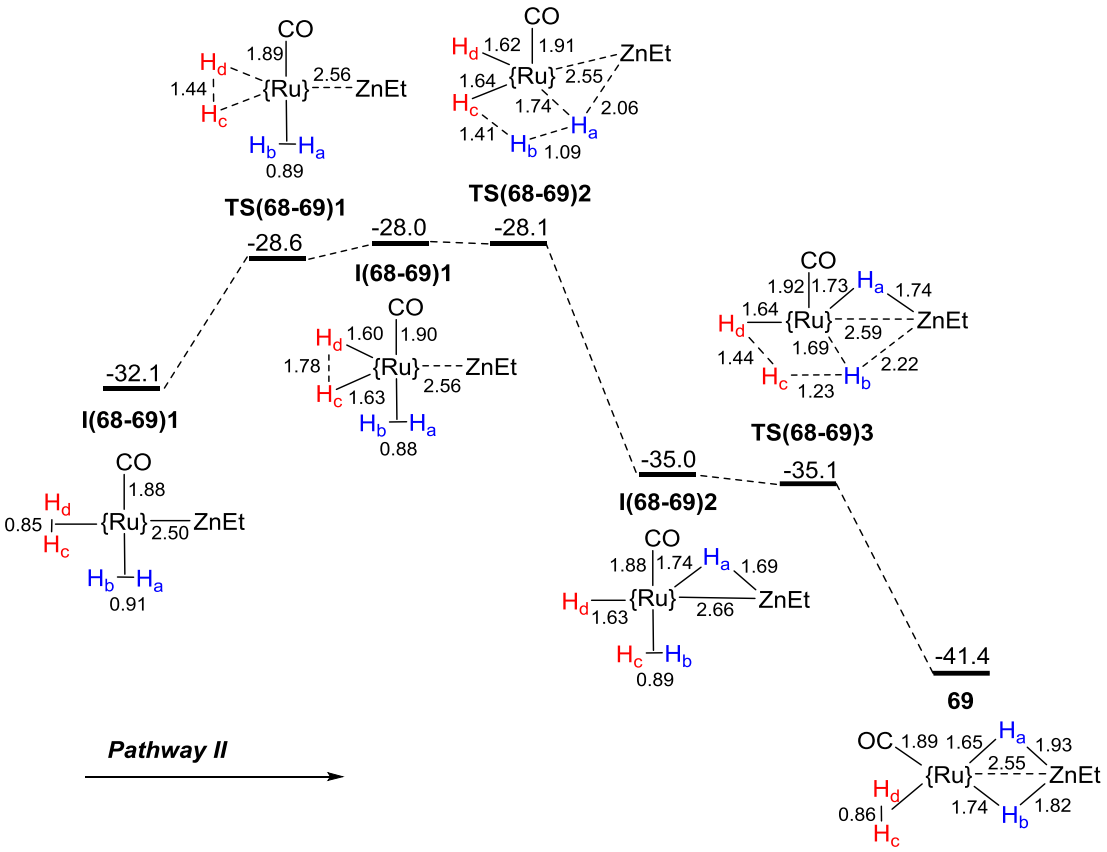

*Figure 3-19. The computed energy profile for formation of **69** from the reaction of **68** with H_2 via Pathway **II**. Free energies are in kcal/mol. Schematic structures show key distances (Å) within the equatorial plane, as well as the labelling scheme for the H atoms; {Ru} = $Ru(IPr)_2^+$.*

Another possibility to form **69** is the isomerisation of **I(68-69)4** to **I(68-69)2** via Pathway **III**. As shown in Figure 3-20, once the mono–η^2–H_2 species **I(68-69)4** is formed via Pathway **I**, the H–H bond which is trans to the Zn moiety can be broken by a σ-CAM (sigma-complex-assisted metathesis)[148] process to form the new H–H bond cis to the Zn moiety. This process occurs via **TS(68'-69)4** at -32.0 kcal/mol and forms **I(68'-69)2** at -35.9 kcal/mol. It is interesting to note that as the σ-CAM process forms the H_b–H_c bond cis to the Zn moiety, the rotation of the {RuH_aZn} unit about the Ru-Zn vector does not occur. Thus, this step takes place separately via **TS(68'-69)3** at -32.2 kcal/mol to generate **I(68-69)2** at -35.0 kcal/mol. Once **I(68-69)2** is formed, it can follow Pathway **II** to form **69**.

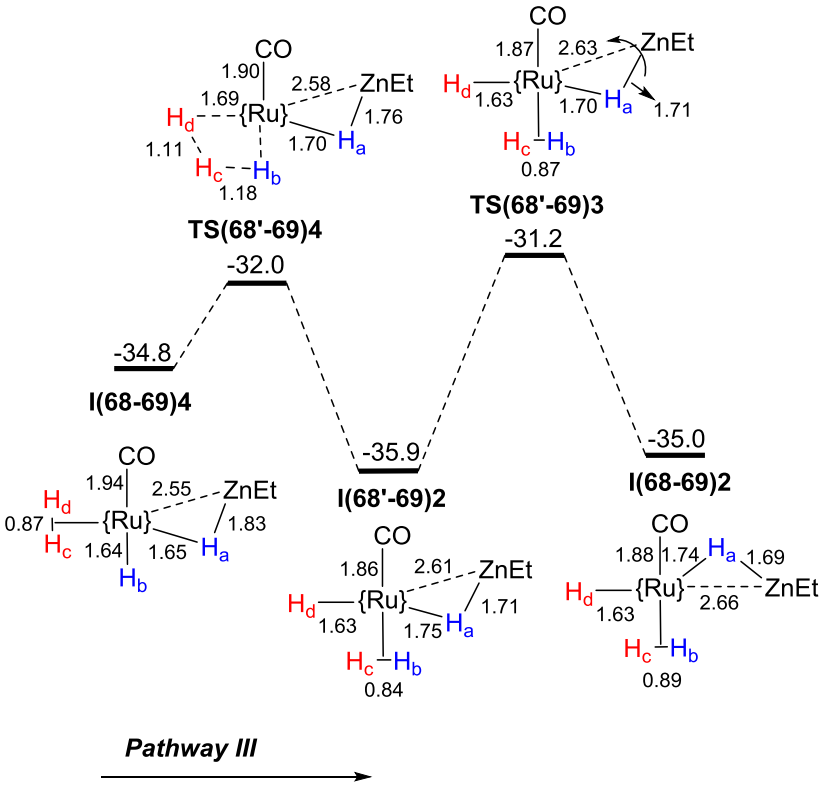

*Figure 3-20. The computed energy profile for isomerisation of **I(68-69)4** to **I(68-69)2**. Free energies are in kcal/mol. Schematic structures show key distances (Å) within the equatorial plane, as well as the labelling scheme for the H atoms; {Ru} = Ru(IPr)$_2^+$.*

The computed mechanisms for the formation of **69** show that in Pathways **I**, **II** and **III**, formation of the dihydride species complex **69** requires a low energy barrier of 0.3, 4.5 and 4.7 kcal/mol, respectively. This indicates that Pathway **I** is the most kinetically accessible pathway to generate **69**. However the energy barriers in all three computed mechanisms are very low and hence they are accessible under the reaction conditions. From the thermodynamic point of view, the reaction energy for the formation of **69** (from the reaction of **68** and 2H_2) is computed to be exergonic by 9.3 kcal/mol (relative to **68**). This is indeed consistent with the facile cleavage of H_2 and rapid formation of **69** at room temperature. It is worth noting that in Pathway **III**, the highest energy barrier corresponds to the rotation of the {RuH$_a$Zn} unit with the energy barrier of 4.7 kcal/mol (relative to **I(68'-69)2**).

3.4.3.3 Mechanism of H–H Bond Cleavage in the bis(η^2–H_2) Species I(68-69)1

As shown in Figure 3-19, the first step of Pathway **II** shows a classical example of H_2 oxidative cleavage at the Ru centre which generates two terminal Ru–H bonds. However, in the case of Pathway **I**, the mechanism of the H_a–H_b bond cleavage is less clear as it transfers one hydrogen atom (H_a) into the bridging position while the other hydrogen atom (H_b) remains at the Ru centre. The question therefore arises whether the H_a–H_b bond activation happens at the Ru centre via an oxidative cleavage mechanism, as in Pathway **II**, or it happens heterolytically through the metal–metal cooperation in which the Zn centre accepts the hydride and the proton remains on the Ru centre.

To assess this, NBO charge analysis was performed on the bis–η^2–H_2 intermediate (**I(68-69)1**) along with two key transition structures **TS(68-69)1** and **TS(68-69)4**. As shown in Figure 3-21, all four hydrogens in the bis–η^2–H_2 intermediate (**I(68-69)1**) feature positive charges ranging from +0.05 to +0.07. Going from **I(68-69)1** to **TS(68-69)4**, there is a marginal decrease in the charge of H_c from +0.07 to +0.02 while a marginal increase can be seen in the charge of H_d from +0.05 to +0.11. In **I(68-69)1**, the charge of the H_a and H_b atoms are +0.06 and +0.07 which slightly reduces to +0.02 and +0.05 in **TS(68-69)1**, respectively. If the process were to occur heterolytically then one would assume the corresponding transition structure would show a significantly polarised H–H bond with one hydrogen having a significant –ve charge and the other a significant +ve charge. However, this cannot be seen in transition structures **TS(68-69)1** and **TS(68-69)4**. This therefore rules out the heterolytic mechanism for the H–H activation. In fact, the positive charges of the hydrogen atoms of the elongated H···H moiety in both **TS(68-69)1** and **TS(68-69)4** imply that they follow a similar mechanism for the H–H bond cleavage. With respect to this and also the fact that in **TS(68-69)4**, this process occurs by an oxidative cleavage mechanism, a similar mechanism can be expected for the H–H activation via **TS(68-69)1**. Interestingly, this is supported by the geometry of the transition structure **TS(68-69)1**. In **TS(68-69)1**, the Zn···H_a distance is 2.16 Å which shows that the Zn centre is not directly involved in the H_a–H_b bond cleavage. In fact, it is only after the oxidative cleavage of the H_a–H_b bond at the Ru centre that the H_a transfers into the bridging position between the Ru and Zn centres while the H_b remains at the Ru centre.

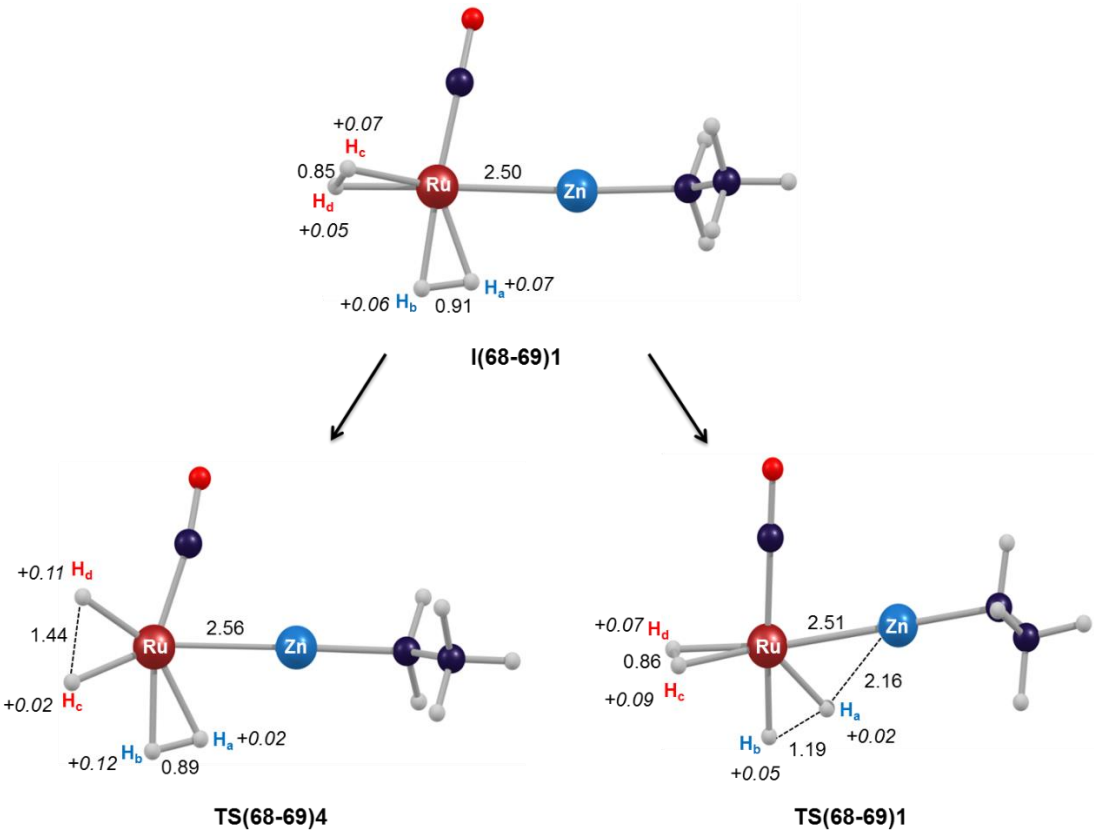

*Figure 3-21. NBO charges (in italics) of the H atoms in **I(68-69)1**, **TS(68-69)1** and **TS(68-69)4**. The IPr ligands are removed for clarity. Schematic structures show key distances (Å) within the equatorial plane, as well as the labelling scheme for the H atoms; {Ru} = Ru(IPr)$_2^+$.*

3.4.3.4 H_2 Loss from 69 to Give $[Ru(IPr)_2(CO)(H)_2(ZnEt)]^+$ (70)

69 can undergo H_2 loss via **TS(69-70)** with an energy barrier of 15.7 kcal/mol relative to **69** (Figure 3-22). In this process, as H_2 dissociates from the Ru centre, the C–H agostic interaction comes in to form **70** at -36.4 kcal/mol. Although this reaction is kinetically accessible at the elevated temperature of 50°C, it is an endergonic process by 5.0 kcal/mol, showing the Ru centre is reluctant to lose H_2. However, under a vacuum, H_2 can be removed from the system which then shifts the equilibrium toward the formation of **70**.

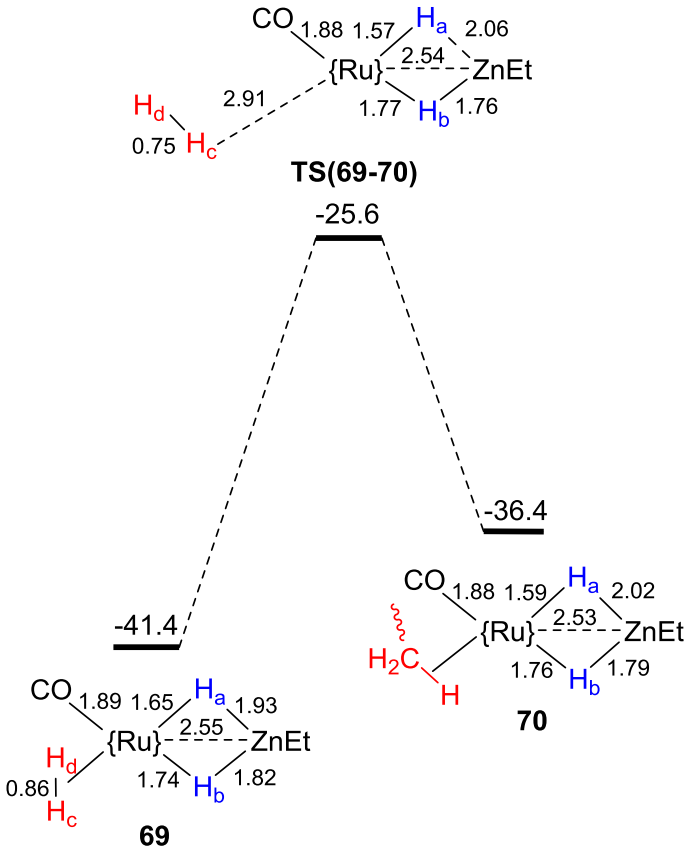

*Figure 3-22. The computed energy profile for H_2 loss reaction in **69** to generate **70**. Free energies are in kcal/mol. Schematic structures show key distances (Å) within the equatorial plane, as well as the labelling scheme for the H atoms; {Ru} = $Ru(IPr)_2^+$.*

3.4.4 H/H Exchange Processes

3.4.4.1 H/H Exchange Process at 69

As outlined in the section 3.1.2, **69** can undergo a facile H/H exchange between the dihydrogen ligand, H_c–H_d and the cis bridging hydride, H_b. As shown in Figure 3-23, this reaction is computed to start with the isomerisation of **69** to **I(68-69)2** with a low energy barrier of 6.3 kcal/mol (Figure 3-19). **I(68-69)2** then undergoes a facile H_2-rotation via **TS(69E$_{b\text{-}c}$)2** with a small overall energy barrier of 9.8 kcal/mol. A reverse process then completes the H_b/H_c exchange process.

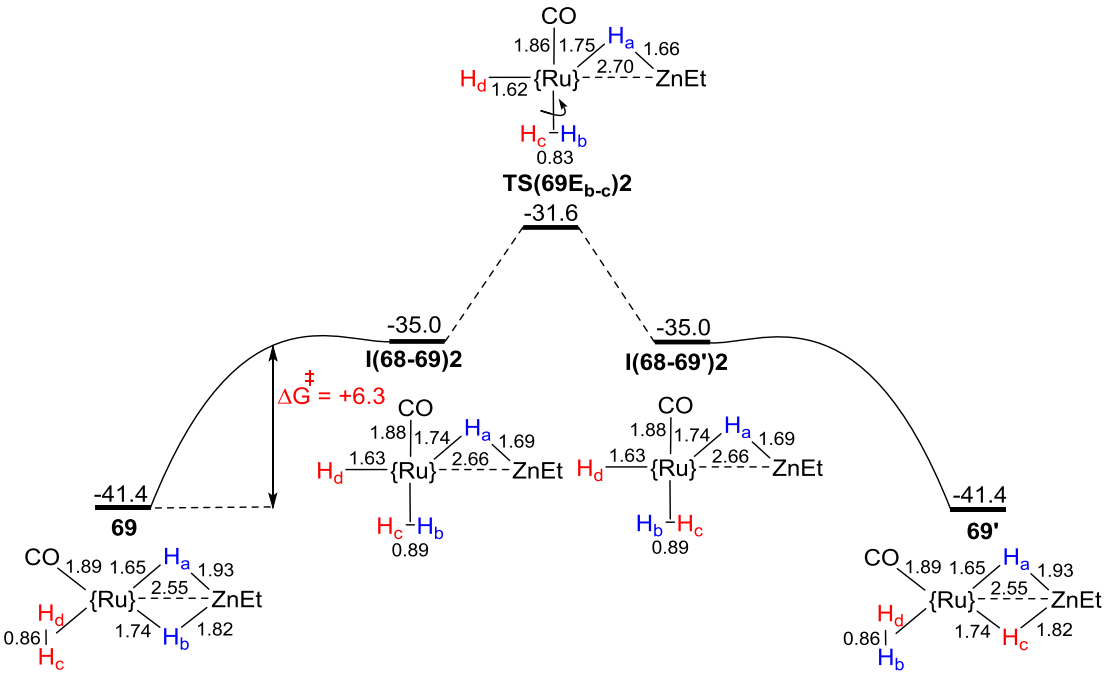

*Figure 3-23. The computed energy profile for H_b/H_c process in **69**. Free energies are in kcal/mol. Schematic structures show key distances (Å) within the equatorial plane, as well as the labelling scheme for the H atoms; {Ru} = $Ru(IPr)_2^+$.*

The H/H exchange between the bridging hydrogens H_a and H_b involves reforming the bis–η^2–H_2 species **I(68-69)1** with an energy barrier of 9.6 kcal/mol (i.e. the reverse process for the formation of **69** via the reaction of **68** with H_2, Figure 3-19). As shown in Figure 3-24, once **I(68-69)1** is formed, rotation of the η^2–H_a–H_b ligand via **TS(69E$_{a-b}$)1** at -28.3 kcal/mol followed by transfer of H_b and H_a atoms into the bridging positions completes the H_a/H_b exchange process. The overall energy barrier accounting for this process is computed to be 13.1 kcal/mol which is accessible at room temperature.

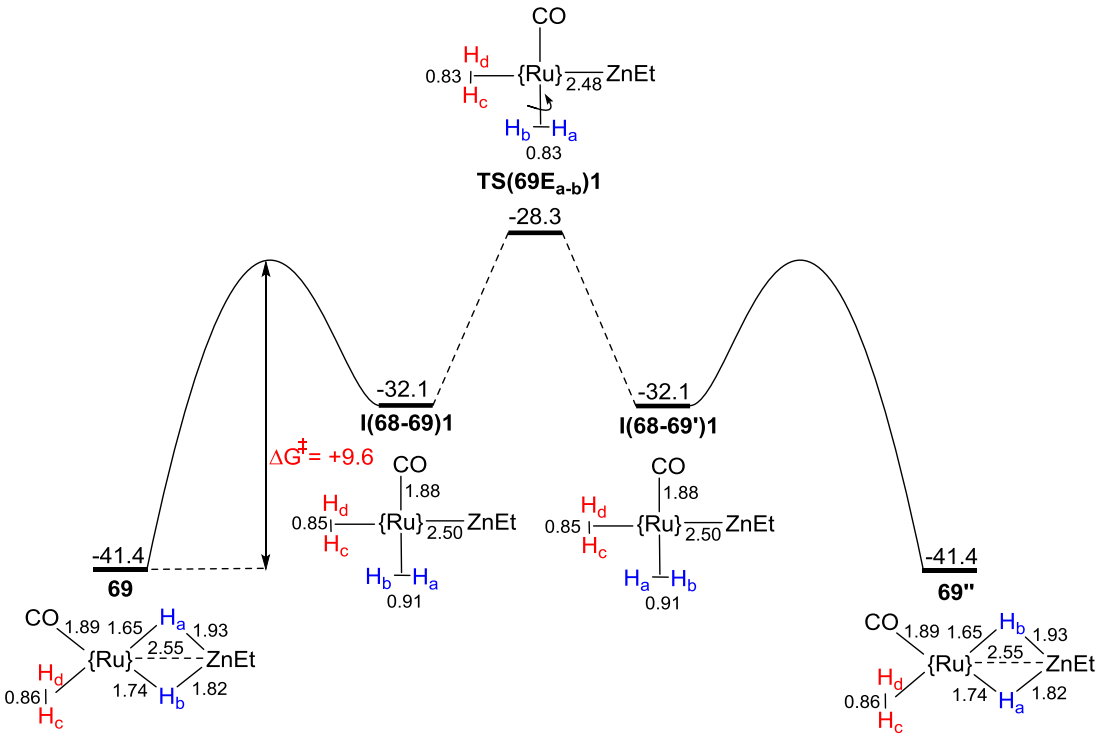

Figure 3-24. The computed energy pathway for the exchange of H_a and H_b at ***69****. Free energies are in kcal/mol. Schematic structures show key distances (Å) within the equatorial plane, as well as the labelling scheme for the H atoms; {Ru} = Ru(IPr)$_2^+$.*

In comparison to the H_c–H_d/H_b exchange, exchange of the bridging hydrides H_a and H_b is found to be more energy-demanding. This is consistent with the experimental data, showing the exchange process in the former is faster than the latter.

3.4.4.2 H/H Exchange Process in 70

On the basis of the room temperature ^{1}H NMR spectrum of **70**, H_a and H_b are equivalent and a computed exchange process that could explain this is shown in Figure 3-25. In this process, the initial rotation of the {RuH$_a$Zn} moiety about the Ru–Zn vector transfers H_b onto the Ru centre. This process occurs via **TS(70E$_{a\text{-}b}$)1** at -22.9 kcal/mol and gives **I(70E$_{a\text{-}b}$)1** at -26.8 kcal/mol. In **I(70E$_{a\text{-}b}$)1**, H_a and H_b are cis to each other allowing a reductive coupling mechanism to form the mono–η^2–H_2 species **I(68-69)**. This process can occur via **TS(70E$_{a\text{-}b}$)2** at -26.6 kcal/mol and forms **I(68-69)** at -30.3 kcal/mol. Once **I(68-69)1'** is formed, it can undergo H_2-rotation via **TS(70E$_{a\text{-}b}$)2** at -29.5 kcal/mol. A

reverse process toward the formation of **70'** then completes the H_a/H_b exchange with the overall energy barrier of 7.4 kcal/mol.

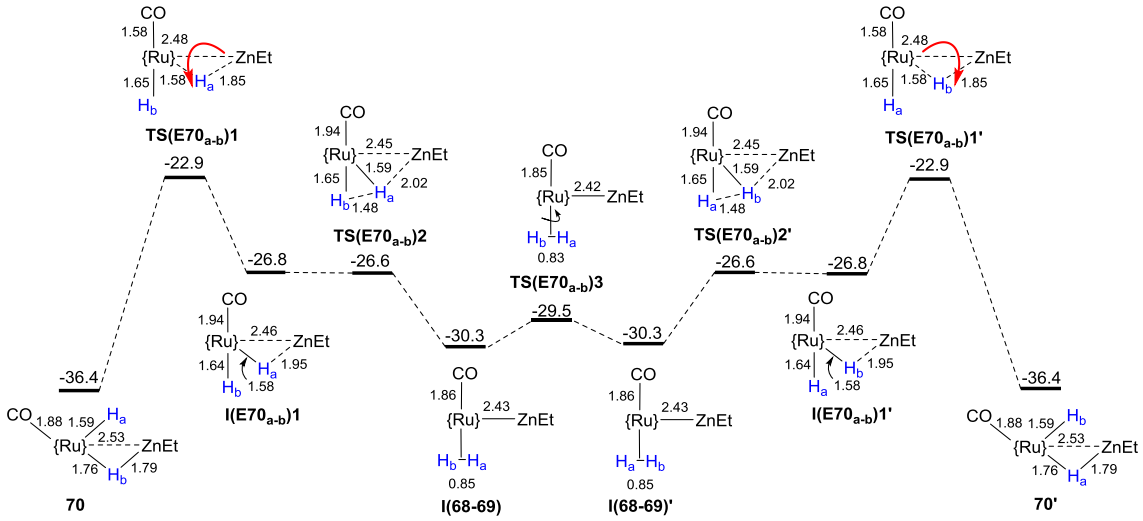

*Figure 3-25. The computed energy profile for the exchange of H_a with H_b at **70**. The {Ru} unit represents $Ru(IPr)_2^+$ moiety. Free energies are in kcal/mol.*

Alternatively, the movement of the CO ligand from the position trans to the H_b atom to trans to the H_a atom would also render the H_a and H_b positions equivalent. Such a process demands a transition structure with a distorted trigonal bipyramid geometry (i.e. Y-shape) as in **TS(70-70')** shown in Figure 3-26. However, this transition state is extremely unstable relative to **69** by 31.5 kcal/mol. This is mainly due to the fact that in the Y-shape geometry, the interaction of the lone pair of the CO ligand with the occupied d orbitals of the Ru centre is maximised (Ru–CO = 2.01 Å) and consequently, this makes the transition structures significantly destablised.[149]

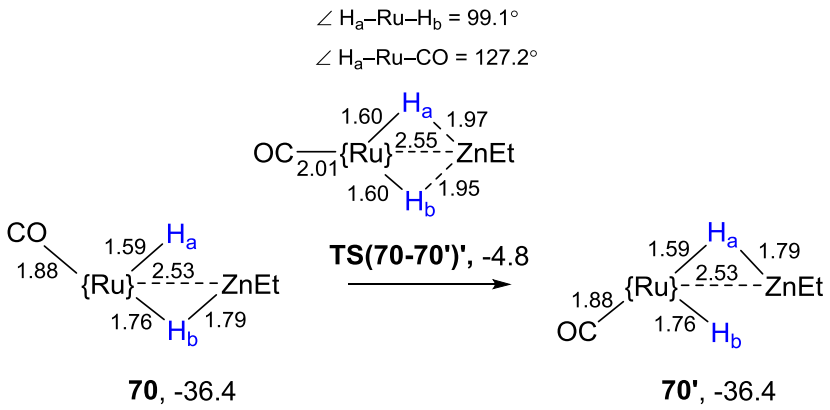

*Figure 3-26. The movement of the CO ligand to make the H_a and H_b positions equivalent at **70**. Free energies are in kcal/mol. Schematic structures show key distances (Å) within the equatorial plane, as well as the labelling scheme for the H atoms; {Ru} = $Ru(IPr)_2^+$.*

3.5 Conclusions

On the basis of DFT studies on the heterobimetallic Ru-Zn species, a number of broad conclusions can be drawn about the nature of metal–metal bonding in **68**, **69** and **70**, and metal-hydride interactions in **69** and **70**:

I. The nature of the interaction between the monovalent zinc (ZnEt) complexes of ruthenium has been investigated. QTAIM analysis of the Ru-Zn complexes shows a Ru–Zn BCP, exhibiting a small $\rho(r)$, positive $\nabla^2\rho(r)$ and a small negative H(r). Such QTAIM metrics have been interpreted as dative interaction between the metal centres. NBO Donor-acceptor interaction analysis confirmed this and indicated that in this interaction Ru acts as a LB centre and donates electron density to the divalent Zn moiety. i.e. Ru→Zn interaction. In comparison to **69** and **70**, **68** exhibits the strongest Ru→Zn interaction. This along with the presence of the Ru–Zn bonding orbital supports a Ru(0)–Zn(II) formulation in **68**. A significantly weaker Ru–Zn interaction in **69** and **70** relative to **68** and the absence of the Ru–Zn bonding orbital supports a Ru(II)–Zn(II) formulation in **69** and **70**. This was also confirmed by a significantly lower CO stretching frequency of **68** relative to that in **69** and **70**.

II. The nature of the bonding in the {$Ru/H_a/H_b/Zn$} unit was also assessed by the same computational techniques. QTAIM analysis shows that the nature of the hydrides H_a and H_b is determined by the trans influence of the ligands opposing the hydride. A strong trans influence results in a hydride ligand with a more bridging character while a weak trans influence results in a more terminal character. NBO charge distribution analysis shows that the former exhibits a more electron-rich hydride.

The following specific conclusions can also be drawn based on the computed mechanisms for the formation of **68**, **69** and **70**.

III. The computed mechanism for the reaction of **67** with $ZnEt_2$ involves the transfer of one alkyl group from the Zn moiety to onto the Ru centre followed by the reductive elimination of ethane to yield **68**. The former requires the rotation of the hydride around the Ru–Zn vector, pushing the Et group onto the Ru centre and placing the hydride cis to this ethyl group.

IV. This process in which heterobimetallic complexes can be formed by the reaction of a TM-H species and a metal-alkyl precursor can be used as a strategy to generate other heterobimetallic complexes, featuring unsupported metal-metal bonds.

V. The computed mechanism for the reaction of **68** with H_2 shows that H–H bond activation across the Ru–Zn bond occurs homolytically at the Ru centre. In this process, after the H–H bond cleavage, the Zn centre accepts the first hydride to stablise the consequent intermediate by a {Ru–H–Zn} bridge. The second hydride then transfers into the bridging position once the hydride rotates around the Ru–Zn vector, giving a vacant site for the second hydride to produce **69**.

VI. Formation of **70** requires the displacement of the η^2–H_2 ligand of **69** by the C–H agostic interaction. This reaction is computed to be an endergonic process, consistent with the elevated temperature and vacuum conditions of the reaction.

VII. H/H exchange in the dihydride species **69** and **70** involves σ-CAM and H_2-rotation steps. In **69**, the H/H exchange between the bridging hydrides was computed to be more energy demanding than the exchange of the η^2–H_2 and the bridging hydride. This shows that the H/H exchange process between the η^2–H_2 and bridging hydrides occurs more feasibly than the exchange of the bridging hydrides, consistent with the experiment.

Chapter 4 – DFT Studies on the Characterisation, Formation and Reactivity of the Heterobimetallic Ru-In Species 71, $[Ru(IPr)_2(CO)(Me)(InMe)]^+$

Ligands based on group 13 elements (E) have received an increasing attention in organometallic chemistry because of their abilities to tune reactivity at TMs.[35, 150] Most studies however have focused on boron and fewer reports have appeared on heavier group 13 elements such as In and Ga, as metalloligands. Coordination of metalloligands to TM centres can be either supported or unsupported. The former can be generated by the combination of multidentate ligands with group 13 elements to give a scaffold for TM–E bonds.[126-129, 151] However, this approach is found to be synthetically challenging.[49] An alternative to this approach is the reaction of TM species with metal alkyl precursors to form unsupported TM–E bonds.[72-74, 80, 83, 84, 87] In this regard, building from the Ru-Zn chemistry,[132] Whittlesey and co-workers synthesised complex $[Ru(IPr)_2(CO)(Me)(InMe)]BAr^F_4$ (**71**) by the reaction of the Ru-H species **67** ($[Ru(IPr)_2(CO)(H)]BAr^F_4$) with $InMe_3$.[152] **71** features an unsupported Ru–In bond which in reaction with H_2 results in loss of a molecule of methane to give complex $[Ru(IPr)_2(CO)(\eta^2\text{–}H_2)(H)(InMe)]BAr^F_4$, **72**. Treatment of **71** with CO transfers the alkyl group back to the In centre to yield $[Ru(IPr)_2(CO)_3(InMe_2)]BAr^F_4$, **74**.

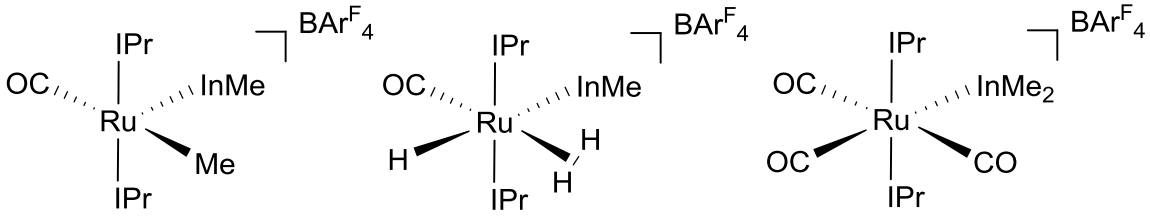

Herein, the first section of this chapter describes the experimental results given by Whittlesey and co-workers. In the next section, computational results for the study of metal–metal bonding of the Ru–In species are described. The last section is dedicated to modelling the mechanism of the formation and reactivity of the Ru-In species.

4.1 Experimental Background

Whittlesey and co-workers showed that the treatment of the Ru-H species **67** with $InMe_3$ forms the Ru-In species **71** characterised crystallographically as $[Ru(IPr)_2(CO)(InMe)(Me)]BAr^F{}_4$ (Figure 4-1). Similar to the Ru-Zn chemistry, this reaction eliminates a gaseous alkane to form an unsupported metal-metal bond. Additionally, formation of **71** is accompanied by the transfer of a second alkyl group onto the Ru centre.

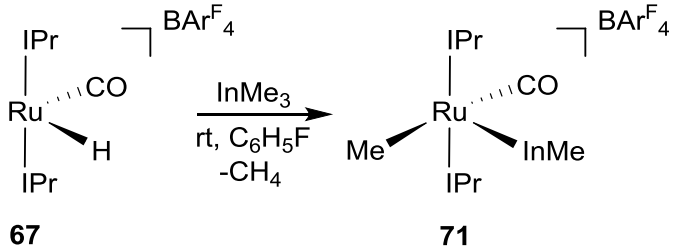

67 **71**

*Figure 4-1. Formation of **71** from the reaction of **67** with $InMe_3$. The C–H agostic interactions in **67** are omitted for clarity.*

In contrast to the Ru-Zn chemistry, reaction of the heterobimetallic species **71** with H_2 does not add hydride across the unsupported metal–metal bond but instead, it activates the Ru–Me bond, eliminating methane to produce $[Ru(IPr)_2(CO)(\eta^2\text{–}H_2)(H)(InMe)]BAr^F{}_4$, **72** (Figure 4-2).

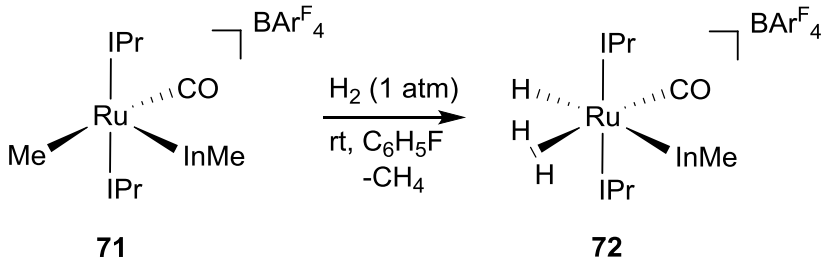

71 **72**

*Figure 4-2. Formation of **72** by reaction of **71** with H_2.*

Reaction of **71** with CO monitored by low temperature ^{13}C NMR at 245 K shows the formation of a dicarbonyl species identified as $[Ru(IPr)_2(Me)(CO)_2(InMe)]BAr^F{}_4$, **73**

(Figure 4-3). Raising the reaction temperature however forms the tricarbonyl complex characterised crystallographically as $[Ru(IPr)_2(CO)_3(InMe_2)]BAr^F{}_4$, **74**.

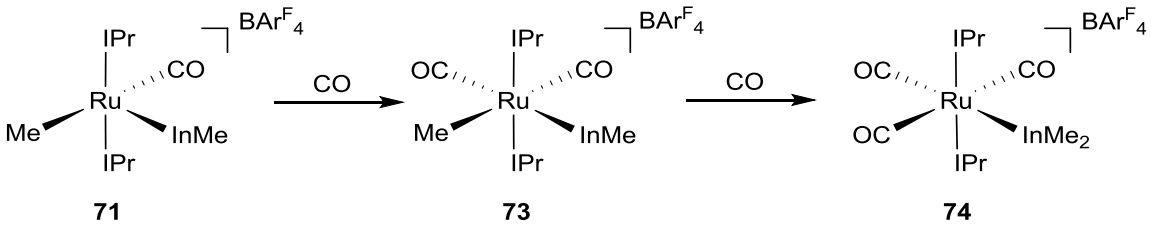

71 **73** **74**

*Figure 4-3. Reaction of **71** with CO to give the dicarbonyl species **73** and tricarbonyl species **74**.*

Comparison of the X-ray molecular structures of the Ru-In species shows that **74** exhibits a significantly longer Ru–In distance than **71** and **72** (**71**: 2.4534(3) Å, **72**: 2.5220(3) Å, **74**: 2.7325(3) Å). However, in all the three Ru-In species, the Ru–In distances are shorter than the sum of the covalent radii of the Ru and In centres (2.88 Å)[134], suggesting a covalent interaction between the metal centres.

4.2 Aims

Herein, DFT studies have been performed to characterise the nature of the interaction between the Ru and In centres in **71**, **72** and **74**. Formation of the Ru-In species **71** and its reaction with H_2 and CO are well-defined examples of the reactivity of heterobimetallic species featuring an unsupported TM–E bond. Thus, particular attention was given to study the mechanism of the formation of the Ru-In species **71**, **72**, **73** and **74**. A similar computational approach to the Ru-Zn systems in **Chapter 3** was used to have a fair comparison with the computational results obtained for the Ru–Zn complexes.

4.3 Results and Discussion

4.3.1 Optimisation of the Ru-In Species

Table 4-1 presents selected structural parameters of the experimental and BP86-optimised molecular geometries of the Ru–In species **71**, **72** and **74** (see Figure 4-4 for the labelling scheme).

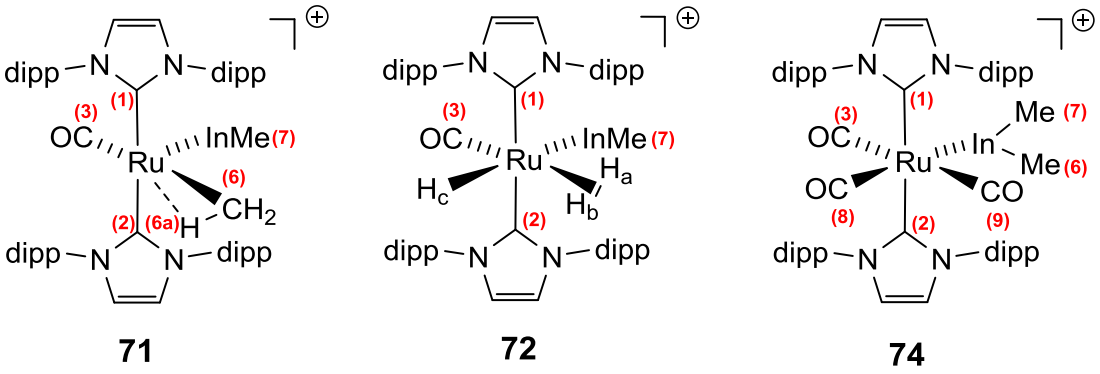

*Figure 4-4. Structures of the Ru-In species **71**, **72** and **74** with the labelling scheme on selected atoms.*

*Table 4-1. Comparison of selected structural parameters of the experimental and computed (BP86/BS1) geometries of the Ru-In species **71**, **72** and **74**. Selected bond lengths and angles are reported with Å and degrees, respectively.*

Species	**71**		**72**		**74**	
	Exp.	*Comp.*	*Exp.*	*Comp.*	*Exp.*	*Comp.*
Ru–In	2.4534(3)	2.454	2.5220(3)	2.593	2.7325(3)	2.805
Ru–IPr(1)	2.113(3)	2.130	2.120(3)	2.137	2.150(2)	2.187
Ru–IPr(2)	2.124(3)	2.134	2.118(3)	2.121	2.173(2)	2.204
Ru–CO(3)	1.993(4)	1.862	1.889(4)	1.870	1.932(3)	1.920
Ru–Me(6)	2.037(4)	2.235	–	–	2.163(3)	2.170
C(6)–H(6a)	–	1.113	–	–	–	–
Ru···H(6a)	–	2.427	–	–	–	–
In···Me(6)	2.867	2.690	–	–	–	–
In–Me(6)	–	–	–	–	2.163(3)	2.170
In–Me(7)	2.150(4)	2.141	2.133(4)	2.174	2.164(3)	2.173
Ru–CO(8)	–	–	–	–	1.937(3)	1.931
Ru–CO(9)	–	–	–	–	1.967(3)	1.930
Ru–H_a	–	–	1.782(5)	1.771	–	–
Ru–H_b	–	–	1.781(5)	1.733	–	–
Ru–H_c	–	–	1.601(5)	1.626	–	–
∠Me(6)–Ru–In	–	69.856	–	–	–	–
∠C(1)–Ru–C(2)	172.94(11)	172.942	174.26(10)	174.816	173.95(9)	174.196

Based on the computed geometries, the Ru–In distance in **71** is very well reproduced by the calculations. Going to **72** and **74**, the Ru–In distances are slightly overestimated by the calculations. However, from **71** to **72** and **74**, they follow the right trend of the lengthening of the Ru–In distances.

In all three Ru-In species, the C(1)–Ru–C(2) angles are well reproduced by the computed geometries. In **71**, a significant discrepancy can be seen between the experimental and computed Ru–C(3) and Ru–C(6) distances. This is mainly due to the structural disorder of the X-ray molecular structure of **71** which cannot differentiate the C(3) and C(6) positions from each other. It can be seen that, in the computed structure of **71**, the InMe(7) moiety is slightly oriented toward the Me(6) group ($\angle$Me(6)–Ru–In = 69.90°) to give a short In···Me(6) distance (2.690 Å). This may suggest that the Me(6) group has some bridging character. The Me(6) group also exhibits a C–H bond which is slightly longer by 0.01 Å than the two other C(6)–H bonds, suggesting an α-agostic interaction with the Ru centre.

Overall, the BP86-optimised geometries provide a reasonable agreement with the experimental geometries of the Ru-In species **71**, **72** and **74**.

4.3.2 Characterisation of the Ru–In Interactions in 71, 72 and 74

QTAIM, NBO and LMO analyses have been performed on the BP86-optimised geometries of **71**, **72** and **74** to study the nature of the interaction between the Ru and In centres. Figure 4-5 displays the 2D contour plot of the electron denisty in the {Ru/In/C(O)} plane along with the QTAIM parameters ($\rho(r)$, $\nabla^2\rho(r)$, ε and H(r)). The molecular graphs of all the three Ru-In species display a bond path between the Ru and In centres, indicating an interaction between the metal centres consistent with the sum of the covalant radii of the Ru and In atoms. Similar to the Ru-Zn complexes, the metal–metal interactions in the Ru-In species exhibit a small $\rho(r)$, a positive $\nabla^2\rho(r)$ and a small negative H(r), indicating a dative bond between the Ru and In centres. In **71**, the value of $\rho(r)$ at the Ru–In BCP is 0.079 which reduces to 0.061 in **72** and 0.048 in **74**. This shows a decreases in strength of the Ru–In interaction in the order **71** > **72** > **74**. Comparison of the H(r) at the Ru–In BCPs shows that **71** exhibits a slightly more negative value of H(r)

(-0.028) than **72** and **74** (**72**: -0.020 and **74**: -0.014), indicating the former features a stronger Ru–In interaction, consistent with the trend of the ρ(r) values.

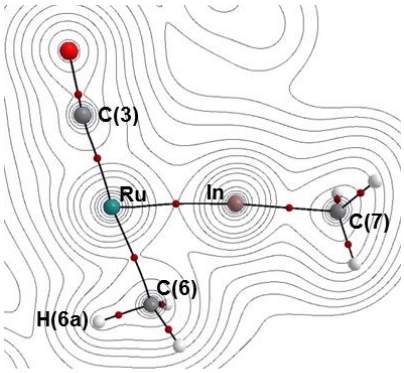

71

BCP	ρ(r)/eÅ^{-3}	$\nabla^2\rho(r)$/eÅ^{-5}	ε	H(r)/a.u.
Ru–In	0.079	0.154	0.135	-0.028

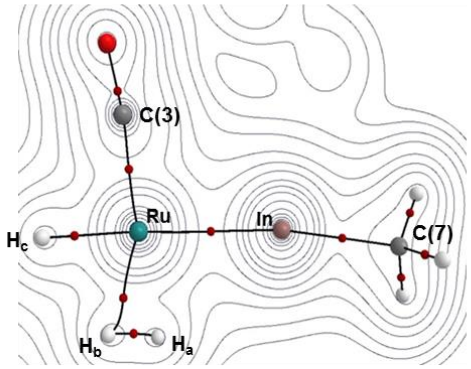

72

BCP	ρ(r)/eÅ^{-3}	$\nabla^2\rho(r)$/eÅ^{-5}	ε	H(r)/a.u.
Ru–In	0.068	0.124	0.055	-0.024

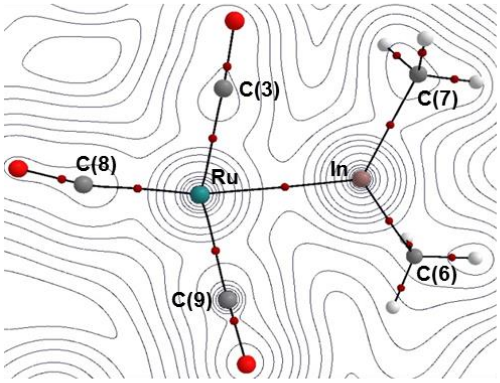

74

BCP	ρ(r)/eÅ^{-3}	$\nabla^2\rho(r)$/eÅ^{-5}	ε	H(r)/a.u.
Ru–In	0.048	0.033	0.094	-0.014

*Figure 4-5. Details of the QTAIM molecular graphs of **71**, **72** and **74** showing the electron density contours in the {Ru/In/C(O)} plane. BCPs are shown as red spheres.*

In **71**, the ellipticty of the Ru–In BCP is 0.135 which reduces to 0.057 in **72** and slightly increases to 0.094 in **74**. The slightly larger value of the Ru–In bond ellipticity in **71**

relative to that in **72** and **74** might be indicative of π-character of the Ru–In interaction. This is assessed by an LMO analysis of the Ru-In species shown in Figure 4-6. The LMO analysis shows a σ–bonding orbital. It also shows an interaction between the Ru d_{xz} orbital and the p_z In orbital which is dominated by the Ru d_{xz} character. This is consistent with the findings reported by Frenking and co-workers, showing the monosubstituted In moiety is not a good π-acceptor.[107]

It should be noted that in **71**, no BCP was found between the C(6) and In centres, showing no interaction between these atoms. Moreover, no BCP can be seen between the H(6a) and the Ru centres, showing no α-C–H(6a) agostic interaction. A similar situation can be seen in unsaturated Ti-methyl complexes where, despite the very short Ti···H_α distance, no BCP can be seen between the metal and hydrogen centres.[153, 154] This situation can happen when a BCP is annihilated by the coalescence with another CP. Thus, lack of the BCP between the TM centre and the H_α does not rule out the presence of an α-agostic interaction.[155, 156] In this regard, an NBO analysis identifies a donor-acceptor interaction between the C(6)–H(6a) bonding orbital and the Ru–C(O) anti-bonding orbital. The E(2) value corresponding to this interaction however is small, computed to be 3.0 kcal/mol which indicates the presence of a very weak α-C(6)–H(6a) agostic interaction.

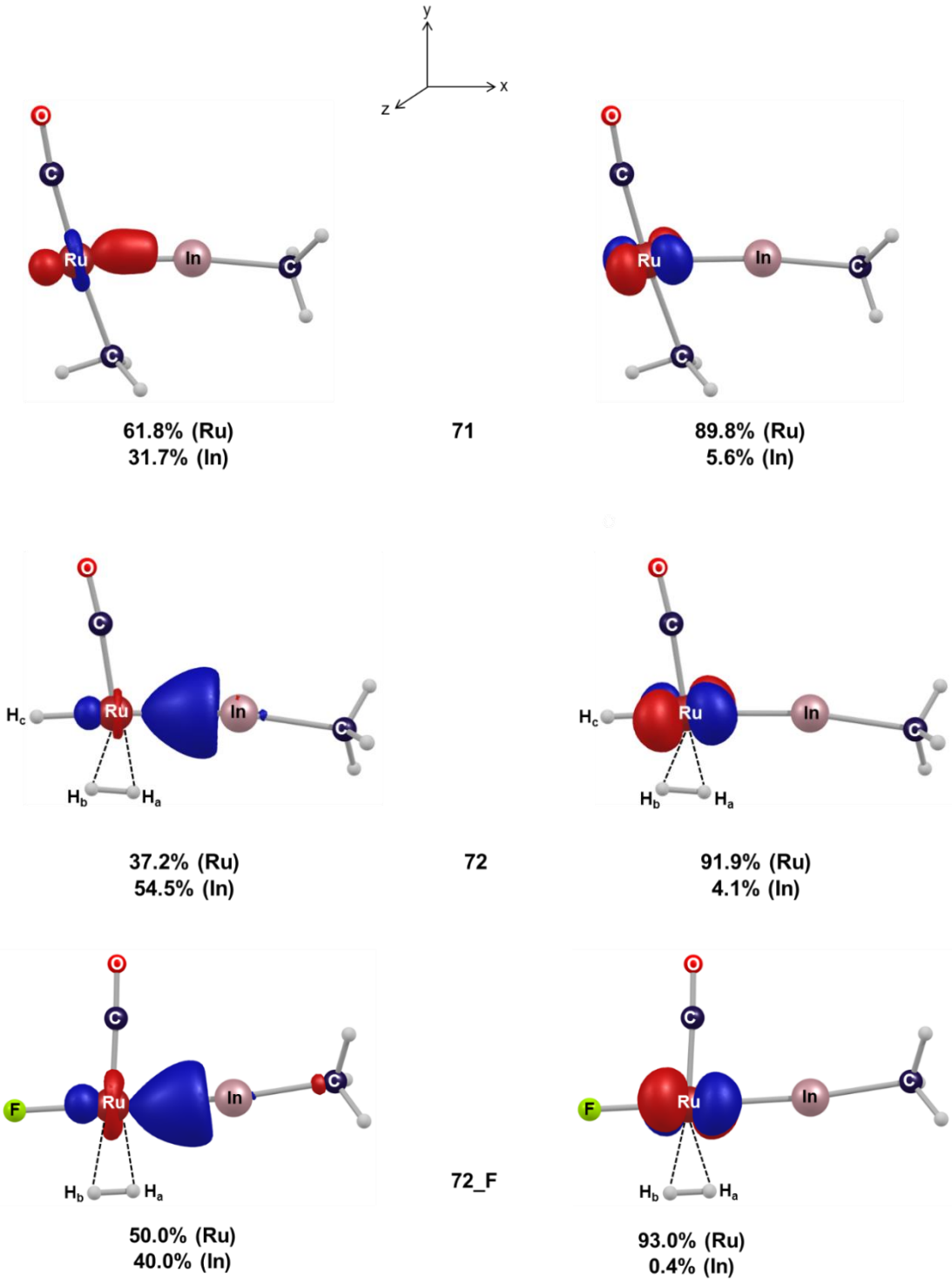

*Figure 4-6. The LMOs of the Ru–In interactions in **71**, **72** and **72_F**; the Ru–In σ-interaction (left) and the small dπ-interaction of Ru with In (right). The IPr ligands are omitted for clarity. Isosurfaces plotted with Chemcraft with a contour value of 0.1.*

In **71**, LMO shows that the Ru–In σ-bonding orbital is significantly polarised toward the Ru centre (Ru = 61.8% and In = 31.7%). This can be rationalised by invoking the greater electronegativity of Ru relative to In. However, in **72** the Ru–In σ-bonding orbital is significantly more polarised to the In centre (Ru = 37.2% and In = 54.5%). This can be due to the high trans-influence exerted by the hydride ligand whereas in **71**, the InMe moiety is trans to a vacant site. This can be supported by the replacement of the hydride with a weak trans-influence ligand such as fluoride in **72** to give **72_F**. In this case, it can be seen that the σ-bonding orbital polarises back toward the Ru centre (Ru = 50.0% and In = 40.0%). This therefore shows that the Ru–In interactions in **71** and **72** are very sensitive to the trans influence of the ligand trans to the In moiety.

There are two possibilities to describe the dative interaction between the metal centres; 1) Ru→In bond and 2) Ru←In bond. The nature of the Ru–In dative interaction can be assessed by comparison of NBO charges of In in **71** and **72** with the isolated InMe fragment. For the first scenario, the isolated InMe fragment would have a 2+ overall charge, consistent with an In(III) moiety and hence describing the Ru→In bond. For the second case scenario, the InMe fragment is neutral, resembling an In(I) moiety and thus describing the Ru←In dative bond.

The calculated NBO charge distribution shows that In centres in **71** and **72** exhibit a charge of +1.46 and +1.27 respectively. For comparison, the In centre in the isolated $[InMe]^{2+}$ species has a charge of +1.00. One might expect a lower positive charge for In if **71** and **72** exhibit a Ru→In bond. However, both **71** and **72** display even more positive charge. This therefore does not support a Ru→In bond in **71** and **72**.

The charge of the In centre in the neutral isolated [InMe] structure is +0.69. This is significantly lower than the charge of In in **71** and **72**. The reduced charge density of In in **71** and **72** relative to that in the isolated InMe species shows a charge transfer from In to Ru, i.e. Ru←In(I) bond. The higher positive charge of In in **71** relative to **72** can be attributed to the fact that the InMe moiety in the former is trans to the high trans influence of hydride while in the latter, the InMe moiety is trans to a vacant site. This causes a lower electron donation from the InMe moiety to the Ru centre in **72**.

The experimental CO stretching frequency of **71** is 1913 cm^{-1} which is significantly lower than in **72** (1975 cm^{-1}). A similar trend can also be seen with the computed CO stretching

frequencies of **71** and **72**. This shows that the Ru centre in **72** is more electron deficient than that in **71**.

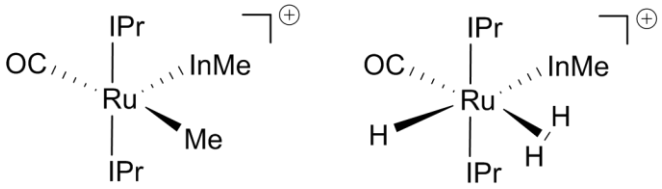

υ_{CO}	**71**	**72**
Exp.	1913 cm^{-1}	1975 cm^{-1}
Comp.	1906 cm^{-1}	1969 cm^{-1}

Figure 4-7. The experimental and computed CO stretching frequencies of the Ru species.

Therefore, **71** and **72** can be described by the Ru(II)–In(I) formulation in which the monovalent In(I) moiety acts as a Lewis base centre and the Ru(II) acts a Lewis acid moiety. This is consistent with TM←E(I)R interaction reported by Fisher and Frenking (TM = Pt, E = Al, Ga, In).[104, 105]

Figure 4-8 displays the experimental CO stretching frequencies of the Ru-In species **74**, its hydride analogue (**74_H**) and [Ru(IMes)$_2$(CO)$_3$], **75**. [157, 158] **74_H** is a Ru(II) complex while **75** is a Ru(0) complex. It should be noted that **75** is the only experimentally available tricarbonyl Ru(0) complex with two NHC ligands to make comparison with the tricarbonyl Ru(II) species **74** and **74_H**.

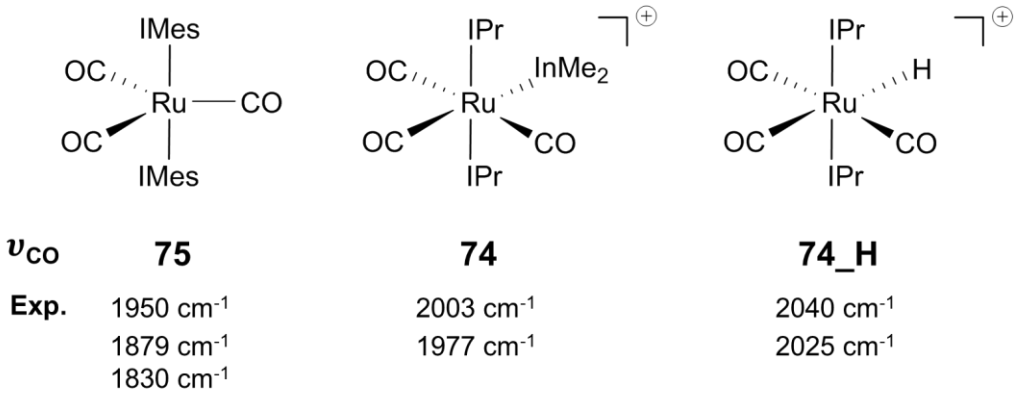

υ_{CO}	**75**	**74**	**74_H**
Exp.	1950 cm^{-1} 1879 cm^{-1} 1830 cm^{-1}	2003 cm^{-1} 1977 cm^{-1}	2040 cm^{-1} 2025 cm^{-1}

Figure 4-8. The experimental CO stretching frequencies of the Ru species.

Comparison of the CO stretching frequencies of the Ru complexes shows that **74** lies closer to **74_H** than **75**. However, the slightly lower CO stretching frequencies of **74** compared with those in **74_H** shows that the former exhibits a more electron rich Ru centre. This can also be supported by the higher contribution of the Ru centre in the Ru–In σ-bonding orbital in **74** relative to that in the Ru–H σ-bonding orbital in **74_H** (Figure 4-9).

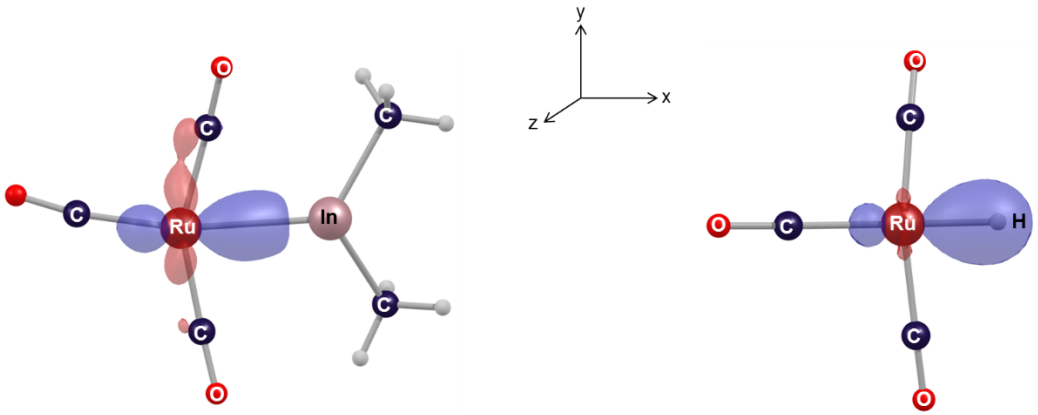

74
63% (Ru)
16% (In)

74_H
52%(Ru)
44%(H)

*Figure 4-9. LMO analysis of **74** and **74_H** showing the Ru–In σ-bonding orbital (left) and Ru–H σ-bonding orbital (right), respectively. The IPr ligands are omitted for clarity. Isosurfaces plotted with Chemcraft with a contour value of 0.1.*

Taken all the findings together, it can be found that **74** more closely resembles a Ru(II) species. Thus, the divalent indium moiety in **74** is an anionic fragment ($[InMe_2]^-$) consistent with findings reported by Pandey for TM-GaX_2 complexes.[83] Therefore, **74** exhibits a Ru(II)–In(I) formulation in which the In(I) centre acts as a Lewis base centre while the Ru(II) acts a Lewis acid moiety.

4.3.3 Study of the Mechanism of the Formation of 71

DFT calculations to investigate the adduct(s) formed upon the reaction of **67** with $InMe_3$ located **I(67-71)** at +6.7 kcal/mol (relative to **67** and $InMe_3$, Figure 4-10). In **I(67-71)**, the $InMe_3$ moiety adopts a side-on orientation in the {Ru/H/CO} plane. Formation of such an adduct however is in contrast with previously reported Ru-indane complexes.[72, 74]

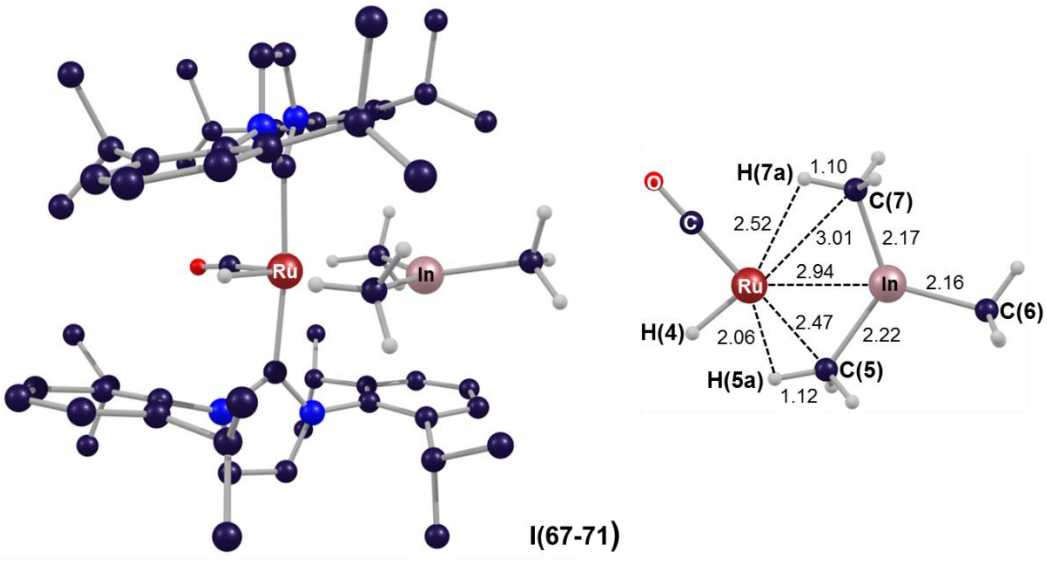

*Figure 4-10. Representation of **I(67-71)**; a) the full structure (the hydrogen of the IPr ligands are omitted for clarity) and b) within the equatorial plane with the labelling scheme for selected atoms. Selected distances are shown in Å.*

For example, in **76** (*fac*-$[Ru(NCMe)_3(CO)_2(InBr_3)]$), the $InBr_3$ exhibits a tetrahedral geometry at the In centre. This rather contradictory result between the geometry of the $InMe_3$ moiety in **I(67-71)** and **76** may be due to the presence of the bulky IPr ligands in **I(67-71)** which may only allow the side-on orientation of $InMe_3$. This can be examined

computationally with the replacement of the bulky IPr ligands with small ligands such as PH_3 and IMe in $[RuL_2(CO)(H)(InMe_3)]^+$ to give **I(67_71)_PH$_3$** and **I(67_71)_IMe**, respectively. However, as shown in Figure 4-11 while the {$InMe_3$} now lies out of the {Ru/H/CO} plane, the $InMe_3$ fragment still exhibits a trigonal planar geometry around the In centre. Therefore, the steric hindrance is not the determining factor in the side-on geometry of the $InMe_3$ moiety in **I(67-71)**. This therefore suggests that the trigonal planar geometry at the In centre in **I(67_71)** is due to the low Lewis basicity of the Ru centre as in **I(67-71)**, the Ru centre has an oxidation state of 2+ whereas in **76**, the oxidation state of the Ru centre is zero. An additional factor may also be the lower Lewis acidity of In in $InMe_3$ compared to that in $InBr_3$.

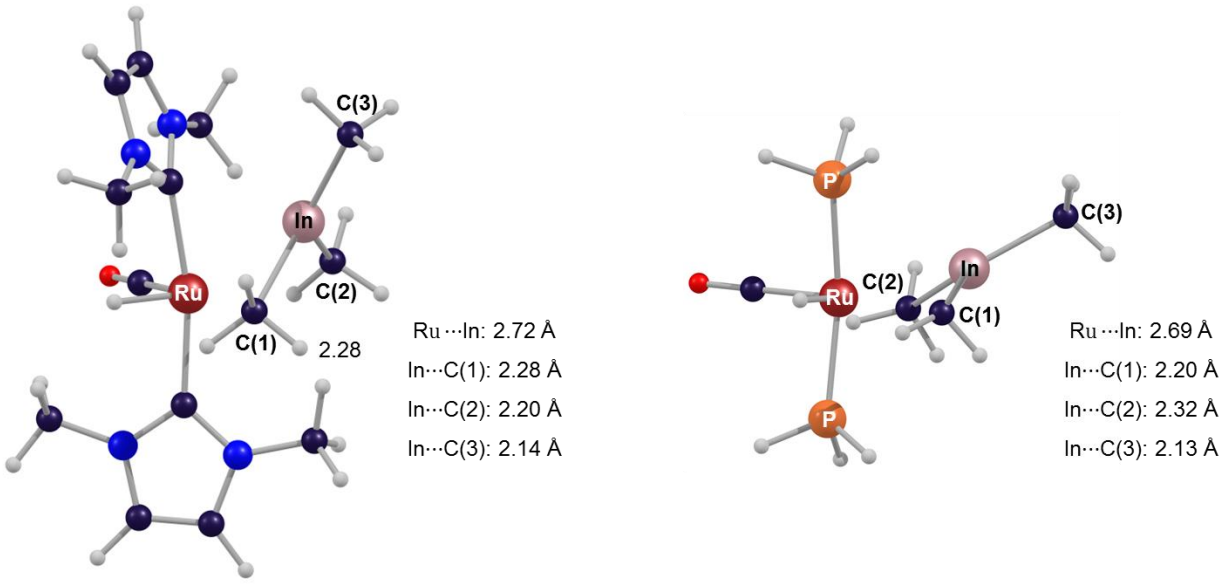

*Figure 4-11. Computed structures of **I(67-71)_IMe** (left) and **I(67-71)_PH$_3$** (right).*

In **I(67-71)**, the In–C(5) bond which is cis to the H(4) position is slightly longer than the two other In–C bonds by 0.06 Å. In addition, the C(5) centre is also situated in closer proximity to the Ru centre than the C(7) centre by 0.05 Å. This may suggest a 3c-2e interaction between the In–C(5) sigma bond and the Ru centre. In addition, the C(5)–H(5a) bond is slightly longer than the two other C(5)–H bonds by 0.02 Å, suggesting that C(5)–H(5a) bond has an agostic interaction with the Ru centre.

As shown in Figure 4-12, the QTAIM molecular graph of **I(67-71)** exhibits no BCP between the Ru and In centres which is consistent with the fact that **I(67-71)** exhibits a Ru···In distance greater than the sum of the covalent radii of the Ru and In centres. The In–C(5) BCP has a smaller value of ρ(r) relative to the In-C(6) and In–C(7) BCPs. This shows a weaker In–C interaction in the former, consistent with the longer In–C(5) bond distance relative to In–C(6) and In–C(7) distances. No BCP can be seen between the Ru and C(5) centres, showing no interaction between the corresponding centres. However, there can be seen BCPs between the Ru with the H(5a) and the H(7a) centres, enclosing an RCP in the {Ru···H(5a)–C(5)–In–C(7)–H(7a)···} unit. The value of the ρ(r) of the BCP along the Ru···H(5a) bond path is 0.046 which lowers to 0.019 for the Ru···H(7a) BCP. This shows a stronger interaction in the former. The Ru···H(5a) bond path has a low H(r) value of -0.003 while for the Ru···H(7a) BCP, the H(r) value is effectively zero. This shows a stronger covalent interaction in the former, consistent with the trend of ρ(r) values and bond distances.

The C(5)–H(5a) BCP has also a slightly lower value of ρ(r) compared with the C(5)–H(5b) BCP, showing a weaker interaction in the former. The presence of a covalent interaction between Ru and H(5a) centre along with the relatively weaker C(5)–H(5a) bond suggests a 3c-2e interaction between C(5)–H(5a) bond and the Ru centre. This is supported by an NBO analysis which identifies a donor-acceptor interaction between the C(5)–H(5a) bonding orbital and the Ru–CO anti-bonding orbital with the E(2) of 18.9 kcal/mol.

It should also be noted that NBO identifies a donor-acceptor interaction between the C–H(7a) bonding orbital and the Ru–H anti-bonding orbital. The E(2) value corresponds for this interaction is 2.7 kcal/mol which is significantly lower than the interaction of the C–H(5a) bonding orbital and the Ru moiety, consistent with the QTAIM results.

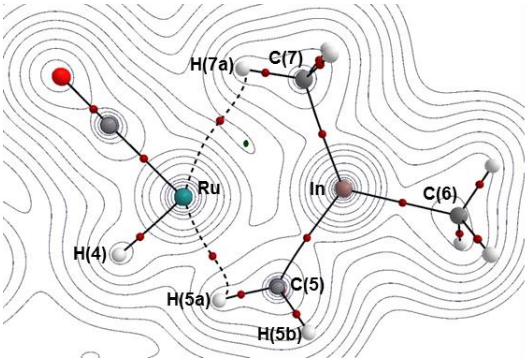

BCP	ρ(r)/eÅ^{-3}	∇^2ρ(r)/eÅ^{-5}	ε	H(r)/a.u.
Ru···H(5a)	0.046	0.180	2.136	-0.003
Ru···H(7a)	0.019	0.058	0.760	0.000
C(5)–H(5a)	0.248	-0.729	0.054	-0.233
C(7)–H(7a)	0.263	-0.841	0.027	-0.259
C(5)–H(5b)	0.265	-0.850	0.047	-0.263
In–C(5)	0.084	0.165	0.056	-0.027
In–C(6)	0.094	0.172	0.027	-0.036
In–C(7)	0.096	0.168	0.013	-0.034

*Figure 4-12. Details of the QTAIM molecular graphs of **I(67-71)** showing the electron density contours in the {Ru/In/C(O)} plane. BCPs and RCPs are shown as red and green spheres, respectively.*

As shown in Figure 4-13, rearrangement of **I(67-71)** gives **I(67-71)1** at +3.4 kcal/mol. The potential energy surface corresponding to this process is flat and therefore, attempts to locate this transition structure were inconclusive. **I(67-71)1** exhibits a longer In–C(5) distance and a significantly shorter Ru–C(5) distance than **I(67-71)**. Moreover, it has an elongated C(5)–H bond (1.15 Å) to give a short Ru···H distance, suggesting a C–H agostic interaction with the Ru centre.

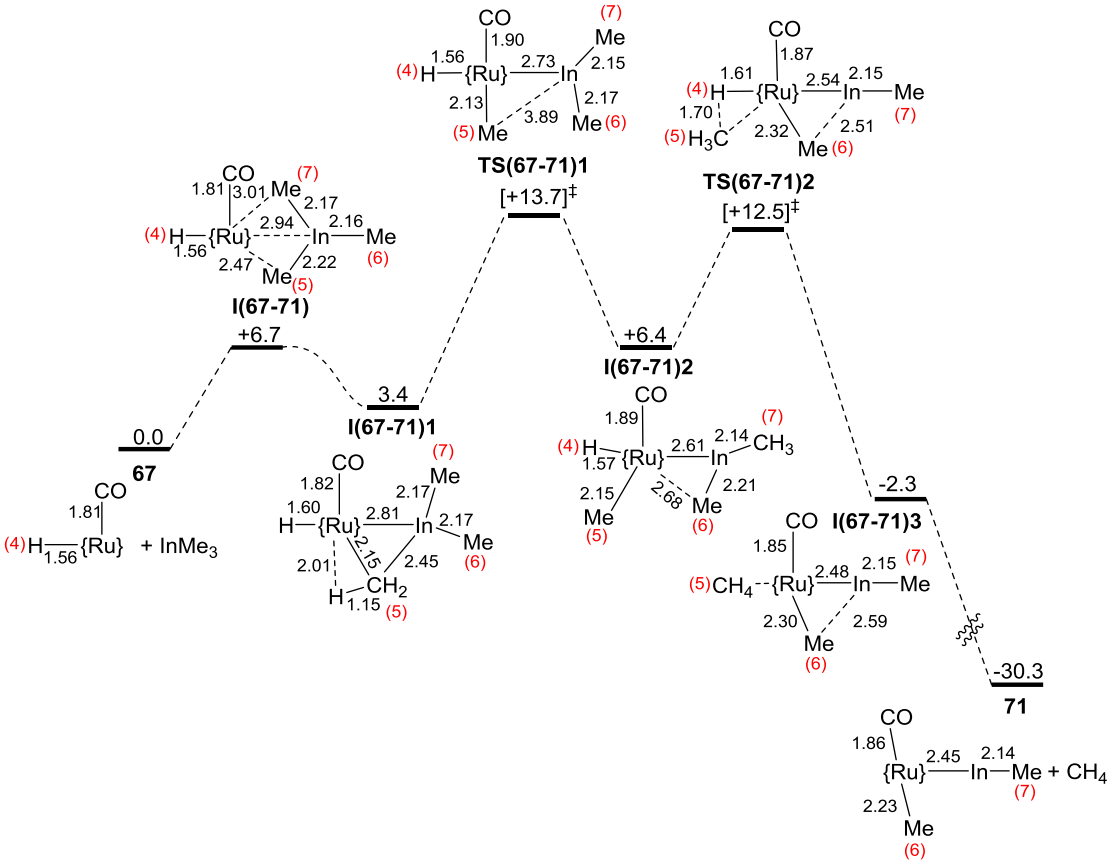

*Figure 4-13. Computed reaction profile (BP86/BS1) for the formation of **71** and CH_4 from **67** and $InMe_3$; schematic structures show key distances (Å) within the equatorial plane; {Ru} = $Ru(IPr)_2^+$.*

As shown in Figure 4-14(a), the QTAIM molecular graph of **I(67-71)1** displays BCPs between the three atoms of the {Ru/C(5)/In} unit, that therefore enclose an RCP. However, due to the very flat electron density of the RCP, it coalesces with the Ru–In BCP. The BCP along the Ru–In bond path has a negative H(r) value of -0.008, suggesting a weak dative interaction between the metal centres. LMO analysis shows a very small interaction between the d_{xy}(Ru) orbital and the In centre, showing a marginal π-interaction between the Ru and In centres (Figure 4-14 (b)). The presence of BCPs between the C(5) centre and the metal centres shows that the Me(5) group has bridging character. The ρ(r) value of the Ru–C(5) BCP is 0.094 which is slightly larger than the In-C(5) BCP (0.054). This shows that the C(5) centre is more strongly bound to the Ru centre than the In centre. The H(r) value of the Ru–C(5) BCP is -0.030 which is slightly more negative than the In–C(5) BCP (-0.012). This supports a stronger interaction in the former, consistent with the

trend of ρ(r) values. In comparison with the In–C(6) BCP, the In–C(5) BCP has a lower ρ(r) by 0.043. This shows that the In centre exhibits a stronger interaction with the terminal Me(6) group than the bridging Me(5) group. It can be seen that the ellipticity of the In–C(5) BCP is 0.254 which reduces to 0.003 in the In–C(6) BCP. As expected, this indicates that a Me group with bridging character has a significantly higher ellipticity than a Me group with a terminal character. It can be seen that the ρ(r) value of the C(5)–H(5a) BCP is slightly smaller than the C(5)–H(5b) BCP by 0.037. A similar trend can also be seen in the values of $|H(r)|$, showing a weaker interaction in the former. The C(5)–H(5a) oriented toward the Ru centre and also experiences a reduced electron density. This may be due to a 3c-2e interaction with the Ru centre. However, no BCP is seen between the Ru and the H(5a) centres. An NBO analysis identifies a donor-acceptor interaction between the C(5)–H(5a) bonding orbital and the Ru–C(O) anti-bonding orbital with the E(2) value of 33.7 kcal/mol, supporting the α-agostic interaction between the involving moieties.

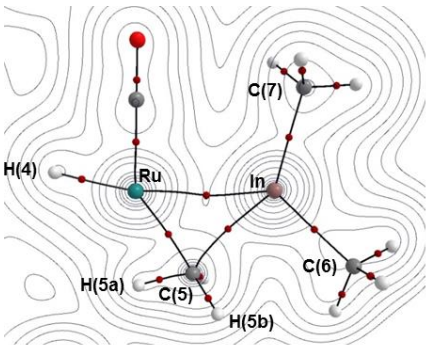

BCP	ρ(r)/eÅ^{-3}	$\nabla^2\rho(r)$/eÅ^{-5}	ε	H(r)/a.u.
Ru···In	0.039	0.064	7.569	-0.008
Ru···C(5)	0.094	0.205	0.082	-0.030
In···C(5)	0.054	0.099	0.254	-0.012
In–C(6)	0.097	0.170	0.003	-0.034
C(5)–H(5a)	0.233	-0.613	0.066	-0.205
C(5)–H(5b)	0.270	-0.898	0.025	-0.270

(a)

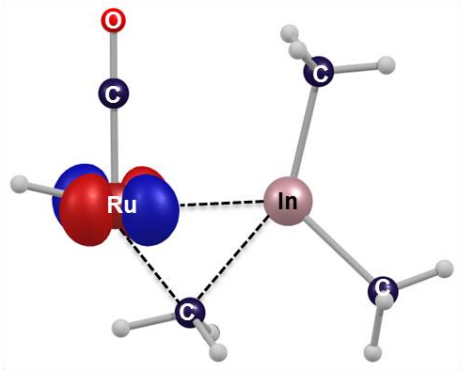

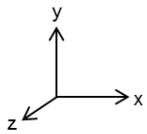

(b)

90.9% (Ru) 2.5% (In)

*Figure 4-14. a) Details of the QTAIM molecular graphs of **I(67-71)1** showing the electron density contours in the {Ru/In/C(O)} plane; b) LMO analysis of **I(67-71)1** showing the small interaction of the d_{xz}(Ru) orbital with the In centre.*

Further activation of the In–C(5) bond in **I(67-71)1** results in the full transfer of the Me(5) group onto the Ru centre via **TS(67-71)1** at +13.7 kcal/mol and forms **I(67-71)2** at +6.4 kcal/mol.

It is well established that electron-rich TM complexes can undergo the oxidative addition of In–R bonds to the TM centre[84] while **I(67-71)1** is an electron deficient Ru(II) species. However, the oxidative addition mechanism can be accessible when electron deficient TMs are supported by strong electron donor ligands.[112] Thus, the coordination of two strong electron donor NHC ligands at the Ru centre in **I(67-71)1** may allow the stabilisation of a Ru(IV) centre in **I(67-71)2**. Similar to complex **74**, **I(67-71)2** has an $[InMe_2]^-$ moiety. This indeed supports a Ru(IV) species in **I(67-71)2** and suggests that the activation of the In–C(5) bond at the Ru centre occurs via an oxidative coupling mechanism via **TS(67-71)1**. **TS(67-71)1** is a late transition state with a long In···C(5)

distance of 3.89 Å. Figure 4-15(a) displays the QTAIM molecular graph of **I(67-71)2**. In comparison with **I(67-71)1**, **I(67-71)2** exhibits a slightly larger value of ρ(r) and also a more negative H(r) at the Ru–In BCP, showing a stronger Ru–In interaction in the latter (Figure 4-15(b)). However, similar to **I(67-71)1**, in **I(67-71)2**, the interaction of the d_{xz} Ru orbital with the In centre is still negligible. From **I(67-71)1** to **I(67-71)2**, LMO analysis shows a new Ru–In bonding orbital, i.e. a σ-bonding orbital, which is significantly more polarised toward the Ru centre.

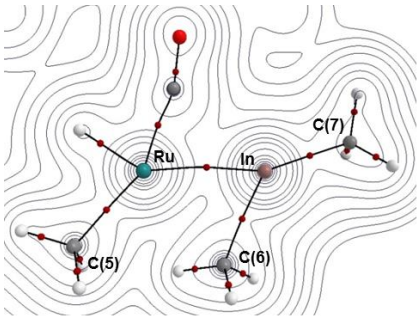

BCP	ρ(r)/eÅ^{-3}	$\nabla^2\rho(r)$/eÅ^{-5}	ε	H(r)/a.u.
Ru–In	0.057	0.097	0.133	-0.017
Ru–C(5)	0.106	0.112	0.082	-0.039
In–C(6)	0.087	0.154	0.072	-0.029
In–C(7)	0.102	0.171	0.002	-0.039

(a)

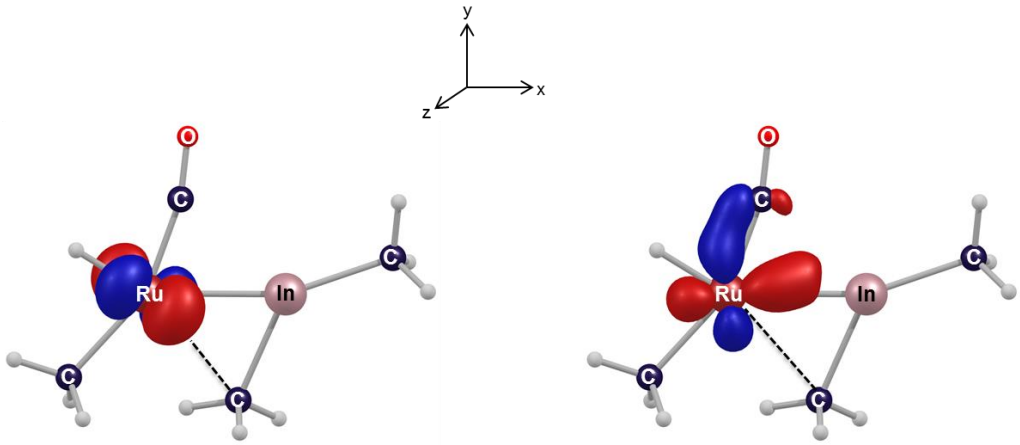

92.2% (Ru)
3.6% (In)

(b)

69.1% (Ru)
14.3% (In)
13.8% (C(O))

*Figure 4-15. a) Details of the QTAIM molecular graphs of **I(67-71)2** showing the electron density contours in the {Ru/In/C(O)} plane; b) LMO analysis of **I(67-71)2** showing the weak interaction of the d_{xz}(Ru) orbital with the In centre (left) and the Ru–In σ-bonding orbital (right).*

In **I(67-71)2**, it can also be seen that the In–C(6) bond is oriented toward the Ru centre. The BCP associated with this interaction exhibits a ρ(r) value of 0.087 which is slightly lower than the In–C(7) BCP (0.102), indicating a weaker interaction in the former. The H(r) value of the In–C(6) BCP is also slightly less negative than the In–C(7) bond, showing a weaker interaction in the former, consistent with the trend of the ρ(r) values. The ellipticity of the In–C(6) BCP is 0.072 which is slightly greater than the ellipticity of the In–C(7) BCP (0.002). This indicates that the Me(6) group has some bridging character.

I(67-71)2 then undergoes a facile C–H reductive coupling process at the Ru centre which spontaneously induces the transfer of the second Me (i.e. Me(6)) group onto the Ru centre. This process occurs via **TS(67-71)2** at 12.5 kcal/mol and generates **I(67-71)3** at -2.3 kcal/mol. **I(67-71)3** then can lose methane to give **71** at -30.3 kcal/mol.

It is interesting to note that there is a very small difference between the bond ellipticities of the Ru–Me(6) BCPs in **71** (ε = 0.008) and **I(67-71)3** (ε = 0.003). This therefore shows that the Me(6) group in **71** has terminal character.

In order to understand why the Me group transfers from the In centre onto the Ru centre upon the C–H coupling process, the reverse process of transferring the Me group back to the In centre from **71** was computed (Figure 4-16). This process occurs with the low energy barrier of 10.3 kcal/mol (relative to **71**) via **TS(71-71')** and gives **71'**, lying 4.0 kcal/mol above **71**. This therefore indicates that transfer of a second Me to the Ru centre is not necessarily spontaneous in the absence of the C-H reductive coupling process. This however requires a vacant site at the Ru centre which is affordable upon the C–H coupling process. It is interesting to note that the mechanism of double In–C bond activation at the Ru centre is similar to the mechanism of double Ga–H bond activation at TM complexes.[108] In both mechanisms, the E–R oxidative addition at the TM centre is followed by the migration of the second R group from the E centre to the TM centre to give the TM-E(I)R complex.

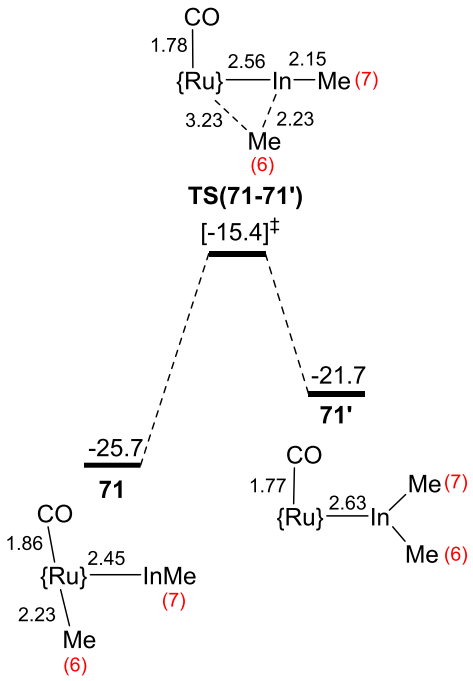

*Figure 4-16. Computed reaction profile (free energy, kcal/mol, BP86/BS1) Me transfer between Ru and In in **71**; schematic structures show key distances (Å) within the equatorial plane; {Ru} = Ru(IPr)$_2^+$.*

4.3.4 Reaction of the Ru-In Species 71 with H_2 to Give 72

Figure 4-17 displays the computed energy profile for the reaction of **71** with H_2 to generate **72**. Addition of one H_2 to the Ru vacant site of **71** forms the η^2–H_2 adduct **I(71-72)1** at +3.3 kcal/mol (relative to **71** and H_2).

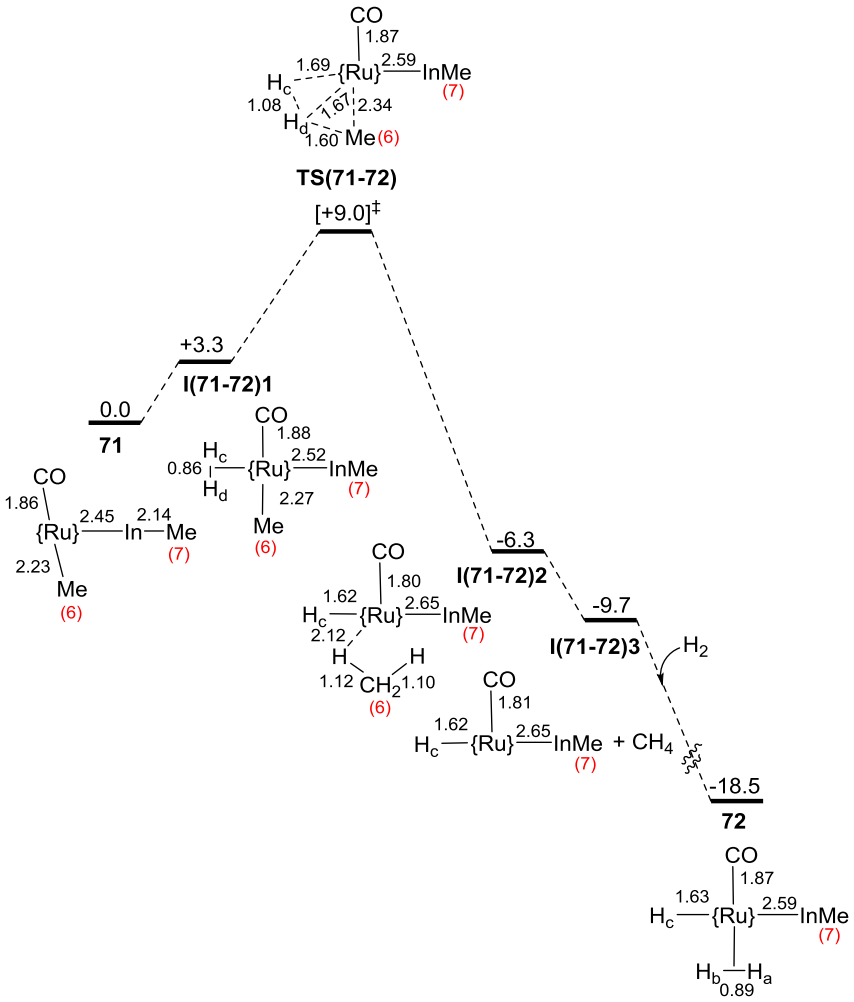

*Figure 4-17. Computed reaction profile (free energy, kcal/mol, BP86/BS1) for the formation of **72** from **71** and H_2; schematic structures show key distances (Å) within the equatorial plane; {Ru} = $Ru(IPr)_2^+$.*

The QTAIM molecular graph of **I(71-72)1** shows that the Ru–In interaction exhibits a slightly less negative H(r) compared with **71** (**71** : -0.028 and **I(71-72)1** : -0.026). This is mainly due to the small trans influence of the H_2 ligand which slightly weakens the Ru–In interaction. In addition, LMO analysis shows that the trans influence of H_2 ligand also slightly polarises the Ru–In σ-bonding orbital toward the In centre. (**71**: Ru (61.8%) and In (31.7%), **I(71-72)1**: Ru (55.3%) and In (36.9%)). However, the Ru character in the Ru–In σ-bonding interaction is still dominant over the In character.

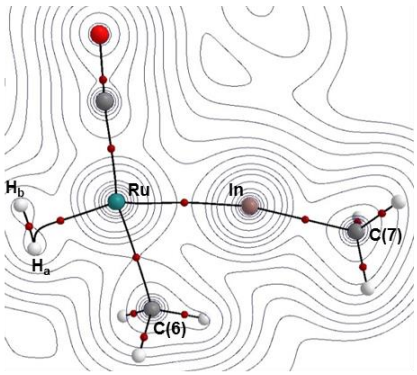

BCP	ρ(r)/eÅ^{-3}	∇^{2}ρ(r)/eÅ^{-5}	ε/a.u.	H(r)/a.u.
Ru–In	0.072	0.108	0.189	-0.026
Ru···H$_a$	0.093	0.351	5.194	-0.025
Ru–C(6)	0.081	0.147	0.015	-0.022

(a)

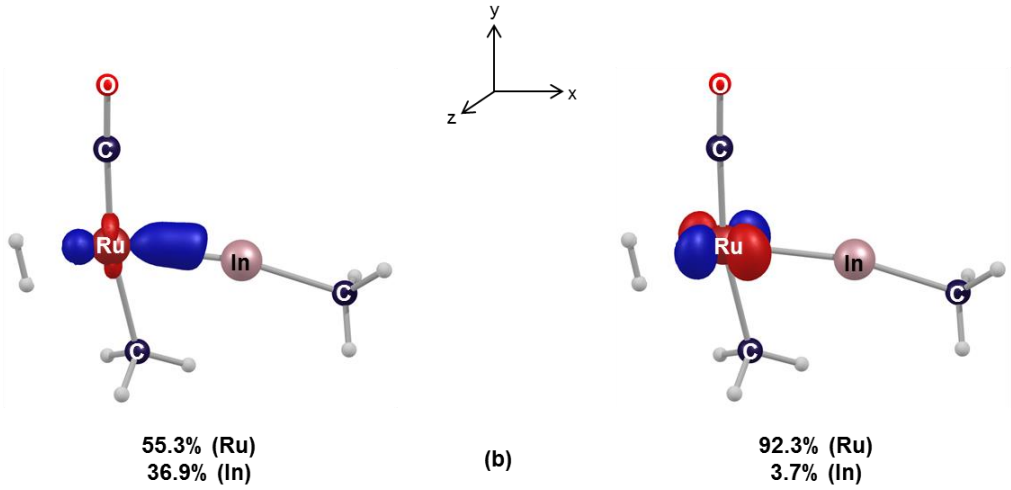

55.3% (Ru)
36.9% (In)

(b)

92.3% (Ru)
3.7% (In)

*Figure 4-18. a) Details of the QTAIM molecular graphs of **I(71-72)1** showing the electron density contours in the {Ru/In/C(O)} plane; b) LMO analysis of **I(71-72)1** showing the Ru–In σ-bonding orbital (left) and the weak interaction of the d_{xz}(Ru) orbital with the In centre (right).*

In **I(71-72)1**, H–H bond cleavage occurs at the Ru centre via a σ-CAM mechanism[148] and forms **I(71-72)2** as a methane complex. This process takes place via **TS(71-72)** at +9.0 kcal/mol and forms the methane-complex **I(71-72)2** at -6.3 kcal/mol. The QTAIM molecular graph of **I(71-72)2** shown in Figure 4-19(a) displays a weaker Ru–In interaction relative to that in **I(71-72)1.** This is mainly due to the high trans influence exerted by the hydride ligand in the former**.** This also causes a significant polarisation of the Ru–In σ-bonding orbital toward the In centre (Figure 4-19 (b), Ru (37.1%) and In(57.9%)).

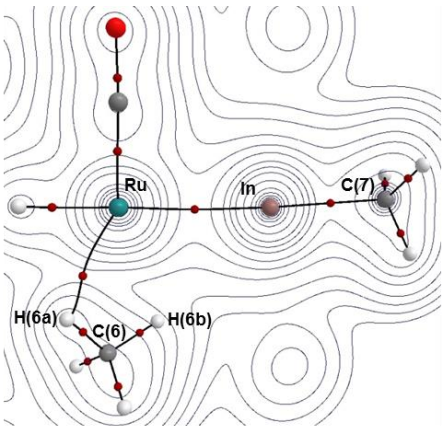

BCP	ρ(r)/eÅ^{-3}	$\nabla^2\rho(r)$/eÅ^{-5}	ε/a.u.	H(r)/a.u.
Ru–In	0.057	0.090	0.098	-0.018
Ru···H(6a)	0.045	0.132	0.132	-0.008
C(6)–H(6a)	0.242	-0.690	0.024	-0.220
C(6)–H(6b)	0.269	-0.891	0.013	-0.266

(a)

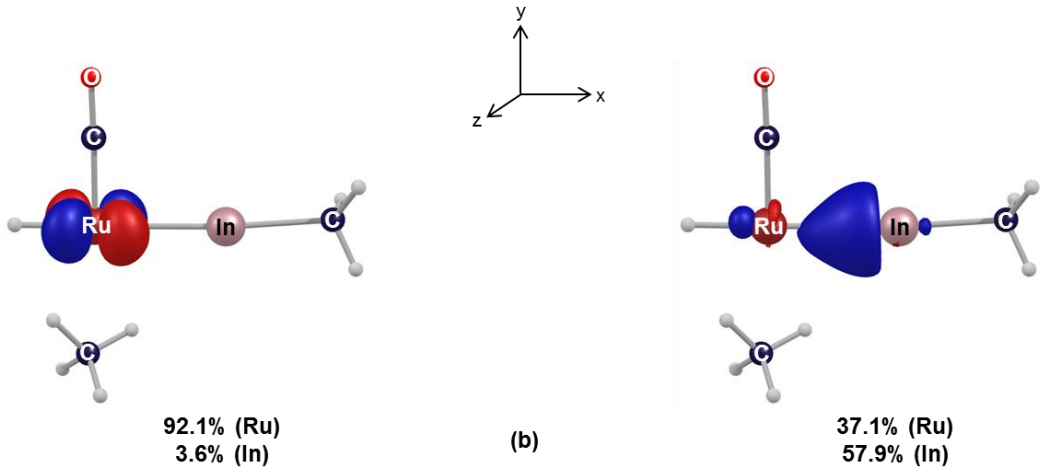

*Figure 4-19. a) Details of the QTAIM molecular graphs of **I(71-72)2** showing the electron density contours in the {Ru/In/C(O)} plane; b) LMO analysis of **I(71-72)2** showing the Ru–In σ-bonding orbital (left) and the weak interaction of the d_{xz}(Ru) orbital with the In centre (right).*

As methane dissociates from the Ru centre, one of the C–H bonds of the isopropyl substituents of the IPr ligand interacts with the Ru centre via a 3c-2e interaction (i.e. C–H agostic interaction) and forms **I(71-72)3** at -9.7 kcal/mol. This interaction then can be displaced by the second H_2 to generate **72** at -18.5 kcal/mol.

The overall energy barrier for the formation of **72** from the reaction of **71** with H_2 is computed to be 9.0 kcal/mol. This reaction is also computed to be exergonic by 18.5 kcal/mol, consistent with the facile formation of **71**.

4.3.5 Reaction of the Ru-In Species 71 with CO to Give 73 and 74

Figure 4-20 displays the computed mechanism for the reaction of **71** with CO. Addition of a CO ligand to the vacant site at Ru in **71** results in the formation of **73** which is downhill by 14.3 kcal/mol (relative to **71** and CO). The coordination of the CO results in a significant elongation in the Ru–In distance from 2.45 Å to 2.58 Å due to high trans influence exerted by the CO ligand. In **73**, the Me(6) group can migrate from the Ru centre to the In centre via **TS(73-74)** with a low energy barrier of 10.7 kcal/mol. This forms the indyl species **I(73-74)** at -14.1 kcal/mol. Going from **73** to **I(73-74)**, the Ru–In distance sees a notable increase from 2.58 Å to 2.84 Å. This shows a weaker Ru–In interaction in the latter. Addition of the second CO ligand to the Ru vacant site then forms **74** at -41.5 kcal/mol.

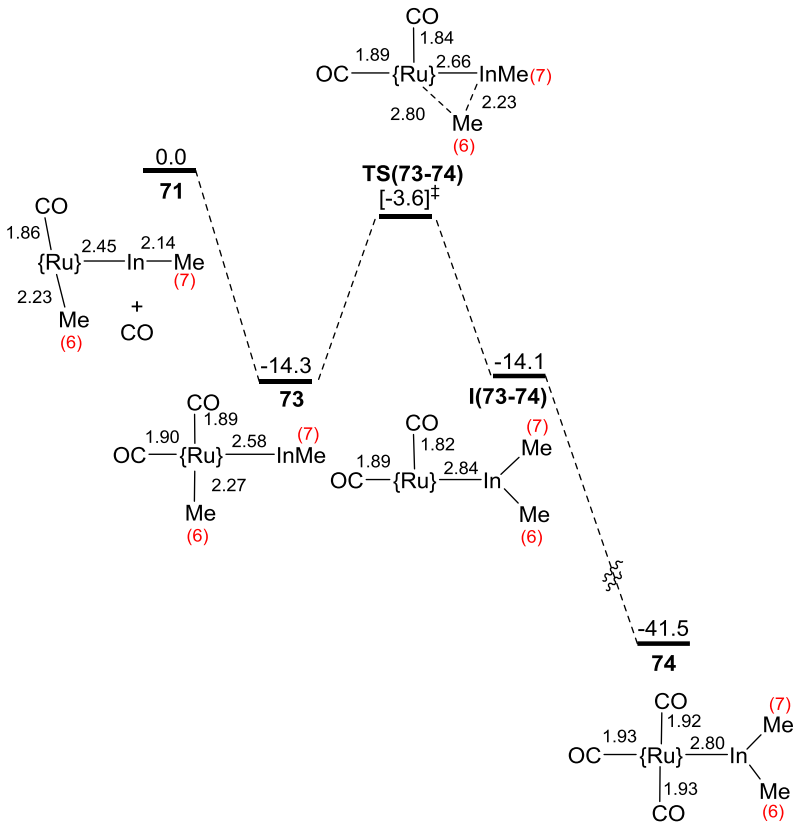

*Figure 4-20. Computed reaction profile (free energy, kcal/mol, BP86/BS1) for the formation of **73** and **74** from **71** and CO; schematic structures show key distances (Å) within the equatorial plane; {Ru} = $Ru(IPr)_2^+$.*

Alternatively, in **73**, the Me(6) group can transfer to the CO ligand situated trans to the InMe moiety via **TS'(73-74)** (Figure 4-21). The energy barrier for this process is approximately same as transfer of the Me group onto the In centre. This reveals that the tendency to accept the Me group by the CO and the In moiety is similar. However, the resultant acyl species **I'(73-74)** is 7.0 kcal/mol uphill relative to **73**. Thus, the Me group can follow the reverse pathway to reform **73** and then transfer onto In to give **I(73-74)**. In **I'(73-74)**, a C–H agostic interaction involving the Me group of the acyl moiety is situated cis to the In moiety. The agostic interaction however can be displaced by a second CO ligand to give **74'** at -24.7 kcal/mol. It should be noted that **74'** is significantly less stable than **74** by 16.8 kcal/mol.

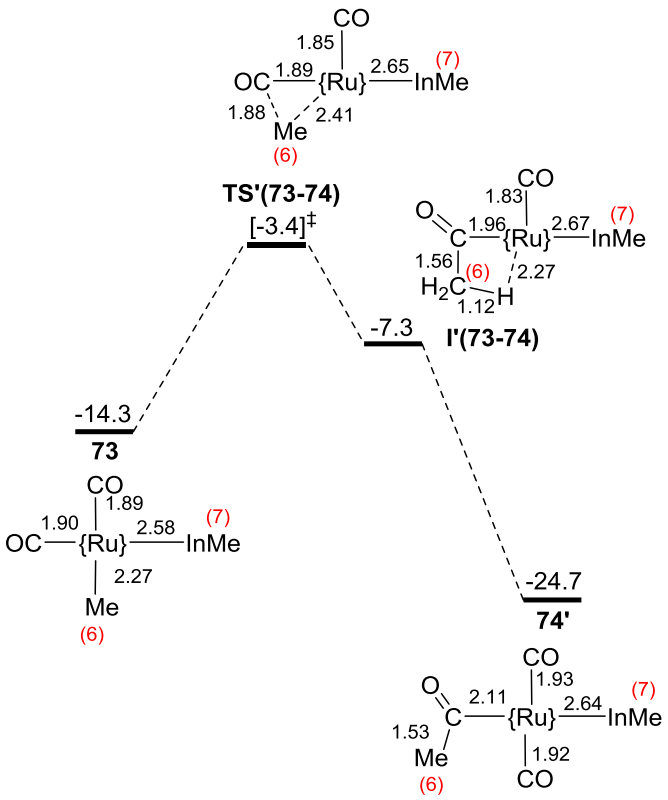

*Figure 4-21. Computed reaction profile (free energy, kcal/mol, BP86/BS1) for the formation of **74'** from **73** and CO; schematic structures show key distances (Å) within the equatorial plane; {Ru} = $Ru(IPr)_2^+$.*

4.4 Conclusions

Several important conclusions can be gained from DFT studies of the heterobimetallic complexes of Ru-In species **71**, **72** and **74**.

I. The heterobimetallic Ru-In species exhibit BCPs along the metal–metal bond. Similar to the Ru–Zn BCPs, the Ru–In BCPs have a small ρ(r), a positive ρ(r) and a small negative H(r), showing they correspond to a dative interaction. NBO charge distribution analysis reveals that in the Ru–In dative interaction, it is the In centre that acts as a LB moiety and donates electron density to the Ru moiety, i.e. Ru←In bond. This therefore indicates a Ru(II)–In(I) formulation in **71** and **72**. This interaction was also characterised to be very sensitive to the trans influence of the ligand trans to the ^{159} moiety. LMO analysis shows that with low trans influence ligand trans to the In moiety, the Ru←In bonding orbital is polarised toward the Ru centre (**72_F**) while with high trans influence ligand, it is polarised toward the In centre (**72**). The Ru-indyl species **74** was also characterised to have a Ru(II)←In(I) formulation, consistent with the CO stretching frequencies of tricarbonyl species.

II. Similar to the formation of the heterobimetallic Ru-Zn complex, formation of the Ru-In complex **71** starts with the transfer of one alkyl to the Ru centre and ends up with the reductive elimination of one molecule of alkane. The latter however is accompanied with the transfer of the second alkyl to the Ru centre to enhance the stabilisation of the consequent complex. Reaction of the Ru-In species **71** with H_2 activates the Ru–Me bond via a σ-CAM process and produces **72** with methane. With CO, activation of the Ru–Me bond causes that the Me group transfers back to the In centre to form **74**. The ability of Me to transfer between the Ru and In centres provides a well-defined reactivity of heterobimetallic species featuring an unsupported TM–E bond. This highlights the availability of vacant orbitals on both Ru and In which can accommodate the transfer of Me across the Ru–In bond.

Chapter 5 – A DFT Mechanistic Study of the Heterobimetallic Ru-Ga Complex 77, $[Ru(IPr)(CO)(GaMe_2(IPr))]^+$

Whittlesey and co-workers showed that treatment of the Ru-H species **67** with $GaMe_3$ produces the heterobimetallic Ru-Ga species **77**. Similar to the synthesis of the Ru-In complex **71**, formation of **77** is accompanied by the elimination of one equivalent of methane. However, in the former, a second Me transfers from the In centre to the Ru centre whereas in the latter, one IPr ligand transfers from the Ru centre to the Ga centre.

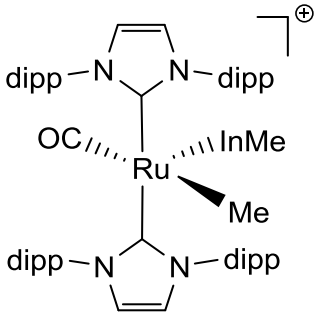

71

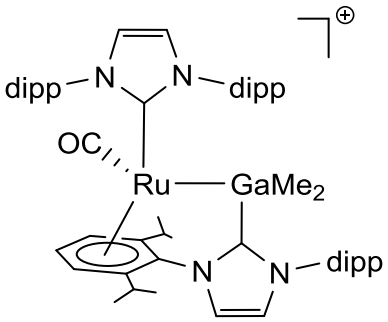

77

Herein, the first section of this chapter describes the experimental results of the formation of the heterobimetallic Ru-Ga complex **77**. The next section is centred on the characterisation of the metal-metal bonding in **77**. In the last section, a particular focus is given to probe the formation of **77** over the gallium congener of **71**.

5.1 Experimental Background

Whittlesey and co-workers investigated the reaction of the cationic Ru-H species **67** with $GaMe_3$ (Figure 5-1). Similar to reaction of **67** with $InMe_3$, reaction of **67** with $GaMe_3$ eliminates one molecule of methane. However, in contrast to the former, formation of **77** involves the transfer of one of the IPr ligands from the Ru centre to the Ga centre. This process takes 10 days to produce **77** and no intermediate is observed during the reaction. It should be also noted that **77** was also characterised in solution by NMR spectroscopy.

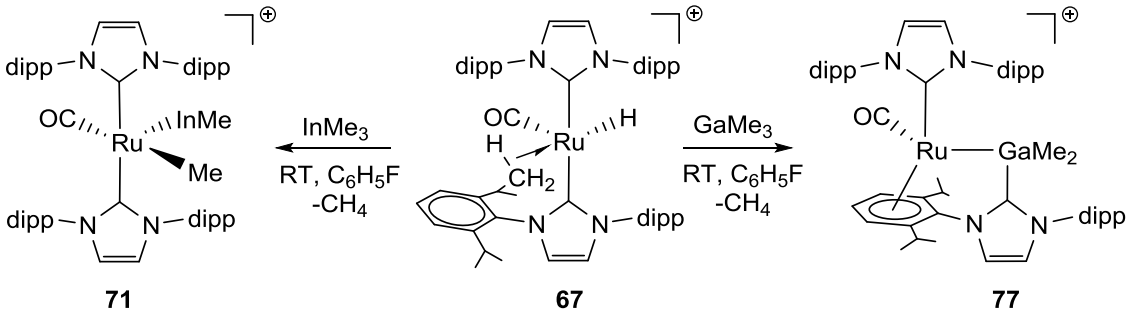

*Figure 5-1. Reaction of **67** with $InMe_3$ and $GaMe_3$ to produce the heterobimetallic species **71** and **77**, respectively.*

The X-ray molecular structure of **77** displays a half-sandwich Ru complex in which one of the aryl groups of the migrated IPr ligand is oriented toward the Ru centre to give the Ru···Cnt distance of 1.819 Å (Cnt = centre of the aryl ring). **77** features a Ru–Ga distance of 2.6742(3) Å which is very slightly shorter than sum of the covalent radii of Ru and Ga centres (2.68 Å)[134], which may suggest a covalent metal–metal interaction.

5.2 Aims

The main objective of the following computational section is to characterise nature of bonding between the Ru and Ga centres in **77**. As outlined above, reaction of $GaMe_3$ with the Ru-H species **67** does not produce the Ga congener of the In product, **71**. Thus, the aim of the final section is to answer the question why different reactivities are seen when **67** is treated with $InMe_3$ and $GaMe_3$.

5.3 Computational Details

DFT calculations were performed with Gaussian 09 (Revision D.01)[160]. Geometry optimisations employed BP86[161] with SDD effective core potentials and associated basis sets[10] for Ru, Ga and In atoms and 6-31G** basis sets for the other atoms.[7, 136] A polarization function was also added to Ga (ζ = 0.185) and In (ζ = 0.143). This basis set combination is referred to BS1. Frequency calculations were carried out at the same level of theory as those for the structural optimisation. All stationary points were fully characterised via analytical frequency calculations as true minima (no imaginary eigenvalues) or transition states (one negative eigenvalue). Transition states were characterized via IRC calculations and subsequent geometry optimizations to confirm they linked to the minima indicated in the text. Single point calculations were performed on the BP86-optimised geometries with BP86/BS1 employing solvent corrections for the effect of fluorobenzene with the PCM approach[14] and dispersion corrections with Grimme's D3 parameter set[22]. QTAIM[162] (AIMALL program) and NBO[163] (NBO 6.010) calculations were performed to study the bonding of **77** and selected intermediates along the computed reaction profiles.

5.4 Results and Discussion

5.4.1 Comparison of the Experimental and Computed Geometries of 77

Table 5-1 shows the selected structural parameters of the experimental and the BP86/BS1 computed geometries of **77** (see Figure 5-2 for the labelling scheme). The computed geometry of **77** exhibits a Ru–Ga distance of 2.828 Å which is slightly longer than that in the experimental structure. It can also be seen that the M–C bond distances (M = Ru and Ga) are well-reproduced by the computed geometry. The shortest and longest computed Ru···C_{aryl} distances are 2.228 Å (Ru···C(a)) and 2.505 Å (Ru···C(b)), respectively, which are slightly longer than those in the experimental geometry. However, the trend in the Ru···C_{aryl} distances is well reproduced by the computed geometry. There is also a good agreement between the experimental and computed distance of the Ru to the centre of the aryl ring, Ru···Cnt. Thus, apart from some small discrepancies, there is reasonable agreement between the experimental and computed geometries of **77**.

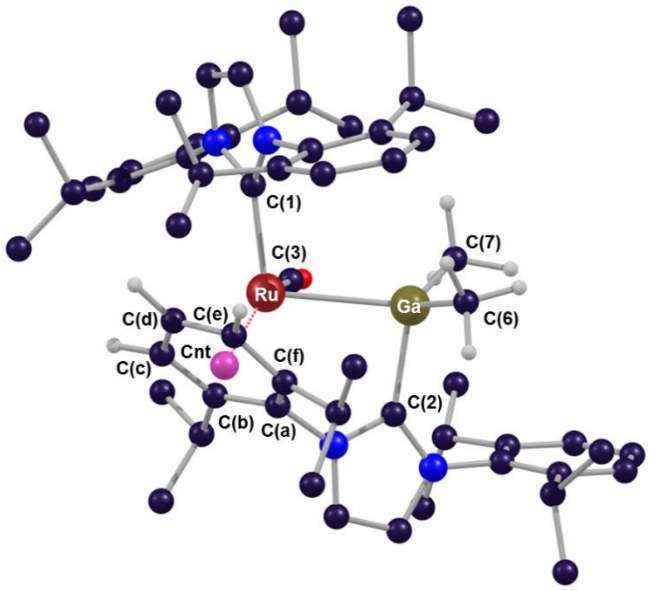

*Figure 5-2. Structure of the Ru-Ga species **77** with labelling scheme on selected atoms. Except for the Me groups connected to the Ga centre and the hydrogens of the aryl group interacting with the Ru centre, all hydrogens are omitted for clarity.*

*Table 5-1. Selected structural parameters of the experimental and computed geometries of **77**. Selected distances are reported in Å.*

	Exp.	**Calc.**
Ru–Ga	2.6742(3)	2.828
Ru···Cnt	1.819	1.875
Ru···C(a)	2.191(2)	2.228
Ru···C(b)	2.206(2)	2.254
Ru···C(c)	2.306(3)	2.345
Ru···C(d)	2.335(3)	2.363
Ru···C(e)	2.364(3)	2.444
Ru···C(f)	2.412(2)	2.505
Ru–C(1)	2.097(3)	2.116
Ru–C(2)	1.837(3)	1.825
Ga–C(3)	2.080(3)	2.155
Ga–C(4)	1.977(3)	2.022
Ga–C(5)	1.997(3)	2.041

5.4.2 Characterisation of the Nature of the Ru-Ga Interaction in 77

QTAIM and NBO calculations were performed on **77** with a structure based on the experimental heavy atom positions derived from the X-ray structure of species **77** with only the H atoms positions being optimized.

Figure 5-3 displays the QTAIM molecular graph of **77** which exhibits a BCP between the Ru and Ga centres, showing an interaction between the metal centres. Similar to the Ru–In BCP in complex **71**, the Ru–Ga BCP in **77** features a small $\rho(r)$, a positive $\nabla^2\rho(r)$ and a small negative H(r). These parameters of $\rho(r)$ are indicative of a metal–metal dative interaction.

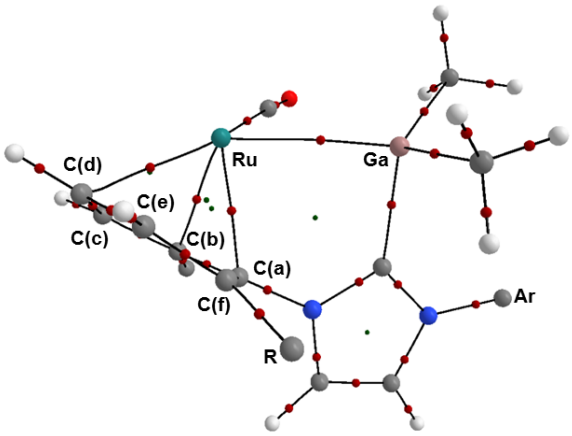

BCP	ρ(r)/eÅ^{-3}	$\nabla^2\rho(r)$/eÅ^{-5}	ε	H(r)/a.u.
Ru–Ga	0.039	0.024	0.172	-0.009
Ru···C(a)	0.078	0.206	0.423	-0.020
Ru···C(b)	0.075	0.196	0.566	-0.018
Ru···C(d)	0.058	0.194	2.368	-0.008

*Figure 5-3. Details of the QTAIM molecular graph of **77**. BCPs and RCPs are shown as red and green spheres, respectively. The BCP parameters are shown by electron density (ρ(r)), Laplacian of electron density ($\nabla^2\rho(r)$), ellipticity (ε) and total energy density (H(r)). The IPr ligand coordinated to the Ru centre via C(1) is omitted for clarity. Ar = 2,6-diisopropylphenyl and R = isopropyl.*

Figure 5-4 shows the NBO analysis of the Ru–Ga interaction in **77**. NBO analysis identifies a donor-acceptor interaction between the Ru and Ga centres. In this interaction, one of the lone pairs of the Ru centre donates electron density to a Ga vacant orbital. This therefore indicates a Ru(0)→[Ga(III)(L)Me_2] interaction and shows that the Ga centre is formally cationic. As a result, the E(2) value associated with this interaction has a very large value of 454.6 kcal/mol, showing a strong Ru→Ga interaction. It is interesting to note that the tetrahedral geometry at the Ga centre can also support the Ru(0)→Ga(III) formulation in **77**. This is in contrast with the bonding situation in the Ru-In complex **71**, which exhibits a Ru(II)←In(I) formulation.

With respect to the oxidation state of the Ru centre, the Ru centre should have an η^6-coordination with the aryl group to obey the 18-electron rule. It should be noted that the QTAIM molecular graph of **77** shows only three BCPs between the Ru and C_{aryl} centres, two of which are associated with the shortest Ru···C_{aryl} distances, i.e. Ru···C(a) and Ru···C(b), and one BCP between the Ru and C(d) centres. However, the absence of the other three BCPs is not inconsistent with an η^6-interaction as similar examples have been reported in literature.[164]

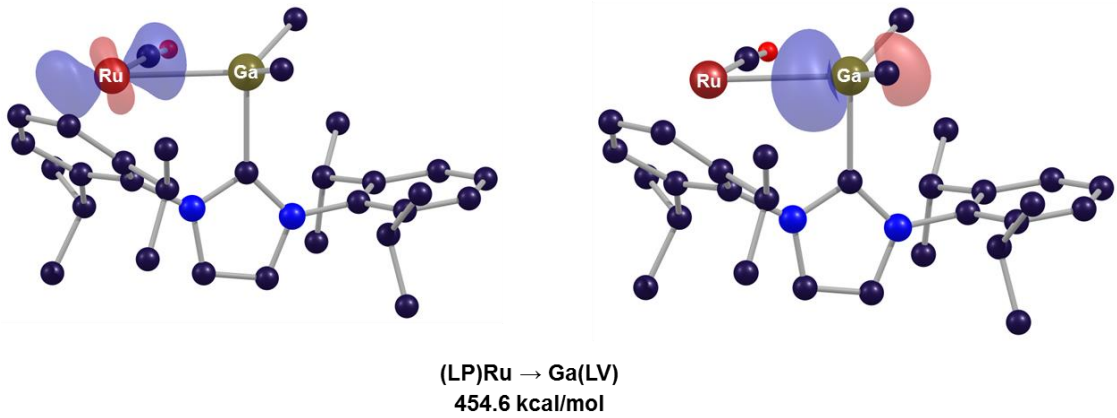

Figure 5-4. NBO donor-acceptor interaction between one of the lone pairs (LPs) of the Ru centre and the Ga vacant orbital with the interaction energy of E(2). The IPr ligand coordinated to the Ru centre via C(1) and all hydrogen atoms are omitted for clarity. Isosurfaces plotted with Chemcraft with a contour value of 0.1.

5.4.3 Study of the Mechanism of the Formation of 77

In the process of the formation of **77**, two mechanisms have been considered, Pathway **I** and Pathway **II**. In Pathway **I**, the process starts with the initial transfer of an IPr ligand from the Ru centre to the Ga centre and then one Me transfers from the Ga centre to the Ru centre. In Pathway **II**, the process starts with the transfer of the Me onto the Ru centre and then an IPr ligand transfers from the Ru centre onto the Ga centre. In both pathways a reductive elimination of methane followed by isomerisation processes then generates the Ru-Ga species **77**.

Figure 5-5 displays the computed energy profile for the formation of **77** via Pathway **I**.

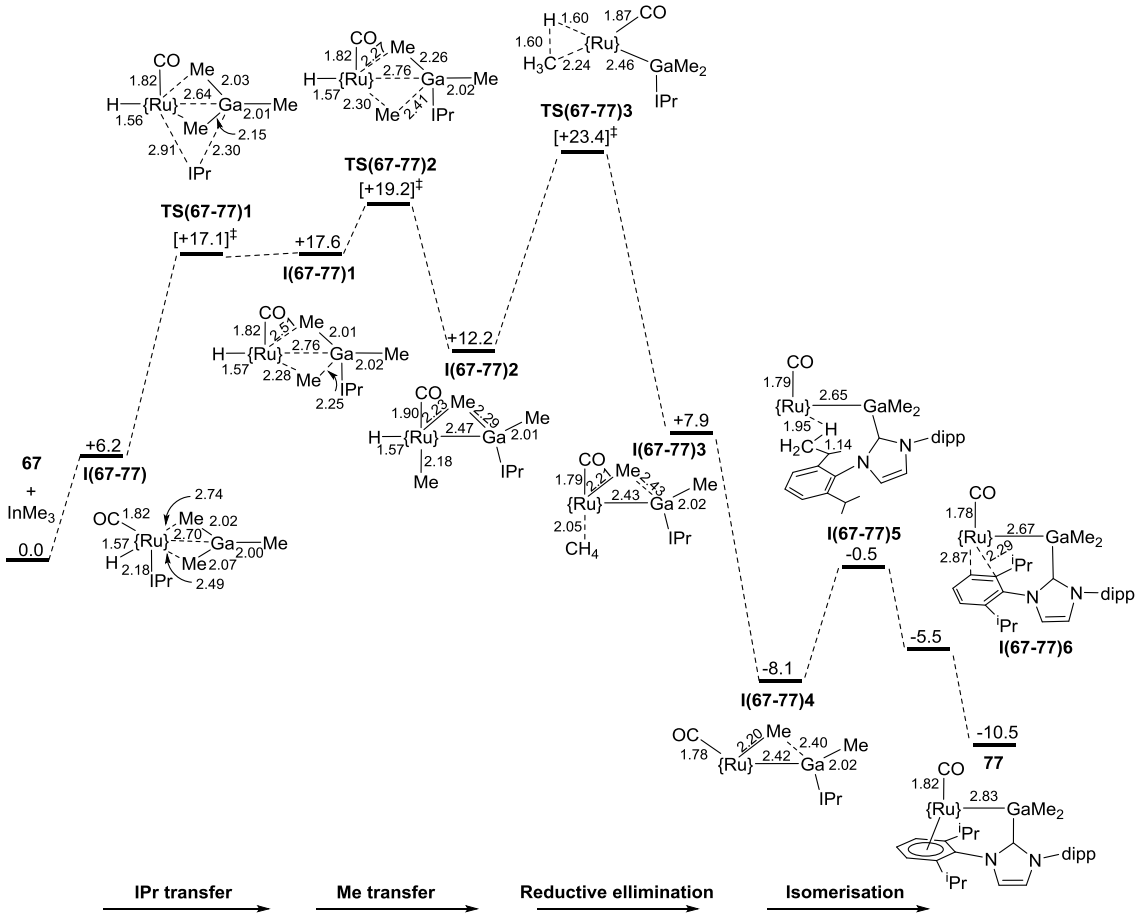

*Figure 5-5. Computed energy profile (Pathway **I**) for the formation of **77**. Free energies are in kcal/mol and selected distances are in Å. {Ru} = Ru(IPr)$^{+}$.*

DFT calculations to study the reaction of **67** with $GaMe_3$ located the adduct precursor **I(67-77)** at +6.2 kcal/mol. As shown in Figure 5-6, similar to the Ru-In adduct **I(67-71)**, the Ru-Ga adduct **I(67-77)** exhibits a trigonal planar geometry at the Ga centre. However, in the latter, the structure of $GaMe_3$ is slightly oriented toward the carbenic carbon (C(2)) of one of the IPr ligands to give a short Ga···C(2) distance of 2.93 Å (Ru–C(1) = 2.15 Å and Ru–C(2) = 2.18 Å). **I(67-77)** exhibits a Ru···Ga distance of 2.70 Å which is slightly larger than sum of the covalent radii of the Ru and Ga centres (2.68 Å).[134] The Ga–C(5) bond is slightly longer than the Ga–C(6) bond to give a short Ru···C(5) distance of 2.49 Å. In addition, the C(5)–H(5a) bond is slightly elongated to 1.12 Å give a short Ru···H(5a) distance of 2.10 Å, showing a C–H agostic interaction with the Ru centre. This therefore indicates that, similar to the indium analogue, **I(67-77)** is a sigma complex.

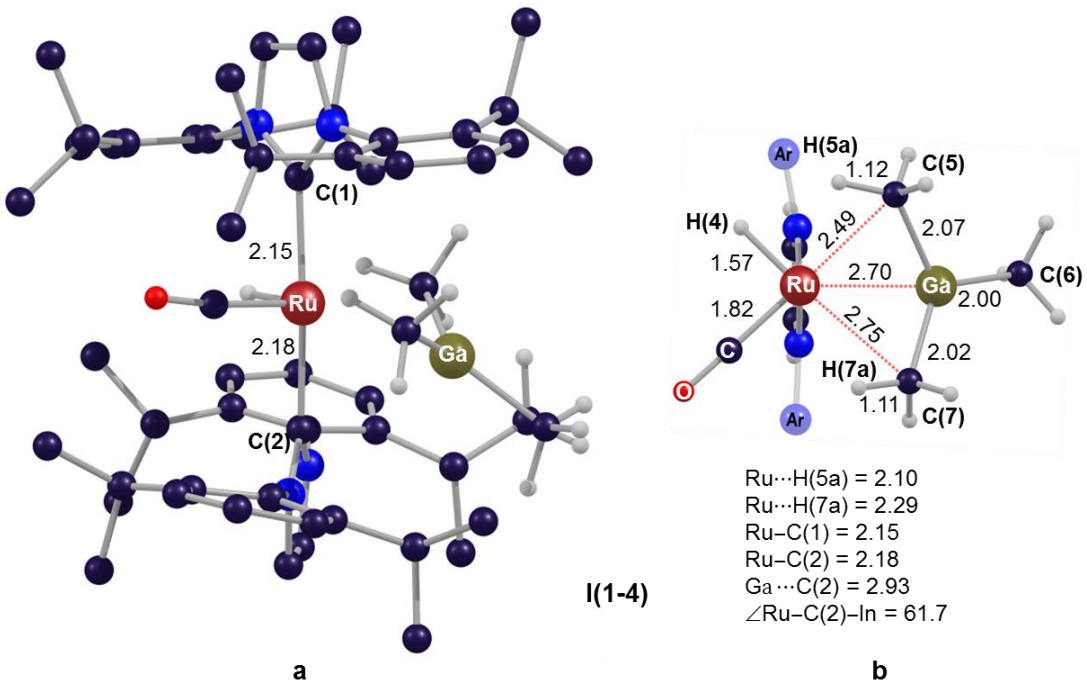

*Figure 5-6. Representation of **I(67-77)**; a) the full structure (the hydrogens of the IPr ligands are omitted for clarity) and b) within the equatorial plane of {Ru/H/C(O)} (the IPr ligand connected to the Ru centre via C(1) is omitted for clarity). Selected distances and angles are shown in Å and degrees, respectively. Ar = 2,6-diisopropylphenyl.*

In **I(67-77)**, the IPr ligand based on the C(2) atom centre can transfer to the Ga centre via **TS(67-77)1** at +17.1 kcal/mol (Figure 5-7). From **I(67-77)** to **TS(67-77)1**, the Ru···C(2) distance is significantly elongated to 2.91 Å to give a short Ga···C(2) contact of 2.30 Å. It can also be seen that the Ga centre is distorted from a trigonal planar geometry to accommodate the IPr transfer process.

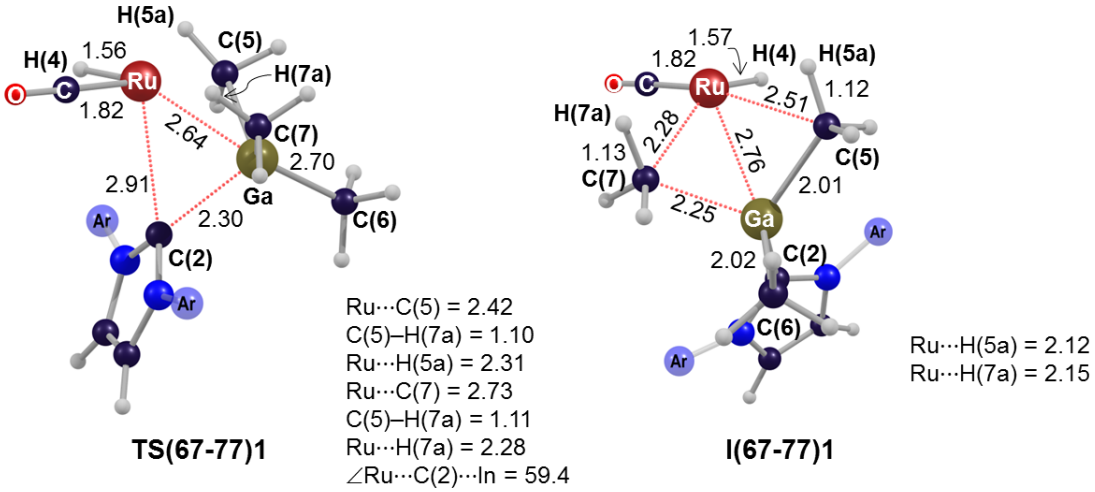

*Figure 5-7. Structures of **TS(67-77)1** and **I(67-77)1** with the labelling scheme for selected atoms. The IPr ligand coordinated to the Ru centre via C(1) is omitted for clarity. Selected distances and angles are shown in Å and degrees, respectively. Ar = 2,6-diisopropylphenyl.*

Transfer of the IPr ligand onto the Ga centre gives **I(67-77)1** which lies slightly higher than **TS(67-77)1**, at +17.6 kcal/mol (Figure 5-7). This is mainly due to the higher contribution of dispersion interaction energy in the corrected free energy of the transition structure **TS(67-77)1** than **I(67-77)1** which makes the former slightly more stable. In **I(67-77)1**, the Ga moiety has a tetrahedral geometry and is displaced out of the {Ru/H(4)/C(O)} plane. Going from **I(67-77)** to **I(67-77)1**, the Ru···Ga distance gets slightly longer to 2.76 Å. The Ga···C(7) distance is significantly elongated to give a short Ru···C(7) distance. A QTAIM analysis of **I(67-77)1** reveals BCPs along the M−C(5) and M−C(7) bond paths (M = Ru and Ga), indicating Me(5) and Me(7) groups have bridging character. The C(5) centre however has a stronger interaction with the Ga centre (H(r): Ru···C(5) = -0.003 and Ga···C(7) = -0.033) while the C(7) atom exhibits slightly stronger interaction with the Ru centre (H(r): Ru···C(7) = -0.018 and Ga···C(5) = -0.017).

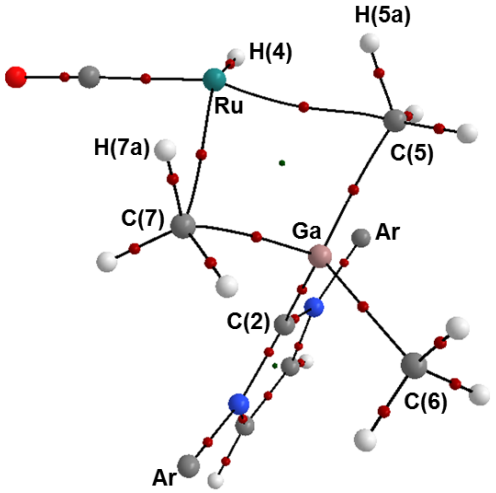

BCP	ρ(r)/eÅ^{-3}	∇^{2}ρ(r)/eÅ^{-5}	ε	H(r)/a.u.
Ru···C(5)	0.043	0.138	2.069	-0.003
Ru···C(7)	0.073	0.168	0.271	-0.018
Ga···C(5)	0.090	0.124	0.080	-0.033
Ga···C(7)	0.063	0.093	0.253	-0.017
Ga–C(6)	0.108	0.124	0.007	-0.046

*Figure 5-8. Details of the QTAIM molecular graph of **I(67-77)1**. BCPs and RCPs are shown as red and green spheres, respectively. The IPr ligand coordinated to the Ru centre via C(1) is omitted for clarity. Ar = 2,6-diisopropylphenyl.*

In **I(67-77)1**, the Me(5) group is situated cis to the hydride which can transfer onto the Ru centre to allow for the reductive elimination of methane. This occurs via **TS(67-77)2** at +19.2 kcal/mol and gives **I(67-77)2** at +12.2 kcal/mol. This process significantly reduces the Ru···Ga distance to 2.47 Å. A QTAIM analysis of **I(67-77)2** shows a BCP along the Ru···Ga bond path featuring a small negative H(r) value of -0.021 (Figure 5-9), showing a covalent interaction between the metal centres. Similar to **I(67-77)1**, the C(7) centre in **I(67-77)2** is in a bridging position between the metal centres.

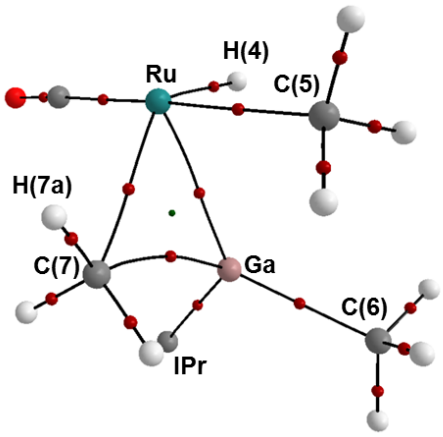

BCP	ρ(r)/eÅ^{-3}	∇^{2}ρ(r)/eÅ^{-5}	ε	H(r)/a.u.
Ru–Ga	0.065	0.066	0.083	-0.021
Ru–C(5)	0.099	0.152	0.011	-0.034
Ru···C(7)	0.084	0.160	0.086	-0.024
Ga···C(7)	0.062	0.074	0.497	-0.015
Ga–C(6)	0.110	0.117	0.012	-0.048

*Figure 5-9. Details of the QTAIM molecular graphs of **I(67-77)2**. BCPs and RCPs are shown as red and green spheres, respectively. The IPr ligand coordinated to the Ru centre via C(1) is omitted for clarity.*

In **I(67-77)2**, the Me(5) group is in the plane of the {Ru/H(4)/C(O)} unit, situated cis to the hydride ligand. Thus, it can undergo a C(5)–H(4) reductive coupling process via **TS(67-77)3** at +23.4 kcal/mol to give the methane complex **I(67-77)3** at +7.9 kcal/mol. Once methane is dissociated from the Ru centre, similar to the Ru-In chemistry, partial transfer of the second Me group (i.e. Me(7)) to the Ru centre to form **I(67-77)4** at -8.1 kcal/mol. The Me(7) group can however transfer back onto the Ga centre to give **I(67-77)5** at -0.5 kcal/mol. The potential energy surface corresponding to this process is flat and thus, attempts to locate this transition structure were unsuccessful. A systematic shortening of the Ga···C(7) distance to transfer Me(7) to Ga to give **I(67-77)4** shows that the energy barrier corresponding to this process is approximately 14.8 kcal/mol with respect to **I(67-77)4**.

Once the Me(7) group transfers to the Ga centre, one of the C–H bonds (i.e. C(14)–H(14a) bond) of the isopropyl substituent of the IPr ligand coordinated to the Ga centre orients toward the Ru centre to give to **I(67-77)5** at -0.5 kcal/mol. In **I(67-77)5**, the C(14)–H(14a) is significantly elongated to 1.14 Å to give a short Ru···H(14a) distance of 1.95 Å. A QTAIM analysis of **I(67-77)5** shows a BCP between the Ru and H(14a) centres with the H(r) value of -0.011 (Figure 5-10). This, along with the reduced electron density of the C(14)–H(14a) BCP (relative to C(14)–H(14b)), is consistent with a C–H agostic interaction with the Ru centre.

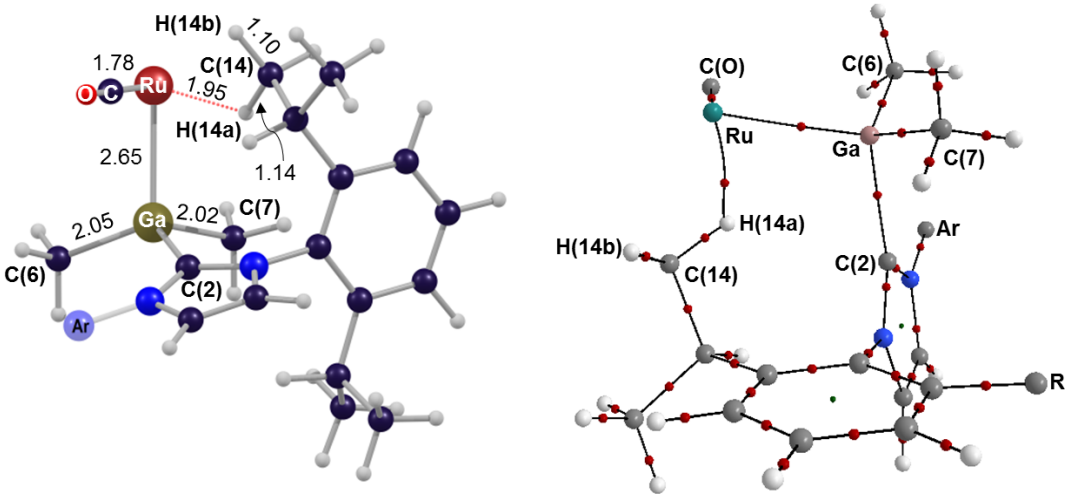

BCP	ρ(r)/eÅ^{-3}	$\nabla^2\rho(r)$/eÅ^{-5}	ε	H(r)/a.u.
Ru–Ga	0.052	0.037	0.016	-0.015
Ru···H(14a)	0.056	0.196	0.209	-0.011
C(14)–H(14a)	0.235	-0.634	0.029	-0.206
C(14)–H(14b)	0.269	-0.896	0.004	-0.267

*Figure 5-10. Structure of **I(67-77)5** with the labelling scheme for selected atoms. Selected distances are shown in Å; Ar = 2,6-diisopropylphenyl. Details of the QTAIM molecular graph of **I(67-77)5**. BCPs and RCPs are shown as red and green spheres, respectively. The IPr ligand coordinated to the Ru centre via C(1) is omitted for clarity; R = isopropyl.*

In **I(67-77)5**, rotation of the IPr ligand around the Ga–C(2) would lead to the formation of the Ru-Ga complex **77**. However, the potential energy surface associated with this process is again very flat. Therefore, attempts to locate transition states for this process remained inconclusive. The rotation of the Ga moiety around the Ru–Ga vector firstly produces **I(67-77)6** at -5.5 kcal/mol (Figure 5-11). Based on the scan calculation, this process involves a minimal barrier. **I(67-77)6** exhibits a short Ru···C(10) distance 2.30 Å. This suggests an interaction between the C(9)–C(10) bond and the Ru centre. As shown in Figure 5-12, the QTAIM molecular graph of **I(67-77)6** shows a BCP between the Ru and the C(10) centres of the aryl ring. The Ru···C(10) BCP has a small negative H(r) of -0.019 which supports a covalent interaction between the participating atoms.

While in **I(67-77)6**, the Ru···Cnt distance (Cnt = ring centroid) is 2.71 Å, further rotation of the IPr ligand along the Ga–C(2) vector decreases the Ru···Cnt distance to 1.87 Å to form **77** at -10.5 kcal/mol. Based on the scan calculations, the energy barrier related to this process is approximately 3.1 kcal/mol with respect to **I(67-77)6**.

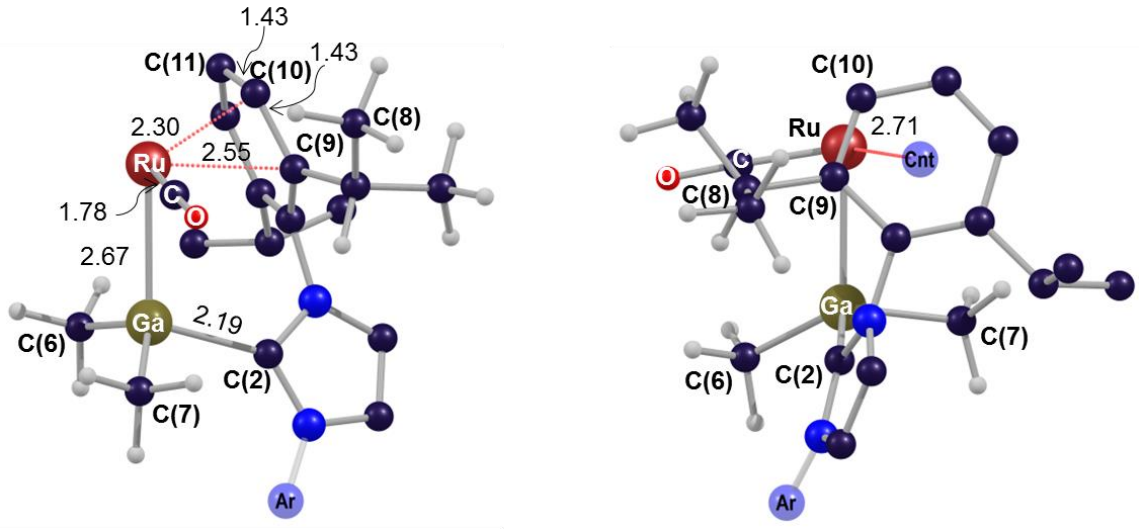

*Figure 5-11. Structure of **I(67-77)6** with the labelling scheme for selected atoms. The IPr ligand coordinated to the Ru centre via C(1) is omitted for clarity. Selected distances are shown in Å; Ar = 2,6-diisopropylphenyl.*

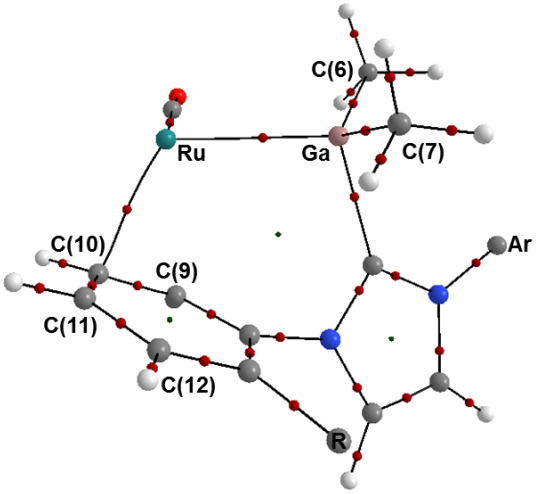

BCP	ρ(r)/eÅ^{-3}	$\nabla^2\rho(r)$/eÅ^{-5}	ε	H(r)/a.u.
Ru–Ga	0.050	0.036	0.073	-0.014
Ru···C(10)	0.070	0.122	0.125	-0.019
C(9)–C(10)	0.289	-0.708	0.189	-0.270
C(10)–C(11)	0.288	-0.718	0.150	-0.267
C(11)–C(12)	0.311	-0.825	0.210	-0.311

*Figure 5-12. Details of the QTAIM molecular graph of **I(67-77)6**. BCPs and RCPs are shown as red and green spheres, respectively. The IPr ligand coordinated to the Ru centre via C(1) is omitted for clarity; Ar = 2,6-diisopropylphenyl and R = isopropyl.*

As shown in Figure 5-13, in Pathway **II**, the Me(5) group in **I(67-77)** can transfer from the Ga centre to the Ru centre via a two-step process. In the first step, the Me(5) transfers to the bridging position between the Ru and Ga centres via **TS'(67-77)1** at +12.0 kcal/mol to give **I'(67-77)1** at +11.2 kcal/mol.

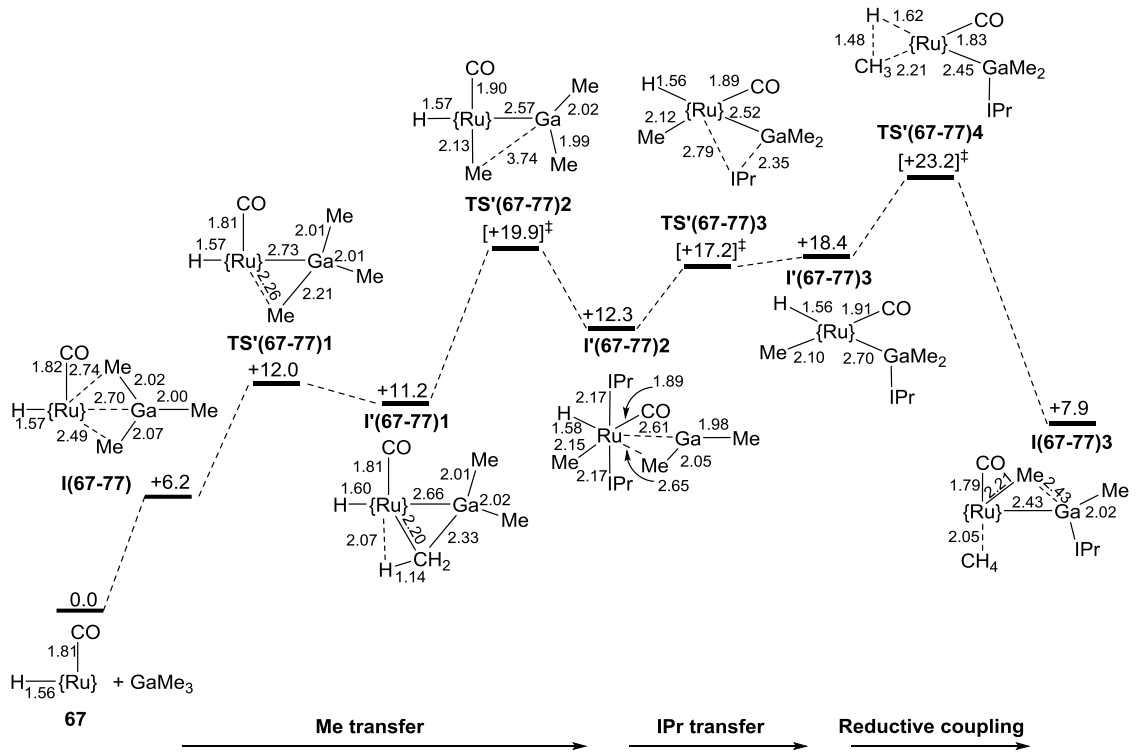

*Figure 5-13. Computed energy profile (Pathway **II**) for the formation of intermediate **I(67-77)3**. Free energies are in kcal/mol and selected distances are in Å.*

I'(67-77)1 has an elongated Ga···Me(5) distance of 2.33 Å and a short Ru···Me(5) distance of 2.20 Å. As shown in Figure 5-14, the QTAIM molecular graph of **I'(67-77)1** exhibits a bridging Me between the Ru and Ga centres. However, it has a stronger interaction with the Ru centre than the Ga centre (H(r): Ru–C(5) = -0.024, Ru–C(5) = -0.013).

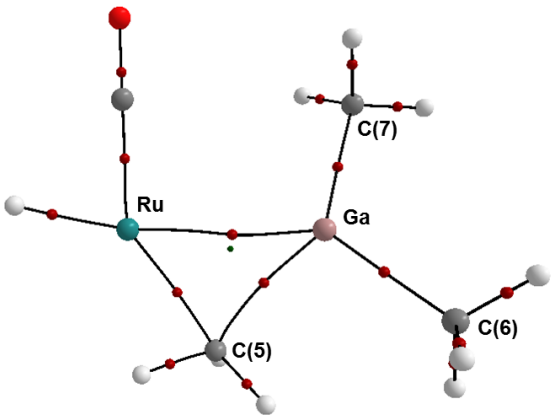

BCP	ρ(r)/eÅ^{-3}	$\nabla^2\rho(r)$/eÅ^{-5}	ε	H(r)/a.u.
Ru–Ga	0.044	0.052	1.416	-0.011
Ru···C(5)	0.085	0.196	0.127	-0.024
Ga···C(5)	0.057	0.074	0.293	-0.013
Ga–C(6)	0.109	0.113	0.001	-0.047

*Figure 5-14. Details of the QTAIM molecular graph of **I'(67-77)1**. BCPs and RCPs are shown as red and green spheres, respectively. The IPr ligand coordinated to the Ru centre via C(1) is omitted for clarity; Ar = 2,6-diisopropylphenyl.*

The full transfer of the Me(5) group to the Ru centre takes place via **TS'(67-77)2** at +19.9 kcal/mol and generates **I'(67-77)2** at +12.3 kcal/mol. In **I'(67-77)2**, one IPr ligand transfers to the Ga centre via **TS'(67-77)3** at +17.2 kcal/mol to give **I'(67-77)3** which lies slightly higher that **TS'(67-77)3**, at +18.4 kcal/mol (Figure 5-15). It should be noted that the energy barrier corresponding to the IPr transfer process via Pathway **II** is 4.9 kcal/mol (with respect to **I'(67-77)2**) which is significantly lower than that in Pathway **I** (11.9 kcal/mol with respect to **I(66-77)**).

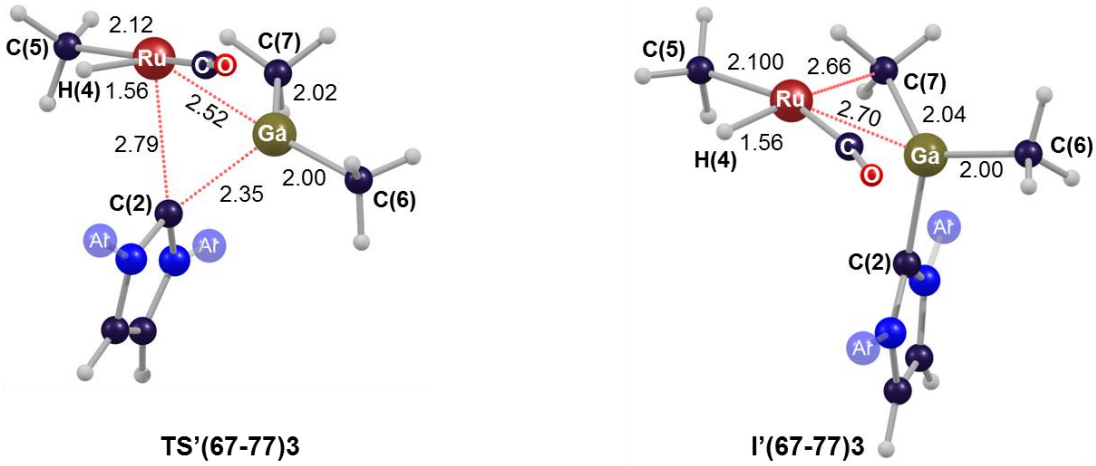

*Figure 5-15. Structures of **TS'(67-77)3** and **I'(67-77)3** with the labelling scheme for selected atoms. The IPr ligand coordinated to the Ru centre is omitted for clarity. Selected distances are shown in Å; Ar = 2,6-diisopropylphenyl.*

In **I'(67-77)3**, there is no BCP between the Ru and C(7) centres (Figure 5-16). However, the Ga–C(7) BCP has a slightly lower H(r) compared with the Ga–C(6) BCP, showing the former exhibits a slightly weaker interaction. In addition, the former has a higher ellipticity, indicating the Me(7) group has some bridging character.

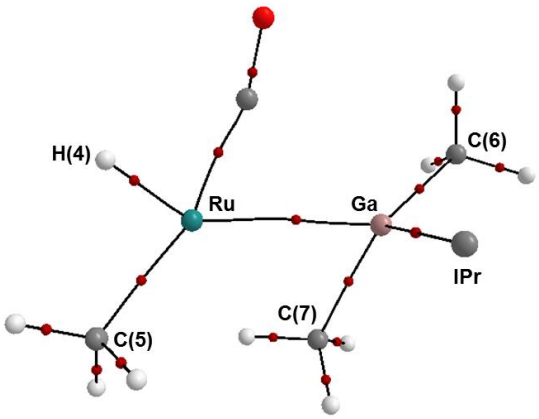

BCP	ρ(r)/eÅ^{-3}	$\nabla^2\rho(r)$/eÅ^{-5}	ε	H(r)/a.u.
Ru–Ga	0.045	0.041	0.719	-0.012
Ru–C(5)	0.115	0.142	0.035	-0.046
Ga–C(7)	0.102	0.126	0.061	-0.042
Ga–C(6)	0.112	0.119	0.009	-0.049

*Figure 5-16. Details of the QTAIM molecular graph of **I'(67-77)3**. BCPs are shown as red spheres. The IPr ligand coordinated to the Ru centre via C(1) is omitted for clarity; Ar = 2,6-diisopropylphenyl.*

I'(67-77)3 then can undergo a C–H coupling process via **TS'(67-77)4** at +23.2 kcal/mol to give **I(67-77)3** at +7.9 kcal/mol. Once **I(67-77)3** has formed, it follows the same isomerisation steps via Pathway **I** to form **77**.

Comparison of Pathways **I** and **II** shows that in both processes, the transition states corresponding to the reductive coupling step lie at the highest energy level with overall energy barriers of 23.4 kcal/mol and 23.2 kcal/mol, respectively. This therefore indicates that transfer of the IPr ligand to the Ga centre before or after the first Me-transfer only changes the overall energy barrier very slightly. The computed energy barrier for the formation of **77** via Pathways **I** or **II** may be consistent with the reaction conditions as reaction of **67** with $GaMe_3$ takes 10 days to form **77**. Interestingly, the overall energy barrier to form the Ru-In species **71** is 13.7 kcal/mol which is significantly lower than the computed overall energy barrier for the formation of **77**, consistent with the fact that formation of **71** is experimentally very fast.

However, in this case, the computed energy barrier for the formation of the gallium congener of the indium complex, **71_Ga**, should be even higher than +23.2 kcal/mol, as **71_Ga** cannot be observed experimentally. This was therefore assessed by the computed energy profile for the formation of the gallium congener of the indium complex, **71_Ga**.

As shown in Figure 5-17, similar to the mechanism of the formation of **71**, this process starts with the formation of **I(67-77)**, continues with the transfer of the Me(5) group to the Ru centre and then ends up with a reductive elimination step to produce methane and **71_Ga** at -24.6 kcal/mol. It should be noted that apart from **I(67-77)** where the Ga moiety is oriented toward the carbenic position of one of the IPr ligands, the structures involved in this process are very similar to those in the formation process of the Ru-In species **71**.

The overall energy barrier to form **71_Ga** is computed to be +19.9 kcal/mol which is related to the transfer of Me(5) group to the Ru centre. However, this energy barrier is lower than the energy barrier (+22.3 kcal/mol) computed for the formation of the experimentally observed complex **77** via Pathway **II**. This suggests that formation of **71_Ga** is kinetically more accessible than **77**. In addition, formation of **71_Ga** is significantly more thermodynamically favoured over the formation of **77** (**71_Ga**: -24.6 kcal/mol, **77**: -8.9 kcal/mol). Thus from both the kinetic and thermodynamic points of view, formation of **77** is predicted and this is not consistent with the experimental observations. Thus, in the next section, particular attention has been paid to see if there is

a functional dependency in the thermodynamic stabilities of the experimentally observed Ru-In species **71** and Ru-Ga species **77** relative to their computed heterobimetallic congeners **77_In** and **71_Ga**, respectively.

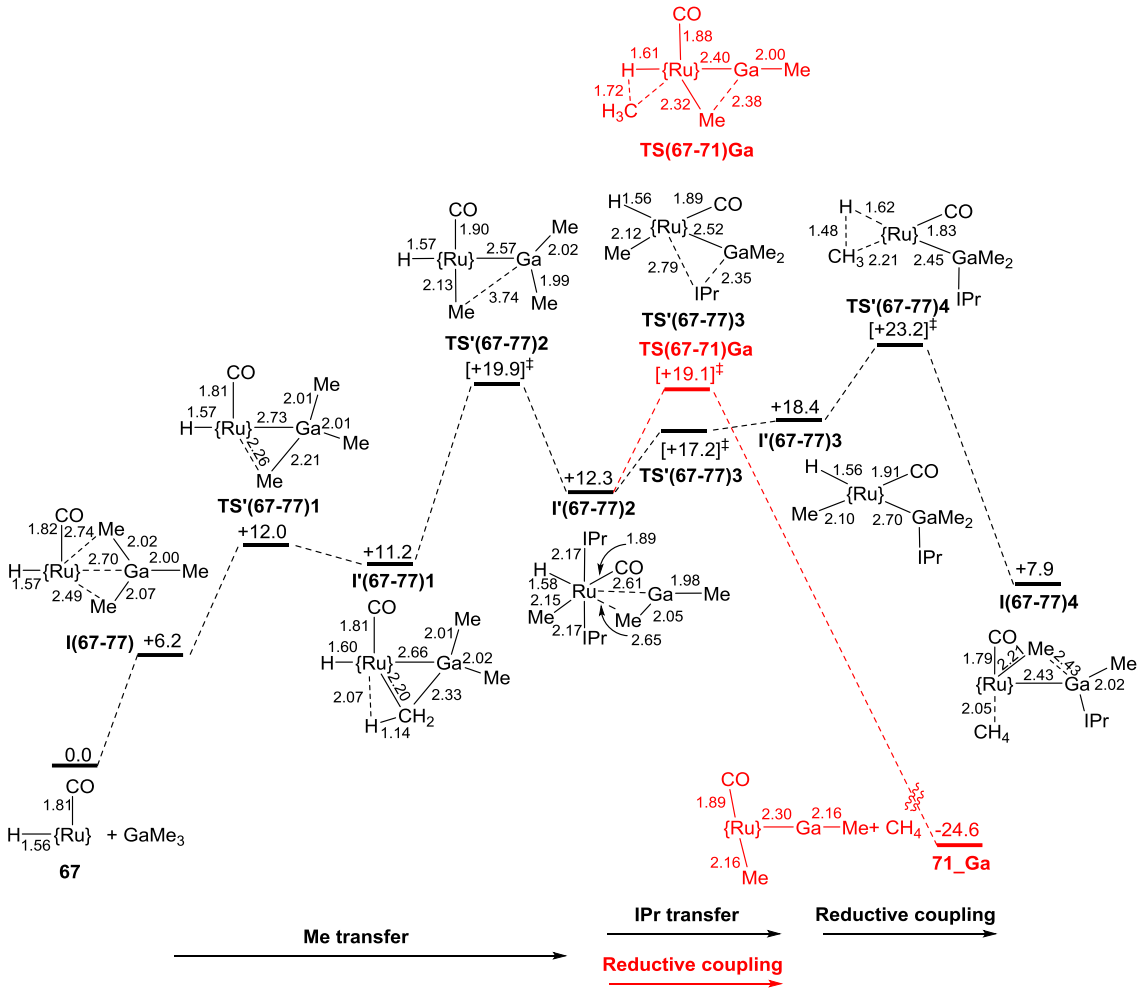

*Figure 5-17. Computed energy profiles for the formation of **I(67-77)4** (Pathway **II**) and **71_Ga**. Free energies are in kcal/mol and selected distances are in Å.*

5.4.3.1 Thermodynamic stability of 71 and 77

Figure 5-18 displays the In congener of the Ga complex, **77_In**, and the Ga congener of the In complex, **71_Ga**. One may expect that for the Ru-In complexes, **71** should be more stable than **77_In** and conversely, for the Ru-Ga complexes, **77** should be more stable than **71_Ga**.

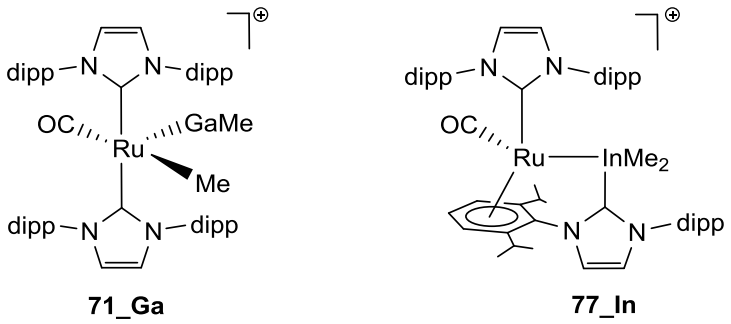

*Figure 5-18. The Ga congener of the Ru-In complex **71** (**71_Ga**) and the In congener of the Ru-Ga complex **77** (**77_In**).*

In order to assess the thermodynamic stability of **71** versus **77_In** and **77** versus **71_Ga**, these structures were first optimised with the BP86/BS1 approach. Single point calculations then were run on the BP86/BS1 geometries using a wide range of functionals including GGA functionals (BP86, B97D[165], PBE[166] and BLYP[4]), hybrid-GGA functionals (ωB97xD[167] and B3LYP[4, 6, 168]) a meta-GGA functional (TPSS[169]) and a Minnesota functional (M06[170]). In addition, larger basis sets BS2 and BS3 were also tested. BS2 employs the same basis set as in BS1 for the metal centres and 6-311++G** basis sets for other atoms. BS3 employs Def2TZVP basis set for all the atoms and pseudopotentials for Ru and In. Free energies (kcal/mol) include a correction for fluorobenzene solvent (PCM[14] approach) and also a correction for dispersion (Grimme's D3 parameter set[22]) for those functionals that do not already include a treatment of dispersion effects. The type of dispersion correction was also considered for the B97D functional with Grimme's D3 and D3BJ[24] parameter sets.

Figure 5-19 displays the difference in free energy between **77_In** and **71** (ΔG_{In}). Interestingly, it can be seen that with all the functionals and basis set combinations, the ΔG_{In} values are positive. This shows that **71** is more stable than **77_In** which indicates that the thermodynamic preference for **71** over **77_In** is not functional or basis sets dependent. Comparing the results obtained with BS1 with BS2, except for the BP86 functional, the ΔG_{In} values become slightly smaller. With BS3, the ΔG_{In} values are larger than BS1 and BS2. Using different dispersion parameter sets makes a significant change to the ΔG_{In} values. For example, with B97D/BS3, ΔG_{In} is +17.0 kcal/mol. Going to B97(D3), the ΔG_{In} value significantly increases to +26.7 kcal/mol while with B97(D3BJ), it reduces to +24.0 kcal/mol.

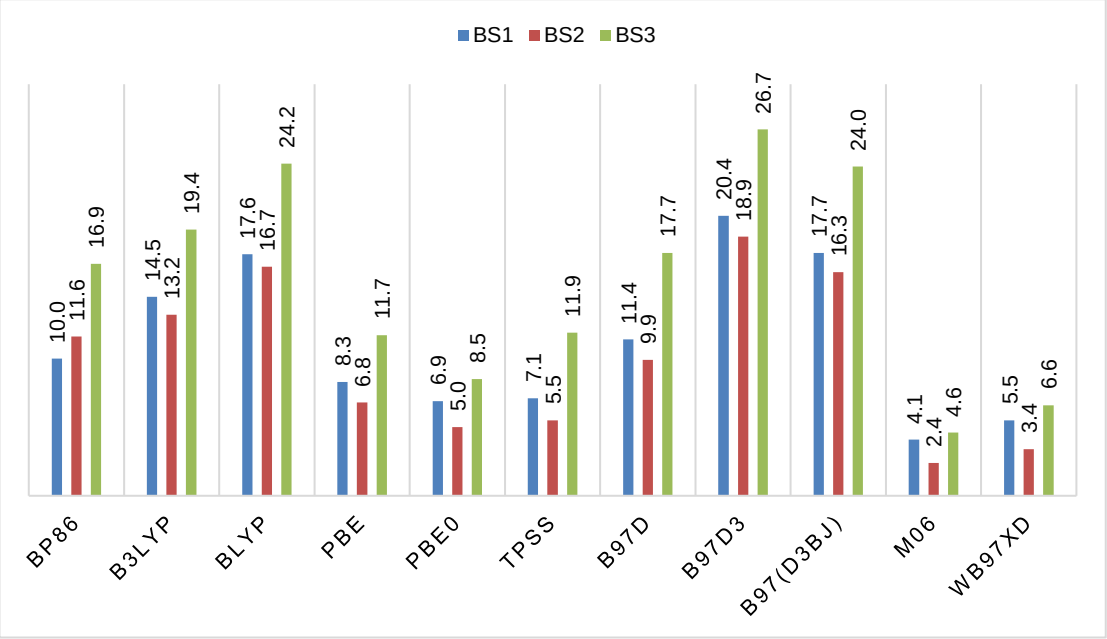

*Figure 5-19. Computed energy difference (ΔG_{In}, kcal/mol) between **77_In** and **71** with various functionals and BS1, BS2 and BS3. Energies include solvent and dispersion corrections where appropriate.*

Figure 5-20 shows the ΔG_{Ga} values for the gallium complexes. Similar to the indium complexes, with BS1 and BS2, all the ΔG values for the gallium complexes are positive. Compared to BS1, BS2 gives slightly smaller ΔG_{Ga} values (except for the BP86 functional). Interestingly, while the BS3 basis set give the highest ΔG_{In} values for the indium complexes, it gives the lowest ΔG_{Ga} values for the gallium complexes. However, it is only with the M06 and ωB97xD functionals that ΔG_{Ga} is negative, and only then by a very small amount (M06 = -1.0 kcal/mol and ωB97xD = -0.4 kcal/mol).

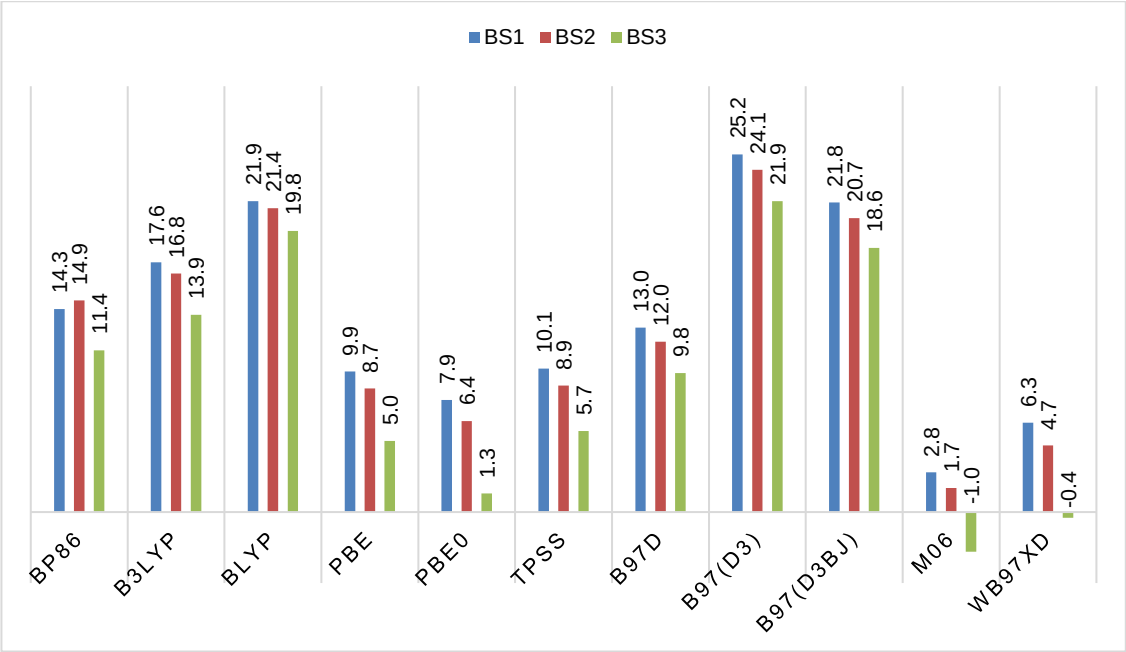

*Figure 5-20. Computed energy difference (ΔG_{Ga}, kcal/mol) between **77** and **71_Ga** with various functionals and the BS1, BS2 and BS3 basis sets. Energies include solvent and dispersion corrections where appropriate.*

It should be note that using different dispersion parameter sets significantly changes the ΔG values. This denotes the importance of the way of capturing dispersion interactions in **77_In** and **77** which can be important in description of the η^6 interaction. Thus, the gallium and indium structures were optimised with those functionals that have a treatment for dispersion correction (i.e. M06, ωB97XD and B97D) with BS1. PCM calculations then were run using the same level of theory to compute the relative stabilities of **77_In** versus **71** and **77** versus **71_Ga**. As shown in Table 5-2, with the M06-, ωB97XD- and B97D-optimised geometries, a similar trend to the BP86-optimised geometries is obtained. This therefore shows that optimisation including dispersion does not affect the thermodynamic preference of the formation of the Ru-Ga and Ru-In species.

Table 5-2. a) Computed ΔG values with the BP86/BS1-optimised geometries and single point calculations with the M06, ωB97XD and B97D functionals and BS1 including PCM corrections. b) Computed ΔG values with the M06, ωB97XD and B97D optimised geometries and single point calculations with BS1 including PCM corrections.

Functional	ΔG_{In}[a]	ΔG_{In}[b]	ΔG_{Ga}[a]	ΔG_{Ga}[b]
M06	+2.8	+1.3	+4.1	+3.1
ωB97xD	+6.3	+4.3	+5.5	+3.9
B97D	+13.0	+11.7	+11.4	+15.8

As outlined above, in the case of the Ru-In complexes, **71** is significantly more stable than **77_In** which is consistent with the experimental observations. However, for the Ru-Ga complexes, in most of cases, **71_Ga** is more stable than **77**. It is only with certain functionals and large basis sets that **77** is computed to be slightly more stable than **71_Ga**. Thus, from the thermodynamic point of view, this clearly shows inconsistency with the experimental observations and reveals a problem in the DFT model, as it is not able to correctly describe the relative stability of **77** versus **71_Ga**.

5.5 Conclusions

In conclusion, the Ru-Ga species **77** was characterised as a Ru(0)-Ga(III) complex featuring a direct Ru→Ga bond. A computed mechanism for the formation of **77** shows that transfer of Me from the Ga centre to the Ru centre facilitates the transfer of IPr from the Ru centre to the Ga centre. Reductive elimination of methane followed by the isomerisation steps then produce **77**. The overall energy barrier of this process is computed to be 23.2 kcal/mol (with respect to **67** + $GaMe_3$), related to the reductive coupling step. This energy barrier is consistent with the fact that reaction of **67** with $GaMe_3$ takes 10 days to produce **77**. This implies a qualitative agreement as the reaction with $GaMe_3$ takes much longer than that with $InMe_3$. Surprisingly, it was found that the formation of the Ga congener of the experimentally observed Ru-In complex **71** (**71_Ga**) requires a lower energy barrier than the formation of **77**.

Using different functionals and basis set combinations, the experimentally observed Ru-In species **71** was found to be always more stable than the In congener of the Ru-Ga complex **77**, **77_In**. This indicates the thermodynamic preference for **71** over **77_In**, consistent with the experimental observation. However, in the case of the Ru-Ga complexes, **77** was also found to be less stable than **71_Ga** and it is only with certain functionals and basis set combinations that **77** is slightly more stable than **71_Ga**. This discrepancy between the experimental and computational results reveals a large error in the DFT model. Perhaps, this inadequacy is due to underestimation of the stability of the Ru(0)-Ga(III) species **77** versus Ru(II)-Ga(I) species **71_Ga** which highlights the fact that how well the stabilities of the Ga centre with the oxidation states of 3+ and 1+ are described by DFT. This is however unknown at this time and needs to be addressed in future studies.

Chapter 6 – DFT Studies of Two Cu-Borate Complexes, [(6-Mes)CuHBR$_3$] (R = Et, C_6F_5)

It is well-established that Cu-H species can be employed as mild reducing agents for hydrogenation of unsaturated organic compounds.[171-174] The active species in this process is proposed to be a monomeric Cu-H intermediate.[175-177] Thus, significant attention has been paid to stabilise and isolate such species.[175, 178-180] In this regard, Whittlesey and co-workers isolated two new [(6-Mes)CuHBR$_3$] complexes (R = Et (**111**), C_6F_5 (**112**), 6-Mes: 1,3-bis(2,4,6-trimethylphenyl)-3,4,5,6-tetrahydropyrimidin-1-ylidene).[181]

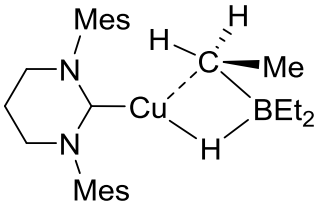

111

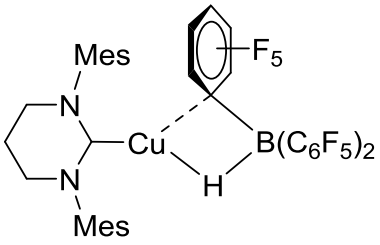

112

Herein, the first section of this chapter provides a literature review on copper hydrides and in particular attempts to synthesize monomeric Cu-H species. The next section then summarizes the experimental results for the synthesis of **111** and **112**. The final sections then describe the computational results to characterise the bonding of **111** and **112**, modelling the structures of **111** and **112** in the gas phase and the crystalline solid state and then the thermodynamic stability of monomeric and dimeric Cu-H species.

6.1 Introduction

The history of copper hydride species can be dated back as early as 1840s.[182] Since that time, copper (I) hydride complexes have been the subject of considerable interest as mild reducing agents in reduction reactions of organic substrates such as alkynes.[176, 183, 184] The first example of an isolated copper hydride complex was the hexameric copper hydride complex **79** which was characterised by Churchill and Osborn in 1971 (Figure 6-1).[185] **79** was synthesised by the reaction of copper alkoxide **78** with triphenylphosphine under H_2 gas. The catalytic reactivity of **79** then was explored by Stryker in 1988. He showed that **79** could be used for the regioselective reduction of α,β-unsaturated carbonyl compounds such as **80**.[186] Later in 1998, Lipschutz used silanes as an alternative source of hydride to enhance the efficiency of the reduction process.[187] Following on from that, in 1999, Buchwald showed that copper hydride species could be used to reduce organic substrates with high enantioselectivity. He treated CuCl with alkenes and PMHS (polymethylhydrosiloxane) as source of hydride in the presence of chiral bidentate phosphine ligands such as **85**.[173]

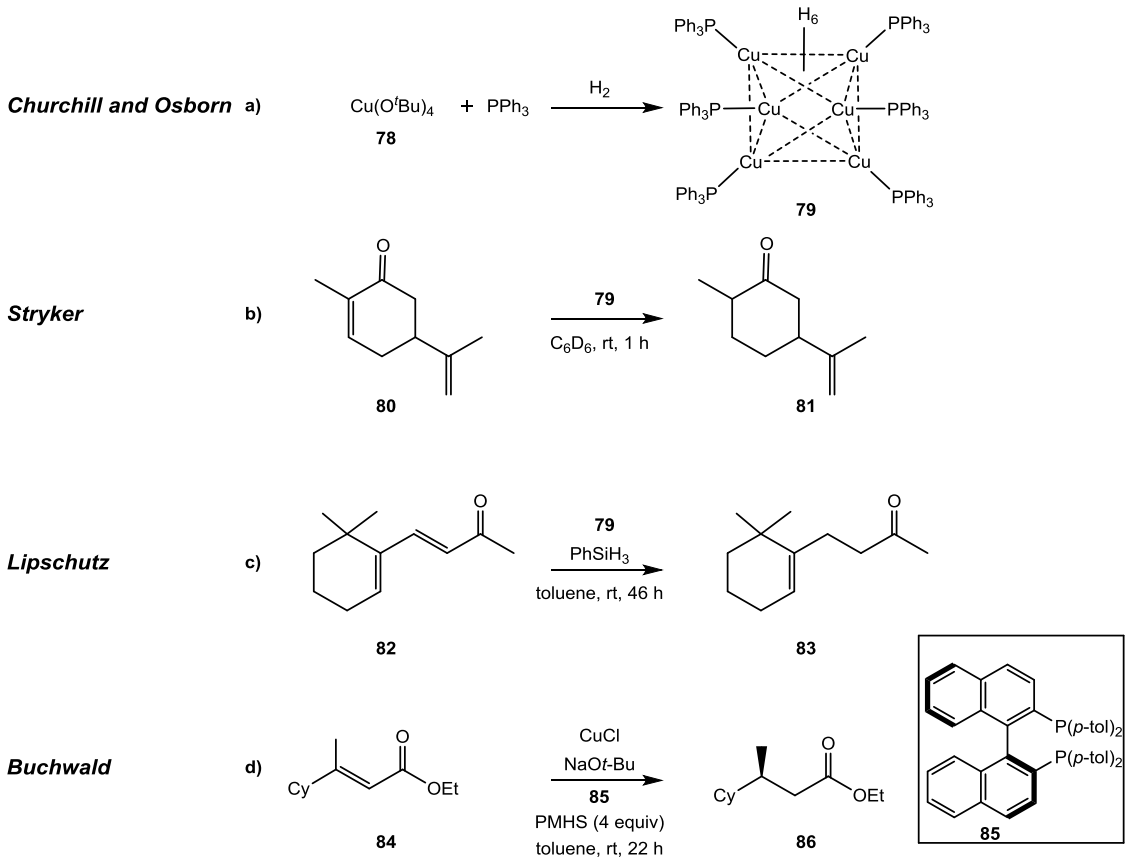

Figure 6-1. Reduction of unsaturated organic compounds with different source of hydrides.

With phosphine ligands, most of the copper hydride complexes were cluster-like structures (i.e. hexameric or pentameric analogues). There were only two isolated copper hydride complexes featuring bidentate and tridentate phosphine ligands; the trinuclear dicationic complex **87**,[188] and dinuclear complex **88**,[189] respectively (Figure 6-2).

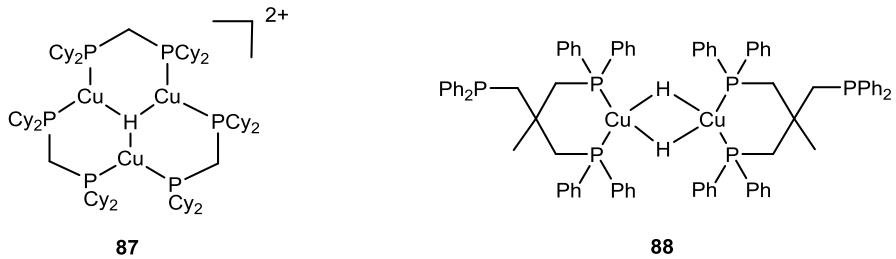

Figure 6-2. Isolated phosphine-supported copper hydride complexes.

6.1.1 Formation of Hydride-Bridged Copper Complexes Supported by Five-Membered NHC Ligands

In the last few years, more attention has been focused on the synthesis of copper hydride complexes with lower nuclearity.[183] This required chemists to consider significant changes in the environment around the copper centre.[190] Therefore, attention turned to changing the supporting ligands coordinated to the metal centre from phosphines to NHCs as their electronic and steric properties can be tuned.[184] This could allow the stabilisation of low-coordinate metal centres.[191, 192]

In 2004, Sadighi and co-workers reported the first isolated five-membered NHC-supported copper hydride complex.[172] They showed that the reaction of [(IPr)Cu(O^{t}Bu)] complex **89** (IPr = 1,3-bis(2,6-diisopropylphenyl)imidazol-2-ylidene) with $(EtO)_3SiH$ could yield the dinuclear copper hydride complex $[(IPr)CuH]_2$, **90** (Figure 6-3). Species **90** was also shown to be stable enough in solution to be characterised by ^{1}H NMR. However, it decomposed after an hour in solution or after several days in the solid form. Sadighi and co-workers demonstrated that upon the reaction of **90** with 3-hexyne, the alkyne inserts into the Cu–H bond to form the alkenyl copper complex **91**, indicating the monomeric copper hydride species could be trapped by the addition of unsaturated organic substrates.

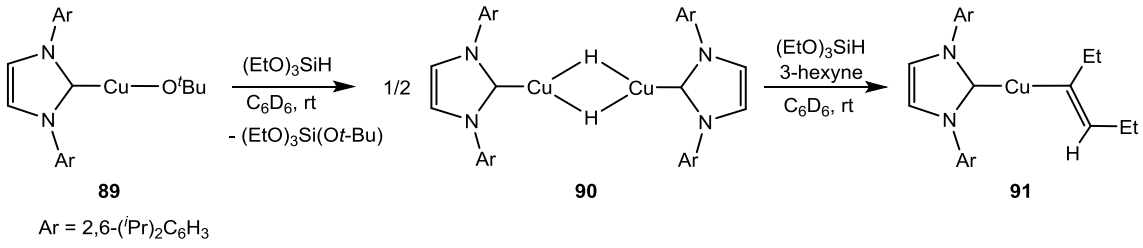

*Figure 6-3. Formation of **90** and its reaction with 3-hexyne to form **91**.*

Nolan and co-workers used a different copper precursor to synthesize the dimeric copper hydride **90**.[174] They reacted the copper precursor **92** with triethoxysilane (Figure 6-4). However, they were only able to characterise **90** in solution by ^{1}H NMR.

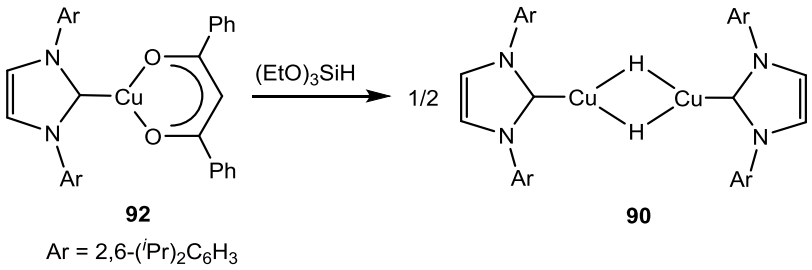

*Figure 6-4. Reaction of copper precursor complex **92** with triethoxysilane.*

Bertrand and co-workers showed that the treatment of [(CAAC^{Cy})CuO^{t}Bu] (CAAC = Cyclic (Alkyl)(Amino)Carbene)) complex **93** with HLiBEt$_3$ as source of hydride affords the dinuclear copper hydride species **94** (Figure 6-5).[178] **94** is found to be stable in solution and persisted for weeks in the solid form at room temperature.

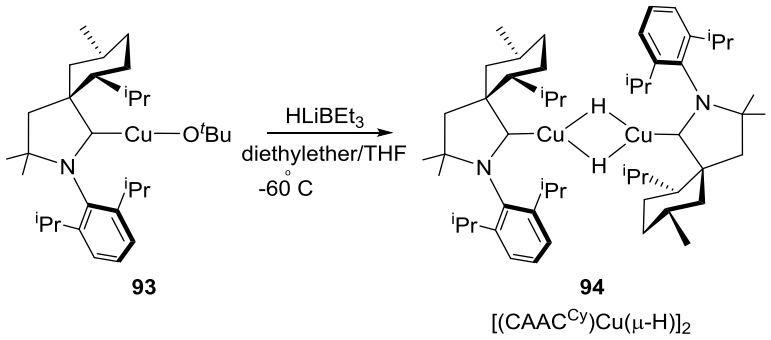

*Figure 6-5. The reaction of copper alkoxide precursor **93** with HLiBEt$_3$ to afford **94**.*

It can be expected that in solution, **95** can dissociate into the monomeric copper hydride species **96** (Figure 6-6). However, the monomer is not stable enough to be isolated or characterised. One might assume that the coordination of Lewis basic ligands such as phosphines to the Cu atom might stabilise the monomer to form the tricoordinate copper complex **97**. However, as shown by Bertrand and co-workers, reaction with phosphines induces hydride transfer onto the carbenic position of CAAC^{Cy} and forms **98**.[178] The authors suggested that the coordination of Lewis base ligands to the Cu centre in **96** can make it even more electron rich. As the result, this makes the monomeric copper hydride **96** more reactive.

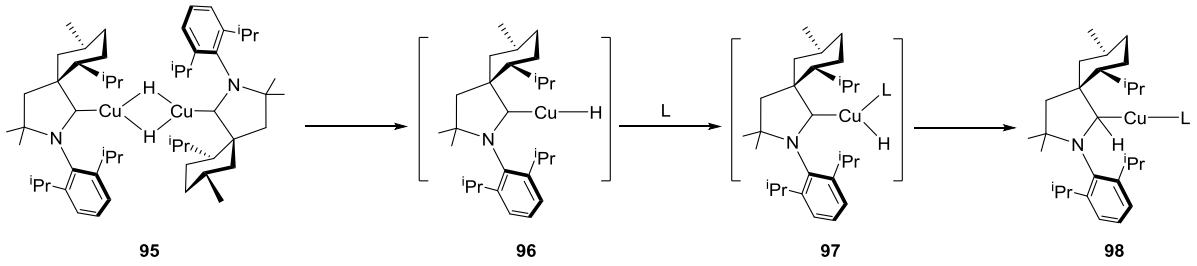

*Figure 6-6. Reaction of the dimeric Cu-hydride species **95** with L (L = PCy_3, PMe_3).*

In the course of the attempts to synthesize and isolate a monomeric copper hydride complex, Bertrand and co-workers used a less sterically demanding CAAC-supported copper precursor **99** (Figure 6-7).[193] They reported that upon the reaction of **99** with $NaBH_4$, halide abstraction occurs to give the copper(I) complex **100** which is the first example of a Cu-BH_4 complex. This suggests that the borate moiety might stabilise the mononuclear copper(I) moiety and so avoid aggregation.

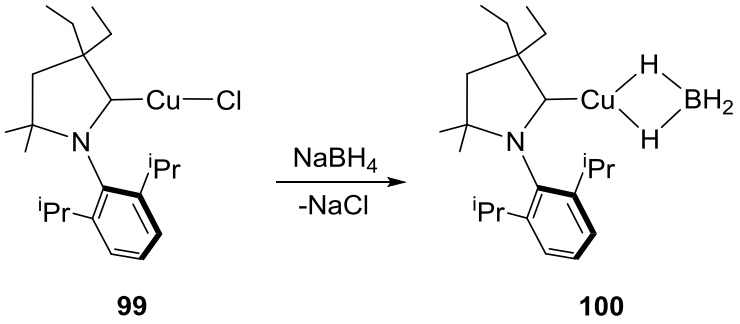

*Figure 6-7. The reaction of Cu precursor **99** with $NaBH_4$ to give **100**.*

The experimental results discussed above show that the reaction of copper complexes featuring five-membered CAAC ligands with a source of hydride can yield two different types of copper complexes: **1**) Dinuclear copper hydride complexes (e.g. **95**) and **2**) Mononuclear copper complexes featuring a κ^2–BH_4 ligand (e.g. **100**). However, with phosphine-supported copper complexes, copper hydride complexes with higher nuclearity can also be formed (e.g. **87** and **88**). This therefore suggests that a subtle difference in the supporting ligand can yield copper complexes with different nuclearities.

6.1.2 Formation of Hydride-Bridged Cu Complexes Supported by Ring Expanded NHC Ligands

Recently, Whittlesey and co-workers reported the reaction of the [(6MesDAC)Cu-O^{t}Bu] (DAC = diamidocarbene), **101**, with Et_3SiH to generate the dinuclear copper complex **103** (Figure 6-8).[177] **103** bears a bridging alkoxide ligand between the Cu centres and one hydrogen at the carbenic carbon of the NHC. A similar process occurs when a Lewis base such as P(*p*-tolyl)$_3$ is added to the reaction mixture (**101** + Et_3SiH), forming the mononuclear species **104**.

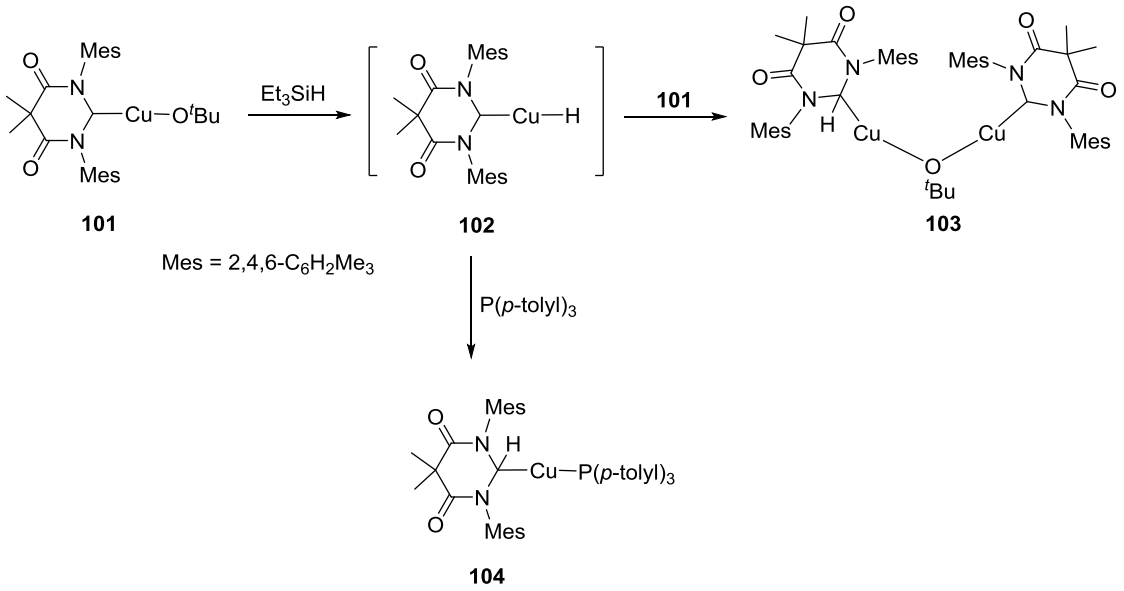

*Figure 6-8. Trapping of the monomeric copper hydride **102** with copper alkoxide species **101** and P(p-tolyl)$_3$.*

In contrast to the reaction of [(6-MesDAC)Cu-O^{t}Bu] (**101**) with Et_3SiH, reaction of [(6-Mes)Cu-O^{t}Bu] (**105**) with Et_3SiH produces the dimeric copper hydride species **106**.[177] **106** can however be dissociated to a monomeric copper hydride species and react with phenylpropyne to give the copper alkenyl species **107**. Interestingly, upon the addition of ^{t}BuOH to the reaction mixture, semi-reduction of the phenylpropyne occurs via the protonolysis of **107** to give *E*- and *Z*-isomers of propenylbenzene while the catalyst is regenerated. In addition, **105** also proved to be a precatalyst for hydrosilylation of ketones.[177]

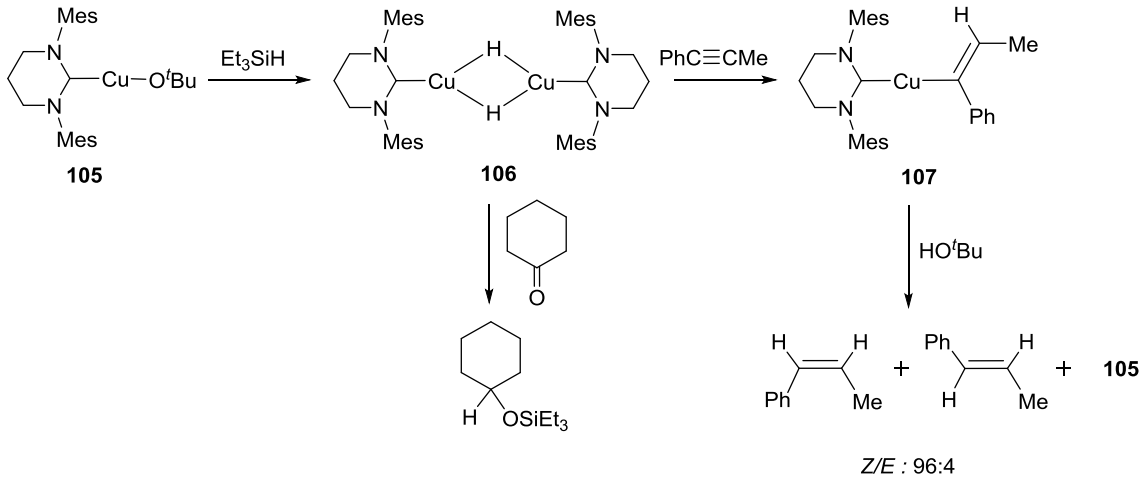

*Figure 6-9. Semi-reduction of phenylpropyne and hydrosilylation of cyclohexanone by copper complex **106**.*

In further attempts to isolate a monomeric copper hydride complex, Sadighi and co-workers used the Cu-O^{t}Bu supported by six and seven-membered NHCs, **108a** and **108b**.[175] As shown in Figure 6-10, upon the addition of [LCuO^{t}Bu] complex **108** (L = 6/7 Dipp) to HBpin (HBpin = 4,4,5,5-tetramethyl-1,3,2-dioxaborolane), the dimeric copper hydride complex **109** is formed. It is interesting to note that upon the reaction of **109** with CO_2 at room temperature, the copper carboxylate species **110** is formed, showing **109** can be dissociated into a monomeric copper hydride that then reacts with CO_2.

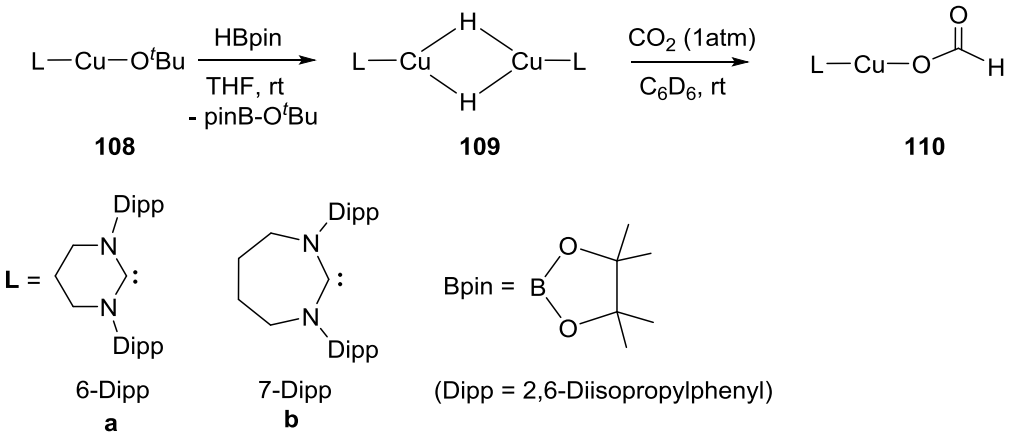

*Figure 6-10. The reaction of copper alkoxide **108** with HBpin forming the dimeric copper hydride **109** and reaction of **109** with CO_2 forming new copper carboxylate species **110**.*

As outlined above, significant attempts have been made to isolate the monomeric Cu-H species. However, the monomeric Cu-H species has been only characterised in situ or trapped by unsaturated organic compounds. Whittlesey and co-workers also investigated the reaction of the Cu-alkoxide species **105** with different source of hydrides. The experimental results are summarized in the next section.

6.2 Experimental Background

In an attempt to synthesize a monomeric Cu-H complex, Whittlesey and co-workers treated the copper alkoxide **105** with the "super-hydride" reagent, $LiHBEt_3$, in THF at 178 K (Figure 6-11). This reaction however resulted in the generation of complex **111** characterised crystallographically as [(6-Mes)CuHBEt$_3$].

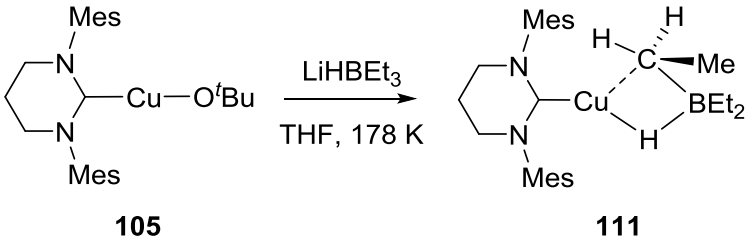

105 **111**

*Figure 6-11. Formation of **111** from the reaction of **105** with LiHBEt$_3$.*

As previously reported by Whittlesey and co-workers, treatment of [(6-Mes)CuO^{t}Bu], **105**, with Et$_3$SiH forms the dimeric copper hydride complex **106** (Figure 6-12).[177] **106** can be dissociated to the monomeric Cu-H species in solution and subsequently can be trapped by reaction with phenylpropyne.

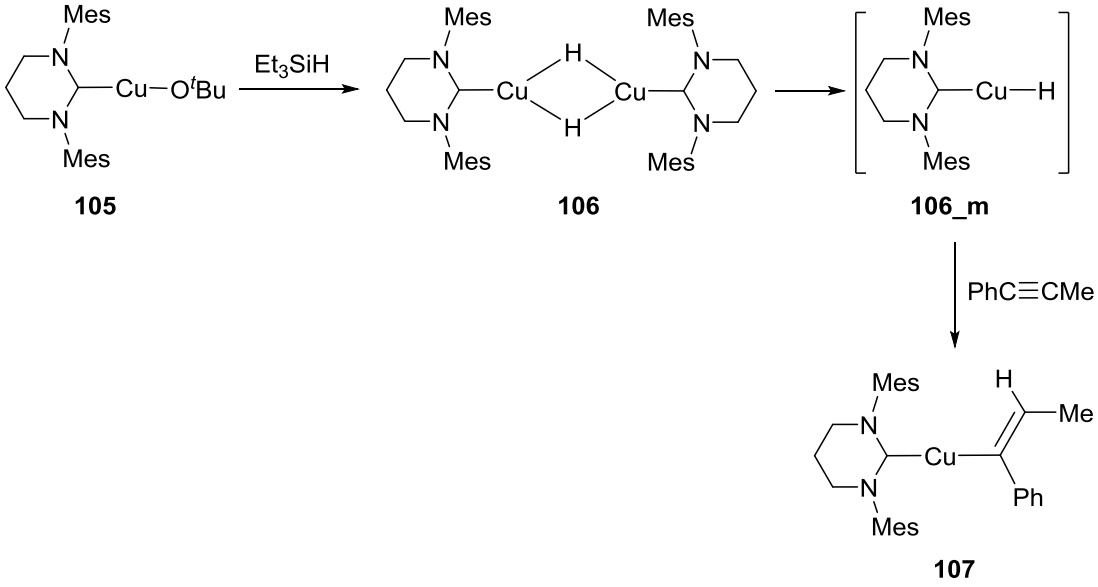

105 **106** **106_m** **107**

*Figure 6-12. Formation of the dimeric Cu-H species **105** and trapping the monomer **106_m** with alkyne.*

Thus, in order to trap the Cu-H intermediate **106_m**, **106** was reacted with HSiR$_3$ (R$_3$ = Et$_3$ or PhMe$_2$) in the presence of B(C$_6$F$_5$)$_3$ in C$_6$D$_6$ at room temperature (Figure 6-13). This reaction led to the formation of the analogue of **111**, complex **112**, characterised crystallographically as [(6-Mes)CuHB(C$_6$F$_5$)$_3$].

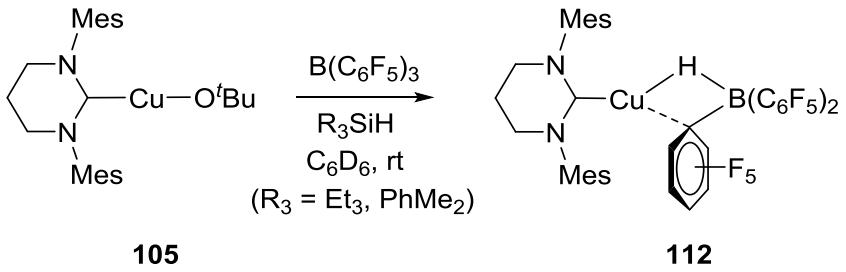

*Figure 6-13. Formation of [(6-Mes)CuHB(C_6F_5)$_3$], **112**, by reaction of [(6-Mes)CuO^{t}Bu], **105**, with R_3SiH (R = Et_3 and $PhMe_2$) in the presence of B(C_6F_5)$_3$.*

The X-ray molecular structure of **112** shows a hydride (H(1)) in the bridging position between the Cu and B centres (Cu···H(1) = 1.56(3) Å B···H(1) = 1.22(3) Å, Figure 6-14). **111** also exhibits close contacts between the Cu centre and one of the ethyl (C(2)) substituents (Cu···C(2) = 2.619(3) Å, and Cu···C(3) = 3.677 Å, Cu···C(4) = 2.871 Å).

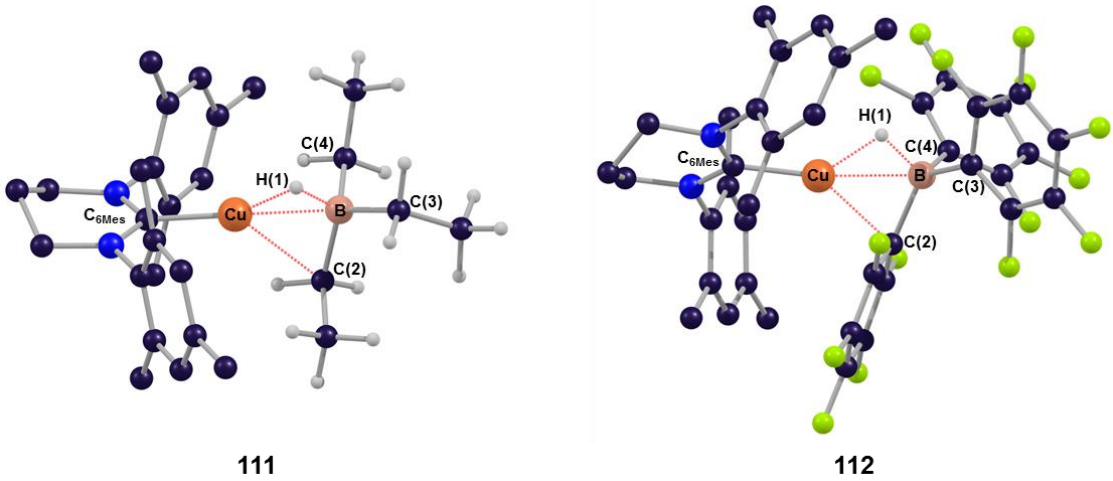

*Figure 6-14. Molecular structures of **111** and **112** with labelling scheme on selected atoms.*

Similar to **111**, the X-ray molecular structure of **112** bears a hydride (H(1)) situated in a bridging position between the Cu and B centres (Cu···H(1) = 1.58(2) Å and B···H(1) = 1.16(2) Å, Figure 6-14). Additionally, **112** features a short Cu···C contact to one of the C_6F_5 rings (Cu···C(2) = 2.2183(17) Å). Moreover, the B–C(2) bond length is 1.657(3) Å which is slightly longer relative the other B–C bonds (B–C(3) = 1.624(3) Å and B–C(4) = 1.624(3) Å).

As shown in Figure 6-15, the nature of the interaction in the {$CuHBR_3$} unit in **111** and **112** can be described with various Lewis structures. In type **I**, the B centre acts as a Lewis acid moiety and is stablised by electron donation from the Cu–H bond. This can occur the other way around when the B–H bond stabilises the cationic Cu moiety, type **II**. There is another scenario in which the B centre acts as a Z-type ligand and accepts electron density from the Cu moiety, type **III**. In this type, the terminal Cu–H bond does not interact with the BR_3 moiety.

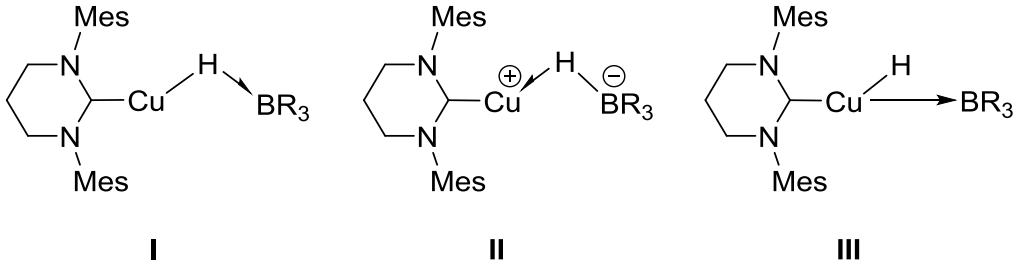

*Figure 6-15. Different Lewis structures to describe the {$CuHBR_3$} moiety in **111** and **112**.*

6.3 Aims

As outlined above, the structure of {$CuHBR_3$} in **111** and **112** can be represented by different Lewis structures **I**, **II** and **III**. In addition, **111** and **112** may also feature some other potential intramolecular interactions such as an agostic interaction in **111** and a Cu···C(2) interaction in **112**. Herein, with the aid of DFT calculations, a particular focus was given to study the bonding of **111** and **112**. It should be noted that reaction of [LCu-O^{t}Bu] with different hydride sources can result in a dimeric copper hydride or a copper borate complex. Thus, the thermodynamic stability of the dimer species versus monomer species ([LCu-H] and [LCu-(HBR_3)]) was also investigated.

6.4 Computational Details

For the molecular calculations, Gaussian 09 (Revision D.01)[160] was used to optimise the structures of the copper species **111** and **112** with a broad range of DFT functionals. The SDD effective core potential and associated basis set[10] were chosen to describe Cu while

6-31G** basis sets were used for the other atoms (BS1).[7, 136] Frequency calculations were carried out at the same level of theory as those for the structural optimisation. All stationary points were fully characterised via analytical frequency calculations as true minima (no imaginary eigenvalues).

QTAIM[162] (AIMALL program) and NBO[163] (NBO 6.010) calculations were carried out on **111** and **112** with the structures based on the experimental heavy atom positions derived from the X-ray structure of **111** and **112** with the H atoms positions being optimized with BP86[161]/BS1. These optimised structures along with the optimised structures of [(6-Mes)CuH], $[(6\text{-Mes})Cu]^+$, BR_3 and $[HBR_3]^-$ (R = Et and C_6F_5) were also used for the NBO and QTAIM charge analysis.

The functional testing on the molecular structures of **111** and **112** includes GGA functionals (BP86, PBE[166] and BLYP[4]), hybrid-GGA functionals (ωB97xD[167] and B3LYP[4, 6, 168]), a meta-GGA functional (TPSS[169]) and a Minnesota functional (M06[170]). Dispersion corrections also applied using Grimme's D3 parameter set[22] with BP86, B3LYP, BLYP, PBE and TPSS functionals (i.e. those functionals that do not already include a treatment of dispersion effects). The computed free energies (in Table 6-6) are based on gas-phase free energies optimised with BP8/BS1, corrected for dispersion (Grimme's D3 parameter set) and THF solvent (PCM[14] approach).

Full solid-state optimisations of **111** and **112** were performed using Kohn-Sham DFT level of theory within the Gaussian plane wave (GPW) formalism as implemented in the Quickstep[194] module of the CP2K program package (versions 2.5 and 3.0).[195] Double-ζ valence plus polarisation basis sets in their short-range variant (DZVPMOLOPT-SR-GTH)[196] were employed for all atom types (Cu, B, C, N, F, H). Goedecker-Teter-Hutter (GTH) pseudopotentials were used to describe the interaction between the core electrons and the valence shell (Cu: 11, B: 3, C: 4, N: 5, F: 7, H: 1) electrons.[197-199] The GGA functionals BP86, PBE and BLYP were used in geometry optimisations of the full solid state structure of **111** and **112** with and without Grimme's dispersion under periodic boundary conditions using the experimentally determined unit cell parameters. Based on the test calculations shown in Figure **6-16**, the geometries were converged at the plane wave (PW) energy cutoff of 500 Ry. Therefore, the cutoff value of 500 Ry was set in the optimisation calculations. Optimised stationary points located with the PBE and PBE(D3) functionals were characterised by analysis of their numerical second derivatives with a

displacement of 0.01 Bohr. Minima are confirmed through the absence of imaginary eigenvalues of the Hessian matrix.

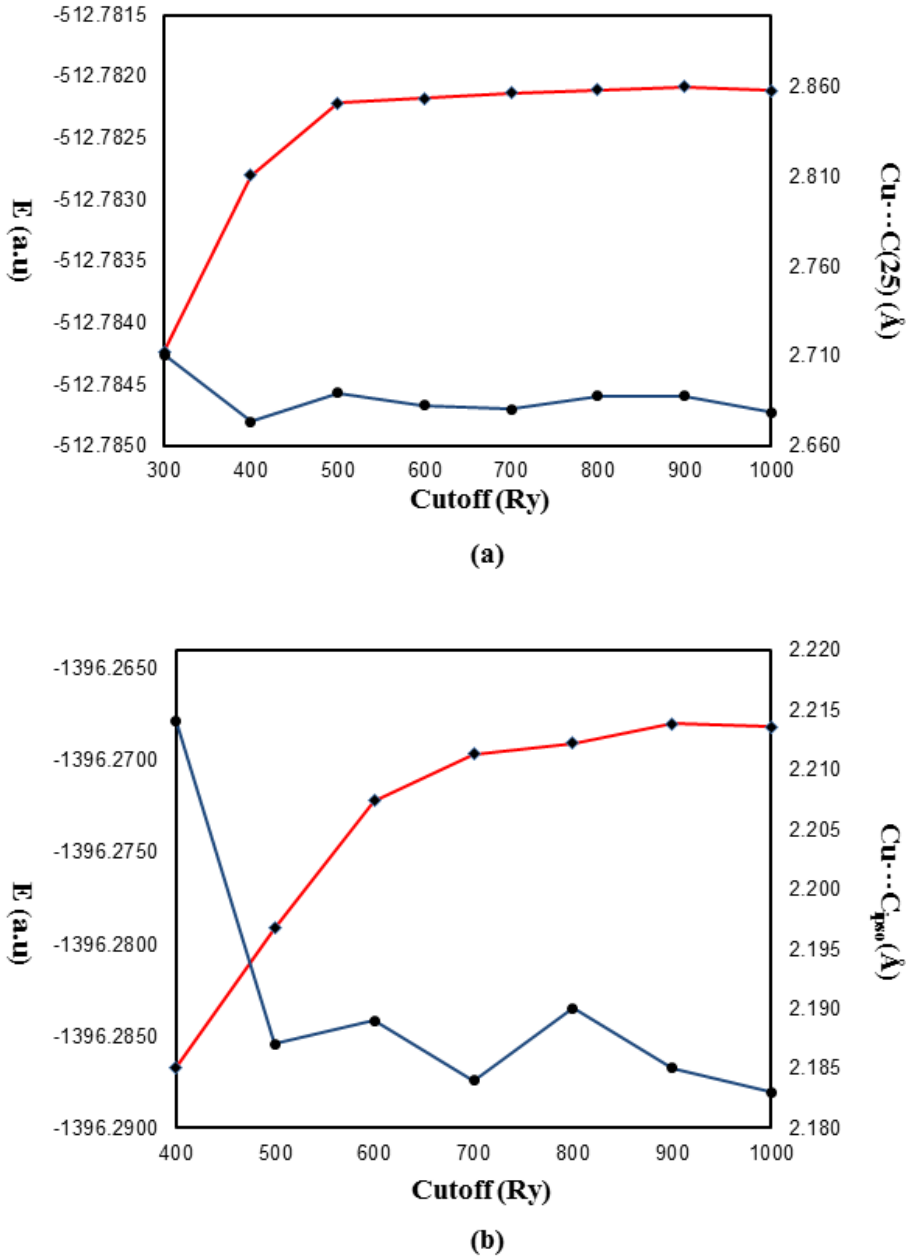

*Figure 6-16. Plots of energy (red) and Cu···C distance (blue) with respect to the auxiliary plane wave basis set cutoff for a) species **111** and b) species **112**.*

6.5 Results and Discussion

6.5.1 Molecular Optimisation of Structures 111 and 112

Table 6-1 presents the key structural parameters of the experimental and computed geometries of **111** and **112** (see Figure 6-14 for labelling scheme).

In **111** and **112**, the Cu–C_{6Mes}, B–C(2) and Cu···B distances are well reproduced by calculations. However, in all the cases, the distances involving hydrogen atoms positions are overestimated in the computed geometries. This is however consistent with the fact that the positions of hydrogens atoms in X-ray crystal structures are not well defined. Similar to the experimental geometries of **111** and **112**, the computed Cu···H(1) distance is longer than the computed B···H(1) distance. Going from **111** to **112**, it can be seen that the B···H(1) distance becomes slightly shorter and as the result, the Cu···H(1) distance gets longer. This can be due to the electron withdrawing nature of the C_6F_5 groups connected to the B centre in **112** which results in a more electropositive B centre compared with that in **111** and therefore makes the B···H(1) shorter. In **111**, the computed Cu···C(2) distance is underestimated by 0.149 Å while in **112**, it is well reproduced by the calculations. Apart from this discrepancy, there is a good agreement between the experimental and computational geometries of both **111** and **112**.

*Table 6-1. Selected experimental and computed structural parameters of **111** and **112**.*

111	**Cu–C_{6Mes}**	**Cu···C(2)**	**B–C(2)**	**Cu···B**	**Cu···H(1)**	**B···H(1)**
Exp.	1.908(3)	2.619(3)	1.627	2.282(3)	1.56(3)	1.22(3)
BP86	1.900	2.470	1.671	2.243	1.602	1.361
112	**Cu-C_{6Mes}**	**Cu···C(2)**	**B–C(2)**	**Cu···B**	**Cu···H(1)**	**B···H(1)**
Exp.	1.8991(18)	2.2183(17)	1.657(3)	2.267(2)	1.58(2)	1.16 (2)
BP86	1.912	2.222	1.659	2.295	1.660	1.289

6.5.2 Characterization of 111 and 112 by QTAIM

Figure 6-17 displays the 2D contour plot of the electron density in the {Cu/H/B} plane of **111** and **112**. The QTAIM molecular graph of **111** exhibits bond paths between the H(1) centre with both Cu and B centres, showing the hydride H(1) interacts with both Cu and B centres. The ρ(r) at the Cu–H(1) BCP is 0.092 which is slightly smaller than the ρ(r) at the B–H(1) BCP (0.105). This therefore indicates that the hydride H(1) interacts with the B centre more strongly than the Cu centre. This trend is also consistent with the more negative value of H(r) at the B–H(1) BCP (-0.090) relative to the Cu–H(1) BCP (-0.022), showing a stronger covalent interaction in the former. Interestingly, no bond path is seen between the Cu and B centres, showing no direct Cu–B interaction. This therefore rules out the Lewis structure **III** (Figure 6-15). Furthermore, no bond path is seen between the Cu and H(2) centres. This therefore shows no agostic interaction with the C(2)–H bond.

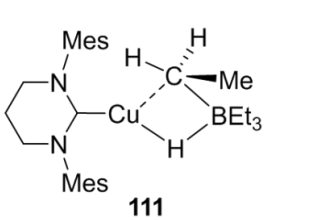

111

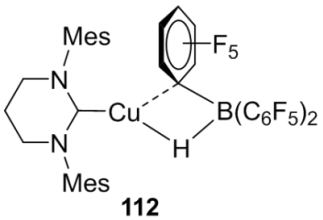

112

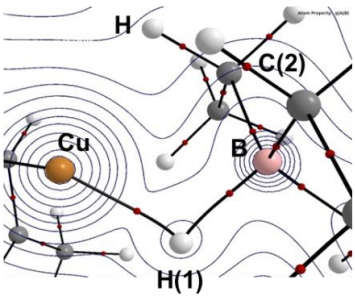

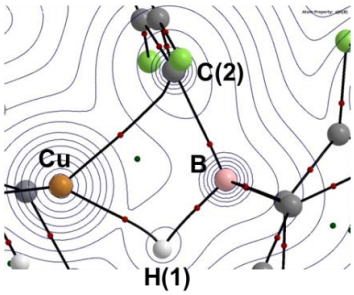

BCP	ρ(r)/eA^{-3}	$\nabla^2\rho$ (r)/eA^{-5}	ε	H(r)/a.u.
Cu–H(1)	0.092	+0.283	0.208	-0.022
B–H(1)	0.105	+0.014	0.286	-0.090

BCP	ρ(r)/eA^{-3}	$\nabla^2\rho$ (r)/eA^{-5}	ε	H(r)/a.u.
Cu–H(1)	0.083	+0.291	0.330	-0.016
B–H(1)	0.135	-0.115	0.014	-0.131
Cu–C(2)	0.055	+0.181	1.016	-0.006

*Figure 6-17. Detail of the QTAIM molecular graph for **111** and **112**. Bond critical points (BCPs) and RCPs are shown with small red and green spheres, respectively.*

Similar to **111**, **112** exhibits BCPs between the H(1) and the B and Cu centres in which the former has a slightly larger ρ(r) (Cu–H(1): 0.083 and B–H(1): 0.135). However

compared to **111**, **112** features a slightly larger ρ(r) at the B−H(1) BCP and hence a smaller ρ(r) at the Cu−H(1) BCP. This shows that the B–H(1) interaction in **112** is stronger than that in **111** while the Cu–H(1) interaction in **111** is stronger than in **112**. This is mainly due to the fact that the B centre in **112** is more electron deficient than that in **111** and therefore, it gives a stronger B–H(1) interaction. This is also shown by the more negative H(r) value at the B–H(1) BCP than the Cu–H(1) BCP. Similar to **111**, in **112**, no BCP can be seen between the Cu and B centre. Additionally, **112** exhibits a bond path between the Cu and C(2) centres. This shows the presence of an interaction between the Cu and C(2) centres which encloses an RCP in the {Cu/H(1)B/C(2)} unit. The Cu−C(2) BCP has a lower ρ(r) than the Cu–H(1) BCP, suggesting a weaker interaction in the former. The H(r) associated with the Cu–C(2) BCP is a small negative value, indicating a covalent interaction between the corresponding atoms. The smaller H(r) value of the Cu–C(2) BCP relative to the Cu–H(1) BCP shows a weaker interaction in the former, consistent with the trend of the ρ(r) values.

It should be noted that due to the weaker B–H(1) interaction in **111** than **112** and hence stronger Cu–H(1) interaction in the former, the hydride H(1) is more evenly shared between the Cu and B centres in **111**. Thus, from **112** to **111**, as the hydride H(1) becomes more evenly shared, the ellipticity of the B–H(1) BCP becomes higher. This trends is reversed for the Cu–H(1) BCP.

6.5.3 NBO Analysis of 111 and 112

NBO calculations were performed on H-atom optimised geometries of **111** and **112** to gain more insight into the nature of interaction between the bridging hydride and the Cu and B centres. As shown in Figure 6-18, in both **111** and **112**, NBO identifies a donor-acceptor interaction between the B–H(1) bonding orbital and the vacant Cu 4s orbital. This therefore indicates that the cationic Cu fragment is stabilised by the borate fragment and rules out Lewis structures **I** and **III** and confirms Lewis structure **II** for **111** and **112** (Figure 6-15). In **111**, the interaction energy between these two NBOs is computed to be 67.1 kcal/mol which becomes notably lower in **112** to 42.9 kcal/mol. This shows that in **111**, the interaction between the B–H bonding orbital and the Cu vacant orbital is stronger than in **112**.

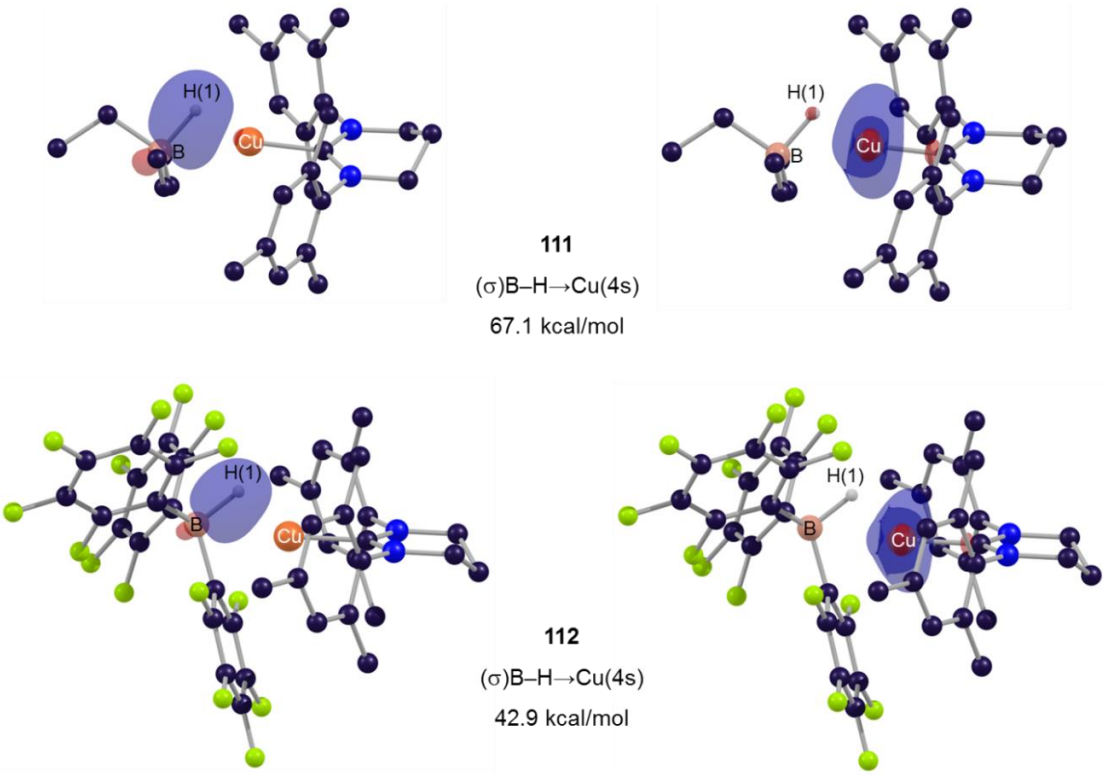

*Figure 6-18. NBO donor-acceptor interactions computed for **111** and **112**.*

Consistent with the QTAIM results, NBO analysis found no C–H agostic interaction in **111** while in **112**, a donor-acceptor interaction between the B–C(2) bonding orbital and the vacant orbital of Cu was identified with a small interaction energy of 7.1 kcal/mol (Figure 6-19). Additionally, another weak interaction was also characterised between the C(2)–C_{ortho} bonding orbital and the Cu vacant orbital with small interaction energy of 7.9 kcal/mol.

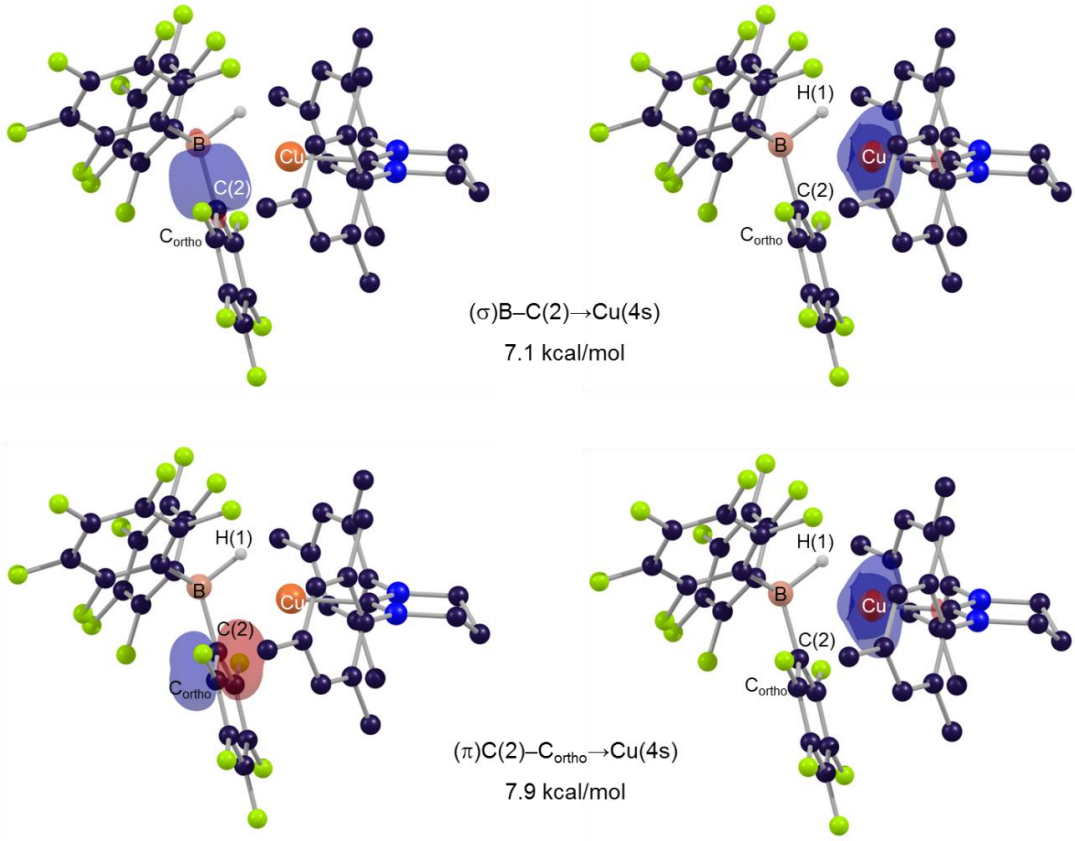

*Figure 6-19. NBO Donor-acceptor interaction between the B–C(2) and C(2)–C_{ortho} bonding orbitals with Cu vacant orbital in **112**.*

6.5.4 NBO and QTAIM Charge Distribution Analyses of 111 and 112

As outlined above, NBO analysis shows that **111** and **112** can be described as cationic Cu complexes which accept electron density from the borate moieties. This can be further assessed by the charge distribution analysis with NBO and QTAIM. In this regard, **111** and **112** were firstly fragmented into a series of neutral ([(6-Mes)Cu-H], BR_3 (R = Et, C_6F_5)), cationic ($[(6\text{-Mes})Cu]^+$) and anionic moieties ($[HBR_3]^-$). The free species then were fully optimised and NBO and QTAIM charge distribution analysis were performed on these species. As listed in Table 6-2, the NBO charge of the Cu atom in **111** and **112** is computed to be +0.62 and +0.70, respectively. Going to the free copper species, the charge of the Cu atoms in $[(6\text{-Mes})Cu]^+$ and [(6-Mes)CuH] species are +0.59 and +0.29, respectively. Thus, the charge of the Cu atom in **111** and **112** more closely resembles that in the free cationic species than the neutral species.

*Table 6-2. Computed atomic charges (QTAIM charges and NBO charges) for **111** and **112** with the selected comparator species.*

	B		Cu		H(1)	
Species	NBO	QTAIM	NBO	QTAIM	NBO	QTAIM
[(6-Mes)CuHBEt$_3$] (111)	+0.21	+1.86	+0.62	+0.47	-0.10	-0.50
[(6-Mes)Cu]$^+$	--	--	+0.59	+0.48	--	--
[HBEt$_3$]$^-$	+0.18	+1.92	--	--	-0.07	-0.66
[(6-Mes)CuH]	--	--	+0.29	+0.29	-0.41	-0.43
BEt$_3$	+0.94	+2.02	--	--	--	--
[(6-Mes)CuHB(C$_6$F$_5$)$_3$] (112)	+0.09	+1.84	+0.70	+0.52	-0.03	-0.49
[HB(C$_6$F$_5$)$_3$]$^-$	+0.07	+1.87	--	--	+0.04	-0.56
B(C$_6$F$_5$)$_3$	+0.78	+1.97	--	--	--	--

The NBO charge of the B atom in **111** is +0.21 which is much closer to the free borate moiety (+0.18) rather than the free borane moiety (+0.94). Similar to **111**, the NBO charge of the B atom in **112** (+0.09) more resembles the charge of the B atom in the free borate species (+0.07) than the borane moiety (+0.78).

Moreover, the NBO charges of the H(1) atoms in **111** and **112** are computed to be -0.10 and -0.03, respectively. These values are closer to those in the borate species, $[HBEt_3]^-$ (H(1) = -0.07) and $[HB(C_6F_6)_3]^-$ (H(1) = +0.04), than the copper hydride species (H(1) = -0.41). This therefore indicates that **111** and **112** are Cu-borate species, consistent with QTAIM and NBO donor-acceptor analysis.

It should also be noted that compared with NBO charges, different absolute charges are computed with QTAIM. However, the QTAIM charges still show similar trend to the NBO charges (Table 6-2).

6.5.5 Impact of Chemical Model and Methodology on the Optimised Geometries of 111 and 112

As discussed in section **6.5.1**, with the BP86 functional, apart from the Cu···C(2) distance and the hydrogen atoms positions, there is a good agreement between the computed and

the experimental geometries of **111**. A range of functionals were therefore tested to assess whether this result was functional dependent. Thus, the molecular geometries of **111** and **112** were optimised using different functionals including GGA (BP86, PBE, BLYP), meta-GGA (M06 and TPSS) and hybrid-GGA (B3LYP and ωB97xD) functionals.

The molecular geometry can also be sensitive to the inclusion of dispersion. This can be specifically be important when non-covalent interactions are significant especially in bulky structures. Thus, to assess the effect of dispersion on the geometries of **111** and **112**, the molecular geometries were fully optimised with and without empirical dispersion correction. This however was not considered for those functionals which do have a treatment of dispersion (ωB97xD and M06).

As shown in Table 6-3, in **111**, with different types of functionals, the computed Cu···C(2) distance has a large range of variation, from 2.416 Å to 2.820 Å (experimental Cu···C(2) = 2.619(3) Å). The computed Cu···B distances also shows a range from 2.186 Å to 2.383 Å (experimental Cu···B = 2.282(3) Å). In **112**, the computed Cu···C(2) distances change from 2.142 Å to 2.444 Å and this compares with the experimentally determined distance of 2.2183(17) Å. The computed Cu···B distances vary from 2.258 Å to 2.383Å (experimental Cu···B = 2.267(2) Å). However, in both **111** and **112**, the computed Cu–C_{6Mes} bond distances shows a very small range of variations (**111**: 1.885Å to 1.932 Å, **112**: 1.885Å to 1.932 Å). This therefore indicates that the structures of {$CuHBR_3$} units in **111** and **112** are very sensitive to the functional choice whereas the functional type has a very small effect on the Cu–C_{6Mes} bond distances. This can related to the fact that the former features weak interactions while the latter is a strong interaction.

*Table 6-3. Selected computed interatomic distances (Å) for **111** and **112** modelled as an isolated molecular species and optimised with various functionals using the Gaussian program.*

111				**112**		
Method	**Cu–C_{6Mes}**	**Cu···C(2)**	**Cu···B**	**Cu–C_{6Mes}**	**Cu···C(2)**	**Cu···B**
Experiment	1.908(3)	2.619(3)	2.282(3)	1.8991(18)	2.2183(17)	2.267(2)
BP86	1.900	2.470	2.243	1.912	2.222	2.295
BP86(D3)	1.885	2.435	2.191	1.891	2.142	2.258
PBE	1.899	2.449	2.216	1.912	2.206	2.290
PBE(D3)	1.891	2.409	2.186	1.898	2.144	2.266
B3LYP	1.932	2.734	2.391	1.932	2.463	2.383
B3LYP(D3)	1.920	2.701	2.320	1.912	2.278	2.304
BLYP	1.925	2.820	2.464	1.926	2.444	2.380
BLYP(D3)	1.911	2.733	2.339	1.905	2.256	2.301
TPSS	1.904	2.470	2.235	1.921	2.236	2.317
TPSS(D3)	1.892	2.416	2.195	1.900	2.143	2.281
ωB97xD	1.914	2.513	2.225	1.911	2.190	2.274
M06	1.916	2.558	2.236	1.914	2.166	2.291

Figure 6-20 and Figure 6-21 display the deviation of the Cu···B and Cu···C(2) distances from those in the experimental structures in **111** and **112**, respectively.

For **111**, BP86 provides an excellent agreement for the Cu···B distance with the deviation of 0.039 Å. However, it considerably underestimates the Cu···C(2) distance by 0.149 Å. With BP86(D3), the Cu···B and Cu···C(2) distances become slightly shorter and the discrepancy with experiment increases. The PBE and TPSS functionals result in a slightly poorer agreement compared with the BP86 functional and dispersion again shortens these distances. Going to the B3LYP functional, both Cu···B and Cu···C(2) distances are overestimated with the high values of deviation, 0.109 Å and 0.115 Å, respectively. Interestingly, adding the dispersion correction term shortens the Cu···B and Cu···C(2) distances. This therefore improves the agreement. Similar to B3LYP, BLYP also

overestimates the Cu···B and Cu···C(2) distances with even higher values of deviation, 0.182 Å and 0.201 Å, respectively. They again become shorter with the inclusion of dispersion and this results in a much better agreement. However, this improvement is probably related to the cancellation of error. With dispersion-included functionals, ωB97xD and M06, both Cu···B and Cu···C(2) distances are slightly underestimated. Of all the functionals in the molecular calculations, M06 gives the best overall result with both Cu···B and Cu···C(2) being underestimated by only 0.046 Å and 0.061 Å, respectively.

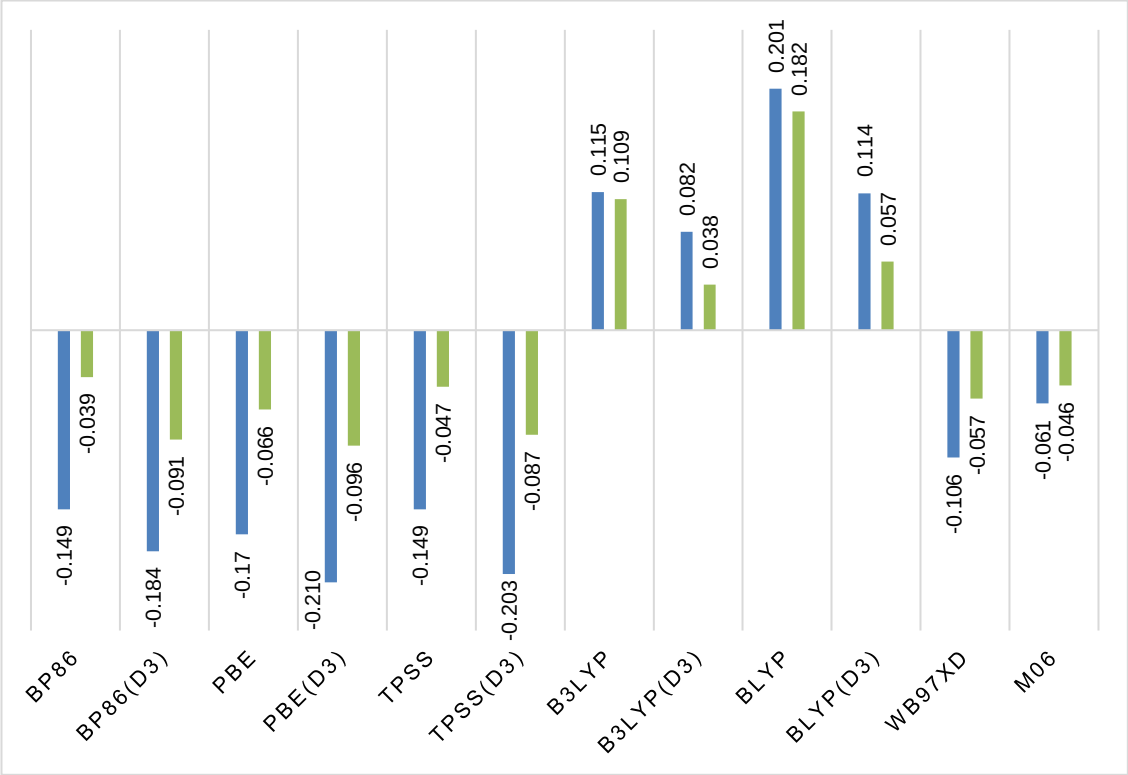

*Figure 6-20. Cu···C(2) (blue bars) and Cu···B (green bars) distances in **111** computed with various functionals and displayed as deviations from the experimental values of 2.283(3) Å and 2.619(3) Å, respectively. Calculations employed the isolated molecule optimised with the Gaussian program.*

Figure 6-21 displays the deviation of the computed Cu···B and Cu···C(2) distances from the experimentally determined geometry of **112**. With BP86, it can be seen that the Cu···B and Cu···C(2) distances are well reproduced by calculations with small deviation of 0.028 Å and 0.004 Å, respectively. Similar to BP86, PBE gives a good agreement for both the

Cu···B and Cu···C(2) distances with deviations of 0.023 Å and 0.012 Å, respectively. However, both B3LYP and BLYP functionals overestimate the Cu···C(2) distance significantly with high discrepancies of 0.245 Å and 0.226 Å, respectively. B3LYP and BLYP also overestimate the Cu···B distance with a fairly similar value of deviation (0.116 Å and 0.113 Å, respectively). Interestingly, similar to **111**, in **112**, dispersion correction makes the Cu···B and Cu···C(2) distances always shorter which can either improve or worsen the agreement. For M06, the Cu···C(2) distance is slightly overestimated by 0.024 Å, and the Cu···C(2) distance is also slightly underestimated by 0.052 Å. With very slight overestimation of Cu···B distance and slight underestimation of Cu···C(2) distance, ωB97xD provides the best agreement among the functionals used.

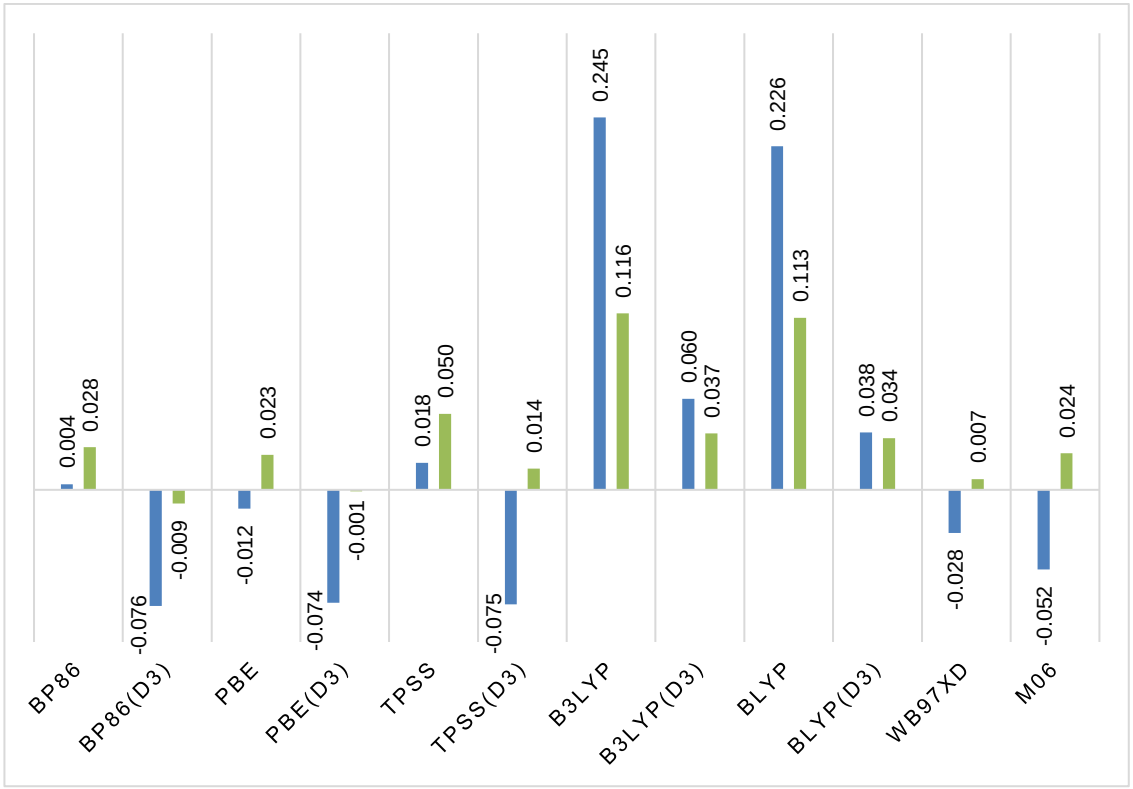

*Figure 6-21. Cu···C(2) (blue bars) and Cu···B (green bars) distances in **112** computed with various functionals and displayed as deviations from the experimental values of 2.267(2) Å and 2.2183(17) Å, respectively. Calculations employed the isolated molecule optimised with the Gaussian program.*

6.5.5.1 Study of the Computed Geometries of 111 and 112 in the Solid State Model with CP2K

As outlined above, the molecular geometries of **111** and **112** are very sensitive to the choice of functional and dispersion correction. On the other hand, in the molecular model, the only dispersion interaction considered is intramolecular dispersion. However, in the crystal structures of **111** and **112**, the unit cells contain more than one entity and each unit cell is surrounded by several other unit cells.

In this regard, as shown in Figure 6-22, the X-ray crystal structure of **111** adopts two symmetric copper borate entities within the unit cell and the X-ray crystal structure **112** features two symmetric copper borate complexes along with a benzene molecule per unit cell. Thus, inter-molecular interactions may also affect the geometries of **111** and **112**. Therefore, an appropriate model is required to address such interactions. Interestingly, during recent years, there has been a significant achievement in development of solid state models using Periodic Boundary Conditions (PBCs).[200] With periodic DFT codes such as CP2K, full solid state structures can be modelled. Therefore, herein, with the available functionals for the CP2K program (BP86, BLYP and PBE), the full solid state structures of **111** and **112** were fully optimised with and without dispersion effects.

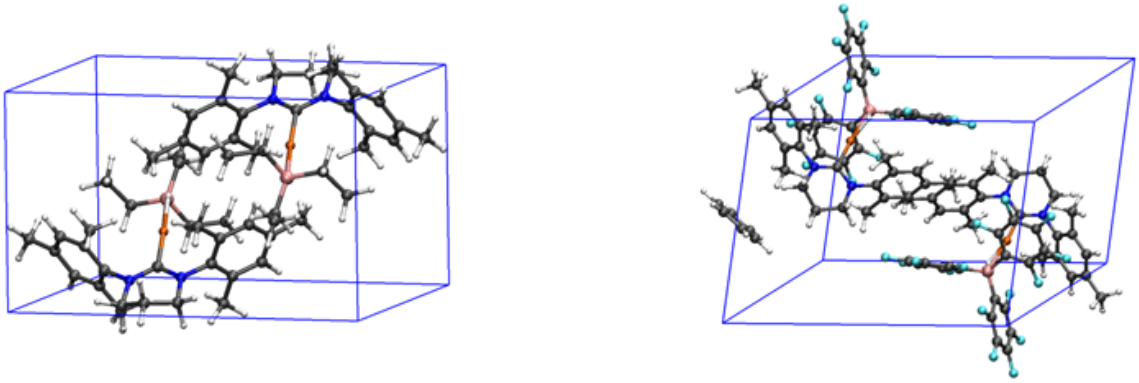

*Figure 6-22. Unit cell contents for **111** (left) and **112** (right) obtained from the single crystal X-ray diffraction analysis. Both species adopt the $P\bar{1}$ space group.*

In the first step, in order to have a fair comparison between the CP2K results and Gaussian results, the isolated structures of **111** and **112** were fully optimised in a 30 × 30 × 30 Å box (this box is large enough to avoid the interaction of Cu complexes between boxes)

using the CP2K program with the PBE functional. As shown in Table 6-4, with CP2K, the computed Cu–C_{6Mes}, Cu···C(2) and Cu···B distances in **111** and **112** are very similar to those computed by Gaussian program. This shows that the type of program does not significantly affect the computational outcomes.

*Table 6-4. Selected computed interatomic distances (Å) of **111** and **112** modelled with Gaussian and CP2K programs with PBE and PBE(D3). For the isolated molecular models, **111** and **112** were optimised in a 30 × 30 × 30 Å unit cell using CP2K package.*

Method (111)	**Program**	**Cu–C_{6Mes}**	**Cu···C(2)**	**Cu···B**
Experiment	--	1.908(3)	2.619(3)	2.282(3)
PBE	Gaussian	1.899	2.449	2.216
PBE(D3)	Gaussian	1.891	2.409	2.186
PBE	CP2K	1.896	2.407	2.213
PBE(D3)	CP2K	1.882	2.369	2.180
Method (112)	**Program**	**Cu–C_{6Mes}**	**Cu···C(2)**	**Cu···B**
Experiment	--	1.8991(18)	2.2183(17)	2.267(2)
PBE	Gaussian	1.912	2.206	2.290
PBE(D3)	Gaussian	1.898	2.144	2.266
PBE	CP2K	1.917	2.198	2.324
PBE(D3)	CP2K	1.906	2.193	2.287

Going to the solid state model, the full solid state structures of **111** and **112** produced by the X-ray diffraction analysis were optimised under periodic boundary conditions with BP86, BLYP and PBE functionals with and without dispersion effect. Table 6-5 shows the Cu–C_{6Mes}, Cu···C(2) and Cu···B distances of **111**. Similar to the molecular models, with all different functionals, there is an excellent agreement between the computed and experimental Cu–C_{6Mes} distances. However, the range of variation in the computed Cu···C(2) distances is still significant, varying from 2.639 Å to 2.967 Å. This is also similar for the Cu···B distance where it changes from 2.283 Å to 2.569 Å. Therefore, similar to the molecular model, in the solid state model, the Cu···C(2) and Cu···B distances are still sensitive to the functional type.

As shown in Table 6-5, similar to **111**, in **112**, there is a very small variation in the computed Cu–C_{6Mes} distance. However, compared with **111**, in **112**, the computed Cu···C(2) distances show much less variation (2.172 Å to 2.243 Å) and it becomes even smaller in the Cu···B distances (2.252 Å to 2.282 Å).

*Table 6-5. Selected computed interatomic distances (Å) for **111** and **112** modelled with periodic DFT and optimised with various functionals in CP2K. For PBE and PBE(D3) results were also obtained using a 2×2×2 super cell.*

	111			**112**		
	Cu–C_{6Mes}	**Cu···C(2)**	**Cu···B**	**Cu···C_{6Mes}**	**Cu···C(2)**	**Cu···B**
Experiment	1.908(3)	2.619(3)	2.282(3)	1.8991(18)	2.2183(17)	2.267(2)
PBE (unit cell)	1.901	2.677	2.283	1.900	2.172	2.253
PBE(D3) (unit cell)	1.903	2.690	2.288	1.900	2.187	2.253
PBE (super cell)	1.901	2.639	2.273	1.900	2.176	2.253
PBE(D3) (super cell)	1.901	2.662	2.283	1.901	2.186	2.252
BLYP (unit cell)	1.905	2.967	2.470	1.906	2.235	2.278
BLYP(D3) (unit cell)	1.903	2.926	2.569	1.903	2.243	2.282
BP86 (unit cell)	1.901	2.722	2.310	1.901	2.186	2.259
BP86(D3) (unit cell)	1.901	2.747	2.324	1.899	2.188	2.266

Figure 6-23 shows the deviation of the selected computed distances of **111** from those in the experimental geometry. For BP86, the Cu···B and Cu···C(2) distances are overestimated by 0.028 Å and 0.103 Å, respectively. With respect to the molecular model of **111**, this is an improvement of the agreement. In contrast to the molecular model, inclusion of dispersion correction with BP86 makes the geometry slightly longer and hence lessens the agreement (Cu···B = 0.128 Å and Cu···C(2) = 0.042 Å). With BLYP, the deviation of Cu···B and Cu···C(2) distances are computed to be 0.188 Å and 0.348 Å, respectively, showing even a poorer agreement compared with the molecular model. The BLYP(D3) functional slightly shortens the Cu···C(2) distance (0.307 Å) but lengthens the Cu···B distance (0.287 Å). The PBE functional gives the best agreement for both Cu···B and Cu···C(2) distances with the very low deviation of 0.001 Å and 0.058 Å, respectively Interestingly, in contrast to the molecular model, inclusion of dispersion with PBE very slightly increases both Cu···B and Cu···C(2) distances. The 2×2×2-unit cell system with the PBE functional gives an excellent agreement for the Cu···C(2) distance (0.009 Å) and also further improves the Cu···B distance (0.038 Å). Addition of dispersion improves the Cu···B distance but slightly lengthens the Cu···C(2) distance.

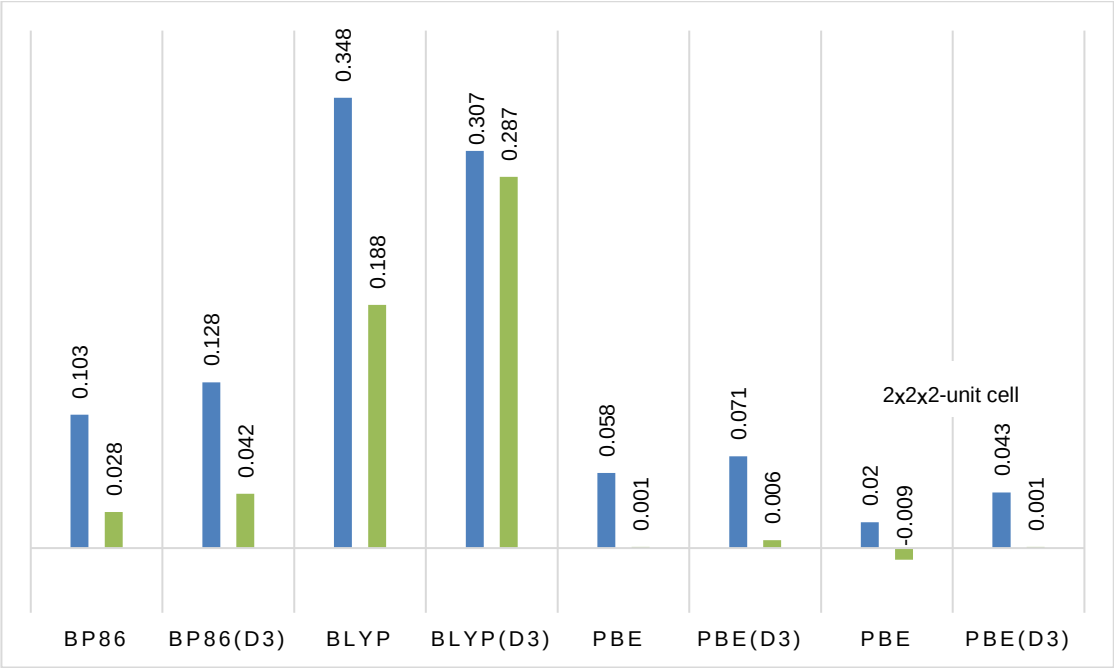

*Figure 6-23. Cu···C(2) (blue bars) and Cu···B (green bars) distances in **111** computed with various functionals and displayed as deviations from the experimental values of 2.283(3) Å and 2.619(3) Å, respectively. Calculations employed the extended solid state via periodic boundary conditions (CP2K).*

Figure 6-24 shows the deviation of computed Cu···B and Cu···C(2) distances in **112** from those in the experimental geometry. With BP86, the Cu···B and Cu···C(2) distances are slightly underestimated by 0.008 Å and 0.032 Å, respectively. Inclusion of the dispersion correction with BP86 however slightly elongates the distances and hence improves the agreement. In contrast to BP86, BLYP slightly overestimates the Cu···B and Cu···C(2) distances by 0.011 Å and 0.017 Å, respectively. However, dispersion correction makes the distances slightly longer and thus, gives a poorer agreement. PBE underestimates the Cu···B and Cu···C(2) distances but with slightly higher deviation of 0.014 Å and 0.046 Å, respectively. PBE(D3) however provides a better agreement. With PBE and PBE(D3) in the 2×2×2-unit cell system, similar results to the one-unit cell system are obtained.

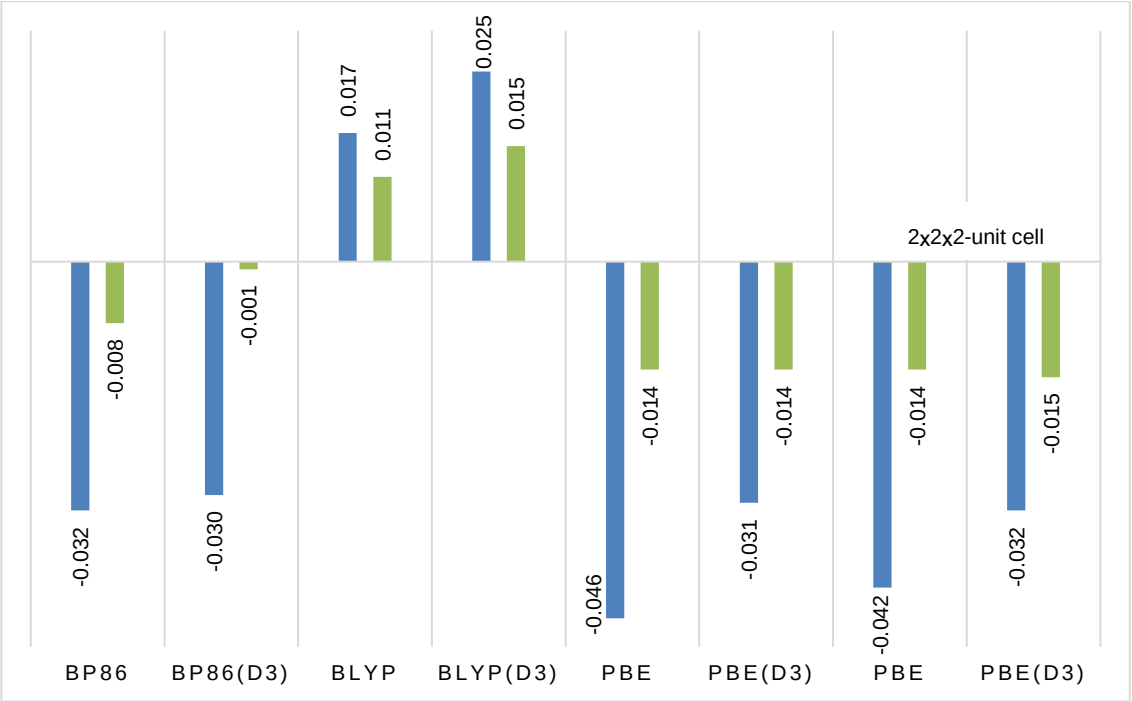

*Figure 6-24. Cu···C(2) (blue bars) and Cu···B (green bars) distances in **112** computed with various functionals and displayed as deviations from the experimental values of 2.267(2) Å and 2.2183(17) Å, respectively. Calculations employed the extended solid state via periodic boundary conditions (CP2K).*

As discussed above, similar to the molecular model, the Cu–C_{6Mes} distance is well reproduced in the solid state model. However, the molecular and solid state models of **111** and **112** show that the Cu···B and Cu···C (2) distances depend on the choice of functional. Interestingly, dispersion effects in the molecular model shortens the Cu···B and Cu···C (2) distances while in solid state, it lengthens both distances. However, compared with the molecular model, in the solid state model, the variations caused by inclusion of dispersion correction are very small. This therefore indicates that in the solid state model, dispersion is well balanced between the inter- and intramolecular interactions.

Figure 6-25 displays the overlay of the optimised full solid state structure with PBE functional from the experiment, showing small deviations of computed geometries from the experimental geometries of **111** and **112**.

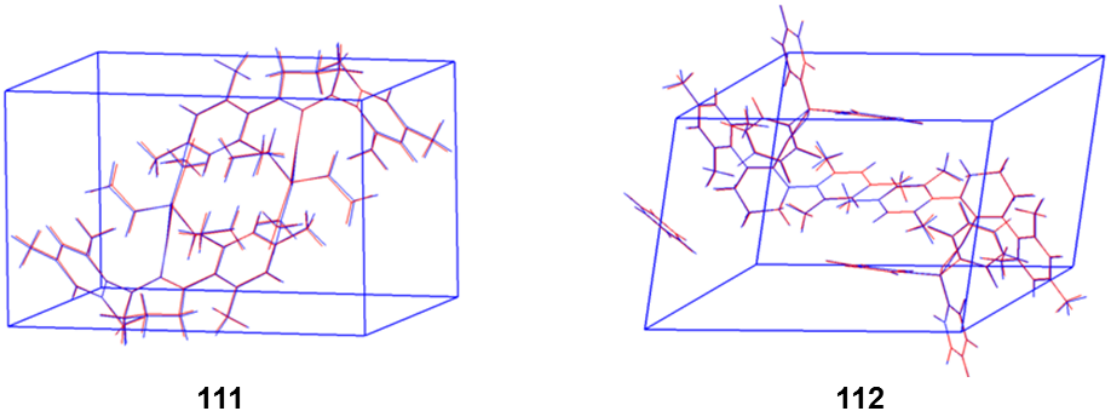

Figure 6-25. Overlays of the experimental crystal structure (red) and the PBE-optimised structure (blue).

6.5.6 Thermodynamic Stability of 111 and 112

As discussed in the first section of this chapter, reaction of copper alkoxides with hydride sources can result in the formation of either a two-coordinate Cu complex, [LCu(HBR_3)], or a dimeric copper hydride complex, $[LCuH]_2$. Bertrand and co-workers showed that a bulky CAAC ligand (e.g. $CAAC^{cy}$) favours the formation of the dimeric species, ($[(CAAC^{cy})Cu(\mu\text{–}H)]_2$). On the other hand, the less bulky CAAC ligand (e.g. $CAAC^{Et}$) gives the Cu-borate complex $(CAAC^{Et})Cu(\kappa^2\text{–}BH_4)_2$. Using [(6-Mes)Cu-O^{t}Bu], Whittlesey and co-workers isolated two copper borate complexes **111** and **112**. Recently, Bertrand and co-workers reported the formation of the dimeric $[LCuH]_2$ species **114**, where L is an extremely bulky NHC ligand (Figure 6-26).[180] Interestingly, **114** was found to be in equilibrium with its monomer (**115**) in solution. This again suggests that the steric feature of NHCs has a subtle effect on the stability of the mononuclear or dinuclear copper complexes.

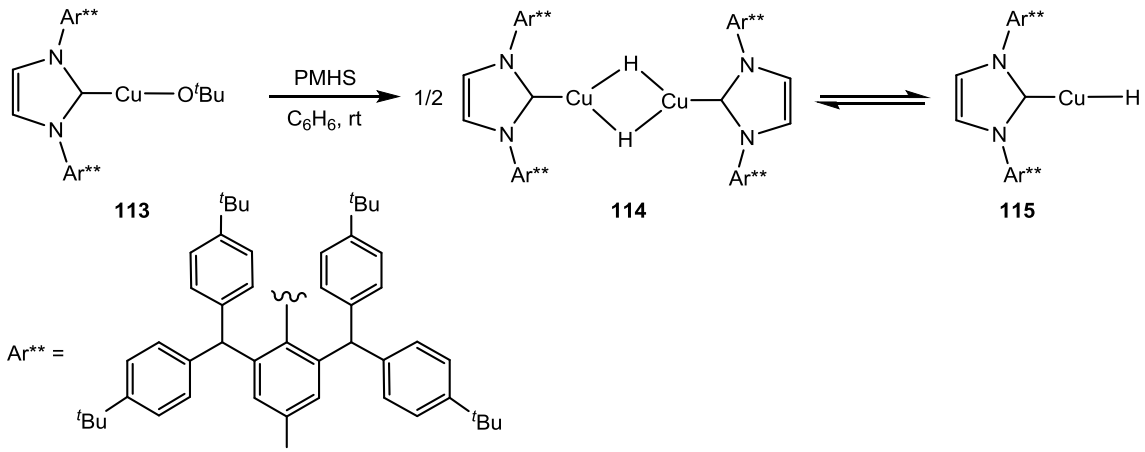

*Figure 6-26. Formation of dimeric copper hydride **114** and its equilibrium with the monomeric species **115**.*

Experimental observations suggest that the reaction of Cu-alkoxides with hydride sources to form $[LCuH]_2$ dimers probably involves the formation of $[LCu(HBR_3)]$ species as intermediates (Scheme 6-1). This species can sometimes be stable enough to be isolated, as in **111** and **112**. Otherwise, the $[LCuHBR_3]$ species can act as an intermediate which then can undergo borane loss to form the monomeric copper hydride species, [LCuH]. The [LCuH] intermediate then dimerizes to form the $[LCuH]_2$ complex.

Scheme 6-1. Borane loss reaction and dimerization of [LCu–H] complex.

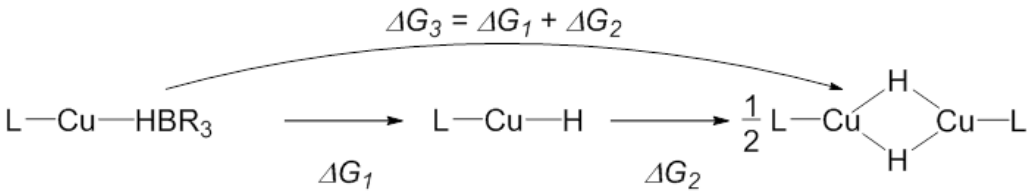

Based on the reaction process shown in Scheme 6-1, the free energy of the reaction steps were computed (Table 6-6). The free energy changes associated with the borane loss and the dimerization process are shown by ΔG_1 and ΔG_2, respectively. The sum of ΔG_1 and ΔG_2 values (ΔG_3) shows the thermodynamic preference for the formation of the $[LCu(HBR_3)]$ or $[LCuH]_2$ complexes. As listed in Table 6-6, the dissociation energies of borane from **111** and **112** are computed to be +10.8 kcal/mol and +38.2 kcal/mol, respectively. This implies the $B(C_6F_5)_3$ moiety is significantly more strongly connected to the hydride than the BEt_3. The dimerization energy for the [(6-Mes)CuH] intermediate is calculated to be -0.4 kcal/mol. However, the combined energies for borane loss and

dimerization in **111** and **112** are calculated to be endergonic by 6.8 and 34.2 kcal/mol, respectively. This shows that the formation of the dimeric copper hydride from the copper borate **111** and **112** is not accessible thermodynamically, consistent with the experiment.

Similar to **112**, the borane dissociation energy in the [(CAAC^{Cy})Cu(κ^2–BH_4)] complex is significantly uphill by 36.9 kcal/mol, showing the BH_3 moiety also strongly bound to the hydride. In [(CAAC^{Cy})Cu($HBEt_3$)], borane loss is significantly easier than in the three other copper borate species but it is still endergonic by 5.8 kcal/mol. The dimerization step for both (CAAC^{Et})CuH and (CAAC^{Cy})CuH complexes is computed to be downhill by 4.1 and 6.5 kcal/mol. Hence, the overall energy for the formation of the dimer from [(CAAC^{Et})Cu(κ^2–BH_4)] is significantly endergonic but slightly exergonic for [(CAAC^{Et})Cu($HBEt_3$)]. For the former, the formation of the dimeric copper hydride species is not accessible but for latter, it is exergonic enough to produce the dimer, consistent with the experiment.

Table 6-6. Computed free energy changes (kcal/mol; BP86-optimised with corrections for dispersion (D3) and THF solvent) for borane loss and dimerization of different [LCu(HBR_3)] complexes.

Structure	L	R	ΔG_1	ΔG_2	ΔG_3
[(6-Mes)Cu($HBEt_3$)] (111)	6-Mes	Et	+10.8	-4.0	+6.8
[(6-Mes)Cu($HB(C_6F_5)_3$] (112)	6-Mes	C_6F_5	+38.2	-4.0	+34.2
[(CAAC^{Et})Cu(κ^2-BH_4)]	CAAC^{Et}	H	+36.9	-4.1	+32.8
[(CAAC^{Cy})Cu($HBEt_3$)]	CAAC^{Cy}	Et	+5.8	-6.5	-0.7

6.6 Conclusions

Based on the QTAIM and NBO analysis, the two-coordinate Cu complexes **111** and **112** display weak interactions in the structure of the {$CuHBR_3$} moiety in which the cationic Cu moiety is stablised by the borate moiety. **112** has also a weak covalent interaction between the cationic Cu and the C(2) centres. A NBO donor-acceptor analysis shows the electron density flow from the C(2)–C_{ortho} π bond to the cationic Cu centre. In **111** however no such interaction is identified which rules out the presence of a C–H agostic interaction.

The computed Cu···B and Cu···C(2) distances of the molecular models of **111** and **112** are either overestimated or underestimated by the calculations. When the computed distances are overestimated, inclusion of dispersion shortens the distances and therefore improves the agreement. However, when the computed distances are underestimated, shortening of the distances with the dispersion correction lessens the agreement. However, this is only due to error cancelation. Interestingly, going to the solid state model, where the environments around the Cu complexes are taken into account, dispersion correction does not make so much difference on the distances. This is mainly due well balancing of the weak intramolecular interactions by the intermolecular interactions.

It is interesting to note that one reason that why **111** and **112** cannot be seen as monomeric [LCu–H] species is the stronger interaction of the hydride with the {BR_3} moiety than the Cu centre. This makes the formation of the monomer species thermodynamically inaccessible.

References

1. E. Schrödinger, *Phys. Rev*, 1926, **28**, 1049-1070.
2. D. K. W. Mok, R. Neumann and N. C. Handy, *J. Phys. Chem.*, 1996, **100**, 6225-6230.
3. A. D. Becke, *Phys. Rev. A*, 1988, **38**, 3098-3100.
4. C. Lee, W. Yang and R. G. Parr, *Phys. Rev. B*, 1988, **37**, 785-789.
5. J. Tao, J. P. Perdew, V. N. Staroverov and G. E. Scuseria, *Phys. Rev. Lett.*, 2003, **91**, 146401-146404.
6. A. D. Becke, *J. Chem. Phys.*, 1993, **98**, 5648-5652.
7. P. C. Hariharan and J. A. Pople, *Theor. Chim. Acta.*, 1973, **28**, 213-222.
8. A. Hellweg and D. Rappoport, *PCCP*, 2015, **17**, 1010-1017.
9. M. J. Frisch, J. A. Pople and J. S. Binkley, *J. Chem. Phys.*, 1984, **80**, 3265-3269.
10. D. Andrae, U. Haussermann, M. Dolg, H. Stoll and H. Preuss, *Theor. Chim. Acta.*, 1990, **77**, 123-141.
11. P. J. Hay and W. R. Wadt, *J. Chem. Phys.*, 1985, **82**, 270-283.
12. T. H. Rod, P. Rydberg and U. Ryde, *J. Chem. Phys.*, 2006, **124**, 174503-174509.
13. C. Curutchet, M. Orozco, F. J. Luque, B. Mennucci and J. Tomasi, *J. Comput. Chem.*, 2006, **27**, 1769-1780.
14. J. Tomasi, B. Mennucci and R. Cammi, *Chem. Rev.*, 2005, **105**, 2999-3094.
15. S. Grimme, *WIREs Comput Mol Sci.*, 2011, **1**, 211-228.
16. G. Rutkai, M. Thol, R. Span and J. Vrabec, *Mol. Phys.*, 2017, **115**, 1104-1121.
17. J. E. Jones, *Proc. R. Soc. Lond.*, 1924, **106**, 463-477.
18. S. Rösel, H. Quanz, C. Logemann, J. Becker, E. Mossou, L. Cañadillas-Delgado, E. Caldeweyher, S. Grimme and P. R. Schreiner, *J. Am. Chem. Soc.*, 2017, **139**, 7428-7431.
19. S. Rosel, C. Balestrieri and P. R. Schreiner, *Chem. Sci.*, 2017, **8**, 405-410.
20. J. Vondrášek, L. Bendová, V. Klusák and P. Hobza, *J. Am. Chem. Soc.*, 2005, **127**, 2615-2619.
21. J. Witte, N. Mardirossian, J. B. Neaton and M. Head-Gordon, *J. Chem. Theory Comput.*, 2017, **13**, 2043–2052.
22. S. Grimme, J. Antony, S. Ehrlich and H. Krieg, *J. Chem. Phys.*, 2010, **132**, 154104-154118.
23. S. Grimme, J. Antony, S. Ehrlich and H. Krieg, *J. Chem. Phys.*, 2010, **132**, 154104.

24. S. Grimme, S. Ehrlich and L. Goerigk, *J. Comput. Chem.*, 2011, **32**, 1456-1465.
25. C. F. Matta and R. J. Boyd, in *The Quantum Theory of Atoms in Molecules*, Wiley-VCH Verlag GmbH & Co. KGaA, Editon edn., 2007, pp. 1-34.
26. R. Bianchi, G. Gervasio and D. Marabello, *Inorg. Chem.*, 2000, **39**, 2360-2366.
27. S. Boonseng, G. W. Roffe, J. Spencer and H. Cox, *Dalton Trans.*, 2015, **44**, 7570-7577.
28. H. A. Sparkes, T. Krämer, S. K. Brayshaw, J. C. Green, A. S. Weller and J. A. K. Howard, *Dalton Trans.*, 2011, **40**, 10708-10718.
29. L. J. Farrugia and C. Evans, *J. Phys. Chem. A*, 2005, **109**, 8834-8848.
30. R. F. W. Bader, *Chem. Rev.*, 1991, **91**, 893-928.
31. F. Weinhold, C. R. Landis and E. D. Glendening, *Int. Rev. Phys. Chem.*, 2016, **35**, 399-440.
32. J. S. Jones, C. R. Wade and F. P. Gabbaï, *Angew. Chem. Int. Ed.*, 2014, **53**, 8876-8879.
33. K. Yamamoto, S. Otsuka, K. Nogi and H. Yorimitsu, *ACS Catal.*, 2017, **7**, 7623-7628.
34. A. R. Paris and A. B. Bocarsly, *ACS Catal.*, 2017, **7**, 6815-6820.
35. J. Bauer, H. Braunschweig and R. D. Dewhurst, *Chem. Rev.*, 2012, **112**, 4329-4346.
36. A. Maity and T. S. Teets, *Chem. Rev.*, 2016, **116**, 8873−8911.
37. R. J. Oeschger and P. Chen, *Organometallics*, 2017, **36**, 1465−1468.
38. T. Cadenbach, T. Bollermann, C. Gemel, M. Tombul, I. Fernandez, M. v. Hopffgarten, G. Frenking and R. A. Fischer, *J. Am. Chem. Soc.*, 2009, **131**, 16063-16077.
39. W.-H. Chan, Z.-Z. Zhang, T. C. W. Mak and C.-M. Che, *J. Chem. Soc., Dalton Trans.*, 1998, 803-810.
40. M. Molon, C. Gemel, R. W. Seidel, P. Jerabek, G. Frenking and R. A. Fischer, *Inorg. Chem.*, 2013, **52**, 7152-7160.
41. M. Molon, C. Gemel and R. A. Fischer, *Eur. J. Inorg. Chem.*, 2013, **2013**, 3616-3622.
42. C. J. Pell, W.-C. Shih, S. Gatard and O. V. Ozerov, *Chem. Commun.*, 2017, **53**, 6456-6459.
43. J. Derosa, V. T. Tran, M. N. Boulous, J. S. Chen and K. M. Engle, *J. Am. Chem. Soc.*, 2017, **139**, 10657-10660.

44. J. Campos, A. Nova, E. L. Kolychev and S. Aldridge, *Chem. Eur. J.*, **23**, 12655-12667.
45. H. Braunschweig, C. Kollann and D. Rais, *Angew. Chem. Int. Ed.*, 2006, **45**, 5254-5274.
46. H. Braunschweig, K. Radacki, D. Rais and D. Scheschkewitz, *Angew. Chem. Int. Ed.*, 2005, **44**, 5651-5654.
47. H. Braunschweig, K. Gruss and K. Radacki, *Inorg. Chem.*, 2008, **47**, 8595-8597.
48. J. Ye, R. C. Cammarota, J. Xie, M. V. Vollmer, D. G. Truhlar, C. J. Cramer, C. C. Lu and L. Gagliardi, *ACS Catal.*, 2018, **8**, 4955-4968.
49. J. Takaya and N. Iwasawa, *J. Am. Chem. Soc.*, 2017, **139**, 6074−6077.
50. J. Li, L. Jin, C. Liu and A. Lei, *Org. Chem. Front.*, 2014, **1**, 50-53.
51. P. Ribagnac, M. Blug, J. Villa-Uribe, X. F. L. Goff, C. Gosmini and N. Mézailles, *Chem. Eur. J.*, 2011, **17**, 14389-14393.
52. B. Fuentes, M. García-Melchor, A. Lledós, F. Maseras, J. A. Casares, G. Ujaque and P. Espinet, *Chem. Eur. J.*, 2010, **16**, 8596-8599.
53. A. L. Liberman-Martin, D. S. Levine, W. Liu, R. G. Bergman and T. D. Tilley, *Organometallics*, 2016, **35**, 1064-1069.
54. A. L. Liberman-Martin, D. S. Levine, M. S. Ziegler, R. G. Bergman and T. D. Tilley, *Chem. Commun.*, 2016, **52**, 7039-7042.
55. M. Ma, A. Sidiropoulos, L. Ralte, A. Stasch and C. Jones, *Chem. Commun.*, 2013, **49**, 48-50.
56. Y. Kratish, G. Molev, A. Kostenko, D. Sheberla, B. Tumanskii, M. Botoshansky, S. Shimada, D. Bravo-Zhivotovskii and Y. Apeloig, *Angew. Chem. Int. Ed.*, 2015, **54**, 11817-11821.
57. O. Ekkert, A. J. P. White and M. R. Crimmin, *Angew. Chem. Int. Ed.*, 2016, **55**, 16031-16034.
58. O. Ekkert, A. J. P. White and M. R. Crimmin, *Chem. Eur. J.*, 2017, **23**, 5682-5686.
59. T. Bollermann, K. Freitag, C. Gemel, R. W. Seidel and R. A. Fischer, *Organometallics*, 2011, **30**, 4123-4127.
60. F. G. Baddour, S. R. Fiedler, M. P. Shores, J. W. Bacon, J. A. Golen, A. L. Rheingold and L. H. Doerrer, *Inorg. Chem.*, 2013, **52**, 13562-13575.
61. D. F. Shriver, *J. Am. Chem. Soc.*, 1963, **85**, 3509-3510.
62. G. W. Parshall, *J. Am. Chem. Soc.*, 1964, **86**, 361-364.

63. M. P. Johnson and D. F. Shriver, *J. Am. Chem. Soc.*, 1966, **88**, 301-304.
64. S. Aldridge and D. L. Coombs, *Coord. Chem. Rev.*, 2004, **248**, 535-559.
65. G. J. Irvine, M. J. G. Lesley, T. B. Marder, N. C. Norman, C. R. Rice, E. G. Robins, W. R. Roper, G. R. Whittell and L. J. Wright, *Chem. Rev.*, 1998, **98**, 2685-2722.
66. H. Braunschweig, K. Radacki, F. Seeler and G. R. Whittell, *Organometallics*, 2004, **23**, 4178-4180.
67. T. Yasue, Y. Kawano and M. Shimoi, *Angew. Chem. Int. Ed.*, 2003, **41**, 1727-1730
68. Y. Kawano, H. Kawakami and M. Shimoi, *Chem. Lett.*, 2001, **30**, 1006-1007.
69. Y. Kawano, T. Yasue and M. Shimoi, *J. Am. Chem. Soc.*, 1999, **121**, 11744-11750.
70. H. Braunschweig, R. D. Dewhurst and C. Schneider, *Organometallics*, 2016, **35**, 1002-1007.
71. H. Braunschweig, K. Gruss and K. Radacki, *Angew. Chem. Int. Ed.*, 2007, **46**, 7782-7784.
72. M. Itazaki, M. Ito and H. Nakazawa, *Eur. J. Inorg. Chem.*, 2015, **2015**, 2033-2036.
73. R. Bissert, H. Braunschweig, R. D. Dewhurst and C. Schneider, *Organometallics*, 2016, **35**, 2567-2573.
74. M. Itazaki, M. Ito, S. Nakashima and H. Nakazawa, *Dalton Trans.*, 2016, **45**, 1327-1330.
75. J. Bauer, H. Braunschweig, P. Brenner, K. Kraft, K. Radacki and K. Schwab, *Chem. Eur. J.*, 2010, **16**, 11985-11992.
76. H. Braunschweig, P. Brenner, A. Müller, K. Radacki, D. Rais and K. Uttinger, *Chem. Eur. J.*, 2007, **13**, 7171-7176.
77. H. Braunschweig, K. Radacki and K. Uttinger, *Angew. Chem. Int. Ed.*, 2007, **46**, 3979-3982.
78. H. Braunschweig, K. Radacki, D. Rais and D. Scheschkewitz, *Angew. Chem. Int. Ed.*, 2005, **44**, 5651-5654.
79. H. Braunschweig, K. Radacki, D. Rais and F. Seeler, *Organometallics*, 2004, **23**, 5545-5549.
80. R. A. Fischer, D. Weiß, M. Winter, I. Müller, H. D. Kaesz, N. Fröhlich and G. Frenking, *J. Organomet. Chem.*, 2004, **689**, 4611-4623.

81. K. K. Pandey, P. Patidar and H. Braunschweig, *Inorg. Chem.*, 2010, **49**, 6994-7000.
82. K. K. Pandey, P. Patidar and S. Aldridge, *J. Phys. Chem. A*, 2010, **114**, 12099-12105.
83. K. K. Pandey, *J. Phys. Chem. A*, 2011, **115**, 8578-8585.
84. R. Bertermann, J. Böhnke, H. Braunschweig, R. D. Dewhurst, T. Kupfer, J. H. Muessig, L. Pentecost, K. Radacki, S. S. Sen and A. Vargas, *J. Am. Chem. Soc.*, 2016, **138**, 16140-16147.
85. F. Hupp, M. Ma, F. Kroll, J. O. C. Jimenez-Halla, R. D. Dewhurst, K. Radacki, A. Stasch, C. Jones and H. Braunschweig, *Chem. Eur. J.*, 2014, **20**, 16888-16898.
86. H. Braunschweig, R. D. Dewhurst, F. Hupp, C. Kaufmann, A. K. Phukan, C. Schneider and Q. Ye, *Chem. Sci.*, 2014, **5**, 4099-4104.
87. T. Cadenbach, C. Gemel, D. Zacher and R. A. Fischer, *Angew. Chem. Int. Ed.*, 2008, **47**, 3438-3441.
88. T. Steinke, C. Gemel, M. Cokoja, M. Winter and R. A. Fischer, *Angew. Chem. Int. Ed.*, 2004, **43**, 2349-2352.
89. T. Cadenbach, C. Gemel, R. Schmid and R. A. Fischer, *J. Am. Chem. Soc.*, 2005, **127**, 17068-17078.
90. M. Molon, C. Gemel and R. A. Fischer, *J. Organomet. Chem.*, 2014, **751**, 573-578.
91. T. Steinke, C. Gemel, M. Cokoja, M. Winter and R. A. Fischer, *Angew. Chem. Int. Ed.*, 2004, **43**, 2299-2302.
92. T. Cadenbach, C. Gemel, R. Schmid, S. Block and R. A. Fischer, *Dalton Trans.*, 2004, 3171-3172.
93. J. Weßing, C. Göbel, B. Weber, C. Gemel and R. A. Fischer, *Inorg. Chem.*, 2017, **56**, 3517-3525.
94. T. Steinke, C. Gemel, M. Cokoja, M. Winter and R. A. Fischer, *Dalton Trans.*, 2005, 55-62.
95. M. Cokoja, C. Gemel, T. Steinke, F. Schroder and R. A. Fischer, *Dalton Trans.*, 2005, 44-54.
96. M. Molon, T. Bollermann, C. Gemel, J. Schaumann and R. A. Fischer, *Dalton Trans.*, 2011, **40**, 10769-10774.
97. C. Gemel, T. Steinke, D. Weiss, M. Cokoja, M. Winter and R. A. Fischer, *Organometallics*, 2003, **22**, 2705-2710.

98. P. Jutzi, B. Neumann, L. O. Schebaum, A. Stammler and H.-G. Stammler, *Organometallics*, 1999, **18**, 4462-4464.
99. P. Jutzi, B. Neumann, G. Reumann and H.-G. Stammler, *Organometallics*, 1998, **17**, 1305-1314.
100. T. Cadenbach, C. Gemel, T. Bollermann, I. Fernandez, G. Frenking and R. A. Fischer, *Chem. Eur. J.*, 2008, **14**, 10789-10796.
101. T. Cadenbach, C. Gemel, T. Bollermann and R. A. Fischer, *Inorg. Chem.*, 2009, **48**, 5021-5026.
102. W. Uhl, M. Benter, S. Melle, W. Saak, G. Frenking and J. Uddin, *Organometallics*, 1999, **18**, 3778-3780.
103. W. Uhl, M. Pohlmann and R. Wartchow, *Angew. Chem. Int. Ed.*, 1998, **37**, 961-963.
104. D. Weiss, T. Steinke, M. Winter, R. A. Fischer, N. Fröhlich, J. Uddin and G. Frenking, *Organometallics*, 2000, **19**, 4583-4588.
105. D. Weiß, M. Winter, K. Merz, A. Knüfer, R. A. Fischer, N. Fröhlich and G. Frenking, *Polyhedron*, 2002, **21**, 535-542.
106. S. Aldridge, A. Rossin, D. L. Coombs and D. J. Willock, *Dalton Trans.*, 2004, 2649-2654.
107. J. Uddin, C. Boehme and G. Frenking, *Organometallics*, 2000, **19**, 571-582.
108. J. A. B. Abdalla, I. M. Riddlestone, J. Turner, P. A. Kaufman, R. Tirfoin, N. Phillips and S. Aldridge, *Chem. Eur. J.*, 2014, **20**, 17624-17634.
109. A. Caise, J. A. B. Abdalla, R. Tirfoin, A. J. Edwards and S. Aldridge, *Chem. Eur. J.*, 2017, **23**, 16906-16913.
110. S. Aldridge, A. Caise, J. Abdalla, R. Tirfoin and A. Edwards, *Chem. Eur. J.*, 2017, **23**, 16906-16913.
111. J. Turner, J. A. B. Abdalla, J. I. Bates, R. Tirfoin, M. J. Kelly, N. Phillips and S. Aldridge, *Chem. Sci.*, 2013, **4**, 4245–4250.
112. J. A. B. Abdalla, A. Caise, C. P. Sindlinger, R. Tirfoin, A. L. Thompson, A. J. Edwards and S. Aldridge, *Nat. Chem.*, 2017, **9**, 1256–1262.
113. A. Amgoune, G. Bouhadir and D. Bourissou, in *Frustrated Lewis Pairs II: Expanding the Scope*, eds. G. Erker and D. W. Stephan, Springer Berlin Heidelberg, Berlin, Heidelberg, Editon edn., 2013, pp. 281-311.
114. G. Bouhadir and D. Bourissou, *Chem. Soc. Rev.*, 2016, **45**, 1065-1079.
115. A. Amgoune and D. Bourissou, *Chem. Commun.*, 2011, **47**, 859-871.

116. S. Bontemps, M. Sircoglou, G. Bouhadir, H. Puschmann, J. A. K. Howard, P. W. Dyer, K. Miqueu and D. Bourissou, *Chem. Eur. J.*, 2008, **14**, 731-740.
117. S. Bontemps, H. Gornitzka, G. Bouhadir, K. Miqueu and D. Bourissou, *Angew. Chem. Int. Ed.*, 2006, **45**, 1611-1614.
118. M. Sircoglou, S. Bontemps, M. Mercy, N. Saffon, M. Takahashi, G. Bouhadir, L. Maron and D. Bourissou, *Angew. Chem. Int. Ed.*, 2007, **46**, 8583-8586.
119. W. H. Harman and J. C. Peters, *J. Am. Chem. Soc.*, 2012, **134**, 5080-5082.
120. B. R. Barnett, M. L. Neville, C. E. Moore, A. L. Rheingold and J. S. Figueroa, *Angew. Chem. Int. Ed.*, 2017, **56**, 7195-7199.
121. M. Sircoglou, S. Bontemps, M. Mercy, N. Saffon, M. Takahashi, G. Bouhadir, L. Maron and D. Bourissou, *Angew. Chem. Int. Ed.*, 2007, **46**, 8583-8586.
122. B. R. Barnett, C. E. Moore, A. L. Rheingold and J. S. Figueroa, *J. Am. Chem. Soc.*, 2014, **136**, 10262-10265.
123. W. H. Harman, T. P. Lin and J. C. Peters, *Angew. Chem. Int. Ed.*, 2014, **53**, 1081-1086.
124. G. Zeng and S. Sakaki, *Inorg. Chem.*, 2013, **52**, 2844-2853.
125. T.-P. Lin and J. C. Peters, *J. Am. Chem. Soc.*, 2013, **135**, 15310-15313.
126. P. A. Rudd, S. Liu, L. Gagliardi, V. G. Young and C. C. Lu, *J. Am. Chem. Soc.*, 2011, **133**, 20724-20727.
127. R. C. Cammarota and C. C. Lu, *J. Am. Chem. Soc.*, 2015, **137**, 12486-12489.
128. M. V. Vollmer, J. Xie and C. C. Lu, *J. Am. Chem. Soc.*, 2017, **139**, 6570–6573.
129. R. C. Cammarota, M. V. Vollmer, J. Xie, J. Ye, J. C. Linehan, S. A. Burgess, A. M. Appel, L. Gagliardi and C. C. Lu, *J. Am. Chem. Soc.*, 2017, **139**, 14244-14250.
130. C. Lu, J. T. Moore and N. E. Smith, *Dalton Trans.*, 2017, **46**, 5689–5701.
131. T. Bollermann, C. Gemel and R. A. Fischer, *Coord. Chem. Rev.*, 2012, **256**, 537-555.
132. I. M. Riddlestone, N. A. Rajabi, J. P. Lowe, M. F. Mahon, S. A. Macgregor and M. K. Whittlesey, *J. Am. Chem. Soc.*, 2016, **138**, 11081-11084.
133. I. M. Riddlestone, D. McKay, M. J. Gutmann, S. A. Macgregor, M. F. Mahon, H. A. Sparkes and M. K. Whittlesey, *Organometallics*, 2016, **35**, 1301-1312.
134. B. Cordero, V. Gómez, A. E. Platero-Prats, M. Revés, J. Echeverría, E. Cremades, F. Barragán and S. Alvarez, *Dalton Trans.*, 2008, 2832–2838.

135. M. Frisch, G. Trucks, H. B. Schlegel, G. Scuseria, M. Robb, J. Cheeseman, G. Scalmani, V. Barone, B. Mennucci and G. e. Petersson, Gaussian, Inc. Wallingford, CT, Editon edn., 2009.
136. W. J. Hehre, R. Ditchfield and J. A. Pople, *J. Chem. Phys.*, 1972, **56**, 2257-2261.
137. D. Andrae, U. Häußermann, M. Dolg, H. Stoll and H. Preuß, *Theor. Chim. Acta.*, 1990, **77**, 123-141.
138. A. Höllwarth, M. Böhme, S. Dapprich, A. W. Ehlers, A. Gobbi, V. Jonas, K. F. Köhler, R. Stegmann, A. Veldkamp and G. Frenking, *Chem. Phys. Lett.*, 1993, **208**, 237-240.
139. E. D. Glendening, C. R. Landis and F. Weinhold, *J. Comput. Chem.*, 2013, **34**, 1429-1437.
140. F. Biegler-König and J. Schönbohm, *J. Comput. Chem.*, 2002, **23**, 1489-1494.
141. F. Neese, *WIREs Comput Mol Sci.*, 2018, **8**, 1-6.
142. F. Weigend and R. Ahlrichs, *PCCP*, 2005, **7**, 3297-3305.
143. A. Schäfer, H. Horn and R. Ahlrichs, *J. Chem. Phys.*, 1992, **97**, 2571-2577.
144. A. Schäfer, C. Huber and R. Ahlrichs, *J. Chem. Phys.*, 1994, **100**, 5829-5835.
145. G. Gervasio, R. Bianchi and D. Marabello, *Chem. Phys. Lett.*, 2004, **387**, 481-484.
146. H. A. Sparkes, T. Kramer, S. K. Brayshaw, J. C. Green, A. S. Weller and J. A. K. Howard, *Dalton Trans.*, 2011, **40**, 10708-10718.
147. A. Kumar, N. A. Beattie, S. D. Pike, S. A. Macgregor and A. S. Weller, *Angew. Chem. Int. Ed.*, 2016, **55**, 6651-6656.
148. R. N. Perutz and S. Sabo-Etienne, *Angew. Chem. Int. Ed.*, 2007, **46**, 2578-2592.
149. J. F. Riehl, Y. Jean, O. Eisenstein and M. Pelissier, *Organometallics*, 1992, **11**, 729-737.
150. S. Dagorne and D. A. Atwood, *Chem. Rev.*, 2008, **108**, 4037-4071.
151. R. C. Cammarota, L. J. Clouston and C. C. Lu, *Coord. Chem. Rev.*, 2017, **334**, 100-111.
152. I. M. Riddlestone, N. A. Rajabi, S. A. Macgregor, M. F. Mahon and M. K. Whittlesey, *Chem. Eur. J.*, 2018, **24**, 1732-1738.
153. I. Vidal, S. Melchor, I. Alkorta, J. Elguero, M. R. Sundberg and J. A. Dobado, *Organometallics*, 2006, **25**, 5638-5647.
154. I. Vidal, S. Melchor and J. A. Dobado, *J. Phys. Chem. A*, 2005, **109**, 7500-7508.

155. K. Sen, D. Ghosh, S. Pakhira, T. Banu and A. K. Das, *J. Chem. Phys.*, 2013, **139**, 234303-234320.
156. J. R. Lane, J. Contreras-García, J.-P. Piquemal, B. J. Miller and H. G. Kjaergaard, *J. Chem. Theory Comput.*, 2013, **9**, 3263-3266.
157. I. M. Riddlestone, D. McKay, M. J. Gutmann, S. A. Macgregor, M. F. Mahon, H. A. Sparkes and M. K. Whittlesey, *Organometallics*, 2016, **35**, 1301−1312.
158. V. L. Chantler, S. L. Chatwin, R. F. R. Jazzar, M. F. Mahon, O. Saker and M. K. Whittlesey, *Dalton Trans.*, 2008, 2603-2614.
159. M. Katari, E. Nicol, V. Steinmetz, G. v. d. Rest, D. Carmichael and G. Frison, *Chem. Eur. J.*, 2017, **23**, 8414-8423.
160. G. W. T. M. J. Frisch, H. B. Schlegel, G. E. Scuseria, M. A. Robb, J. R. Cheeseman, G. Scalmani, V. Barone, B. Mennucci, G. A. Petersson, H. Nakatsuji, M. Caricato, X. Li, H. P. Hratchian, A. F. Izmaylov, J. Bloino, G. Zheng, J. L. Sonnenberg, M. Hada, M. Ehara, K. Toyota, R. Fukuda, J. Hasegawa, M. Ishida, T. Nakajima, Y. Honda, O. Kitao, H. Nakai, T. Vreven, J. A. J. Montgomery, J. E. Peralta, F. Ogliaro, M. Bearpark, J. J. Heyd, E. Brothers, K. N. Kudin, V. N. Staroverov, R. Kobayashi, J. Normand, K. Raghavachari, A. Rendell, J. C. Burant, S. S. Iyengar, J. Tomasi, M. Cossi, N. Rega, J. M. Millam, M. Klene, J. E. Knox, J. B. Cross, V. Bakken, C. Adamo, J. Jaramillo, R. Gomperts, R. E. Stratmann, O. Yazyev, A. J. Austin, R. Cammi, C. Pomelli, J. W. Ochterski, R. L. Martin, K. Morokuma, V. G. Zakrzewski, G. A. Voth, P. Salvador, J. J. Dannenberg, S. Dapprich, A. D. Daniels, O. Farkas, J. B. Foresman, J. V. Ortiz, J. Cioslowski, D. J. Fox, Gaussian 09, Revision D.01, Gaussian, Inc.: Wallingford CT, 2013.
161. J. P. Perdew, *Phys. Rev. B,* 1986, **33**, 8822-8824.
162. P. AIMAll (Version 13.02.26, T. A. Keith, T. K. Grist-mill, Software, Overland Park KS, USA, 2015.
163. J. K. B. NBO 6.0. E. D. Glendening, A. E. Reed, J. E. Carpenter, J. A. Bohmann, C. M. Morales, C. R. Landis and F. Weinhold (Theoretical Chemistry Institute, University of Wisconsin, Madison, WI, 2013.
164. L. J. Farrugia, C. Evans, D. Lentz and M. Roemer, *J. Am. Chem. Soc.*, 2009, **131**, 1251-1268.
165. S. Grimme, *J. Comput. Chem.*, 2006, **27**, 1787-1799.
166. J. P. Perdew, K. Burke and M. Ernzerhof, *Phys. Rev. Lett.*, 1996, **77**, 3865-3868.
167. J.-D. Chai and M. Head-Gordon, *PCCP*, 2008, **10**, 6615-6620.

168. B. Miehlich, A. Savin, H. Stoll and H. Preuss, *Chem. Phys. Lett.*, 1989, **157**, 200-206.
169. J. Tao, J. P. Perdew, V. N. Staroverov and G. E. Scuseria, *Phys. Rev. Lett.*, 2003, **91**, 146401-146404.
170. Y. Zhao and D. G. Truhlar, *Acc. Chem. Res.*, 2008, **41**, 157-167.
171. T. Wakamatsu, K. Nagao, H. Ohmiya and M. Sawamura, *Organometallics*, 2016, **35**, 1354-1357.
172. N. P. Mankad, D. S. Laitar and J. P. Sadighi, *Organometallics*, 2004, **23**, 3369-3371.
173. D. H. Appella, Y. Moritani, R. Shintani, E. M. Ferreira and S. L. Buchwald, *J. Am. Chem. Soc.*, 1999, **121**, 9473-9474.
174. A. Welle, S. Díez-González, B. Tinant, S. P. Nolan and O. Riant, *Org. Lett.*, 2006, **8**, 6059-6062.
175. A. J. Jordan, C. M. Wyss, J. Bacsa and J. P. Sadighi, *Organometallics*, 2016, **35**, 613-616.
176. M. W. Gribble, M. T. Pirnot, J. S. Bandar, R. Y. Liu and S. L. Buchwald, *J. Am. Chem. Soc.*, 2017, **139**, 2192-2195.
177. L. R. Collins, I. M. Riddlestone, M. F. Mahon and M. K. Whittlesey, *Chem. Eur. J.*, 2015, **21**, 14075-14084.
178. G. D. Frey, B. Donnadieu, M. Soleilhavoup and G. Bertrand, *Chem. Asian J.*, 2011, **6**, 402-405.
179. T. Vergote, F. Nahra, D. Peeters, O. Riant and T. Leyssens, *J. Organomet. Chem.*, 2013, **730**, 95-103.
180. E. A. Romero, P. M. Olsen, R. Jazzar, M. Soleilhavoup, M. Gembicky and G. Bertrand, *Angew. Chem. Int. Ed.*, 2017, **56**, 4024-4027.
181. L. R. Collins, N. A. Rajabi, S. A. Macgregor, M. F. Mahon and M. K. Whittlesey, *Angew. Chem. Int. Ed.*, 2016, **55**, 15539–15543.
182. A. Wurtz, *Ann. Chem. Phys*, 1844, **11**, 250-251.
183. A. J. Jordan, G. Lalic and J. P. Sadighi, *Chem. Rev.*, 2016, **116**, 8318-8372.
184. T. Fujihara, K. Semba, J. Terao and Y. Tsuji, *Catal. Sci. Technol.*, 2014, **4**, 1699-1709.
185. S. A. Bezman, M. R. Churchill, J. A. Osborn and J. Wormald, *J. Am. Chem. Soc.*, 1971, **93**, 2063-2065.

186. W. S. Mahoney, D. M. Brestensky and J. M. Stryker, *J. Am. Chem. Soc.*, 1988, **110**, 291-293.
187. B. H. Lipshutz, J. Keith, P. Papa and R. Vivian, *Tetrahedron Lett.*, 1998, **39**, 4627-4630.
188. Z. Mao, J.-S. Huang, C.-M. Che, N. Zhu, S. K.-Y. Leung and Z.-Y. Zhou, *J. Am. Chem. Soc.*, 2005, **127**, 4562-4563.
189. G. V. Goeden, J. C. Huffman and K. G. Caulton, *Inorg. Chem.*, 1986, **25**, 2484-2485.
190. D. Mendoza-Espinosa, A. Alvarez-Hernández, D. Angeles-Beltrán, G. E. Negrón-Silva, O. R. Suárez-Castillo and J. M. Vásquez-Pérez, *Inorg. Chem.*, 2017, **56**, 2092–2099.
191. R. Dorta, E. D. Stevens, C. D. Hoff and S. P. Nolan, *J. Am. Chem. Soc.*, 2003, **125**, 10490-10491.
192. C. A. Laskowski, A. J. M. Miller, G. L. Hillhouse and T. R. Cundari, *J. Am. Chem. Soc.*, 2011, **133**, 771-773.
193. X. Hu, M. Soleilhavoup, M. Melaimi, J. Chu and G. Bertrand, *Angew. Chem. Int. Ed.*, 2015, **54**, 6008-6011.
194. J. VandeVondele, M. Krack, F. Mohamed, M. Parrinello, T. Chassaing and J. Hutter, *Comput. Phys. Commun.*, 2005, **167**, 103-128.
195. J. Hutter, M. Iannuzzi, F. Schiffmann and J. VandeVondele, *WIREs Comput Mol Sci.*, 2013, **4**, 15-25.
196. J. VandeVondele and J. Hutter, *J. Chem. Phys.*, 2007, **127**, 114105-114109.
197. C. Hartwigsen, S. Goedecker and J. Hutter, *Phys. Rev. B*, 1998, **58**, 3641-3662.
198. S. Goedecker, M. Teter and J. Hutter, *Phys. Rev. B*, 1996, **54**, 1703-1710.
199. M. Krack, *Theor. Chem. Acc.*, 2005, **114**, 145-152.
200. J. Moellmann and S. Grimme, *Organometallics*, 2013, **32**, 3784-3787.

JACS
JOURNAL OF THE AMERICAN CHEMICAL SOCIETY
Communication
pubs.acs.org/JACS

Activation of H_2 over the Ru−Zn Bond in the Transition Metal−Lewis Acid Heterobimetallic Species $[Ru(IPr)_2(CO)ZnEt]^+$

Ian M. Riddlestone,[#] Nasir A. Rajabi,[§] John P. Lowe,[#] Mary F. Mahon,[#] Stuart A. Macgregor,*[,§] and Michael K. Whittlesey*[,#]

[#]Department of Chemistry, University of Bath, Claverton Down, Bath BA2 7AY, U.K.
[§]Institute of Chemical Sciences, Heriot-Watt University, Edinburgh EH14 4AS, U.K.

Supporting Information

ABSTRACT: Reaction of $[Ru(IPr)_2(CO)H]BAr^F_4$ with $ZnEt_2$ forms the heterobimetallic species $[Ru(IPr)_2(CO)ZnEt]BAr^F_4$ (**2**), which features an unsupported Ru-Zn bond. **2** reacts with H_2 to give $[Ru(IPr)_2(CO)(\eta^2\text{-}H_2)(H)_2ZnEt]BAr^F_4$ (**3**) and $[Ru(IPr)_2(CO)(H)_2ZnEt]BAr^F_4$ (**4**). DFT calculations indicate that H_2 activation at **2** proceeds via oxidative cleavage at Ru with concomitant hydride transfer to Zn. **2** can also activate hydridic E-H bonds (E = B, Si), and computed mechanisms for the facile H/H exchange processes observed in **3** and **4** are presented.

Metal−ligand cooperativity is a widely used strategy for the activation and catalytic transformation of small molecules.[1] Many such systems are predicated on transition metal−Lewis base (TM-LB) combinations,[2,3] as well as those featuring electronically flexible ligand scaffolds, exemplified by Milstein's (de)aromatization approach.[4] More recently, TM-LA (LA = Lewis acid) cooperativity has (re)emerged,[5] with reports of H_2 cleavage,[6] the activation of C-H and more polar E-H bonds,[6a,f,7] and, in some cases, involvement in catalytic processes.[6a,b,7,8] To date, such TM-LA cooperativity has been dominated by cases where the LA is a B or Al center that is brought into proximity with the TM via a constrained geometry ligand, typically a bi- or polydentate P- or N-based species.[6−9] Herein, we report on the preparation and reactivity of a novel TM-LA system, $[Ru(IPr)_2(CO)ZnEt]BAr^F_4$ (**2**),[10] which features a direct, unsupported Ru-Zn bond and is accessed via the simple addition of $ZnEt_2$ to $[Ru(IPr)_2(CO)H]BAr^F_4$ (**1**).[11] Complex **2** can activate H_2 with net addition across the Ru-Zn bond to give $[Ru(IPr)_2(CO)(\eta^2\text{-}H_2)(H)_2ZnEt]BAr^F_4$ (**3**).[12] The observation of facile intramolecular H/H exchange in **3**, along with DFT calculations, highlights the ability of the TM-LA {Ru-Zn} moiety to act as a flexible and reversible hydride shuttle.

In line with the reported electrophilic reactivity of the hydride ligand in $[Ru(IPr)_2(CO)H]BAr^F_4$ (**1**),[11] addition of 1 equiv of $ZnEt_2$ to a fluorobenzene solution of this species gave the Ru-Zn complex **2** (Scheme 1), which was isolated as a red solid in 76% yield. ^{1}H NMR spectroscopy confirmed the absence of any hydride ligand in **2** as well as the presence of a single ZnEt group on the basis of the 8:3:2 ratio of ^{i}Pr methine protons to low-frequency signals at δ 0.73 (CH_3) and δ −0.11 (CH_2).

Upon shaking a C_6H_5F solution of **2** under H_2 (1 atm), there was an instantaneous color change (deep red to colorless) resulting from the formation of the novel dihydrogen dihydride complex $[Ru(IPr)_2(CO)(\eta^2\text{-}H_2)(H)_2ZnEt]BAr^F_4$ (**3**, Scheme 1). The ^{1}H NMR spectrum of **3** exhibited two hydride resonances, a broad signal at δ −5.33 and a sharp peak at δ −12.13, in a relative ratio of 3:1. Cooling to −28 °C resolved the broad resonance into two signals (relative ratio 2:1) at δ −5.09 and −7.79 (with T_1 values of 31 and 72 ms, respectively),[13] assigned to $Ru(\eta^2\text{-}H_2)$ and Ru-H-Zn (trans to CO), respectively. Both signals remained broad, indicative of exchange; this was confirmed by exchange spectroscopy (EXSY) and magnetization transfer experiments (Figure S11). No exchange with the remaining Ru-H-Zn trans to dihydrogen (δ −12.13, T_1 = 809 ms; T_1(min) = 638 ms (CD_2Cl_2, 400 MHz, −41 °C)) was found. However, upon exposure of **3** to 1 atm D_2, ^{1}H and ^{2}H NMR spectra showed unequivocally that all three sites underwent a slower chemical exchange, with deuterium incorporated into the $Ru(\eta^2\text{-}H_2)$ and at both Ru-H-Zn positions.

The η^2-H_2 ligand in **3** proved hard to dissociate, with only ca. 20% conversion to $[Ru(IPr)_2(CO)(H)_2ZnEt]BAr^F_4$ (**4**) apparent, even after a C_6H_5F solution of **3** was evaporated to complete dryness. In fact, full conversion to **4** required heating a solid sample of **3** at 50 °C under dynamic vacuum for 24 h. Subjecting solid **3** to vacuum/heat for further time (ca. 72 h) showed that all four hydride ligands could be removed, although re-formation of **2** was also accompanied by additional, unidentified side products. Complex **4** displayed a low-frequency (δ −27.06) Ru-H-Zn signal, which now exchanged on the NMR time scale (magnetization transfer and EXSY measurements, Figure S12), with a second Ru-H-Zn resonance at δ −3.75.

The molecular structures of the cations in **2**, **3**, and **4** are shown in Figure 1, along with a comparison to computed data for the central $\{Ru(H)_nZn\}$ moieties in each case (n = 0, 4, and 2, respectively). **2** exhibits a Ru-Zn distance of 2.4069(7) Å[14] and

Scheme 1. Formation and Reactivity of 2−4[a]

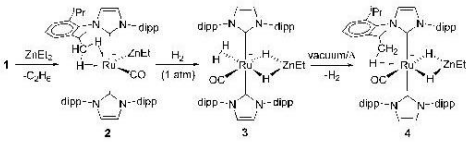

[a]dipp = 2,6-diisopropylphenyl. BAr^F_4 anions not shown.

Received: May 21, 2016
Published: August 4, 2016

DOI: 10.1021/jacs.6b05243
J. Am. Chem. Soc. 2016, 138, 11081−11084

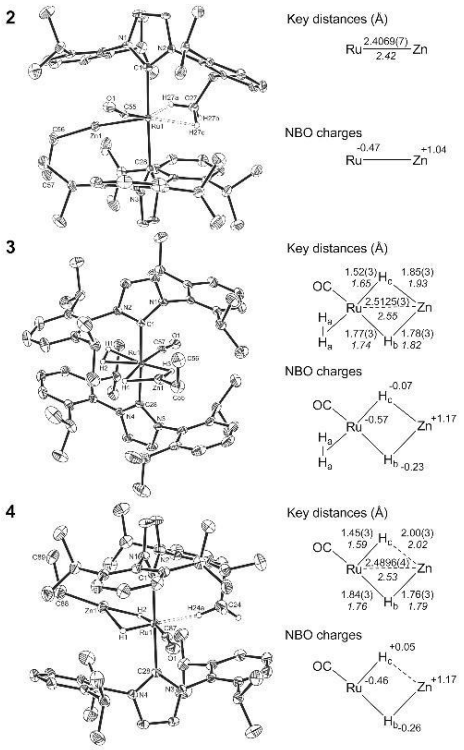

Figure 1. Molecular structures of the cations in **2**, **3**, and **4**. Thermal ellipsoids are shown at 30%. All non-hydride and non-agostic H-atoms are omitted for clarity. Also shown are comparisons of the key experimental and (in italics) computed distances around the central {Ru-Zn} moiety, along with the accompanying NBO charges.

also features two short Ru···H-C agostic interactions to one of the IPr ligands (Ru(1)···H(27A)-C(27), 2.13(3) Å; Ru(1)···H-(27C)-C(27), 2.31(4) Å), similar to those seen previously in **1**.[11] In **3** and **4**, the η^2-H_2 and hydride hydrogens were included in the model, the latter being refined without restraint. Both of these species have elongated Ru-Zn distances (2.5125(3) and 2.4896(4) Å, respectively) and have distinctly asymmetric {Ru(H)$_2$Zn} moieties that reflect the relative trans influences of the ligands completing the coordination sphere. Thus, the bridging hydrides trans to CO in **3** and **4** are approximately evenly shared between Ru and Zn, whereas the hydride trans to η^2-H_2 in **3** is significantly closer to Ru. This asymmetry is even more marked for the hydride trans to the agostic interaction in **4**.

DFT calculations[15] provide good absolute agreement for the Ru-Zn distances as well as the various Ru-H and Zn-H distances in **2**, **3**, and **4**, allowing for the inherent uncertainty in the H-atom positions (see Figure 1, right-hand side). NBO calculations characterize **2** as a Ru(0) species interacting with a cationic {ZnEt}$^+$ moiety via Ru→Zn σ-donation. In contrast, no significant direct Ru-Zn interaction is seen in either **3** or **4** (see Supporting Information for full details and orbital plots). NPA

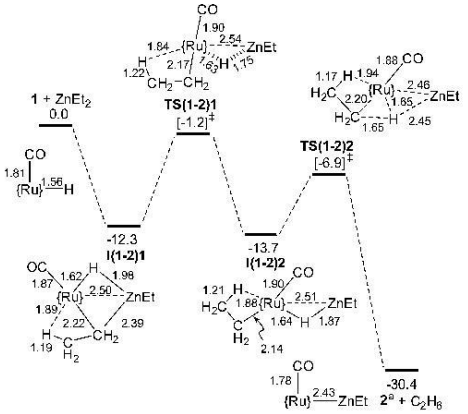

Figure 2. Computed reaction profile (free energy, kcal/mol) for the formation of **2** and C_2H_6 from **1** and $ZnEt_2$. Schematic structures show key distances (Å) within the equatorial plane; {Ru} = Ru(IPr)$_2^+$. An ethane σ-complex, **I(1-2)3**, generated from **TS(1-2)2** is omitted for clarity. [a]Non-agostic isomer of **2** located.

charges were used to characterize the nature of the hydride ligands. These indicate that the more evenly shared hydrides, H_b (trans to CO in **3** and **4**), exhibit a significant negative charge (q_H = −0.23 and −0.26, respectively), while this reduces and becomes positive as the hydride moves closer to Ru (H_c: q_H = −0.07 trans to η^2-H_2 in **3**; q_H = +0.05 trans to the agostic in **4**). For comparison, the terminal hydride in **1** (which lies trans to a vacant site) has q_H = +0.16. H_c in **4** therefore more resembles a terminal Ru-hydride. Indeed, an Atoms in Molecules study on **4** shows the absence of any Zn···H_c bond path (Figure S14).[16] The {Ru(H)$_2$Zn} moieties in these species are therefore structurally flexible and able to access both bridging and terminal hydride character, depending on the precise coordination environment.

Although examples of {M(H)$_n$Zn} complexes exist for M = Ru,[17] as well as for other late TMs,[18] these all result from metal hydride precursors, and, to the best of our knowledge, formation via bimetallic M-Zn cleavage of H_2 has no precedent.[19,20] We have therefore used DFT calculations to study the formation of **2** as well as its onward reactivity with H_2 to **3** and **4**. Figure 2 indicates that the initial addition of $ZnEt_2$ to **1** forms an intermediate **I(1-2)1** at −12.3 kcal/mol in which the {Ru-Zn} moiety is bridged by both a hydride and an ethyl ligand; the latter also engages in a β-agostic interaction with the Ru center. Ethyl group transfer onto Ru proceeds via **TS(1-2)1** with a barrier of 11.1 kcal/mol and is induced by rotation of the {Ru(H)Zn} moiety, the movement of the bridging hydride below the equatorial coordination plane allowing the CO ligand to move trans to the developing Ru-Et ligand (**I(1-2)2**, −13.7 kcal/mol). The bridging hydride can now couple with the adjacent ethyl group via **TS(1-2)2** at −6.9 kcal/mol, leading, after release of ethane, to the formation of **2** at −30.4 kcal/mol. In this case, an alternative isomer of **2** devoid of agostic interactions is located, similar to the situation described previously for **1**, for which several isomers were also found.[11]

Figure 3 shows one possible mechanism for the reaction of **2** with H_2 to give **3** and **4**. Addition of two molecules of H_2 to **2** forms the bis-η^2-H_2 intermediate **I(2-3)1** at −32.1 kcal/mol. A very flat free energy surface then sees an essentially barrierless

DOI: 10.1021/jacs.6b05243
J. Am. Chem. Soc. 2016, 138, 11081−11084

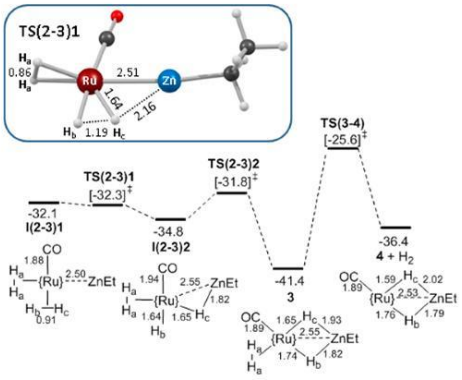

Figure 3. Computed reaction profile (free energy, kcal/mol) for the formation of **3** and **4** from **2**. Schematic structures show key distances (Å) within the equatorial plane, as well as the labeling scheme for the H-atoms; {Ru} = $Ru(IPr)_2^+$. Inset: Geometry of H_2 activation transition state **TS(2-3)1** (IPr ligands omitted).

cleavage of the H_b-H_c ligand, with net addition over the Ru-Zn bond to give **I(2-3)2** at −34.8 kcal/mol. Rotation about the Ru···Zn vector then allows transfer of H_b onto Zn to form **3** at −41.4 kcal/mol. H_2 loss from **3** is computed to be kinetically accessible ($\Delta G^{\ddagger}$ = 15.8 kcal/mol) but endergonic, **4** (+H_2) lying 5 kcal/mol above **3**. This is consistent with the observed reluctance of **3** to lose H_2.

The computed structure of the key H_2 activation transition state **TS(2-3)1** (inset, Figure 3) exhibits an elongated H_b-H_c moiety (1.19 Å, cf. 0.91 Å in **I(2-3)1**). At this point the Zn···H_c distance of 2.16 Å implies little, if any, interaction with the Zn center, and it is only after the cleavage that the Zn participates by accepting a hydride ligand. In addition, minimal polarization of the H_b-H_c bond is computed in the transition state (q_{Hb} = +0.05; q_{Hc} = +0.02). We therefore propose that H_2 activation occurs via oxidative cleavage mediated by Ru, followed by hydride transfer to Zn. In support of Ru being the key player in the H_2 cleavage, the activation of H_a-H_a trans to Zn in **I(2-3)1** was also characterized: this proceeds via a structurally similar transition state at −28.6 kcal/mol, which leads to a $Ru(\eta^2\text{-}H_2)(H)_2$ complex in which the Zn is unable to accept either hydride (Figure S17).

The mechanisms of H/H exchange in **3** and **4** have also been modeled. For **3**, exchange occurs between the η^2-H_2 ligand and the cis bridging hydride (H_a/H_b exchange) as well as between the two chemically distinct bridging hydrides (H_b/H_c exchange). H_b/H_c exchange can proceed via the mechanism in Figure 3, with reversible formation of the bis-η^2-H_2 complex **I(2-3)1** and rotation of the H_b-H_c ligand. The latter occurs via a transition state at −28.3 kcal/mol, giving an overall exchange barrier of 13.1 kcal/mol. For H_a/H_b exchange, a σ-CAM process[21] was characterized that sees formation of the H_a/(η^2-H_a-H_b) complex, **I(3-3′)** (Figure 4a). H_a-H_b rotation and reversal of the σ-CAM completes the exchange, the rotation transition state being the highest point in this process and equating to an overall barrier of 9.8 kcal/mol. The lower barrier for H_a/H_b exchange is consistent with the EXSY experiments indicating that only that process proceeded on the NMR time scale.[22] H_b/H_c exchange in **4** proceeds by a mechanism similar to that in **3** (Figure 4b). Thus, initial rotation about the Ru···Zn vector cleaves the Zn-H_b bond and forms **I(4-4′)1**; H_c can then transfer onto H_b to form the η^2-H_b-H_c complex **I(4-4′)2**. H_2 rotation and reversal of these processes complete the exchange. The highest transition states in this process are at −22.9 kcal/mol and correspond to an overall barrier of 13.5 kcal/mol. In principle, movement of the CO ligand from trans to H_b to trans to H_c would also render these two sites equivalent. However, this process has a barrier of 31.5 kcal/mol as it passes through a symmetrical Y-shaped {RuCO(H)$_2$} moiety, which is strongly disfavored for a d^6 configuration.[23]

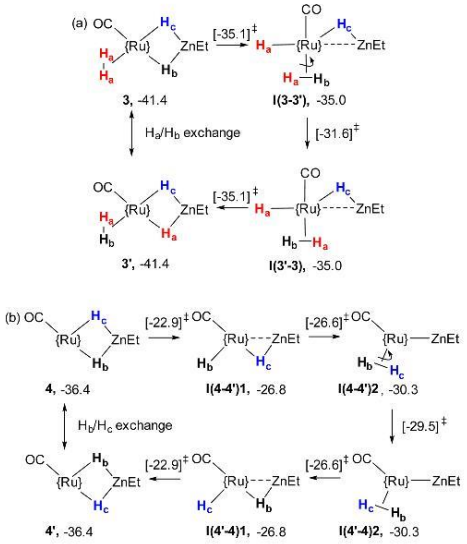

Figure 4. Computed mechanisms (free energy, kcal/mol) for (a) H_a/H_b in **3** and (b) H_b/H_c in **4**; {Ru} = $Ru(IPr)_2^+$. Transition-state energies for each step are given in square brackets.

To probe whether other E-H bonds could add across the Ru-Zn bond in **2**, preliminary investigations with both protic and hydridic reagents have been undertaken. NH_3 simply coordinated to form the ammonia complex [Ru(IPr)$_2$(CO)(NH_3)ZnEt]-$BAr^F{}_4$ (**5**, Figure S13). With HBcat and $PhSiH_3$, room-temperature dehydrogenation took place to give **3** as the major Ru-containing product of both reactions. Surprisingly, even a 1:1 ratio of **2**:HBcat generated hydride signals characteristic of **3**, suggesting that a strong driving force exists for formation of the {Ru(H)$_2$Zn} moiety. ^{11}B NMR spectroscopy confirmed the formation of B_2cat_2 (δ 31) but also showed a second major product at δ 22, consistent with the formation of B_2cat_3.[24] In the reaction of **2** with $PhSiH_3$, ^{29}Si NMR spectroscopy showed that Ph_3SiH and Ph_2SiH_2 were the major Si-containing reaction products, although a number of other, lower intensity signals were also present which we believe arise from the presence of three reactive Si-H bonds in the starting material, as well as the need for SiH_4 formation for atom balance. There is a clear silane dependence to this chemistry since no reaction was seen between **2** and either Ph_2SiH_2 or $PhMe_2SiH$. Further studies are required to elucidate the pathways of the borane/silane dehydrogenation reactions.

In conclusion, we have described the facile formation of a TM-LA heterobimetallic species, **2**, featuring an unconstrained and

DOI: 10.1021/jacs.6b05243
J. Am. Chem. Soc. 2016, 138, 11081−11084

unsupported Ru-Zn bond. This species is a rare example of an active TM-LA system derived from a non-group 13 element LA: **2** reacts directly with H_2 to form the $\{Ru(H)_2Zn\}$ species **3** and then **4**. DFT calculations indicate that H_2 activation proceeds via oxidative cleavage at Ru, with the adjacent Zn acting as a (reversible) hydride acceptor. H/H exchange experiments and calculations on **3** and **4** show that intermediates with unsupported Ru-Zn bonds retain kinetic accessibility even after H_2 addition. This, along with the observation of the activation of hydridic E-H bonds (E = B, Si), suggests that such unconstrained hetero-bimetallic TM-LA species may have potential applications in catalysis, and this possibility is being pursued in our laboratories.

■ ASSOCIATED CONTENT

Supporting Information

The Supporting Information is available free of charge on the ACS Publications website at DOI: 10.1021/jacs.6b05243.

Cartesian coordinates of all computed structures (XYZ)
Crystallographic data for **2**−**5** (CIF)
Synthesis, characterization, and computational data, including Figures S1−S23 and Tables S1−S4 (PDF)

■ AUTHOR INFORMATION

Corresponding Author

*s.a.macgregor@hw.ac.uk; m.k.whittlesey@bath.ac.uk

Notes

The authors declare no competing financial interest.

■ ACKNOWLEDGMENTS

We acknowledge financial support from the EPSRC (grant EP/J009962/1 for I.M.R.) and Heriot-Watt University (James Watt Scholarship to N.A.R.). We thank Prof. Ged Parkin for enlightening and very valuable discussions.

■ REFERENCES

(1) (a) Cooper, B. G.; Napoline, J. W.; Thomas, C. M. *Catal. Rev.: Sci. Eng.* **2012**, *54*, 1. (b) van der Vlugt, J. I. *Eur. J. Inorg. Chem.* **2012**, *2012*, 363. (c) Eisenstein, O.; Crabtree, R. H. *New J. Chem.* **2013**, *37*, 21. (d) Khusnutdinova, J. R.; Milstein, D. *Angew. Chem., Int. Ed.* **2015**, *54*, 12236. (e) Bouhadir, G.; Bourissou, D. *Chem. Soc. Rev.* **2016**, *45*, 1065.

(2) For LB = N, see: (a) Noyori, R.; Ohkuma, T. *Angew. Chem., Int. Ed.* **2001**, *40*, 40. (b) Sandoval, C. A.; Ohkuma, T.; Muñiz, K.; Noyori, R. *J. Am. Chem. Soc.* **2003**, *125*, 13490. (c) Maire, P.; Büttner, T.; Breher, F.; Le Floch, P.; Grützmacher, H. *Angew. Chem., Int. Ed.* **2005**, *44*, 6318. (d) Friedrich, A.; Drees, M.; Schmedt auf der Günne, J.; Schneider, S. *J. Am. Chem. Soc.* **2009**, *131*, 17552.

(3) For LB = O or S, see: (a) Sweeney, Z. K.; Polse, J. L.; Bergman, R. G.; Andersen, R. A. *Organometallics* **1999**, *18*, 5502. (b) Linck, R. C.; Pafford, R. J.; Rauchfuss, T. B. *J. Am. Chem. Soc.* **2001**, *123*, 8856. (c) Sellmann, D.; Prakash, R.; Heinemann, F. W.; Moll, M.; Klimowicz, M. *Angew. Chem., Int. Ed.* **2004**, *43*, 1877. (d) Ohki, Y.; Sakamoto, M.; Tatsumi, K. *J. Am. Chem. Soc.* **2008**, *130*, 11610. (e) Matsumoto, T.; Nakaya, Y.; Itakura, N.; Tatsumi, K. *J. Am. Chem. Soc.* **2008**, *130*, 2458. (f) Klare, H. F. T.; Oestreich, M.; Ito, J.; Nishiyama, H.; Ohki, Y.; Tatsumi, K. *J. Am. Chem. Soc.* **2011**, *133*, 3312.

(4) Gunanathan, C.; Milstein, D. *Acc. Chem. Res.* **2011**, *44*, 588.

(5) For early work on TM-LA complexes, see: (a) St Denis, J. N.; Butler, W.; Glick, M. D.; Oliver, J. P. *J. Organomet. Chem.* **1977**, *129*, 1. (b) Burlitch, J. M.; Leonowicz, M. E.; Petersen, R. B.; Hughes, R. E. *Inorg. Chem.* **1979**, *18*, 1097. For recent, pertinent reviews, see: (c) Amgoune, A.; Bourissou, D. *Chem. Commun.* **2011**, *47*, 859. (d) Maity, A.; Teets, T. S. *Chem. Rev.* **2016**, *116*, 8873.

(6) (a) Harman, W. H.; Peters, J. C. *J. Am. Chem. Soc.* **2012**, *134*, 5080. (b) Lin, T. P.; Peters, J. C. *J. Am. Chem. Soc.* **2013**, *135*, 15310. (c) Zeng, G.; Sakaki, S. *Inorg. Chem.* **2013**, *52*, 2844. (d) Harman, W. H.; Lin, T.-P.; Peters, J. C. *Angew. Chem., Int. Ed.* **2014**, *53*, 1081. (e) Cowie, B. E.; Emslie, D. J. H. *Chem. - Eur. J.* **2014**, *20*, 16899. (f) Barnett, B. R.; Moore, C. E.; Rheingold, A. L.; Figueroa, J. S. *J. Am. Chem. Soc.* **2014**, *136*, 10262. (g) Devillard, M.; Bouhadir, G.; Bourissou, D. *Angew. Chem., Int. Ed.* **2015**, *54*, 730. (h) Li, Y.; Hou, C.; Jiang, J.; Zhang, Z.; Zhao, C.; Page, A. J.; Ke, Z. *ACS Catal.* **2016**, *6*, 1655. (i) Devillard, M.; Declercq, R.; Nicolas, E.; Ehlers, A. W.; Backs, J.; Saffon-Merceron, N.; Bouhadir, G.; Slootweg, J. C.; Uhl, W.; Bourissou, D. *J. Am. Chem. Soc.* **2016**, *138*, 4917.

(7) (a) Fong, H.; Moret, M.-E.; Lee, Y.; Peters, J. C. *Organometallics* **2013**, *32*, 3053. (b) MacMillan, S. N.; Harman, W. H.; Peters, J. C. *Chem. Sci.* **2014**, *5*, 590. (c) Nesbit, M. A.; Suess, D. L. M.; Peters, J. C. *Organometallics* **2015**, *34*, 4741.

(8) (a) Tsoureas, N.; Kuo, Y.-Y.; Haddow, M. F.; Owen, G. R. *Chem. Commun.* **2011**, *47*, 484. (b) Cammarota, R. C.; Lu, C. C. *J. Am. Chem. Soc.* **2015**, *137*, 12486.

(9) (a) Bontemps, S.; Bouhadir, G.; Gu, W.; Mercy, M.; Chen, C.-H.; Foxman, B. M.; Maron, L.; Ozerov, O. V.; Bourissou, D. *Angew. Chem., Int. Ed.* **2008**, *47*, 1481. (b) Sircoglou, M.; Bontemps, S.; Bouhadir, G.; Saffon, N.; Miqueu, K.; Gu, W.; Mercy, M.; Chen, C.-H.; Foxman, B. M.; Maron, L.; Ozerov, O. V.; Bourissou, D. *J. Am. Chem. Soc.* **2008**, *130*, 16729. (c) Rudd, P. A.; Liu, S.; Gagliardi, L.; Young, V. G.; Lu, C. C. *J. Am. Chem. Soc.* **2011**, *133*, 20724. (d) Cowie, B. E.; Tsao, F. A.; Emslie, D. J. H. *Angew. Chem., Int. Ed.* **2015**, *54*, 2165.

(10) IPr = 1,3-bis(2,6-diisopropylphenyl)imidazol-2-ylidene; BAr^F_4 = $B\{C_6H_3(3,5\text{-}CF_3)_2\}_4^-$.

(11) Riddlestone, I. M.; McKay, D.; Gutmann, M. J.; Macgregor, S. A.; Mahon, M. F.; Sparkes, H. A.; Whittlesey, M. K. *Organometallics* **2016**, *35*, 1301.

(12) For a recent review of molecular Zn-H complexes, see: Wiegand, A.-K.; Rit, A.; Okuda, J. *Coord. Chem. Rev.* **2016**, *314*, 71.

(13) In CD_2Cl_2 (−28 °C), T_1 = 47 ms for the Ru-H-Zn resonance at δ −7.79. See SI.

(14) (a) Cadenbach, T.; Bollermann, T.; Gemel, C.; Tombul, M.; Fernandez, I.; von Hopffgarten, M.; Frenking, G.; Fischer, R. A. *J. Am. Chem. Soc.* **2009**, *131*, 16063. (b) Bollermann, T.; Gemel, C.; Fischer, R. A. *Coord. Chem. Rev.* **2012**, *256*, 537.

(15) Calculations were run with the Gaussian programs employing the BP86 functional. Free energies include corrections for fluorobenzene solvent and dispersion effects. See SI for references and full details, as well as functional testing.

(16) As the nature of the hydrides in the $\{Ru(H)_2Zn\}$ moiety is ambiguous, we did not adopt the half-arrow formalism of Parkin et al.: Green, J. C.; Green, M. L. H.; Parkin, G. *Chem. Commun.* **2012**, *48*, 11481.

(17) (a) Ohashi, M.; Matsubara, K.; Iizuka, T.; Suzuki, H. *Angew. Chem., Int. Ed.* **2003**, *42*, 937. (b) Ohashi, M.; Matsubara, K.; Suzuki, H. *Organometallics* **2007**, *26*, 2330. (c) Plois, M.; Hujo, W.; Grimme, S.; Schwickert, C.; Bill, E.; de Bruin, B.; Pöttgen, R.; Wolf, R. *Angew. Chem., Int. Ed.* **2013**, *52*, 1314. (d) Molon, M.; Gemel, C.; Fischer, R. A. *Eur. J. Inorg. Chem.* **2013**, *2013*, 3616. (e) Plois, M.; Wolf, R.; Hujo, W.; Grimme, S. *Eur. J. Inorg. Chem.* **2013**, *2013*, 3039.

(18) (a) Geerts, R. L.; Huffman, J. C.; Caulton, K. G. *Inorg. Chem.* **1986**, *25*, 590. (b) Fryzuk, M. D.; McConville, D. H.; Rettig, S. J. *Organometallics* **1993**, *12*, 2152. (c) Ekkert, O.; White, A. J. P.; Toms, H.; Crimmin, M. R. *Chem. Sci.* **2015**, *6*, 5617.

(19) For examples of Zn-H bond formation by activation of H_2, see: (a) Jochmann, P.; Stephan, D. W. *Angew. Chem., Int. Ed.* **2013**, *52*, 9831. (b) Jochmann, P.; Stephan, D. W. *Chem. Commun.* **2014**, *50*, 8395.

(20) Fafard, C. M.; Chen, C.-H.; Foxman, B. M.; Ozerov, O. V. *Chem. Commun.* **2007**, 4465.

(21) Perutz, R. N.; Sabo-Etienne, S. *Angew. Chem., Int. Ed.* **2007**, *46*, 2578.

(22) A pathway linking **I(2-3)2** (Figure 3) to **I(3-3′)** (Figure 4a) was also characterized and provides an alternative route from **2** to **3** via a transition state at −31.2 kcal/mol (see Figure S18).

(23) Riehl, J.-F.; Jean, Y.; Eisenstein, O.; Pélissier, M. *Organometallics* **1992**, *11*, 729.

(24) Westcott, S. A.; Blom, H. P.; Marder, T. B.; Baker, R. T.; Calabrese, J. C. *Inorg. Chem.* **1993**, *32*, 2175.

DOI: 10.1021/jacs.6b05243
J. Am. Chem. Soc. 2016, 138, 11081−11084

ChemPubSoc Europe

DOI: 10.1002/chem.201705796

CHEMISTRY
A European Journal
Full Paper

Heterobimetallic Complexes

Well-Defined Heterobimetallic Reactivity at Unsupported Ruthenium–Indium Bonds

Ian M. Riddlestone,*[a] Nasir A. Rajabi,[b] Stuart A. Macgregor,*[b] Mary F. Mahon,*[a] and Michael K. Whittlesey*[a]

Abstract: The hydride complex $[Ru(IPr)_2(CO)H][BAr^F{}_4]$, **1**, reacts with $InMe_3$ with loss of CH_4 to form $[Ru(IPr)_2(CO)(InMe)(Me)][BAr^F{}_4]$, **4**, featuring an unsupported Ru–In bond with unsaturated Ru and In centres. **4** reacts with H_2 to give $[Ru(IPr)_2(CO)(\eta^2\text{-}H_2)(InMe)(H)][BAr^F{}_4]$, **5**, while CO induces formation of the indyl complex $[Ru(IPr)_2(CO)_3(InMe_2)][BAr^F{}_4]$, **7**. These observations highlight the ability of Me to shuttle between Ru and In centres and are supported by DFT calculations on the mechanism of formation of **4** and its reactions with H_2 and CO. An analysis of Ru-In bonding in these species is also presented. Reaction of **1** with $GaMe_3$ also involves CH_4 loss but, in contrast to its In congener, sees IPr transfer from Ru to Ga to give a gallyl complex featuring an η^6 interaction of one aryl substituent with Ru.

Introduction

Heterobimetallic complexes featuring bonds between transition metals (TMs) and Group 13 (Gp 13) elements have received considerable recent attention[1] due to their ability to bring about stoichiometric and catalytic reactions (Scheme 1) of small molecules through co-operative effects.[2] Thus, TM–B systems have been developed for catalytic hydrogenation and hydrosilylation by Peters (TM = Fe, Co and Ni)[3] and Szymczyk (Ru),[4] while Takaya and Iwasawa reported a Pd–Al catalyst for CO_2 hydrosilylation.[5] Moving to the heavier Gp 13 congeners, Lu and co-workers combined Ni and Ga to bring about the hydrogenation of both alkenes and CO_2.[6,7] One fundamental question that arises in these systems is whether the Gp 13 element acts cooperatively with the TM to bring about substrate activation and catalysis, or whether it participates indirectly as a ligand that tunes the properties of the TM centre.[8]

In the above examples the Gp 13 element is tethered to the TM centre by incorporation into a polydendate metalloligand scaffold. An alternative approach is to strip away the scaffold to leave two coordinatively unsaturated metals held together by an "unsupported" bond.[9] We recently described such a complex with an unsupported TM-Gp 12 bond, $[Ru(IPr)_2(CO)(ZnEt)][BAr^F{}_4]$ (**1**→**2**, Scheme 2).[10] This readily adds H_2 across the Ru–Zn bond to give **3**. DFT calculations showed that the Zn centre acts as a reversible hydride acceptor that participates directly in bond cleavage. Examples of unsupported TM-Gp 13 bonds formed by combining TM-hydrides and Gp 13 alkyls have been described before.[11,12] None of these, however, feature coordinative unsaturation at both centres and so their reactivity towards small molecules is necessarily limited.[13] Herein, we describe the reactivity of Ru-hydride **1** with $InMe_3$ to afford $[Ru(IPr)_2(CO)(InMe)(Me)][BAr^F{}_4]$, **4**, which features an unsupported Ru–In bond. As a result, **4** exhibits well-defined reactivity with both H_2 and CO. The mechanism of formation of **4** and its reactivity with CO highlight how the Ru–In bond can accommodate Me transfer between the two metal centres. In contrast to the In chemistry, the reaction of **1** with $GaMe_3$ results in transfer of a carbene ligand from the TM to the Group 13 element.

[a] Dr. I. M. Riddlestone, Dr. M. F. Mahon, Prof. M. K. Whittlesey
Department of Chemistry
University of Bath
Claverton Down
Bath, BA2 7AY (United Kingdom)
E-mail: ianriddlestone@aol.com
m.f.mahon@bath.ac.uk
m.k.whittlesey@bath.ac.uk

[b] N. A. Rajabi, Prof. S. A. Macgregor
Institute of Chemical Sciences
Heriot-Watt University
Edinburgh, EH14 4AS (United Kingdom)
E-mail: S.A.Macgregor@hw.ac.uk

Supporting information and the ORCID identification number(s) for the author(s) of this article can be found under https://doi.org/10.1002/chem.201705796.

Results and Discussion

Reaction of 1 with $InMe_3$

Addition of around 1 equivalent $InMe_3$ to a fluorobenzene solution of **1** gave an immediate colour change from orange–red to deep red, loss of the Ru–H resonance for **1** at $\delta = -23.69$ ppm in the ^1H NMR spectrum (presumably through elimination of CH_4) and the appearance of two new methyl signals in a 1:1 ratio at $\delta = 0.08$ and -0.96 ppm. The new product was identified as the Ru–In complex $[Ru(IPr)_2(CO)(InMe)(Me)][BAr^F{}_4]$ (**4**, Scheme 3), which was isolated in 66% yield and

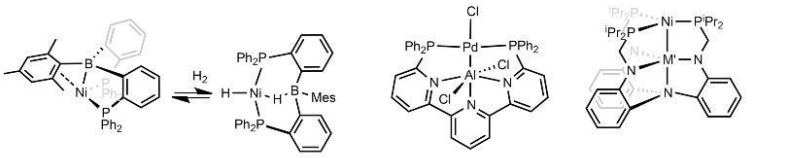

Scheme 1. Catalytically active TM-Gp 13 element heterobimetallic complexes.

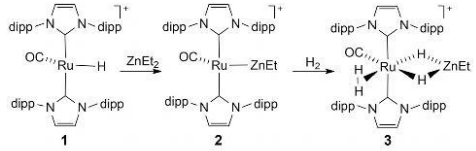

Scheme 2. Formation of $[Ru(IPr)_2(CO)(ZnEt)]^+$ (**2**; dipp = 2,6-diisopropylphenyl). Agostic interactions involving the IPr ligands in **1** and **2** and the $[BAr^F_4]^-$ anions in **1**–**3** are omitted for clarity.

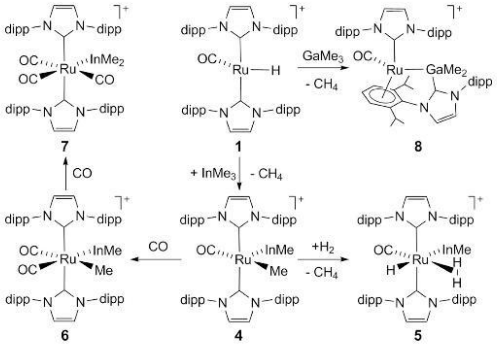

Scheme 3. Summary of the reactivity of **1** (dipp = 2,6-diisopropylphenyl) with EMe_3 to give **4** (E = In) and **8** (E = Ga) and the onward reactivity of **4** with H_2 and CO to form **5** and **7** respectively. $[BAr^F_4]^-$ anions are omitted for clarity.

characterised via NMR spectroscopy and X-ray crystallography. The molecular structure of **4** (Figure 1) displayed a square-pyramidal geometry at Ru with a slightly bent axial InMe ligand(∢Ru-In-C = 171.91(19)°) and a Ru–In distance of 2.4534(3) Å.[11c,14] The central imidazol-2-ylidene rings of the two IPr ligands were approximately co-planar with the Ru–In bond and exhibited a distinct in-plane tilting toward the vacant site on ruthenium to accommodate the InMe moiety.

Disorder about the OC-Ru-Me axis precluded discussion of the associated metrics, however, DFT calculations (see Computational Details in the Experimental section) provided a good comparison with the overall structure, yielding computed Ru–In, Ru–C(O) and Ru–Me distances of 2.45, 1.86 and 2.23 Å respectively. The calculated structure also indicated a movement of the InMe moiety toward the Me ligand (∢In-Ru-Me = 69.9°, ∢In-Ru-C(O) = 105.9°).

The reaction of **4** with 1 atm H_2 resulted in further alkane elimination and coordination of dihydrogen to afford $[Ru(IPr)_2(CO)(\eta^2\text{-}H_2)(InMe)(H)][BAr^F_4]$ (**5**, Scheme 3). **5** showed a single broad resonance of relative integral 3 in the low frequency region ($\delta = -6.39$ ppm) of the ^1H NMR spectrum assigned to rapidly exchanging Ru–H and Ru(η^2-H_2) groups. A further signal, also of relative integral 3, at $\delta = -0.11$ ppm was assigned to the InMe group. Colourless crystals of **5** were isolated from fluorobenzene/hexane under a hydrogen atmosphere. The presence of H_2 proved necessary for complete stabilisation of **5**, as even isolated crystals of the complex developed a red tinge when left under an argon atmosphere, but rapidly reverted to colourless upon re-admission of H_2. More-

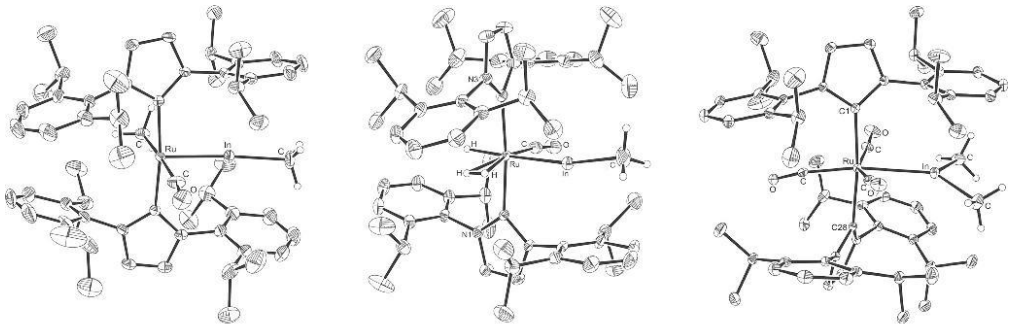

Figure 1. X-ray crystal structures of the cations in **4**, **5** and **7** (ellipsoids at 30% probability). Only one component of the disorder in **4** is shown, for clarity. Hydrogens are omitted with the exception of the In-Me substituents and those bonded to Ru in **5**.

over, the solution IR spectrum (C_6H_5F) showed two Ru–CO bands (1975, 1938 cm^{-1}) under Ar, but only the higher frequency band in an H_2-saturated solution. The molecular structure of **5** exhibited an elongated Ru–In distance of 2.5220(3) Å, likely due to the *trans* influence of the opposing hydride ligand.

Exposure of **4** to CO gave $[Ru(IPr)_2(CO)_3(InMe_2)][BAr^F_4]$ (**7**, Scheme 3) in which the additional CO ligands induced the migration of the originally Ru-bound methyl group back onto In. The molecular structure of the cation in **7** (Figure 1) revealed further elongation of the Ru–In distance to 2.7325(3) Å. The IPr ligands were again staggered and showed significant distortions due to the presence of the $InMe_2$ and three CO ligands in the equatorial plane. Of note is an out-of-plane pitch angle[15] of 166° involving the imidazol-2-ylidene ring based on C28.

In order to probe the pathway to formation of **7** in more detail, **4** was reacted with ^{13}CO at low temperature (245 K) and the reaction followed spectroscopically. An initial ^1H NMR spectrum showed a mixture of the starting material and a second species (ratio 1:0.7) believed to be $[Ru(IPr)_2(CO)_2(InMe)(Me)][BAr^F_4]$ (**6**, Scheme 3), which is simply the product of CO addition prior to Me migration. **6** showed two methyl proton resonances at $\delta = -0.17$ and 1.22 ppm (1:1 ratio) and a single ^{13}C enhanced carbonyl signal at $\delta = 200$ ppm.[16] Warming to ca. 267 K resulted in complete loss of **4**, while raising the temperature to 283 K brought about loss of **6** and the appearance of **7**, which was characterised by the presence of two ^{13}C enhanced doublet ($^2J(C,C) = 2$ Hz) carbonyl resonances at $\delta = 203$ and 193 ppm.[17]

Mechanisms for the formation of **4** and its onward reactions with H_2 and CO were modelled with DFT calculations, where we report free energies derived from optimisations with the BP86 functional in the gas-phase, corrected for the effects of dispersion and fluorobenzene solvent (see Computational Details, Experimental section). Addition of $InMe_3$ to **1** gives an adduct **I(1–4)1** ($G = +3.4$ kcal mol^{-1}, Figure 2), in which the {$InMe_3$} moiety is approximately co-planar with the {Ru(CO)H} unit and one Me has moved into a bridging position between Ru and In (Ru–C = 2.15 Å, In–C = 2.45 Å). This contrasts to the known Ru-indane complexes, *fac*-[Ru(NCMe)$_3$(CO)$_2$(InX$_3$)] (X=Cl, Br),[18] which exhibit tetrahedral In centres. This difference may reflect the steric bulk of the IPr ligands in **4**; however, the same side-on orientation is also computed with the smaller model systems, $[RuL_2(CO)(InMe_3)(H)]^+$, (L = IMe_2,[19] PH_3), and so presumably reflects the low-Lewis basicity of the e^--deficient Ru centre in **1**. For **I(1–4)1**, this is alleviated by the partial transfer of a Me group from In to Ru and the presence of an α-agostic C–H→Ru interaction. Indeed the computed Ru–In distance of 2.81 Å is consistent with a Ru-$InMe_2$ bond and this is confirmed by an Atoms in Molecules analysis that also highlights Ru–C and In–C bond paths to the bridging Me ligand (see below and Figure S14, Supporting Information).

The bridging Me group in **I(1–4)1** readily transfers from In to Ru via **TS(1–4)1** to give **I(1–4)2** at +6.4 kcal mol^{-1}. This occurs with a shortening of the Ru-In distance to 2.61 Å and movement of a second In-Me substituent into an incipient bridging position (Ru···C = 2.68 Å, In–C = 2.21 Å). Reductive coupling of

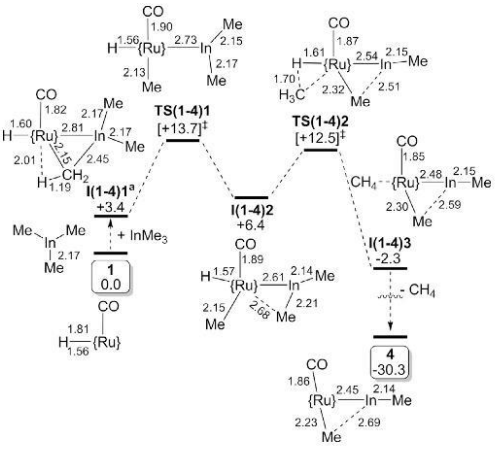

Figure 2. Computed reaction profile (free energy, kcal mol^{-1}, BP86(D3, C_6H_5F) level) for the formation of **4** and CH_4 from **1** and $InMe_3$; schematic structures show key distances (Å) within the equatorial plane; {Ru} = Ru(IPr)$_2$. [a] A more symmetrical isomer, **I(1–4)1′**, in which the {$InMe_3$} moiety is bound through two C–H→Ru σ-interactions was located at +6.7 kcal mol^{-1} (Figure S14, Supporting Information).

CH_4 proceeds with a barrier of 6.1 kcal mol^{-1} to give initially a methane σ-complex, **I(1–4)3** ($G = -2.3$ kcal mol^{-1}). The transfer of the second Me group onto Ru is further advanced at this stage and is completed upon CH_4 loss to give **4**. The formation of **4** from **1** and $InMe_3$ is computed to be strongly exergonic ($\Delta G = -30.3$ kcal mol^{-1}) and proceeds with a relatively low overall barrier (13.7 kcal mol^{-1}), consistent with an efficient room temperature process.

Computed profiles for the reactions of **4** with H_2 and CO are shown in Figure 3 (where species **4** is now set to 0.0 kcal mol^{-1}). With dihydrogen, an initial η^2-H_2 adduct, **I(4–5)1** is formed from which σ-CAM[20] activation of H_2 accesses methane σ-complex **I(4–5)2** at −6.3 kcal mol^{-1} with an overall barrier of 9.0 kcal mol^{-1}. CH_4/H_2 substitution then gives **5** at −18.5 kcal mol^{-1}. **4** also readily adds CO to give **6** at −14.0 kcal mol^{-1}. Me transfer onto the neighbouring InMe ligand then proceeds with a barrier of 10.4 kcal mol^{-1} to form the indyl intermediate **I(6–7)** ($G = -14.1$ kcal mol^{-1}). This species adds a second CO molecule to give **7** at −41.5 kcal mol^{-1}.[21]

The computed geometries in Figures 2 and 3 show a range of Ru–In distances, from 2.45 Å for species **4** to 2.84 Å in **I(6–7)**. For **5** and **7** the calculations slightly overestimate the Ru–In distances, a trend seen in related studies on dialkylgallyl adducts.[22] All computed Ru–In distances are below 2.88 Å, the sum of the covalent radii defined by Alvarez and co-workers.[23] Atoms-in Molecules (AIM) analyses accordingly locate Ru–In bond paths for **4**, **5** and **7**, although the associated bond critical points (BCPs) exhibit low electron densities, $\rho(r)$, and relatively small positive values for the Laplacian, $\nabla^2\rho(r)$ (Table 1). These data, along with the near-zero, but negative, total energy densities, $H(r)$, suggest closed-shell metal–metal inter-

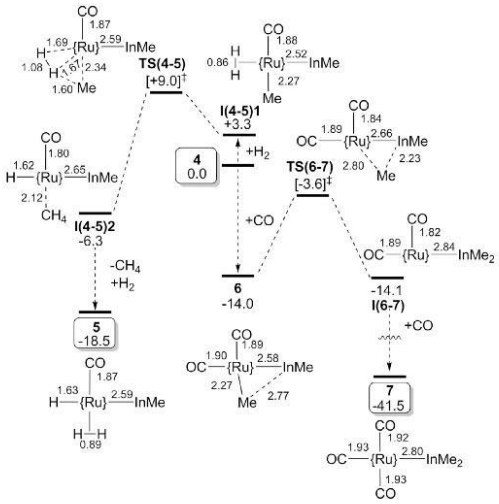

Figure 3. Computed reaction profile (free energy, kcal mol^{-1}, BP86(D3, C_6H_5F) level) for the reactions of **4** (centre) with H_2 and CO to form **5** (left) and **7** (right) respectively; schematic structures show key distances (Å) within the equatorial plane; {Ru} = $Ru(IPr)_2^+$.

Table 1. AIM bond critical point data associated with the Ru–In bond paths in **4**, **5** and **7** (see text for definitions).

Ru–In BCP	4	5	7
$\rho(r)$/eÅ^{-3}	+0.079	+0.061	+0.048
$\nabla^2\rho(r)$/eÅ^{-5}	+0.154	+0.099	+0.033
$H(r)$ (a.u.)	−0.028	−0.020	−0.014
Delocalisation Index	0.95	0.79	0.48

actions that exhibit a degree of dative–covalent character.[24] The Ru–In delocalization indices follow the trend in the computed distances.

The Ru–In bonding in **4**, **5** and **7** was also explored by computing the Pipek–Mezey localised orbitals. For **7**, the Ru-In σ-bonding orbital is dominated by Ru character (63% compared to 16% on In, see Figure 4); moreover, the Ru 4d_{xz} orbital exhibits negligible interaction with the $InMe_2$ ligand despite the availability of a formally vacant *p*-orbital on the latter. The Ru–In σ-bonding orbital is more evenly shared in **4** (Ru 62%; In 32%), while the polarisation reverses in **5** (Ru 37%; In 55%). No significant Ru–In π-interaction was seen in either **4** or **5** (Supporting Information).

Further insight into the Ru–$InMe_2$ interaction in **7** was obtained by comparing experimental CO stretching frequencies ($\tilde{\nu}_{CO}$ = 2003, 1977 cm^{-1}) with those of the analogous Ru^{II} hydride cation, $[Ru(IPr)_2(CO)_3H]^+$ ($\tilde{\nu}_{CO}$: 2040, 2025 cm^{-1}),[25] and the related Ru^0 species $[Ru(IMes)_2(CO)_3]$ ($\tilde{\nu}_{CO}$: 1950, 1879 and 1830 cm^{-1}; the IPr analogue is unknown).[26] These data suggest that **7** lies closer to the Ru^{II} species, but that it exhibits a more e$^-$-rich metal centre than its hydride analogue, consistent with the computed polarisation of the Ru–In bonding electron density toward Ru in Figure 4.

In terms of reaction chemistry the computed reaction profiles for the formation of **4** and **7** show a propensity of the In centre toward facile Me-group transfer, not only from In to Ru, but also from Ru to In. Several computed structures show either a bridging Me (**I(1–4)1**) or short, non-bonded In···Me contacts (**I(1–4)2**, **4** and **6**). Similar contacts have been noted in both $[Pt(dcpe)(InR_2)(R)]$ (dcpe = $Cy_2P(CH_2)_2PCy_2$, R = CH_2tBu)[22] and $[Ir(PMe_3)_3(InEt_2)(Et)H]$,[11f] which are the only crystallographically characterised precedents that feature adjacent alkyl and indyl ligands. That the present system allows for Me transfer between the metal centres reflects the dual unsaturation that is present at both metal centres.

Given the reactivity found with $InMe_3$, we were keen to explore the chemistry of **1** with $GaMe_3$. In contrast to the rapid reaction with $InMe_3$ to give **4**, complete reaction of $GaMe_3$ with **1** in fluorobenzene required about 12 days to yield a single species, characterised as the novel Ru gallyl complex **8** (Scheme 3). The X-ray crystal structure of **8** (Figure 5) showed a half-sandwich Ru complex bound to a $GaMe_2$ unit, which was itself coordinated to a migrated IPr ligand.[27] This carbene displayed an η^6 interaction to the Ru centre involving one of the dipp rings. The η^6 binding was apparent in solution from the appearance of two upfield ^{1}H NMR aromatic signals (δ = 6.00, 5.85 ppm) in a 2:1 ratio.[28] NMR monitoring of the progression

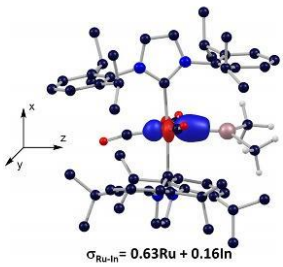

Figure 4. Localised Pipek–Mezey orbital showing Ru–In σ-bonding in **7**. Hydrogen atoms on the IPr ligands are omitted for clarity.

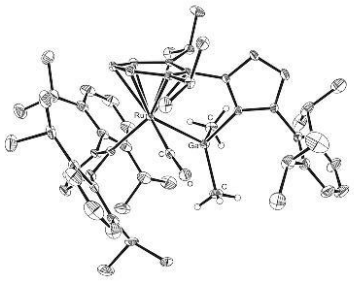

Figure 5. Molecular structure of the cation in **8** (ellipsoids at 30% probability). Hydrogens have been omitted with the exception of those in gallium-bound methyl groups.

of the reaction only ever showed signals from **1** or **8**, with no evidence for any intermediate. Very few dialkylgallyl complexes are known,[11b,f,29] and the formation of **8** in this case presumably again involves initial methane loss to form, by analogy with $InMe_3$, an unsupported Ru-gallyl system. However, in this case IPr transfer from Ru to Ga is now preferred over a second Me transfer to Ru. The reasons for these intriguing differences in selectivity between Ga and In are the subject of ongoing studies.

Conclusion

We have shown that the electrophilic hydride complex $[Ru(IPr)_2(CO)H][BAr^F{}_4]$, **1**, undergoes diverse reactivity with EMe_3 species (E = Ga, In). With $InMe_3$, two methyl groups transfer to Ru with loss of one equivalent of methane to form Ru-InMe complex **4** featuring an unsupported Ru–In bond.[9] With $GaMe_3$, CH_4 is also lost but the reaction then takes a different course with IPr transfer from Ru to Ga. Indium complex **4** reacts with both H_2 and CO, with the latter inducing Me group transfer from Ru back onto In. This reflects the availability of vacant coordination sites at both Ru and In that is a built-in feature of the unsupported Ru–In bond. Future work will target new unsupported metal–metal bonds as a means to explore well-defined reactivity in order to develop new heterobimetallic catalysts.

Experimental Section

General procedures and materials: All manipulations were carried out using standard Schlenk, high vacuum and glovebox techniques using dried and degassed solvents. $InMe_3$ (99.99%) and $GaMe_3$ (99.99%) were provided by Dr A. L. Johnson and used as received. NMR spectra were recorded on a Bruker Avance 500 MHz NMR spectrometer and run locked in either $[D_8]$THF (referenced to δ = 3.58 ppm (^{1}H) and δ = 67.6 ppm (^{13}C)) or unlocked in C_6H_5F (referenced to the centre of the downfield ^{1}H multiplet at δ = 7.11 ppm), while ^{13}C NMR spectra reported in C_6H_5F are referenced relative to the residual solvent peak for an internal standard of $[D_6]$benzene (δ = 128.0 ppm). IR spectra were recorded in C_6H_5F solution on a Nicolet Nexus spectrometer. Elemental analyses were performed by Elemental Microanalysis Ltd, Okehampton, Devon, UK. $[Ru(IPr)_2(CO)H][BAr^F{}_4]$ (**1**) was prepared according to the literature.[25]

$[Ru(IPr)_2(CO)(InMe)(Me)][BAr^F{}_4]$ (4): A J. Young's resealable NMR tube was charged with solution of $[Ru(IPr)_2(CO)H][BAr^F{}_4]$ (0.017 g, 0.009 mmol) in C_6H_5F (0.5 mL) and $InMe_3$ (0.003 g, 0.02 mmol) added to afford a red solution. After 2 h, the solvent was removed under vacuum and the resulting red solid washed with hexane (3× 0.6 mL) and dried under vacuum. The product was recrystallised from C_6H_5F/hexane to give deep red crystals of **4**·0.5C_6H_{14}. Yield 0.012 g, 66%. ^{1}H NMR (500 MHz, C_6H_5F, 298 K): δ = 8.37 (s, 8H, *o*-BAr*H*), 7.67 (s, 4H, *p*-BAr*H*),* 2.86 (sept, ^3J(H,H) = 6.8 Hz, 4H, C*H*$(CH_3)_2$), 2.73 (sept, ^3J(H,H) = 6.8 Hz, 4H, *CH*$(CH_3)_2$), 1.15 (d, ^3J(H,H) = 6.8 Hz, 12H, CH$(CH_3)_2$), 1.10 (d, ^3J(H,H) = 6.8 Hz, 12H, CH$(CH_3)_2$), 0.99 (d, ^3J(H,H) = 6.8 Hz, 12H, CH$(CH_3)_2$), 0.97 (d, ^3J(H,H) = 6.8 Hz, 12H, CH$(CH_3)_2$), 0.08 (s, 3H, InCH_3), −0.86 (s, 3H, RuCH_3) ppm (*aryl and NCH resonances obscured by solvent); ^{1}H NMR (500 MHz, $[D_8]$THF, 298 K): δ = 7.79 (s, 8H, *o*-BAr*H*), 7.57 (s, 4H, *p*-BAr*H*), 7.55 (s, 1H, Ar*H*), 7.54 (s, 1H, Ar*H*), 7.37–7.31 (m, 10H, Ar*H*), 7.29 (br s, 2H, NC*H*), 7.27 (br s, 2H, NC*H*), 2.86 (sept, ^3J(H,H) = 6.8 Hz, 4H, C*H*$(CH_3)_2$), 2.73 (sept, ^3J(H,H) = 6.9 Hz, 4H, *CH*$(CH_3)_2$), 1.19 (d, ^3J(H,H) = 6.8 Hz, 12H, CH$(CH_3)_2$), 1.14 (d, ^3J(H,H) = 6.8 Hz, 12H, CH$(CH_3)_2$), 1.07 (d, ^3J(H,H) = 6.9 Hz, 12H, CH$(CH_3)_2$), 1.03 (d, ^3J(H,H) = 6.9 Hz, 12H, CH$(CH_3)_2$), −0.02 (s, 3H, InCH_3), −0.74 ppm (s, 3H, RuCH_3); ^{13}C{^{1}H} NMR (126 MHz, $[D_8]$THF, 298 K) δ = 196.6 (s, Ru-*C*O), 189.1 (s, Ru-C_{NHC}), 162.6 (1:1:1:1 q, ^1J(C,B) = 50 Hz, *i*-BAr*C*), 147.3 (s, Ar*C*), 147.2 (s, Ar*C*), 136.8 (s, NAr*C*), 135.4 (s, *o*-Ar*C*), 132.7 (s, Ar*C*), 129.8 (qq, ^2J(C,F) = 32 Hz, ^4J(C,F) = 3 Hz, *m*-BAr*C*), 127.4 (s, Ar*C*), 127.0 (s, Ar*C*), 126.7 (s, NCH), 125.3 (q, ^1J(C,F) = 271 Hz, *C*F_3), 118.0 (m, *p*-Ar*C*), 29.4 (s, *C*H$(CH_3)_2$), 29.3 (s, *C*H$(CH_3)_2$), 25.9 (s, CH$(CH_3)_2$), 25.7 (s, CH$(CH_3)_2$), 23.4 (s, CH$(CH_3)_2$), 22.8 (s, CH$(CH_3)_2$), 14.0 ppm (s, InCH_3), 9.6 (s, RuCH_3); IR (C_6H_5F): $\tilde{\nu}_{CO}$ = 1913 cm^{-1}; Anal. Calcd for $C_{89}H_{90}BN_4OF_{24}RuIn{\cdot}0.5C_6H_{14}$ C 56.45, H 4.99, N 2.86. Found: C 56.85, H 4.67, N 2.89.

$[Ru(IPr)_2(CO)(\eta^2\text{-}H_2)(InMe)(H)][BAr^F{}_4]$ (5): A J. Young's resealable NMR tube was charged with solution of **1** (0.018 g, 0.01 mmol) in C_6H_5F (0.5 mL) and $InMe_3$ (0.003 g, 0.02 mmol) to give a red solution. After 1 h, the solvent was removed in vacuo and the red solid washed with hexane (3×0.6 mL) and dried under vacuum to afford a crude sample of **4**. This was redissolved in C_6H_5F (0.5 mL), the solution degassed via three freeze-pump-thaw cycles and exposed to 1 atm H_2. Upon shaking, the reaction mixture became colourless. Upon layering with hexane under a H_2 atmosphere, colourless crystals of **5** were formed. Yield 0.08 g, 45%. ^{1}H NMR (400 MHz, C_6H_5F under 1 atm H_2, 298 K): δ = 8.36 (s, 8H, *o*-BAr*H*), 7.67 (s, 4H, *p*-BAr*H*),* 2.21 (sept, ^3J(H,H) = 6.6 Hz, 8H, *CH*$(CH_3)_2$), 1.11 (d, ^3J(H,H) = 6.7 Hz, 12H, CH$(CH_3)_2$), 1.06 (d, ^3J(H,H) = 6.7 Hz, 12H, CH$(CH_3)_2$), 0.93–0.91 (m, 24H, CH$(CH_3)_2$), −0.11 (s, 3H, InCH_3), −6.39 ppm (br s, 3H, Ru(η^2-H_2) and Ru-*H*) (*aryl and NCH resonances obscured by solvent); ^{13}C{^{1}H} NMR (126 MHz, C_6H_5F, 298 K) δ = 201.3 (s, Ru-*C*O), 186.1 (s, Ru-C_{NHC}), 162.8 (1:1:1:1 q, ^1J(C,B) = 50 Hz, *i*-Ar*C*), 146.2 (s, Ar*C*), 145.1 (s, Ar*C*), 138.0 (s, Ar*C*), 135.4 (s, *o*-Ar*C*), 131.2 (s, Ar*C*), 130.0 (m, *m*-Ar*C*), 125.5 (s, Ar*C*), 125.0 (s, Ar*C*), 118.0 (br s, *p*-Ar*C*), 33.0 (s, InCH_3), 29.0 (s, *C*H$(CH_3)_2$), 28.9 (s, *C*H$(CH_3)_2$), 25.4 (s, CH$(CH_3)_2$), 25.2 (s, CH$(CH_3)_2$), 22.5 ppm (s, CH$(CH_3)_2$); IR (H_2-saturated C_6H_5F): $\tilde{\nu}_{CO}$ = 1974 cm^{-1}; Anal. Calcd for $C_{88}H_{90}BN_4OF_{24}RuIn{\cdot}C_6H_{14}$: C 56.77, H 5.27, N 2.82. Found: C 56.89, H 4.80, N 3.05.

$[Ru(IPr)_2(CO)_3(InMe_2)][BAr^F{}_4]$ (7): A. J. Young's resealable NMR tube was charged with a C_6H_5F (0.5 mL) solution of **1** (0.018 g, 0.01 mmol) and $InMe_3$ (0.003 g, 0.02 mmol) to yield a red solution. After 1 h, the solvent was removed in vacuo and the red solid washed with hexane (3×0.6 mL) and dried under vacuum. The crude sample of **4** was redissolved in C_6H_5F (0.5 mL), degassed via three freeze-pump-thaw cycles, cooled to 243 K and exposed to 1 atm CO. The sample was inverted repeatedly until the solution became colourless, placed back at 243 K and allowed to slowly warm to room temperature. After 15 h, the tube was degassed by a single freeze-pump-thaw cycle and the reaction mixture layered with hexane to afford colourless crystals of **7**. Yield 0.015 g, 76%. ^{1}H NMR (500 MHz, C_6H_5F, 298 K): δ;8.41 (s, 8H, *o*-Ar*H*), 7.70 (s, 4H, *p*-Ar*H*),* 2.39 (sept, ^3J(H,H) = 6.7 Hz, 8H, *CH*$(CH_3)_2$), 1.25 (d, ^3J(H,H) = 6.7 Hz, 24H, CH$(CH_3)_2$), 0.91 (d, ^3J(H,H) = 6.7 Hz, 24H, CH$(CH_3)_2$), −0.15 ppm (s, 6H, In$(CH_3)_2$) (*aryl and NCH resonances obscured by solvent); ^{13}C{^{1}H} NMR (126 MHz, C_6H_5F, 298 K) δ = 202.9 (s, Ru-*C*O; with ^{13}CO, d, ^2J(C,C) = 3 Hz), 193.1 (br s, Ru-*C*O), 170.0 (s, Ru-C_{NHC}) 162.8 (1:1:1:1 q, ^1J(C,B) = 50 Hz, *i*-Ar*C*), 146.3 (s, Ar*C*), 136.3 (s, NAr*C*), 135.4 (s, *o*-Ar*C*), 132.1 (s, Ar*C*), 130.2 (m overlapping with C_6H_5F, *m*-Ar*C*), 126.4 (s, NCH), 125.8 (s, Ar*C*), 117.9 (br s, *p*-Ar*C*), 29.1 (s, *C*H$(CH_3)_2$), 25.9 (s, CH$(CH_3)_2$), 22.1 (s, CH$(CH_3)_2$), 11.7 ppm (s, In$(CH_3)_2$); IR (C_6H_5F): $\tilde{\nu}_{CO}$ = 2003, 1977 cm^{-1}; Anal. Calcd for $C_{92}{}^{13}C_2H_{97}N_4BO_3F_{24}RuIn$: C 56.13, H 4.81, N 2.78. Found: C 55.74, H 4.57, N 2.66.

[Ru(IPr)(CO)Ga(IPr)Me$_2$][BAr$^F_4$] (8): A. J. Young's resealable NMR tube was charged with a C_6H_5F (0.5 mL) solution of **1** (0.015 g, 0.009 mmol) and $GaMe_3$ (0.006 g, 0.05 mmol) added. After 12 days, the solvent was removed in vacuo and the resulting solid washed with hexane (3×0.6 mL) and dried under vacuum. The product was recrystallised from toluene/hexane to afford **8** as yellow crystals. Yield 0.006 g, 37%. ^{1}H NMR (500 MHz, C_6H_5F, 298 K): δ = 8.34 (s, 8H, *o*-Ar*H*), 7.65 (s, 4H, *p*-Ar*H*),* 5.90 (d, ^3J(H,H) = 6.5 Hz, 2H, Ar*H* η^6-IPr), 5.61 (t, ^3J(H,H) = 6.5 Hz, 1H, Ar*H* η^6-IPr), 2.57 (sept, ^3J(H,H) = 6.7 Hz, 4H, C*H*(CH$_3$)$_2$), 2.45 (sept, ^3J(H,H) = 6.7 Hz, 4H, C*H*(CH$_3$)$_2$), 2.16 (sept, ^3J(H,H) = 6.9 Hz, 4H, C*H*(CH$_3$)$_2$), 1.44 (d, ^3J(H,H) = 6.7 Hz, 12H, CH(C*H*$_3$)$_2$), 1.19 (d, ^3J(H,H) = 6.7 Hz, 6H, CH(C*H*$_3$)$_2$), 1.02–0.99 (overlapping d, ^3J(H,H) = 6.7 Hz, 18H, CH(C*H*$_3$)$_2$), 0.94 (d, ^3J(H,H) = 6.9 Hz, 6H, CH(C*H*$_3$)$_2$), 0.77 (d, ^3J(H,H) = 6.7 Hz, 6H, CH(C*H*$_3$)$_2$), −0.33 ppm (s, Ga(C*H*$_3$)$_2$) (*aryl and NCH resonances obscured by solvent); ^{1}H NMR (500 MHz, [D$_8$]THF, 298 K): δ = 7.96 (d, ^3J(H,H) = 2 Hz, 1H, NCH=C*H*), 7.79 (br m, 8H, *o*-Ar*H*), 7.71 (d, ^3J(H,H) = 2 Hz, 1H, NC*H*=CH), 7.58 (s, 4H, *p*-Ar*H*), 7.54–7.45 (m, 5H), 7.40 (d, ^3J(H,H) = 7.8 Hz, 4H, Ar*H*), 7.31 (d, ^3J(H,H) = 7.7 Hz, 2H, Ar*H*), 6.00 (d, ^3J(H,H) = 6.5 Hz, 2H, *m*-Ar*H* of η^6-IPr), 5.85 (t, ^3J(H,H) = 6.5 Hz, 1H, *p*-Ar*H* of η^6-IPr), 2.60 (sept, ^3J(H,H) = 6.7 Hz, 4H, C*H*(CH$_3$)$_2$), 2.41 (sept, ^3J(H,H) = 6.8 Hz, 2H, C*H*(CH$_3$)$_2$), 2.14 (sept, ^3J(H,H) = 6.7 Hz, 2H, C*H*(CH$_3$)$_2$), 1.48 (d, ^3J(H,H) = 6.7 Hz, 12H, CH(C*H*$_3$)$_2$), 1.19 (d, ^3J(H,H) = 6.7 Hz, 6H, CH(C*H*$_3$)$_2$), 1.16 (d, ^3J(H,H) = 6.7 Hz, 6H, CH(C*H*$_3$)$_2$), 1.09 (d, ^3J(H,H) = 6.7 Hz, 12H, CH(C*H*$_3$)$_2$), 1.02 (d, ^3J(H,H) = 6.8 Hz, 12H, CH(C*H*$_3$)$_2$), 0.80 (d, ^3J(H,H) = 6.7 Hz, 6H, CH(C*H*$_3$)$_2$), 0.55 ppm (s, 6H, Ga(C*H*$_3$)$_2$); ^{13}C{^{1}H} NMR (126 MHz, [D$_8$]THF, 298 K-assignments based on HMBC/HSQC spectra; *identified on basis of ^{1}H-^{13}C HMBC cross-peak) δ = 206.8 (s, Ru-*C*O), 192.0 (s, Ga-*C*$_{NHC}$), 176.7 (s, Ru-*C*$_{NHC}$), 160.0 (1:1:1:1 q, ^1J(C,B) = 50 Hz, *i*-Ar*C*), 147.1 (s, NAr*C*), 146.3 (s, NAr*C*), 138.9 (s, *o*-Ar*C*), 136.0 (s, Ar*C*), 134.2 (s, *o*-Ar*C*), 131.9 (s, Ar*C*), 131.6 (s, Ar*C*), 130.2 (q, $^2J_{CF}$ = 32 Hz, *m*-Ar*C*), 130.0 (s, NC*H*=CH), 128.8 (s, NC*H*=C*H*), 125.5 (s, Ar*C*), 125.0 (s, Ar*C*), 124.0 (s, NCH=C*H*), 121.1* (s, *i*-Ar*C* η^6-IPr), 118.4 (s, Ar*C*), 98.5 (s, *o*-Ar*C* η^6-IPr), 97.3 (s, *m*-Ar*C* η^6-IPr), 91.3 (s, *p*-Ar*C* η^6-IPr), 30.2 (s, *C*H(CH$_3$)$_2$), 29.7 (s, *C*H(CH$_3$)$_2$), 29.4 (s, *C*H(CH$_3$)$_2$), 27.1 (s, CH(*C*H$_3$)$_2$), 26.8 (s, CH(*C*H$_3$)$_2$), 26.0 (s, CH(*C*H$_3$)$_2$), 22.9 (s, CH(*C*H$_3$)$_2$), 22.7 (s, CH(*C*H$_3$)$_2$), 21.1 (s, CH(*C*H$_3$)$_2$), 0.3 ppm (s, Ga(*C*H$_3$)$_2$); IR (C_6H_5F): $\tilde{\nu}_{CO}$ = 1933 cm^{-1}; Anal. Calcd for $C_{89}H_{92}BN_4OF_{24}RuGa$: C 57.12, H 4.96, N 2.99. Found: C 56.65, H 4.82, N 2.89.

Computational Details: Calculations employed Gaussian 09 (Revision D.01)[30] with geometry optimizations using the BP86 functional.[31,32] Ru and In were described with SDD effective core potentials and the associated basis sets,[33] with d-orbital polarization added to In (ξ_d = 0.143).[34] 6-31G** basis sets were used for all other atoms.[35,36] Stationary points were fully characterised via analytical frequency calculations as either minima (all positive eigenvalues) or transition states (one negative eigenvalue). Transition states were also characterised via IRC calculations and subsequent geometry optimizations to confirm the adjacent minima in each case. Gas-phase free energies were corrected for the effects of dispersion (Grimme's D3 parameter set[37]) and fluorobenzene solvent (PCM approach).[38] QTAIM[39] calculations were run with the AIMALL program[40] and Pipek-Mezey localised orbitals[41] were computed with ORCA[42] (Version 4.0.0.2) using def2-TZVP[43] basis for Ru and In atoms and def2-SVP[44] for other atoms. See ESI for further basis set and functional testing and references.

Acknowledgements

We acknowledge the EPSRC (grant EP/J010677/1 for IMR) and Heriot-Watt University (James Watt Scholarship to NAR) for financial support. We thank Dr. Andrew Johnson (Bath) for generous gifts of $InMe_3$ and $GaMe_3$ and Dr. Mark Crimmin (Imperial College London) for useful discussions.

Conflict of interest

The authors declare no conflict of interest.

Keywords: density functional calculations · gallium · heterometallic complexes · indium · ruthenium

[1] a) R. J. Baker, C. Jones, *Coord. Chem. Rev.* **2005**, *249*, 1857–1869; b) H. W. Roesky, S. S. Kumar, *Chem. Commun.* **2005**, 4027–4038; c) M. Asay, C. Jones, M. Driess, *Chem. Rev.* **2011**, *111*, 354–396; d) S. González-Gallardo, T. Bollermann, R. A. Fischer, R. Murugavel, *Chem. Rev.* **2012**, *112*, 3136–3170; e) J. A. B. Abdalla, S. Aldridge in *Molecular Metal-Metal Bonds: Compounds, Synthesis Properties* (Ed.: S. T. Liddle), Wiley-VCH, Weinheim, **2015**, pp. 455–484; f) G. Bouhadir, D. Bourissou, *Chem. Soc. Rev.* **2016**, *45*, 1065–1079.

[2] a) B. E. Cowie, D. J. H. Emslie, *Chem. Eur. J.* **2014**, *20*, 16899–16912; b) B. R. Barnett, C. E. Moore, A. L. Rheingold, J. S. Figueroa, *J. Am. Chem. Soc.* **2014**, *136*, 10262–10265; c) B. E. Cowie, F. A. Tsao, D. J. H. Emslie, *Angew. Chem. Int. Ed.* **2015**, *54*, 2165–2169; *Angew. Chem.* **2015**, *127*, 2193–2197; d) M. Devillard, G. Bouhadir, D. Bourissou, *Angew. Chem. Int. Ed.* **2015**, *54*, 730–732; *Angew. Chem.* **2015**, *127*, 740–742; e) W. C. Shih, W. X. Gu, M. C. MacInnis, S. D. Timpa, N. Bhuvanesh, J. Zhou, O. V. Ozerov, *J. Am. Chem. Soc.* **2016**, *138*, 2086–2089; f) M. Devillard, R. Declercq, E. Nicolas, A. W. Ehlers, J. Backs, N. Saffon-Merceron, G. Bouhadir, J. C. Slootweg, W. Uhl, D. Bourissou, *J. Am. Chem. Soc.* **2016**, *138*, 4917–4926; g) Y. Li, C. Hou, J. Jiang, Z. Zhang, C. Zhao, A. J. Page, Z. Ke, *ACS Catal.* **2016**, *6*, 1655–1662.

[3] a) W. H. Harman, J. C. Peters, *J. Am. Chem. Soc.* **2012**, *134*, 5080–5082; b) G. Zeng, S. Sakaki, *Inorg. Chem.* **2013**, *52*, 2844–2853; c) H. Fong, M.-E. Moret, Y. Lee, J. C. Peters, *Organometallics* **2013**, *32*, 3053–3062; d) W. H. Harman, T.-P. Lin, J. C. Peters, *Angew. Chem. Int. Ed.* **2014**, *53*, 1081–1086; *Angew. Chem.* **2014**, *126*, 1099–1104; e) S. N. MacMillan, W. H. Harman, J. C. Peters, *Chem. Sci.* **2014**, *5*, 590–597; f) M. A. Nesbit, D. L. M. Suess, J. C. Peters, *Organometallics* **2015**, *34*, 4741–4752.

[4] K. N. T. Tseng, J. W. Kampf, N. K. Szymczak, *J. Am. Chem. Soc.* **2016**, *138*, 10378–10381.

[5] J. Takaya, N. Iwasawa, *J. Am. Chem. Soc.* **2017**, *139*, 6074–6077.

[6] R. C. Cammarota, M. V. Vollmer, J. Xie, J. Ye, J. C. Linehan, S. A. Burgess, A. A. Appel, L. Gagliardi, C. C. Lu, *J. Am. Chem. Soc.* **2017**, *139*, 14244–14250.

[7] R. C. Cammarota, C. C. Lu, *J. Am. Chem. Soc.* **2015**, *137*, 12486–12489.

[8] R. C. Cammarota, L. J. Clouston, C. C. Lu, *Coord. Chem. Rev.* **2017**, *334*, 100–111.

[9] J. Bauer, H. Braunschweig, R. D. Dewhurst, *Chem. Rev.* **2012**, *112*, 4329–4346.

[10] a) I. M. Riddlestone, N. A. Rajabi, J. P. Lowe, M. F. Mahon, S. A. Macgregor, M. K. Whittlesey, *J. Am. Chem. Soc.* **2016**, *138*, 11081–11084; b) IPr = 1,3-bis(2,6-diisopropylphenyl)imidazol-2-ylidene, [BAr$_4^F$]$^-$ = [B{C$_6$H$_3$(3,5-CF$_3$)$_2$}$_4$]$^-$.

[11] For an overview of the reactivity of TM-hydride complexes with main group Lewis acids, see: a) A. Maity, T. S. Teets, *Chem. Rev.* **2016**, *116*, 8873–8911. For specific examples, see: b) J. N. St. Denis, W. Butler, M. D. Glick, J. P. Oliver, *J. Organomet. Chem.* **1977**, *129*, 1–16; c) R. A. Fischer, H. D. Kaesz, S. I. Khan, H.-J. Müller, *Inorg. Chem.* **1990**, *29*, 223–224; d) M. Cokoja, C. Gemel, T. Steinke, F. Schröder, R. A. Fischer, *Dalton Trans.* **2005**, 44–54; e) C. J. Durango-García, J. O. C. Jiménez-Halla, M. López-Cardoso, V. Montiel-Palma, M. A. Muñoz-Hernández, G. Merino, *Dalton Trans.* **2010**, *39*, 10588–10589; f) Thorn and Harlow described an early example of an Ir–In complex from Ir–Me and In–Et precursors (upon loss of ethane). See D. L. Thorn, R. L. Harlow, *J. Am. Chem. Soc.* **1989**, *111*, 2575–2580.

[12] It is worth noting that there are older reported examples of reactions between neutral TM hydrides and main group alkyls that afford simple

adducts: a) H. Brunner, P. C. Wailes, H. D. Kaesz, *Inorg. Nucl. Chem. Lett.* **1965**, *1*, 125 – 129; b) F. N. Tebbe, *J. Am. Chem. Soc.* **1973**, *95*, 5412 – 5414; c) J. W. Bruno, J. C. Huffman, K. G. Caulton, *J. Am. Chem. Soc.* **1984**, *106*, 444 – 445.

[13] J. T. Golden, T. H. Peterson, P. L. Holland, R. G. Bergman, R. A. Andersen, *J. Am. Chem. Soc.* **1998**, *120*, 223 – 224.

[14] T. Bollwein, P. J. Brothers, H. L. Hermann, P. Schwerdtfeger, *Organometallics* **2002**, *21*, 5236 – 5242.

[15] J.-N. Luy, S. A. Hauser, A. B. Chaplin, R. Tonner, *Organometallics* **2015**, *34*, 5099 – 5112.

[16] A crude sample of **6** was isolated by shaking a C_6H_5F solution of **4** in the presence of ^{13}CO at $-30\,^{\circ}C$.

[17] No incorporation of ^{13}CO into the third carbonyl position was found after standing at room temperature overnight.

[18] M. Itazaki, M. Ito, H. Nakazawa, *Eur. J. Inorg. Chem.* **2015**, 2033 – 2036.

[19] IMe_2 = 1,3-dimethylimidazol-2-ylidene.

[20] R. N. Perutz, S. Sabo-Etienne, *Angew. Chem. Int. Ed.* **2007**, *46*, 2578 – 2592; *Angew. Chem.* **2007**, *119*, 2630 – 2645.

[21] Intermediate **6** also presents the possibility of Me transfer onto a *cis*-CO ligand and calculations locate a transition state for this process at $-3.3\ kcal\,mol^{-1}$, only marginally above that for transfer onto the InMe group. The 16e acyl intermediate ($G = -7.3\ kcal\,mol^{-1}$) is endergonic and so the reversible formation of this species may account for the observed chemoselectivity for the indyl product.

[22] R. A. Fischer, D. Weiß, M. Winter, I. Müller, H. D. Kaesz, N. Fröhlich, G. Frenking, *J. Organomet. Chem.* **2004**, *689*, 4611 – 4623.

[23] B. Cordero, V. Gómez, A. E. Platero-Prats, M. Revés, J. Echeverria, E. Cremades, F. Barragán, S. Alvarez, *Dalton Trans.* **2008**, 2832 – 2838.

[24] a) R. Bianchi, G. Gervasio, D. Marabello, *Inorg. Chem.* **2000**, *39*, 2360 – 2366; b) B. Vlaisavljevich, P. Miró, C. J. Cramer, L. Gagliardi, I. Infante, S. T. Liddle, *Chem. Eur. J.* **2011**, *17*, 8424 – 8433.

[25] I. M. Riddlestone, D. McKay, M. J. Gutmann, S. A. Macgregor, M. F. Mahon, H. A. Sparkes, M. K. Whittlesey, *Organometallics* **2016**, *35*, 1301 – 1312.

[26] a) R. F. R. Jazzar, P. H. Bhatia, M. F. Mahon, M. K. Whittlesey, *Organometallics* **2003**, *22*, 670 – 683; b) IMes = 1,3-bis(2,4,6-trimethylphenyl)imidazol-2-ylidene.

[27] a) E. Becker, V. Stingl, G. Dazinger, M. Puchberger, K. Mereiter, K. Kirchner, *J. Am. Chem. Soc.* **2006**, *128*, 6572 – 6573; b) T. Hatanaka, Y. Ohki, K. Tatsumi, *Angew. Chem. Int. Ed.* **2014**, *53*, 2727 – 2729; *Angew. Chem.* **2014**, *126*, 2765 – 2767.

[28] a) S. H. Hong, M. W. Day, R. H. Grubbs, *J. Am. Chem. Soc.* **2004**, *126*, 7414 – 7415; b) C. H. Lee, D. S. Laitar, P. Mueller, J. P. Sadighi, *J. Am. Chem. Soc.* **2007**, *129*, 13802 – 13803; c) C. Y. Tang, J. Lednik, D. Vidovic, A. L. Thompson, S. Aldridge, *Chem. Commun.* **2011**, *47*, 2523 – 2525.

[29] a) X. He, R. A. Bartlett, P. P. Power, *Organometallics* **1994**, *13*, 548 – 552; b) A. S. Borovik, S. G. Bott, A. R. Barron, *Organometallics* **1999**, *18*, 2668 – 2676.

[30] M. J. Frisch, G. W. Trucks, H. B. Schlegel, G. E. Scuseria, M. A. Robb, J. R. Cheeseman, G. Scalmani, V. Barone, B. Mennucci, G. A. Petersson, H. Nakatsuji, M. Caricato, X. Li, H. P. Hratchian, A. F. Izmaylov, J. Bloino, G. Zheng, J. L. Sonnenberg, M. Hada, M. Ehara, K. Toyota, R. Fukuda, J. Hasegawa, M. Ishida, T. Nakajima, Y. Honda, O. Kitao, H. Nakai, T. Vreven, J. A. J. Montgomery, J. E. Peralta, F. Ogliaro, M. Bearpark, J. J. Heyd, E. Brothers, K. N. Kudin, V. N. Staroverov, R. Kobayashi, J. Normand, K. Raghavachari, A. Rendell, J. C. Burant, S. S. Iyengar, J. Tomasi, M. Cossi, N. Rega, J. M. Millam, M. Klene, J. E. Knox, J. B. Cross, V. Bakken, C. Adamo, J. Jaramillo, R. Gomperts, R. E. Stratmann, O. Yazyev, A. J. Austin, R. Cammi, C. Pomelli, J. W. Ochterski, R. L. Martin, K. Morokuma, V. G. Zakrzewski, G. A. Voth, P. Salvador, J. J. Dannenberg, S. Dapprich, A. D. Daniels, O. Farkas, J. B. Foresman, J. V. Ortiz, J. Cioslowski, D. J. Fox, Gaussian 09, Revision D.01, Gaussian, Inc., Wallingford CT, **2013**.

[31] J. P. Perdew, *Phys. Rev. B* **1986**, *33*, 8822 – 8824.

[32] A. D. Becke, *Phys. Rev. A* **1988**, *38*, 3098 – 3100.

[33] D. Andrae, U. Häußermann, M. Dolg, H. Stoll, H. Preuß, *Theor. Chim. Acta* **1990**, *77*, 123 – 141.

[34] A. W. Ehlers, M. Böhme, S. Dapprich, A. Gobbi, A. Höllwarth, V. Jonas, K. F. Köhler, R. Stegmann, A. Veldkamp, G. Frenking, *Chem. Phys. Lett.* **1993**, *208*, 111 – 114.

[35] W. J. Hehre, R. Ditchfield, J. A. Pople, *J. Chem. Phys.* **1972**, *56*, 2257 – 2261.

[36] P. C. Hariharan, J. A. Pople, *Theor. Chim. Acta.* **1973**, *28*, 213 – 222.

[37] S. Grimme, J. Antony, S. Ehrlich, H. Krieg, *J. Chem. Phys.* **2010**, *132*, 154104 – 1.

[38] J. Tomasi, B. Mennucci, R. Cammi, *Chem. Rev.* **2005**, *105*, 2999 – 3094.

[39] R. F. W. Bader, *Atoms in Molecules – A Quantum Theory*, Oxford University Press, Oxford, **1990**.

[40] T. A. Keith, T. K. Grist-mill, AIMAll (Version 13.02.26, Professional), Software, Overland Park KS, USA, **2015**, (aim.tkgristmill.com).

[41] J. Pipek, P. G. Mezey, *J. Chem. Phys.* **1989**, *90*, 4916 – 4926.

[42] F. Neese, *WIREs Comput. Mol. Sci.* **2017**, e1327, https://doi.org/10.1002/wcms.1327.

[43] F. Weigend, R. Ahlrichs, *Phys. Chem. Chem. Phys.* **2005**, *7*, 3297 – 3305.

[44] a) A. Schäfer, H. Horn, R. Ahlrichs, *J. Chem. Phys.* **1992**, *97*, 2571 – 2577; b) A. Schäfer, C. Huber, R. Ahlrichs, *J. Chem. Phys.* **1994**, *100*, 5829 – 5835.

Manuscript received: December 7, 2017
Accepted manuscript online: December 14, 2017
Version of record online: January 4, 2018

Copper Borates

International Edition: DOI: 10.1002/anie.201608081
German Edition: DOI: 10.1002/ange.201608081

Experimental and Computational Studies of the Copper Borate Complexes [(NHC)Cu(HBEt$_3$)] and [(NHC)Cu(HB(C$_6$F$_5$)$_3$)]

Lee R. Collins, Nasir A. Rajabi, Stuart A. Macgregor, Mary F. Mahon, and Michael K. Whittlesey**

Abstract: *The synthesis of the Cu-borate complexes [(6Mes)Cu(HBR$_3$)] featuring the unusual [HBEt$_3$]$^-$ (**5**) and [HB(C$_6$F$_5$)$_3$]$^-$ (**6**) ligands is described. Experimental and computational studies show both compounds feature a direct Cu–H interaction, but that while **5** is two-coordinate, **6** displays an additional, stabilizing Cu–C$_{ipso}$(C$_6$F$_5$) interaction.*

There is considerable interest in mononuclear copper hydride species because of their proposed importance as intermediates in copper-catalyzed reductive transformations.[1] However, simple monomeric [LCuH] complexes (L = phosphine, N-heterocyclic carbene (NHC)) remain hitherto unknown: for L = PR$_3$, species ranging from dimers up to octanuclear clusters have been characterized,[1h,2] while even very bulky NHCs still give only dimers (**I** and **II**, Scheme 1).[3] The nearest example to an isolable monomeric [LCuH] species reported to date is the three-coordinate [(CAAC^{Et})Cu(κ^2-BH$_4$)] complex **III**.[4,5] Herein, we report that during efforts to prepare mononuclear Cu–H species, we have instead isolated and structurally characterized two new examples of mononuclear copper borate complexes featuring the highly unusual borate ligands [HBEt$_3$]$^-$ and [HB(C$_6$F$_5$)$_3$]$^-$.

In recent work attempting to prepare [LCuH] species stabilized by large six-membered ring carbenes (e.g. from the reaction of **1** with tertiary silanes, Scheme 2), we showed that

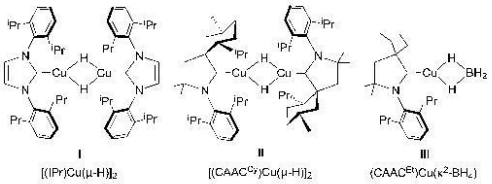

Scheme 1. Cu–H complexes prepared using IPr and CAAC ligands.

[*] Dr. L. R. Collins, Dr. M. F. Mahon, Prof. M. K. Whittlesey
Department of Chemistry, University of Bath
Claverton Down, Bath, BA2 7AY (UK)
E-mail: m.k.whittlesey@bath.ac.uk
N. A. Rajabi, Prof. S. A. Macgregor
Institute of Chemical Sciences, Heriot Watt University
Edinburgh, EH14 4AS (UK)
E-mail: S.A.Macgregor@hw.ac.uk
Supporting information and the ORCID identification number(s) for the author(s) of this article can be found under http://dx.doi.org/10.1002/anie.201608081.

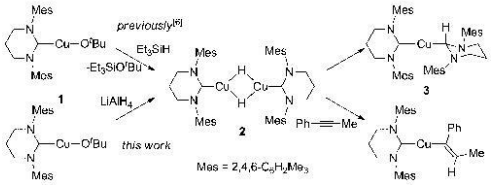

Scheme 2. Synthesis and reactivity of [(6Mes)Cu(μ-H)]$_2$ (**2**).

migratory insertion (MI) products such as **3** formed under mild conditions.[6] This MI process thwarted efforts to spectroscopically characterize any putative Cu-H intermediates (e.g. **2**); however, Cu-H formation was implied through trapping with alkyne to give **4**.

We have now probed the reaction of **1** with alternative hydride sources. Addition of LiAlH$_4$ to a THF solution of **1** at room temperature brought about the instantaneous formation of a yellow solution, indicative of a Cu-H-containing species. Within minutes, this yellow color faded and Cu metal was deposited. A ^{1}H NMR spectrum of the solution showed that **3** was the major species present. However, when LiAlH$_4$ addition was carried out at 178 K, the Cu-H product (**2**) proved to be stable. DOSY measurements showed that it was dimeric (Scheme 2).[7,8] The complex exhibited a low frequency Cu-H resonance at $\delta = 0.96$ ppm, in good agreement with the shifts recently reported for [(6/7Dipp)Cu(μ-H)]$_2$ species.[3d,9] However, whereas [(6/7Dipp)Cu(μ-H)]$_2$ prove stable for days at 298 K, **2** was stable only below 209 K. Above this temperature, the ^{1}H NMR resonances began to broaden and at 255 K signals for **3** were present.[10]

Upon reacting (178 K) **1** with LiHBEt$_3$ instead of LiAlH$_4$, the rapid appearance of a yellow solution was again observed, but now resulting from the new monomeric complex [(6Mes)Cu(HBEt$_3$)] (**5**, Scheme 3) which features an intact {HBEt$_3$} moiety. The formation of **5** was unexpected since [HBEt$_3$]$^-$ typically acts as a potent hydride source; indeed **II** was prepared from [(CAAC^{Cy})Cu(O^{t}Bu)] and LiHBEt$_3$.[3b] Unsurprisingly, examples of isolable triethyl-borohydride

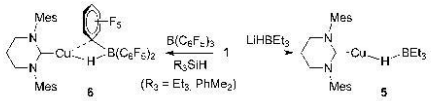

Scheme 3. Synthesis of [(6Mes)Cu(HBR$_3$)] complexes **5** and **6**.

complexes are rare, being confined to very electropositive metals.[11]

The X-ray structure of **5** (Figure 1) showed the presence of a two-coordinate Cu center attached to the carbene and a monodentate {$HBEt_3$} moiety. The hydrogen atom on B(1) was located and refined without restraint, yielding C_{6Mes}-Cu-H and Cu-H-B angles of 162.4(13) and 110.2(18)°, respectively, and B–H and Cu–H distances of 1.22(3) and 1.56(3) Å,

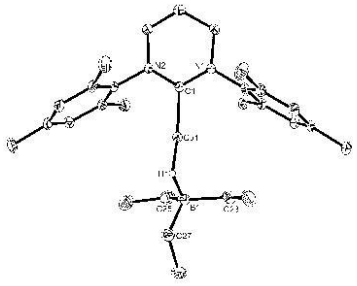

Figure 1. Molecular structure of **5**. Ellipsoids are shown at the 30% level. Hydrogen atoms (except for Cu-H-B) are removed for clarity.

respectively. The latter is comparable to the shortest Cu–H distance in **II**,[3b] but much shorter than either of the Cu–H bond lengths in **III** (1.679(2) Å, 1.717(18) Å). Additional characterization of **5** was performed in solution at low temperature (209 K). The ^{1}H NMR spectrum featured a broad, low frequency signal (relative integral of 1) at $\delta = -2.60$ ppm, assigned to the Cu–H. The ^{1}H-coupled ^{13}C NMR spectrum showed a 12 Hz doublet splitting of the carbenic carbon resonance ($\delta = 202$ ppm), confirming C_{6Mes}-Cu-H connectivity.

The nature of the {Cu-H-BEt_3} interaction in **5** was assessed by QTAIM (quantum theory of atoms in molecules) and NBO (natural bond orbital) analyses using the BP86 functional and geometries based on the crystallographically determined structure.[12] The QTAIM molecular graph (Figure 2a) identifies Cu–H and B–H bond paths, as well as one

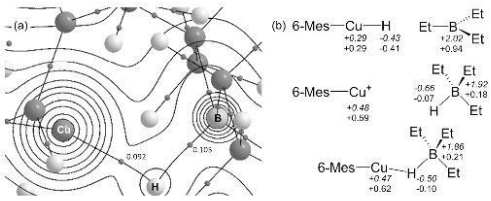

Figure 2. a) Detail of the QTAIM molecular graph of **5** showing electron density contours in the {Cu/H/B plane}. Bond critical points (BCPs) are shown as small gray spheres and key values of $\rho(r)$ (the associated BCP electron densities) are indicated in au. b) Computed atomic charges for **5** and selected comparator species (QTAIM charges in italics; NBO charges in plain text). Full QTAIM metrics are provided in the Supporting Information, along with equivalent $\rho(r)$ values obtained with a range of different functionals.

for the Cu–C_{6Mes} bond. No further bonding interactions involving Cu (e.g. to any atoms of the Et substituents) are seen, thereby supporting the assignment of **5** as a two-coordinate complex.

Figure 2b shows the computed QTAIM and NBO charges at the Cu, H and B centers in **5**, the BP86-optimized free $[(6Mes)Cu]^+$ and $[HBEt_3]^-$ ions as well as the neutral [(6Mes)CuH] and BEt_3 species. Significantly, the charge distribution in **5** more closely resembles that in the free ions, rather than the neutral species. NBO analysis also highlights a $\sigma_{B\text{-}H} \rightarrow$Cu donation that a 2nd order perturbation analysis quantifies at 67.1 kcal mol^{-1} (see Figure S23 in the Supporting Information for NBO plots). The computed evidence therefore indicates that **5** is a borate complex of a $[(6Mes)Cu]^+$ fragment, rather than a Lewis acid-stabilized Cu-hydride (viz. [(6Mes)CuH···BEt_3]).

Experimentally, complex **5** was found to be stable both in THF solution and the solid state for several days below ca. 243 K, but started to decompose within hours upon warming above this temperature through B–H bond cleavage (apparent from the appearance of BEt_3 (^{11}B: $\delta = 73$ ppm)).[11c] **3** and H_2 were also formed, alongside deposition of Cu metal. Interestingly, in contrast to the quantitative formation of the migratory insertion product **3** from **2** (Scheme 1), **5** converted at room temperature to **3** in only ca. 5% yield due to the transformation of $[HBEt_3]^-$ to $[BEt_4]^-$ and $[H_2BEt_3]^-$.[13] This resulted in the formation of the $[BEt_4]^-$ salt of the known bis-carbene cation, $[(6Mes)_2Cu]^+$ (ESI), and a second species believed to be [(6Mes)Cu(H_2BEt_2)] as the ultimate products of the reaction.

The formation of **5** and its formulation as a Cu-borate complex prompted us to consider the formation of related species with properties modulated by the nature of the B-substituents. Taking a lead from the reactions of s-block, early transition metal and lanthanide complexes with Lewis acidic boranes,[14] **1** was treated with R_3SiH in the presence of $B(C_6F_5)_3$. A rapid reaction ensued in the case of Et_3SiH to give a mixture of $[(6Mes)Cu(HB(C_6F_5)_3)]$ (**6**) and $[(6Mes)_2Cu][B(C_6F_5)_4]^-$ (**7**) (ESI).[15] Use of $PhMe_2SiH$ rather than Et_3SiH gave only **6**. An X-ray crystal structure (Figure 3) showed that **6** was mononuclear like **5**, but that, in addition to a Cu–H interaction, there was also one short Cu–C_{ipso} contact (2.2183(17) Å) to the C_6F_5 ring based on C29.[16] The nature of this interaction differs noticeably from those found with more electropositive metals, which invariably involve *ortho*-C–F bond contacts. In particular, the Cu–C_{ipso} interaction in **6** was seen to be concomitant with lengthening of the B(1)–C(29) distance to 1.657(3) Å, relative to the B(1)–C(23) and B1–C(35) distances of 1.624(3) and 1.628(3) Å, respectively. Additionally, the C_{6Mes}-Cu-H angle of 146.5(8)° in **6** is notably more acute than that observed in **5** (162.8(14)°). The Cu–H and B–H distances are each comparatively similar in both structures.

6 was more thermally stable than **5** and could be characterized at room temperature. The ^{11}B NMR spectrum showed a resonance at $\delta = -28.1$ ppm, slightly upfield of the ion-separated species $[X][HB(C_6F_5)_3]$ (X = P^{t}Bu$_3$H, $\delta = -25.5$ ppm;[17a] NBu_4, $\delta = -25.4$ ppm).[17b] Moreover, the ^1J-(B,H) doublet splitting in **6** was smaller (60 Hz) than in either

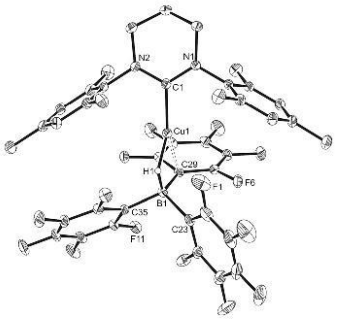

Figure 3. Molecular structure of **6**. Ellipsoids are shown at the 30% level. Hydrogen atoms (except for Cu-H-B) are removed for clarity.

of these compounds (100 and 82 Hz, respectively) or any of the early metal complexes (e.g. $[(C(SiMe_2H)_3)M(THF)_2(HB(C_6F_5)_3)]$, M = Ca: 76 Hz; M = Yb: 73 Hz),[14c] suggestive of a significant Cu-H-B interaction. This was supported by IR spectroscopy (ν(B–H): 2361 cm^{-1})[14c] and the ^{19}F NMR chemical shift difference of 5.4 Hz between the *meta*- and *para*-fluorine atoms.[18] Although we could not observe the Cu–H resonance directly in the ^1H NMR spectrum, ^1H-^{11}B HMQC spectroscopy revealed it at $\delta = 2.08$ ppm. Over ca. 12 h in solution, **6** degraded to **7** and deposited metallic Cu.

The QTAIM molecular graph for **6** (Figure 4a) confirmed the presence of Cu–H and H–B bond paths. Compared to **5**, the Cu–H BCP has a lower $\rho(r)$ (0.083 au, cf. 0.092 au) indicating a weaker interaction, and this is complemented by the higher $\rho(r)$ of the B–H BCP (0.135 au, cf. 0.105 au). Weaker donation to Cu in **6** is also manifest in a higher computed positive charge at Cu (Figure 4b) and the reduced $\sigma_{B\text{-}H}\rightarrow$Cu interaction which the NBO 2nd order perturbation analysis quantifies as 42.9 kcal mol^{-1}. The similar charges at Cu, B and H in **6** and the free $[(6Mes)Cu]^+$ and $[HB(C_6F_5)_3]^-$ ions again suggest **6** is a borate complex. An additional feature, again consistent with a more electron deficient Cu center, is the presence of a Cu–C_{ipso} bond path which entails

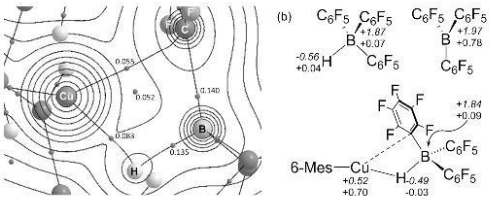

Figure 4. a) Detail of the QTAIM molecular graph for **6** showing electron density contours for the {Cu/H/B plane}. Bond critical points (BCPs) and ring critical points (RCPs) are shown as small gray spheres, and $\rho(r)$ values of key CPs are indicated in au. b) Computed atomic charges for **6** and selected comparator species (QTAIM charges in italics; NBO charges in plain text). Full QTAIM metrics are provided in the Supporting Information along with equivalent $\rho(r)$ values obtained with a range of different functionals.

a ring critical point associated with the $\{CuHBC_{ipso}\}$ unit. The lower value of $\rho(r)$ at the Cu–C_{ipso} BCP (0.055 au) indicates a weaker interaction than the Cu–H bond and the NBO 2nd order perturbation analysis confirms this, providing an interaction energy of only 7.1 kcal mol^{-1} corresponding to donation from the C_{ipso}–B σ-bond to Cu. NBO also suggests an additional stabilization occurs via donation from one of the C_{ipso}–C_{ortho} bonds of the C_6F_5 ring ($\Delta E = -7.9$ kcal mol^{-1}, see Figure S24).

Reproducing the molecular geometries of **5** and **6** presented a challenge to theory; in particular the structure of the $\{Cu(HBEt_3)\}$ moiety in **5** was very sensitive to functional choice. Given this, we also investigated the role of the chemical model used in the calculations by computing the extended solid-state structure of **5** with periodic DFT calculations. Such an approach has been shown to be important in correctly describing ambiguous bonding situations.[19] Figure 5 shows deviations from experiment for the

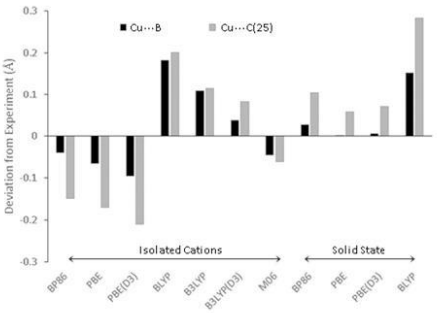

Figure 5. Cu···B and Cu···C(25) distances in **5** computed with various functionals and displayed as deviations from the experimental values of 2.283(3) Å and 2.619(3) Å respectively. Calculations employed either the isolated molecule (Gaussian) or the extended solid state via periodic boundary conditions (CP2K).

Cu···B and Cu···C(25) distances computed in **5** with different functionals, where the latter is a proxy for any additional Cu···H interactions involving the Et substituents. For the molecular calculations, BP86 provides the best agreement for the Cu···B distance, but underestimates Cu···C(25) by 0.15 Å. PBE gives somewhat poorer agreement, and this deteriorates further with PBE(D3), that is, when a dispersion correction is included in the optimization. These geometries imply the presence of a Cu···H-C(25) agostic interaction and thus a three-coordinate Cu center, at odds with the observed two-coordinate geometry. In contrast, BLYP and B3LYP overestimate both distances, a result that has parallels in the description of agostic interactions.[20] B3LYP(D3) improves the situation but this relatively good net performance probably reflects a cancellation of errors, due to the poor B3LYP geometry and an overestimation of intramolecular dispersion effects in the isolated molecular model. Of these molecular calculations, M06 provides the best overall result, with both Cu···B and Cu···C(25) being underestimated by ca.

0.05 Å. A wider comparison of computed structural metrics is provided in the Supporting Information.

Full optimization of the extended solid-state structure of **5** under periodic boundary conditions with BP86 and (particularly) PBE provided improved geometries; moreover, the results are now far less sensitive to the inclusion of dispersion, reflecting how the full solid-state environment can balance the intramolecular dispersion that was overestimated in the calculations using molecular models. Use of an extended model does not guarantee good agreement, however, with BLYP still giving a poor geometry, even with the solid-state model. An equivalent set of calculations was performed for **6** and similar trends were obtained. In this case, the stronger Cu–C_{ipso} interaction makes the computed geometries less functional dependent, although B3LYP significantly overestimates both Cu–C_{ipso} and Cu···B distances. Geometries derived from the periodic calculations are now in good agreement with experiment (see Figure S22).

The isolation of the $[HBEt_3]^-$ adduct **5** contrasts with the $[(CAAC^{Cy})Cu(HBEt_3)]$ analogue that is (presumably) present as an (unseen) intermediate en route to **II** (Scheme 1). We have assessed the stabilities of these species, along with **6** and $[(CAAC^{Et})Cu(\kappa^2\text{-}BH_4)]$ (**III**) by computing the free energy changes associated with borane loss and dimerization (Figure 6). These indicate a significantly stronger H–$B(C_6F_5)_3$ bond in **6** ($\Delta G_1 = +38.2$ kcal mol^{-1}) compared to the H–BEt_3

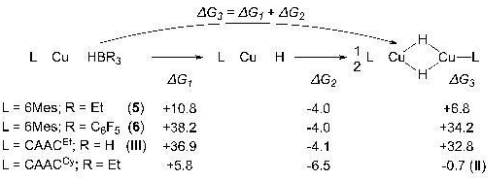

Figure 6. Computed free energy changes (kcal mol^{-1}; BP86-optimised with corrections for dispersion (D3) and THF solvent) for borane loss and dimerization of different $[LCu(HBR_3)]$ complexes.

bond in **5** ($\Delta G_1 = +10.8$ kcal mol^{-1}). **5** may therefore be susceptible to BEt_3 loss to form [(6Mes)CuH], however, dimer formation is not thermodynamically accessible in this case ($\Delta G_3 = +6.8$ kcal mol^{-1}), and so alternative decomposition routes are apparently accessed, as seen experimentally. The BH_3 moiety in **III** is also strongly bound ($\Delta G_1 = +36.9$ kcal mol^{-1}), consistent with the isolation of the borohydride complex.[4] In contrast, BEt_3 loss from $[(CAAC^{Cy})Cu(HBEt_3)]$ is particularly facile ($\Delta G_1 = +5.8$ kcal mol^{-1}) and the subsequent dimerization energy is sufficiently exergonic to rationalize the formation of dimer **II** upon reaction of $[(CAAC^{Cy})Cu(O^tBu)]$ with $LiHBEt_3$.[3b]

The computational findings that **5** and **6** are not simple Lewis acid stabilized forms of [(6Mes)CuH] were reinforced by probing their reactivity with PhC≡CMe. In neither case was the hydrocupration product **4** (Scheme 1) formed. Addition of PhC≡CMe (2 equiv) to **5** at 225 K resulted in no reaction until ca. 288 K, at which point the presence of multiplets in the $\delta = 4$–6 ppm region of the ^{1}H NMR spectrum suggested that some reduction of the alkyne had occurred. However, none of the signals matched those of **4**.[6] The ^{11}B NMR spectrum showed resonances at $\delta = 60$, 52 and −14 ppm suggestive of multiple boron-containing species being produced. There was no reaction between **6** and the alkyne over days at room temperature, with only the transformation to the homoleptic cationic bis-carbene complex **7** apparent from the ^{11}B NMR spectrum.

In conclusion, the synthesis of the novel Cu-borate complexes $[(6Mes)Cu(HBR_3)]$ (R = Et (**5**), C_6F_5 (**6**)) has been reported. Experimental and computational studies show that **5** features a two-coordinate Cu center, while **6** exhibits a further stabilizing Cu–C_{ipso} interaction to one C_6F_5 substituent. Although both species possess a direct Cu–H interaction, neither can be considered as Lewis acid stabilized forms of [(6Mes)CuH]. The isolation of a monomeric [(NHC)CuH] species, therefore, still remains an elusive target.

Acknowledgements

We thank the University of Bath (DTA to L.R.C.) and Heriot-Watt University (James Watt scholarship to N.A.R.) for financial support and Prof Gregory Wildgoose (University of East Anglia) for discussions and experimental assistance. This work used the ARCHER UK National Supercomputing Service (http://www.archer.ac.uk).

Keywords: copper · DFT calculations · hydride ligand · Lewis acids · N-heterocyclic carbene

How to cite: *Angew. Chem. Int. Ed.* **2016**, *55*, 15539–15543
Angew. Chem. **2016**, *128*, 15768–15772

[1] a) C. Deutsch, N. Krause, B. H. Lipshutz, *Chem. Rev.* **2008**, *108*, 2916–2927; b) T. Fujihara, T. H. Xu, K. Semba, J. Terao, Y. Tsuji, *Angew. Chem. Int. Ed.* **2011**, *50*, 523–527; *Angew. Chem.* **2011**, *123*, 543–547; c) A. M. Whittaker, G. Lalic, *Org. Lett.* **2013**, *15*, 1112–1115; d) N. Cox, H. Dang, A. M. Whittaker, G. Lalic, *Tetrahedron* **2014**, *70*, 4219–4231; e) T. Vergote, F. Nahra, A. Merschaert, O. Riant, D. Peeters, T. Leyssens, *Organometallics* **2014**, *33*, 1953–1963; f) M. R. Uehling, A. M. Suess, G. Lalic, *J. Am. Chem. Soc.* **2015**, *137*, 1424–1427; g) S.-L. Shi, S. L. Buchwald, *Nat. Chem.* **2015**, *7*, 38–44; h) A. J. Jordan, G. Lalic, J. P. Sadighi, *Chem. Rev.* **2016**, *116*, 8318–8372.

[2] a) S. A. Bezman, M. R. Churchill, J. A. Osborn, J. Wormald, *J. Am. Chem. Soc.* **1971**, *93*, 2063–2065; b) T. H. Lemmen, K. Folting, J. C. Huffman, K. G. Caulton, *J. Am. Chem. Soc.* **1985**, *107*, 7774–7775; c) G. V. Goeden, J. C. Huffman, K. G. Caulton, *Inorg. Chem.* **1986**, *25*, 2484–2485; d) C. F. Albert, P. C. Healy, J. D. Kildea, C. L. Raston, B. W. Skelton, A. H. White, *Inorg. Chem.* **1989**, *28*, 1300–1306.

[3] a) N. P. Mankad, D. S. Laitar, J. P. Sadighi, *Organometallics* **2004**, *23*, 3369–3371; b) G. D. Frey, B. Donnadieu, M. Soleilhavoup, G. Bertrand, *Chem. Asian J.* **2011**, *6*, 402–405; c) S. C. Schmid, R. Van Hoveln, J. W. Rigoli, J. M. Schomaker, *Organometallics* **2015**, *34*, 4164–4173; d) A. J. Jordan, C. M. Wyss, J. Bacsa, J. P. Sadighi, *Organometallics* **2016**, *35*, 613–616. See also: e) C. M. Wyss, B. K. Tate, J. Bacsa, T. G. Gray, J. P. Sadighi, *Angew. Chem. Int. Ed.* **2013**, *52*, 12920–12923; *Angew. Chem.* **2013**, *125*, 13158–13161.

[4] X. Hu, M. Soleilhavoup, M. Melaimi, J. Chu, G. Bertrand, *Angew. Chem. Int. Ed.* **2015**, *54*, 6008 – 6011; *Angew. Chem.* **2015**, *127*, 6106 – 6109.
[5] The stability of **III** contrasts markedly with that of the phosphine analogue $[(PPh_3)Cu(\kappa^2\text{-}BH_4)]$. R. K. Hertz, R. Goetze, S. G. Shore, *Inorg. Chem.* **1979**, *18*, 2813 – 2816.
[6] L. R. Collins, I. M. Riddlestone, M. F. Mahon, M. K. Whittlesey, *Chem. Eur. J.* **2015**, *21*, 14075 – 14084.
[7] References [3a,c–d] provide examples which associate yellow colored solutions with $[(NHC)Cu(\mu\text{-}H)]_2$ dimers.
[8] DOSY measurements gave a value for r_H of 6.2 Å. Based on previous studies of diamidocarbene copper chloride complexes (L. R. Collins, J. P. Lowe, M. F. Mahon, R. C. Poulten, M. K. Whittlesey, *Inorg. Chem.* **2014**, *53*, 2699 – 2707), the value is consistent with a dimeric structure.
[9] 6Dipp = 1,3-bis(2,6-diisopropylphenyl)-3,4,5,6-tetrahydropyrimidin-2-ylidene; 7Dipp = 1,3-bis(2,6-diisopropylphenyl)-4,5,6,7-tetrahydro-1,3-diazepin-2-ylidene.
[10] All attempts to isolate **2** were unsuccessful. On occasion, crystalline material was isolated (Supporting Information), but this proved to be $[(6Mes)AlH_3]$.
[11] a) D. Baudry, A. Dormond, B. Lachot, M. Visseaux, G. Zucchi, *J. Organomet. Chem.* **1997**, *547*, 157 – 165; b) M. J. Harvey, T. P. Hanusa, M. Pink, *Chem. Commun.* **2000**, 489 – 490; c) F. Basuli, J. Tomaszewski, J. C. Huffman, D. J. Mindiola, *Organometallics* **2003**, *22*, 4705 – 4714; d) W. J. Evans, J. M. Perotti, J. W. Ziller, *Inorg. Chem.* **2005**, *44*, 5820 – 5825; e) D. M. Lyubov, G. K. Fukin, A. A. Trifonov, *Inorg. Chem.* **2007**, *46*, 11450 – 11456; f) S. Krieck, H. Görls, M. Westerhausen, *Inorg. Chem. Commun.* **2010**, *13*, 1466 – 1469; g) X. W. Zhang, G. H. Maunder, S. Gießmann, R. MacDonald, M. J. Ferguson, A. H. Bond, R. D. Rogers, A. Sella, J. Takats, *Dalton Trans.* **2011**, *40*, 195 – 210.
[12] Calculations on the isolated cations within **5** and **6** were run with Gaussian09 while periodic DFT calculations were performed with CP2K. See the Supporting Information for full details.
[13] M. G. Crestani, M. Muñoz-Hernández, A. Arévalo, A. Acosta-Ramírez, J. J. Garcia, *J. Am. Chem. Soc.* **2005**, *127*, 18066 – 18073.
[14] a) W. J. Evans, K. J. Forrestal, M. A. Ansari, J. W. Ziller, *J. Am. Chem. Soc.* **1998**, *120*, 2180 – 2181; b) K. Yan, B. M. Upton, A. Ellern, A. D. Sadow, *J. Am. Chem. Soc.* **2009**, *131*, 15110 – 15111; c) K. Yan, G. Schoendorff, B. M. Upton, A. Ellern, T. L. Windus, A. D. Sadow, *Organometallics* **2013**, *32*, 1300 – 1316; d) M. D. Anker, M. Arrowsmith, P. Bellham, M. S. Hill, G. Kociok-Köhn, D. J. Liptrot, M. F. Mahon, C. Weetman, *Chem. Sci.* **2014**, *5*, 2826 – 2830; e) N. L. Lampland, A. Pindwal, S. R. Neal, S. Schlauderaff, A. Ellern, A. D. Sadow, *Chem. Sci.* **2015**, *6*, 6901 – 6907.
[15] L. R. Collins, T. M. Rookes, M. F. Mahon, I. M. Riddlestone, M. K. Whittlesey, *Organometallics* **2014**, *33*, 5882 – 5887.
[16] A gold analogue of **6** has been spectroscopically identified in the reaction of [(6/7Dipp)AuH] with $B(C_6F_5)_3$. N. Phillips, T. Dodson, R. Tirfoin, J. I. Bates, S. Aldridge, *Chem. Eur. J.* **2014**, *20*, 16721 – 16731.
[17] a) G. C. Welch, D. W. Stephan, *J. Am. Chem. Soc.* **2007**, *129*, 1880 – 1881; b) E. J. Lawrence, V. S. Oganesyan, D. L. Hughes, A. E. Ashley, G. G. Wildgoose, *J. Am. Chem. Soc.* **2014**, *136*, 6031 – 6036.
[18] A. D. Horton, J. de With, *Organometallics* **1997**, *16*, 5424 – 5436.
[19] J. Moellmann, S. Grimme, *Organometallics* **2013**, *32*, 3784 – 3787.
[20] D. A. Pantazis, J. E. McGrady, F. Maseras, M. Etienne, *J. Chem. Theory Comput.* **2007**, *3*, 1329 – 1336.

Manuscript received: August 18, 2016
Revised: October 19, 2016
Final Article published: November 15, 2016

ORGANOMETALLICS

Article

pubs.acs.org/Organometallics

Convergent (De)Hydrogenative Pathways via a Rhodium α-Hydroxylalkyl Complex

Simon Sung,[†] Jie Kang Boon,[†] Johnathan J. C. Lee,[†] Nasir A. Rajabi,[‡] Stuart A. Macgregor,[‡] Tobias Krämer,[‡,*] and Rowan D. Young[†,*]

[†]Department of Chemistry, National University of Singapore, 3 Science Drive 3, 117543 Singapore

[‡]Institute of Chemical Sciences, Heriot-Watt University, Edinburgh EH14 4AS, United Kingdom

Supporting Information

ABSTRACT: We report the convergent reaction pathways between [RhH(PPh$_3$)$_4$] and POP ketone (**1**) and alcohol (**2**) ligands that terminate in the formation of an α-hydroxylalkyl rhodium(I) complex (**3**), representing two halves of a formal reduction/oxidation pathway between **1** and **2**. In the case of hydride transfer to **1**, the formation of the α-hydroxylalkyl rhodium(I) complex (**3**) proceeds via a rare hydrido(η^2-carbonyl) complex (**4**). C−H activation in **2** at the proligand's central methine position, rather than O−H activation of the hydroxy motif, followed by loss of dihydrogen also generates the α-hydroxylalkyl rhodium(I) complex (**3**). The validity of the postulated reaction pathways is probed with DFT calculations. The observed reactivity supports α-hydroxylalkyl complexes as competent intermediates in ketone hydrogenation catalyzed by rhodium hydrides and suggest that ligands **1** and **2** may be "noninnocent" coligands in reported hydrogenation catalyst systems in which they are utilized.

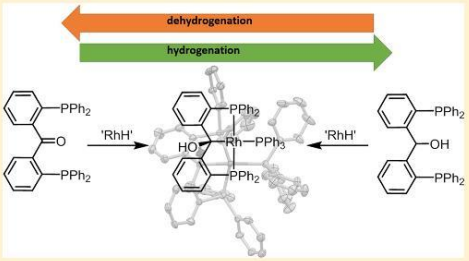

INTRODUCTION

The transfer of hydrogen from metals to ketones and, through reversibility, from alcohols to metals is of fundamental importance to (de)hydrogenation reactions mediated by metal catalysts.[1] Such reactions involve metal hydride intermediates and can proceed via two distinct pathways involving hydride transfer to either the electrophilic carbon or the nucleophilic oxygen of the carbonyl group (Scheme 1).

Scheme 1. Ketone Hydrogenation Proceeding via an Alkoxide Intermediate (Route A) or an α-Hydroxylalkyl Intermediate (Route B)

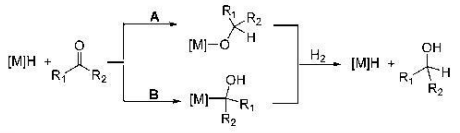

Thus, basic metal monohydrides tend to form metal alkoxide intermediates with ketones (Scheme 1, route **A**); H_2 addition then gives the alcohol product and regenerates the metal hydride.[2,3] In contrast, hydrogenation of aldehydes and ketones with acidic metal hydrides has been observed to proceed via α-hydroxylalkyl intermediates in acidic media (Scheme 1, route **B**).[4]

The mechanism by which a metal hydride is transferred to a bound ketone or aldehyde for cases operating via alkoxide intermediates is well-studied spectroscopically *in situ* and computationally (Scheme 1, **A**).[5] However, the transfer of a metal hydride to generate an α-hydroxylalkyl intermediate has less precedent despite their inference in catalytic hydrogenation[3a,b] and hydroformylation[6] reactions.

Indeed, structurally characterized examples mapping hydride migration to either electrophilic or nucleophilic positions of a bound organocarbonyl are unknown. Intermediates involved in such transitions are of great importance to a wide range of carbonyl reductions but until this study have only been interrogated *in silico* or observed spectroscopically *in situ*.[6]

α-Hydroxylalkyl complexes are typically unstable with respect to β-hydrogen elimination, so examples of isolated complexes are rare.[7] In pioneering work, Gladysz et al. (and later Garralda et al.) demonstrated the formation of α-hydroxylalkyl complexes in constrained environments based on hydride migration to *o*-(diphenylphosphino)benzaldehyde ligands.[7a,b]

If α-hydroxylalkyl complexes lie on the reaction pathway of ketone hydrogenation, then they should also be accessible through the C−H activation of an alcohol. Such selective activation of C−H bonds in the presence of O−H bonds is of great interest regarding simple alcohol functionalization, with

Received: February 28, 2017
Published: April 14, 2017

DOI: 10.1021/acs.organomet.7b00158
Organometallics 2017, 36, 1609−1617

Scheme 2. Formation of 3 from Addition of 1 or 2 to $[RhH(PPh_3)_4]$[a]

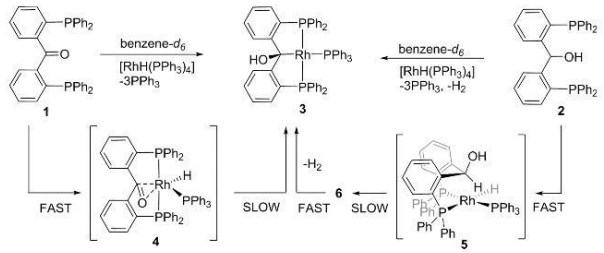

[a]Geometry of compound **6** is discussed below.

the single-step C−H activation and functionalization of alcohol geminal C−H positions remaining a contemporary chemical challenge.[8] However, such selective C−H activation is unknown, so this approach is nontrivial due to the presence of several alternative reaction outcomes.

Herein we describe the controlled hydrogen transfer to and from the ketone and alcohol moieties of the diphosphine POP ligands **1**[9] and **2**[10] mediated by hydridotetrakis-(triphenylphosphine)rhodium(I), $[RhH(PPh_3)_4]$. The results demonstrate a convergent pathway to a common α-hydroxylalkyl complex that is accessible from both ketone and alcohol precursors using a common ligand platform. Within this we demonstrate the formation of an α-hydroxylalkyl species direct from a rare isolated metal-hydride/η^2-ketone precursor, as well as the geminal C−H activation of an alcohol. DFT calculations are utilized to probe the mechanistic details of these processes which are shown to map out fully route **B** shown in Scheme 1. The results also highlight the potential noninnocence of these POP ligands, which are commonly used in asymmetric hydrogenation catalysis.[9]

RESULTS AND DISCUSSION

Addition of POP ketone **1** to $[RhH(PPh_3)_4]$ in benzene-d_6 resulted in the loss of 3 equiv of PPh_3 and the formation of the α-hydroxyl complex **3** over 12 h. Monitoring the reaction at shorter time intervals revealed that **1** and $[RhH(PPh_3)_4]$ initially formed hydrido(η^2-carbonyl) **4** (within minutes) that was converted into **3** over a matter of hours at room temperature (Scheme 2). Formation of **4** was evident by the presence of a rhodium-bound carbon (δ_C 137.8, $^1J_{RhC}$ = 9.2 Hz). The chemical shift and rhodium−carbon coupling constant deviate notably from that of the proligand carbonyl (δ_C 197.3) and imply a bonding mode lying between the extreme cases of η^2-carbonyl and metallaepoxide (defined by the Dewar−Chatt−Duncanson model) and exemplified by recently reported analogues [**1**-Ni(PPh_3)][11] and $[L_1IrX]$[12] (L_1 = κ^3-*P*,(η^2-C,O),*P*′-bis(5-(diisopropylphosphino)3,4-benzo[*b*]-thiophenyl)-methanone, X = Cl or OH). A degree of π-retrodonation to the carbonyl is supported by relatively small one-bond rhodium−phosphorus coupling constants ($^1J_{RhP}$ = 130.6, 108.9 Hz) in **4** indicating an electron-poor rhodium center. FTIR spectroscopy could not provide support for carbonyl coordination with failure to identify a specific C=O stretching band. However, a strong Rh−H stretch was observed at 1969 cm^{-1} (cf. calcd value of 1993 cm^{-1}, see Supporting Information).

Crystals of compound **4** were grown upon layering a toluene solution of **4** with hexane at low temperature (253 K). The molecular structure of **4** (Figure 1) supports the coordination

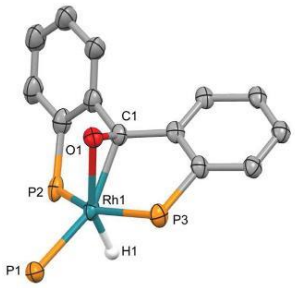

Figure 1. Molecular structure of **4**. Phenyl groups and hydrogens except H1 are omitted for clarity; 50% thermal ellipsoids. H1 was located in a Fourier difference map. Selected distances (Å) and angles (deg): Rh1−C1, 2.118(7); Rh1−O1, 2.187(5); Rh1−P1, 2.382(2); Rh1−P2, 2.318(2); Rh1−P3, 2.262(2); C1−O1, 1.339(8); P2−Rh1−P3, 153.19(8); P1−Rh1−C1, P1, 152.3(2).

of the carbonyl to rhodium, observed spectroscopically in solution. The geometry around rhodium is best described as pseudotrigonal bipyramidal, with numerous examples of analogous pentacoordinate rhodium complexes subtended by η^2-olefin ligands exhibiting such geometry.[13] Significant elongation of the C=O bond (1.339(8) Å) from the free ligand **1** (1.213(3) Å)[9] is observed indicating a significant degree of π-retrodonation. However, the coordination is consistent with a bound carbonyl, falling within the range of previously reported rhodium η^2-carbonyl complexes.[14] Notably, the molecular structure of **4** reveals the hydrido ligand to be *trans* to the oxygen in the coordinated carbonyl, representing a barrier for hydride to carbonyl migration.

In solution, α-hydroxylalkyl complex **3** is generated from **4** upon the transfer of hydrogen from rhodium to oxygen. The ^{1}H NMR spectrum of compound **3** exhibits a hydroxyl resonance at 3.15 ppm ($^4J_{PH}$ = 3.5 Hz). Selective decoupling of a phosphorus signal at δ_P 37.5 resolves the signal at δ_H 3.15 into a singlet, indicative of long-range ^{1}H−^{31}P coupling. The addition of D_2O to a solution of **3** resulted in the disappearance of this signal, while other NMR signals remained unaffected. The carbon−rhodium bond in **3** is characterized by a doublet

DOI: 10.1021/acs.organomet.7b00158
Organometallics 2017, 36, 1609−1617

of doublet of triplets signal in the ^{13}C NMR spectrum at δ_C 106.1 ($^1J_{RhC}$ = 25.2 Hz), with a typical $^1J_{RhC}$ for a rhodium α-hydroxylalkyl moiety.[7b,h,i]

X-ray diffraction study confirms **3** to be an α-hydroxylalkyl complex (Figure 2). In agreement with solution data, **3** assumes

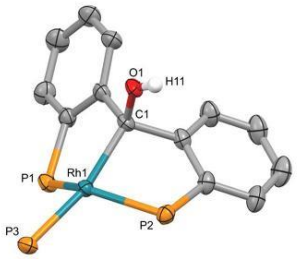

Figure 2. Molecular structure of **3**. Phenyl groups, benzene solvent molecule, and hydrogens except H11 are omitted for clarity; 50% thermal ellipsoids. H11 was located in a Fourier difference map. Selected distances (Å) and angles (deg): Rh1−C1, 2.103(12); C1−O1, 1.458(14); Rh1−P1, 2.231(3); Rh1−P2, 2.254(3); Rh1−P3, 2.315(3); P1−Rh1−P2, 132.45(13); P3−Rh1−C1, 166.4(4); O1−C1−Rh1, 106.4(8).

a distorted square-planar geometry, with P1−Rh1−P2 and C1−Rh1−P3 angles deviating greatly from linear (132.45(13) and 166.4(4)°, respectively). The significantly reduced average Rh−P bond distances in **3** as compared to those in **4** point to a more electron-rich Rh center in the former. The formation of **3** from **4** was monitored with ^1H and ^{31}P NMR spectroscopy across a range of temperatures and in the presence of varying quantities of added PPh_3 (see Supporting Information). Although it was apparent that free PPh_3 accelerated the reaction, the exact reaction order relative to [PPh_3] could not be precisely determined, but it was found to be between 0 and 1. This may be indicative of a nontrivial mechanism. Thus, although accurate activation parameters from these collected data could not be derived, they are discussed in the Supporting Information.

Compound **3** could also be generated by the addition of alcohol proligand **2** to [$RhH(PPh_3)_4$] in benzene-d_6 with concomitant loss of H_2 (Scheme 2). The formation of **3** from **2** and [$RhH(PPh_3)_4$] completes the (de)hydrogenation reaction pathway between **1** and **2** mediated by [$RhH(PPh_3)_4$]. Monitoring the production of **3** from the combination of either **1** or **2** with [$RhH(PPh_3)_4$] reveals that once a maximum concentration of **3** has been achieved very small quantities of **4** are still observed. In the presence of >1 equiv of PPh_3, this equilibrium is established in a matter of days but takes weeks to establish in the absence of PPh_3. The ratio of **3**/**4** after equilibrium is established is ca. 20:1 (see Supporting Information), suggesting a ΔG of −1.8 kcal mol^{-1}.

En route to compound **3** from **2** and [$RhH(PPh_3)_4$], compound **5** is observed. Although **5** is transient at room temperature, at 280 K it can be spectroscopically characterized and is distinguished by the appearance of new signals in the ^1H NMR spectrum at δ_H 9.87 (br s) and 1.39 (d, $^3J_{HH}$ = 3.3 Hz) that correlate to one another in a COSY 2D NMR experiment. A HSQC experiment provided no correlation for the signal at δ_H 1.39 to any ^{13}C atoms but rather correlated the signal at δ_H 9.87 with a signal at δ_C 69.3. These data suggest the identities of the signals at δ_H 9.87 and 1.39 to be the methine CH and OH signals of bound **2** respectively. In the upfield region of the ^1H NMR spectrum of **5**, a broad doublet is observed at δ_H −8.58 ($^2J_{PH}$ = 90 Hz), 0.52 ppm upfield of the hydride signal of [$RhH(PPh_3)_4$] (δ_H −8.06, $^1J_{RhH}$ = 12.7 Hz), suggesting fluxional behavior. The ^{31}P NMR spectrum of **5** further revealed the dynamic behavior of **5**, with two broad doublets present at δ_P 34.3 ($^1J_{RhP}$ = 170 Hz) and 31.0 ($^1J_{RhP}$ = 131 Hz) with a combined integral of three phosphorus nuclei relative to free PPh_3 (integration: 3P).

Analysis by ^{31}P NMR spectroscopy of a solution of **5** and liberated PPh_3 generated from [$RhH(PPh_3)_4$] and **2** in toluene-d_8 at 223 K revealed the presence of at least three separate phosphorus environments on rhodium (integration: 4P) with complex coupling patterns in addition to free PPh_3 (integration: 2P). At this temperature, the ^1H spectrum of **5** revealed that fluxional processes were still occurring on the ^1H NMR time scale. The hydridic signal remained broad. However, it had shifted upfield to −12.22 ppm, and the $^2J_{PH}$ for this signal had increased to 110 Hz. Concurrently, the methine CH signal in bound **2** had shifted upfield from δ_H 9.87 to 9.20. Overall, the NMR data imply that **5** exists in equilibrium with its PPh_3 adduct, **5**·PPh_3, and that the adduct may be preferred at lower temperatures.

A downfield shift for C−H bonds in the vicinity of d^8 metals has been observed in bisphosphino methylene ligands related to **2** (that also undergo C−H activation) and has previously been assigned as an anagostic interaction.[15] Assignment based purely on NMR spectroscopic evidence has recently been reported to be misleading; however, we cautiously assign the C−H−Rh interaction as anagostic with supporting computational analysis (see below).[16]

Further insight into the C−H activation of POP alcohol ligand **2** was obtained from its reaction with [$RhCl(COD)PPh_3$] that led to the formation of the hydridochloride **7** alongside free 1,5-cyclooctadiene (Scheme 3). ^1H NMR data

Scheme 3. Reaction of 2 and [$RhCl(COD)PPh_3$] to Form 7[a]

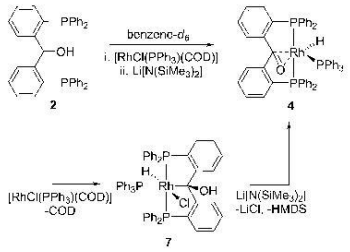

[a]Subsequent treatment of **7** with Li[$N(SiMe_3)_2$] produces **4**.

support compound **7** being an α-hydroxylalkyl complex, with a hydroxyl signal located at δ_H 7.57. This signal appears as a doublet with long-range coupling to phosphorus (d, $^4J_{PH}$ = 7.5 Hz); selective ^{31}P decoupling at δ_P 23.7 collapses this signal to a singlet. The addition of a small quantity of D_2O also resulted in the disappearance of the signal while other NMR data remain unaffected. The ^1H NMR spectrum also reveals the appearance of an upfield hydride shift at δ_H − 16.22 (dtd, $^1J_{RhH}$ = 22.1 Hz (d), $^2J_{PH}$ = 14.3 Hz (t), $^2J_{PH}$ = 9.2 Hz (d)).

DOI: 10.1021/acs.organomet.7b00158
Organometallics 2017, 36, 1609−1617

A molecular structure determination of **7** (Figure 3) reveals its geometry with the PCP ligand adopting a *mer* configuration

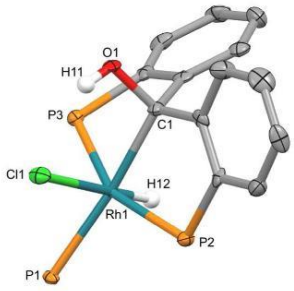

Figure 3. Molecular structure of **7**. Phenyl groups and hydrogens except H11 and H12 are omitted for clarity; 50% thermal ellipsoids. H11 and H12 were located in a Fourier difference map. Selected distances (Å) and angles (deg): Rh1−C1, 2.177(4); Rh1−Cl1, 2.500(1); Rh1−P1, 2.4019(12); Rh1−P2, 2.3189(13); Rh1−P3, 2.2971(12); P2−Rh1−P3, 153.03(4); P1−Rh1−C1, 174.46(12).

after C−H oxidative addition to the rhodium center. It is also observed that the hydroxyl hydrogen (H11), located in a Fourier difference map, is hydrogen-bonded to the proximal chloride ligand ($Cl1{-}H11_{dist}$ = 2.273 Å). Induced elimination of HCl from **7** by treatment with 1 equiv of $Li[N(SiMe_3)_2]$ results in the formation of compound **4**, which then transforms to **3**. This stands in contrast to the reaction between **2** and $[RhH(PPh_3)_4]$ that generates **3** without any observation of **4**, signifying that H_2 loss occurs via a *cis*-dihydride intermediate rather than through elimination of H_2 from a *trans*-dihydride analogue of **7** (i.e., a *trans*-$Rh^{III}(H)_2(COH)P_2$ fragment).

To investigate the possible identity of *cis*-dihydride intermediate **6**, dihydrogen (4 atm) was introduced into an NMR sample tube containing **3** in toluene-d_8 solution. At room temperature, ^{1}H NMR spectroscopy reveals the formation of a broad signal at δ_H −2.8 (integration: 2H). In addition, the signal for free H_2 (expected at δ_H 4.50) is not observed. The hydroxyl signal originally at δ_H 3.15 is broadened and observed to shift downfield to δ_H 3.65 (integration: 1H). The ^{31}P NMR spectrum of this sample reveals resonances at δ_P 45.6 (dd, 2H, $^1J_{RhP}$ = 125.1 Hz, $^2J_{PP}$ = 20.2 Hz) and 41.7 (dt, 1H, $^1J_{RhP}$ = 93.2 Hz, $^2J_{PP}$ = 20.2 Hz), displaying a similar chemical shift to **3**, but reduced coupling constants. As the temperature is lowered to 233 K, the hydridic signal resolves into a broad doublet at δ_H −6.8 ($^2J_{PH}$ = 140 Hz), indicative of a single *trans* phosphorus-hydride environment. T_1 measurements at various temperatures excluded the identity of **6** as a dihydrogen complex (see Supporting Information). At this temperature, the hydroxyl signal is observed at δ_H 4.25 as a doublet ($^4J_{PH}$ = 4.4 Hz), and free hydrogen is observed as a broad signal at δ_H 4.5 that sharpens at lower temperatures. A $^1H\{^{31}P\}$ NMR spectrum with a decoupling window centered at δ_P 40.0 collapses both the hydridic and hydroxyl signals into singlets.

The ^{31}P NMR spectrum of the sample at 233 K shows a broad doublet at δ_P 45.6 ($^1J_{RhP}$ = 86.5 Hz) and a doublet of triplets at δ_P 41.7 ($^1J_{RhP}$ = 84.5 Hz, $^2J_{PP}$ = 14.9 Hz). HMBC experiment at 233 K (optimized for J_{CH} = 10 Hz) exhibits a correlation between the hydroxyl proton at δ_H 4.25 and a signal at δ_C 95.8. A 1D ^{13}C NMR experiment revealed this signal to be a doublet of doublets ($^2J_{PC}$ = 95.2 Hz, $^1J_{RhC}$ = 28.6 Hz). After warming and degassing of the sample, compound **3** was quantitatively reformed. These data are indicative of the formation of a Rh(III) center at low temperature in dynamic equilibrium with **3** and molecular hydrogen. Given these spectroscopic data, **6** is assigned as a *cis* dihydride featuring a facially coordinated PCP ligand (Scheme 4).[15b,e] Selected NMR spectroscopic data for compound **3**−**7** are shown in Table 1.

Scheme 4. Hydrogenation of 3 Generates *Cis* Dihydride 6

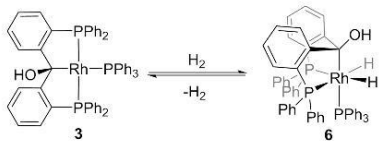

Confirmation that the C−H methine of **2** is activated in reactions with rhodium (as opposed to O−H activation followed by rearrangement) is confirmed by employing isotopologues **2a** and **2b** (Scheme 5).C−H activation is expected on a dehydrogenation pathway that invokes an *α*-hydroxylalkyl intermediate. When $[RhH(PPh_3)_4]$ is reacted with isotopologue **2a**, **3a** is generated (Scheme 5), which is spectroscopically identical to **3**, except that the RhCO*H* signal at δ_H 3.15 was diminished and a signal at 3.25 ppm was located in the ^{2}H NMR spectrum of **3a**, signifying the deuteration of the hydroxyl position. Conversely, when **2b** is reacted with $[RhH(PPh_3)_4]$, compound **3** is produced with loss of HD. Addition of **2b** to $[RhCl(COD)PPh_3]$ resulted in the production of **7b**, identical to **7** (by NMR spectroscopy) with the exception of substitution of the hydride ligand with deuterium, as evident by the absence of a hydridic signal in the ^{1}H NMR spectrum.

To elucidate the mechanistic details of the convergent pathways that convert both the ketone (**4**) and alcohol (**5**) precursors into the *α*-hydroxylalkyl product **3**, a computational analysis of the associated free energy surfaces was carried out using DFT calculations at the B97-D3/BS2//BP86/BS1 level of theory corrected for benzene solvent (see Supporting Information for computational details). The most accessible computed pathways at 298 K for both processes are detailed in Figure 4. The optimized structure of **4** agrees well with the crystallographic data. In particular the C═O (calcd: 1.35 Å, exp.: 1.339(8) Å), Rh−C (calcd: 2.16 Å, exp.: 2.118(7) Å), and Rh−O (calcd: 2.22 Å, exp.: 2.187(5) Å) distances are well-reproduced, along with the *trans*-P−Rh−P angle of the POP ligand (calcd: 154.0°, exp.: 153.19(8)°).

Analysis of the natural bond orbitals (NBOs) in **4** shows that C═O coordination to the metal center is governed by $\pi_{CO} \rightarrow$ Rh donation, reinforced by substantial $\pi^*_{CO} \leftarrow$ Rh back-donation (see Figure S65). The elongation of the C═O bond arises due to notable population of the π^*_{CO} orbital (0.79 e^-) and depopulation of the π_{CO} orbital (1.82 e^-). The partial reduction of the double-bond character of the C═O bond is also reflected in the Wiberg bond index (1.18), lying in between those for the C═O double bond in **1** (1.68) and the C−O(H) single bond in **2** (0.91). In contrast, the indices for the Rh···C (0.39) and Rh···O (0.24) interactions are smaller compared to those found for the Rh−C (0.47) and Rh−H (0.56) bonds in **3** and **4**, respectively, which serve as a reference

DOI: 10.1021/acs.organomet.7b00158
Organometallics 2017, 36, 1609−1617

Table 1. Selected NMR Spectroscopic Data for Compounds 3-7

compound	δ_C (Rh−C)	$^2J_{PC}$ (Hz)	$^1J_{RhC}$ (Hz)	J_{RhP} (Hz)	J_{PP} (Hz)
3	106.1	4.8 (t), 73.5 (d)	25.2	189, 120	28.3
4	137.8	23.7 (d)[a]	9.2	131, 109	10.1
5	N/A	N/A	N/A	170, 131[b]	*a*
6	95.8[c]	95.2 (d)[a,c]	28.6[c]	87, 85[c]	14.9[c]
7	99.4	94.1 (d)[a]	20.8	120, 79	24.0

[a]Coupling to *cis* phosphorus nuclei was not observed. [b]280 K. [c]233 K.

Scheme 5. Isotopomers 2a, 2b React with $[RhH(PPh_3)_4]$ to Generate Isotopologues 3a and 7b, Respectively

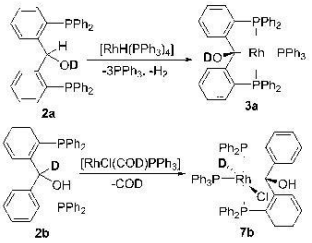

point. Thus, in accordance with the experimental findings the {RhCO} unit is best described as a Rh-bound carbonyl.

The optimized structure of **3** reproduces the distorted square-planar geometry around Rh seen experimentally: *trans*-P−Rh−P (calcd: 132.9°, exp.: 132.45(13); *trans*-C−Rh−P (calcd: 164.1°, exp.: 166.4(4)). The Rh−C distance is reduced from 2.16 Å in **4** to 2.13 Å in **3**, and this is paralleled by an increase in the calculated Rh−C isotropic spin−spin coupling constant (**4**: $^1J_{RhC}$ = −9.1 Hz; **3**: $^1J_{RhC}$ = −17.4 Hz).

The computed mechanism for the formation of **3** from **4** starts with an initial isomerization of **4**, with a calculated barrier of 17.7 kcal mol^{-1} proceeding via **TS(4−Int1)**. The POP ligand undergoes isomerization from a *mer*-κ^3-P,(CO),P to a *fac*-κ^3-P,(CO),P binding mode (∠P−Rh−P 109.1°). Concomitantly, the hydride moves from its equatorial coordination site *trans* to oxygen into the opening axial position. The distortion of the ligand in **TS(4−Int1)** also causes the C═O unit to move away from Rh (Rh−O: 2.52 Å; Rh−C: 2.38 Å), thereby decreasing π-backbonding from the metal center and restoring more double-

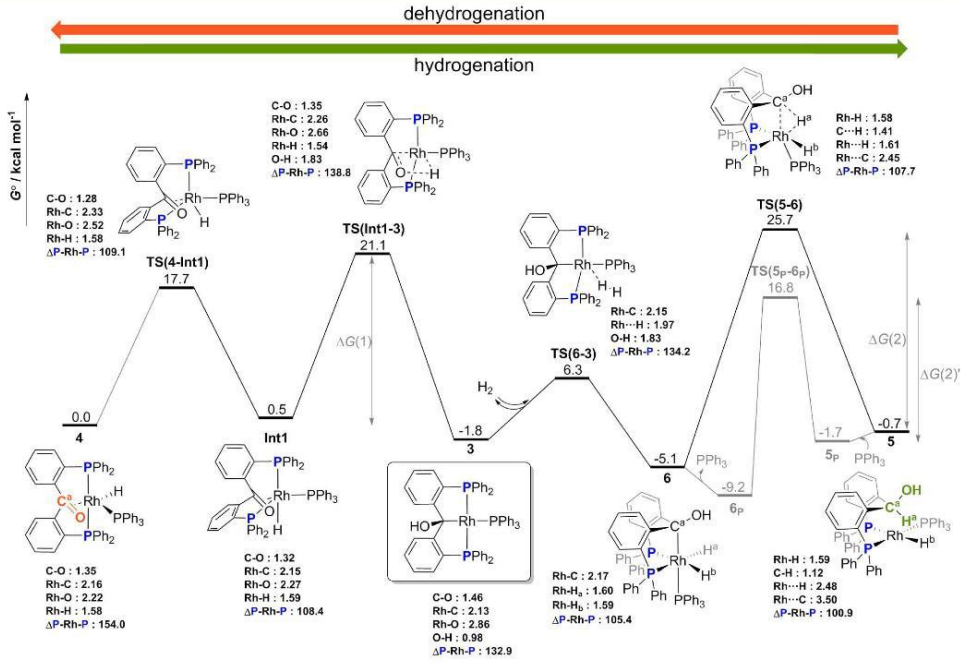

Figure 4. Computed profile (B97-D3/BS2//BP86/BS1) for the transformation of **4** into **3** (left) and **5** into **3** (right). The gray profile is associated with adduct $\mathbf{5}_P$, featuring H-bonded PPh_3. Relative Gibbs free energies (298 K, kcal mol^{-1}), corrected for benzene solvent, are given along with key bond metric data (Å, deg). Double-arrows indicate energy spans $\Delta G(1)$, $\Delta G(2)$, and $\Delta G(2)'$.

DOI: 10.1021/acs.organomet.7b00158
Organometallics 2017, 36, 1609−1617

bond character (C═O: 1.28 Å). The *cis* arrangement of the {Rh(C═O)(H)} moiety in **Int1** ($G°$ = +0.5 kcal mol^{-1}) allows for insertion of the ketone into the Rh−H bond through **TS(Int1−3)** at 21.1 kcal mol^{-1} to form the α-hydroxylalkyl in **3**. By inspection, **TS(Int1−3)** also defines the overall energetic span[17] ($\Delta G(1)$ = +21.1 kcal mol^{-1}) for the transformation of **4** into **3**, with the computed barrier being consistent with the slow process seen experimentally. The hydrogen transfer in **TS(Int1−3)** is accompanied by an isomerization of the ligand to its distorted *mer*-κ^3-P,C,P form ($\angle$P−Rh−P 138.8°). Complex **3** is energetically stabilized by a mere 1.8 kcal mol^{-1} relative to **4**. The marginal exergonicity of this process is in line with the establishment of an equilibrium between these two species, as confirmed by experiment.

The lowest-energy pathway for the formation of **3** from **5** is shown on the right side of Figure 4. Precursor complex **5** features an approximately square-planar geometry around the Rh^{I} center, with the POP ligand adopting a *cis*-κ^2-P,P arrangement ($\angle$P−Rh−P 100.9°) and computed Rh···H^a and Rh···C^a distances of 2.48 and 3.50 Å, respectively, to the central C−H bond of the ligand. Computed AIM and NBO parameters suggest that the Rh···H^a−C^a interaction is of closed-shell electrostatic nature, in line with a weak anagostic interaction.[16,18] Oxidative addition of the C^a−H^a bond across the P$_{POP}$−Rh−PPh$_3$ vector occurs with a barrier of 26.4 kcal mol^{-1} to yield intermediate **6** (−5.1 kcal mol^{-1}). Activation of the C−H bond in **TS(5−6)** is accompanied by movement of the PPh$_3$ ligand into the axial position. We have also considered other possibilities for this reaction step, none of which presented a feasible alternative. Oxidative addition across the P$_{PPh3}$−Rh−H vector in the alternative *trans*-isomer **5′** shifts the energy profile upward by ∼10 kcal mol^{-1} (see Supporting Information). A search for a concerted C−H activation step via σ-bond metathesis proved unsuccessful. Experimentally there is an excess of PPh$_3$ present in solution, so we also scrutinized the possible effect of C(H)OH···PPh$_3$ H-bonding on the C−H activation. Under these circumstances, the barrier is notably lowered ($\Delta G°^{\ddagger}$ = 18.5 kcal mol^{-1}, relative to **5$_P$**, gray profile in Figure 4). The optimized structure of the corresponding transition state **TS(5$_P$-6$_P$)** is shown in Figure 5. The optimized bond parameters in **TS(5$_P$−6$_P$)** closely resemble those in **TS(5−6)**, with Rh···C^a, Rh···H^a, and C^a−H^a distances of 2.45, 1.61, and 1.43 Å, respectively. The (O)H···PPh$_3$ distance is 2.45 Å, similar to the H-bond in complex **5$_P$**. Complex **6** exhibits an octahedral coordination geometry around the Rh^{III} center, featuring a *fac*-κ^3-P,C,P tridentate ligand with the Rh−C bond *trans* to PPh$_3$. Facile reductive elimination of the *cis*-hydrides in **6** proceeds with a barrier of 11.4 kcal mol^{-1} readily generating the final product **3** upon loss of H$_2$. The overall reaction rate is determined by the initial oxidative addition step at 18.5 kcal mol^{-1}, and this reduced barrier is consistent with the observation that **5** is transient at room temperature. Note that although the formation of **3** is computed to be slightly endergonic relative to **6** ($\Delta G°$ = +3.3 kcal mol^{-1}) experimentally species **3** and **6** are in equilibrium which can be driven to **3** by removal of H$_2$ upon degassing the solution.

Experimentally the NMR characterization of **5** points to it being fluxional in solution and, moreover, that temperature-dependent coordination of PPh$_3$ to the Rh center also occurs. Computationally, the trigonal-pyramid and *trans*-κ^2-P,P isomers of **5** lie ∼10 kcal mol^{-1} above the *cis*-isomer, so these may be kinetically accessible in potential H/PPh$_3$ exchange pathways.[19] Formation of a trigonal-bipyramidal 18-electron complex, **5**·PPh$_3$, via axial addition of PPh$_3$ to **5** was computed to be energetically strongly favored ($\Delta G°$ = −7.6 kcal mol^{-1}), even when the basis set superposition error (BSSE) was taken into account. This value runs counter to experimental evidence suggesting a dynamical equilibrium in which PPh$_3$ reversibly binds to **5** (i.e., a thermoneutral process with $\Delta G° \approx 0$ kcal mol^{-1}). Although dispersion-corrected DFT can predict phosphine−metal binding energies with good accuracy,[20] in the present example the metal−ligand bond strength appears to be strongly overestimated by the calculations. Of a range of functionals that were tested, B3LYP-D3 performs well for the phosphine binding energy (see Table 2).[20e] However, with this approach the overall barriers linking **4** to **3** and **5** to **3** are in excess of 25 kcal mol^{-1}, rather too high for these room temperature processes. It seems that no single functional can provide balanced energetics for the various ligand binding and bond activation steps in this system. Nonetheless, our conclusions regarding the mechanism for the convergent formation of **3** from **4** and **5**, respectively, obtained with the B97-D3/BS2//BP86/BS1 protocol are qualitatively in good agreement with the experimental observations.

It is plausible that dissociation of PPh$_3$ from **5**·PPh$_3$ must occur prior to C−H bond activation to give **6**. Indeed, a stepwise relaxed scan of the Rh···C^a distance in **5**·PPh$_3$ induces dissociation of one PPh$_3$ ligand, restoring the square-planar geometry of **5** before accessing **TS(5−6)**. The computed intrinsic reaction coordinate clearly confirms that **TS(5−6)** connects **6** to **5** providing support for **5** as an intermediate along the reaction profile.

Table 2. Summary of the Functional Dependence of Phosphine Binding Energies According to 5 + PPh$_3$ ⇆ 5·PPh$_3$ ($\Delta G_{bind+BSSE}$, in kcal mol^{-1}) as Well as Key Energy Spans for the Overall Reaction Profile in Figure 4[a]

functional	$\Delta G_{bind+BSSE}$	$\Delta G(1)$	$\Delta G(2)$	$\Delta G(2)'$
BP86-D3	−13.6	22.2	22.6	14.6
B97-D3	−7.6	21.1	26.4	18.5
B3LYP-D3	+0.1	25.6	29.9	21.5
M06	+8.6	24.9	33.7	24.4

[a]See Figure 4for the definition of ΔG(1), ΔG(2) ΔG(2)′).

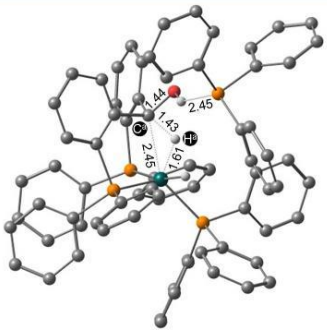

Figure 5. Optimized geometry of **TS(5$_P$−6$_P$)**. Bond distances are in Å.

DOI: 10.1021/acs.organomet.7b00158
Organometallics 2017, 36, 1609−1617

CONCLUSIONS

$[RhH(PPh_3)_4]$ reacts with both the POP ketone (**1**) and POP alcohol (**2**) proligands to produce α-hydroxylalkyl (**3**) through convergent pathways. A number of key intermediates for both branches of this reactivity were either isolated and fully characterized or characterized *in situ* by NMR spectroscopy. In particular, reaction with **1** gives intermediate **4**, a rare example of a trapped η^2-ketone hydrido complex that subsequently undergoes insertion. With **2** the reaction proceeds via C−H activation geminal to the hydroxyl group. Independent synthesis of hydrido chloride complex **7** provided evidence of the feasibility of this novel C−H activation.

The underlying mechanisms were further validated by DFT calculations. These show that the formation of **3** from **4** involves initial *mer-fac*-isomerization of the ligand followed by rate-limiting insertion. For the generation of **3** from POP alcohol precursor **5**, the initial C−H oxidative addition is rate-limiting, and this process is facilitated by the presence of PPh_3 which H-bonds to the C(H)OH moiety of the ligand.

The observed reactivity supports α-hydroxylalkyl complexes as competent intermediates in ketone hydrogenation catalyzed by rhodium hydrides and suggests that **1** and **2** may be "noninnocent" ligands in reported hydrogenation catalyst systems. This work demonstrates a new strategy via ketone insertion to access $PC_{sp3}P$ pincer complexes for metals that disfavor C−H activation. Additionally, the demonstration of C−H activation of a geminal hydroxyl position provides insight into the selective C−H activation in the presence of an alcohol functionality. Ongoing research is being undertaken to determine the reactivity of compound **3** and its analogues, particularly in regards to developing new synthetic routes to $PC_{sp3}P$ and $PC_{sp2}P$ pincer complexes and their potential in catalysis.

EXPERIMENTAL SECTION

General Information. All manipulations were carried out under nitrogen using a glovebox and/or Schlenk techniques. All reactions were performed in glassware that was oven-dried for at least 12 h. Benzene was distilled over sodium and benzophenone under a nitrogen atmosphere and stored over 4 Å molecular sieves prior to use. Diethyl ether and *n*-hexane were dried over activated alumina using an LC Technology Solution Inc. SP-1 Solvent Purification System and deoxygenated prior to use. C_6D_6 used was stirred over CaH_2 at room temperature under a nitrogen atmosphere overnight prior to distillation under reduced pressure and storage over 4 Å molecular sieves. Toluene-d_8 was deoxygenated and stored over 4 Å molecular sieves prior to use. $[RhH(PPh_3)_4]$ and ligands **1** and **2** were prepared according to reported methods.[21]

NMR spectroscopy data were obtained using Bruker AV-300, AV-400, and AV-500 spectrometers. HRMS (ESI-TOF) spectra were obtained using an Agilent Technologies 6230 TOF LC/MS. IR spectroscopy data were obtained using Bruker ALPHA FTIR spectrometers.

Synthesis of Complex 3. **1** (10 mg, 0.018 mmol) and $[RhH(PPh_3)_4]$ (21 mg, 0.018 mmol) were added to a NMR tube under N_2 atmosphere. The components were dissolved in C_6D_6 (0.6 mL) to form an orange solution immediately, which turned green overnight. NMR analyses showed the reaction to be virtually quantitative in the formation of complex **3**. ^{1}H NMR (300 MHz, C_6D_6) = δ_H 3.15 (d, $^4J_{PH}$ = 3.5 Hz, 1H, O*H*), 6.68−7.09 (m, 27H, Ar-*H*), 7.23−7.47 (m, 15H, Ar-*H*), 7.59 (d, $^3J_{HH}$ = 7.8 Hz, 2H, Ar-*H*). $^{13}C\{^1H\}$ NMR (126 MHz, C_6D_6) = δ_C 162.7 (t, J_{PC} = 18.5 Hz), 145.0 (dd, J_{PC} = 19 Hz, 8.5 Hz), 144.6 (d, J_{PC} = 25.3 Hz), 140.0 (d, J_{PC} = 25.2 Hz), 138.9 (d, J_{PC} = 44.2 Hz), 138.7 (d, J_{PC} = 25.7 Hz), 137.3 (t, J_{PC} = 16.0 Hz), 135.1 (s), 134.3 (t, J_{PC} = 11.0 Hz), 133.8 (q, J_{PC} = 6.9 Hz), 131.0 (s), 128.5 (t, J_{CP} = 5.6 Hz), 127.6 (d, J_{CP} = 8.9 Hz), 126.5 (s) 106.1 (ddt, $^2J_{PC}$ = 73.5 (d), 4.8 (t) Hz, $^1J_{RhC}$ = 25.2 Hz). $^{31}P\{^1H\}$ NMR (162 MHz, C_6D_6) = δ_P 37.5 (dt, $^1J_{RhP}$ = 120.4 (d), $^2J_{PP}$ = 28.3 (t) Hz, 1P), 43.3 (dd, $^1J_{RhP}$ = 189.2 (d), $^2J_{PP}$ = 28.3 (d) Hz, 2P). HRMS (ESI-TOF) *m*/*z*: $[M - H]^+$ Calcd for $C_{55}H_{43}OP_3Rh$ 915.1582; Found 915.1546; $[M - OH]^+$ Calcd for $C_{55}H_{43}P_3Rh$ 899.1633; Found 899.1595.

Synthesis of Complex 4. *Method A.* Benzene (5 mL) was added to a mixture of **1** (55.1 mg, 0.100 mmol) and $[RhH(PPh_3)_4]$ (115.3 mg, 0.100 mmol), and the resultant orange solution stirred at room temperature for 30 min, after which the solution was filtered. The filtrate was evaporated to give an orange residue and *n*-hexane (15 mL) was added. After trituration of the mixture for 5 min, the solid was filtered and washed with diethyl ether (2 × 2 mL) and then *n*-hexane (5 × 10 mL). After drying *in vacuo*, the product was isolated as an orange solid (64 mg, 70%).

Method B. $Li[N(SiMe_3)_2]$ (11.7 mg, 0.07 mmol) was added to solution of **7** (66.7 mg, 0.07 mmol) in C_6H_6 (5 mL) at room temperature and stirred for 15 min. The solution was rapidly evaporated under vacuum, and then diethyl ether (5 mL) was added. After trituration of the mixture for 5 min, the solid was filtered and washed with diethyl ether (2 mL) and then *n*-hexane (2 × 10 mL). After drying in vacuo, product **4** was isolated as an orange solid (35 mg, 55%). ^{1}H NMR (500 MHz, C_6D_6) = δ_H −13.27 (ddt, $^1J_{RhH}$ = 21.2 (d), $^2J_{PH}$ = 10.3 (d), $^2J_{PH}$ = 4.2 (d) Hz, 1H, Rh-*H*), 6.64−7.04 (m, 31H, Ar-*H*), 7.48−7.55 (m, 6H, Ar-*H*), 7.59−7.67 (m, 4H, Ar-*H*), 8.05 (d, $^3J_{H-H}$ = 8.0 Hz, 2H, Ar-*H*). $^{13}C\{^1H\}$ NMR (126 MHz, C_6D_6) = δ_C 156.8 (t, J_{PC} = 13.0 Hz), 137.8 (dd, $^1J_{RhC}$ = 23.7 (d), $^2J_{PC}$ = 9.2 (d) Hz), 137.1 (m), 134.7 (d, J_{PC} = 13.5 Hz), 133.8 (s), 133.4 (dt, J_{PC} = 20.0 (d), 6.9 (t) Hz), 129.1 (s), 128.9 (s), 128.4 (s), 128.2 (d, J_{PC} = 28.7 Hz), 127.4 (d, J_{PC} = 8.3 Hz), 127.3 (t, J_{PC} = 4.1 Hz), 126.0 (m), 125.4 (s). $^{31}P\{^1H\}$ NMR (162 MHz, C_6D_6) = δ_P 31.0 (dt, $^1J_{RhP}$ = 108.9 (d), $^2J_{PP}$ = 10.1 (t) Hz, 1P), 40.4 (dd, $^1J_{RhP}$ = 130.6 (d), $^2J_{PP}$ = 10.1 (d) Hz, 2P). IR (nujol mull): 1969 [ν(Rh−H)] cm^{-1}; HRMS (ESI-TOF) *m*/*z*: $[M + H]^+$ Calcd for $C_{55}H_{45}OP_3Rh$ 917.1738; Found 917.1736.

Synthesis of Complex 7. Benzene (2 mL) was added to a mixture of **2** (27.6 mg, 0.05 mmol) and $[RhCl(PPh_3)(COD)]$ (25.4 mg, 0.05 mmol), and the resultant solution was stirred at room temperature for 1 h. The solution was concentrated under vacuum to give a residue, and then *n*-hexane (5 mL) was added to produce a precipitate. The solid was filtered and washed with *n*-hexane (3 × 5 mL). After drying *in vacuo*, the product was isolated as yellow-brown solid (31 mg, 65%). ^{1}H NMR (500 MHz, C_6D_6) = δ_H −16.22 (1 H, dtd, $^1J_{RhH}$ = 22.1 Hz (d), $^2J_{PH}$ = 14.3 Hz (t), $^2J_{PH}$ = 9.2 Hz (d), Rh-*H*), 7.57 (1 H, d, J_{PH} = 7.5 Hz, O*H*), 8.2−6.6 (43 H, m, Ar-*H*). $^{13}C\{^1H\}$ NMR (126 MHz, C_6D_6) = δ_C 163.9 (t, J_{PC} = 15 Hz), 141.9 (t, J_{PC} = 25 Hz), 136.4 (t, J_{PC} = 24 Hz), 135.1 (s (br)), 134.4 (t, J_{PC} = 5.6 Hz), 133.6 (t, J_{PC} = 5.6 Hz), 133.0 (s), 130.0 (s (br)), 129.2 (s), 129.1 (s), 128.9 (s), 128.3 (s), 127.3 (d, J_{PC} = 8.4 Hz), 124.4 (s (br)), 99.4 (dd, J_{PC} = 94.1 Hz, J_{RhC} = 20.8 Hz). $^{31}P\{^1H\}$ NMR (202 MHz, C_6D_6) = δ 39.7 (dd, J_{RhP} = 120.0 Hz, J_{PP} = 24.0 Hz, 2 P), 23.7 (dt, J_{RhP} = 79.0 Hz, J_{PP} = 24.0 Hz, 1 P). IR (nujol mull): 2079 [ν(Rh−H)], 3303 [ν(O−H)] cm^{-1}. HRMS (ESI-TOF) *m*/*z*: $[M -$ Hydride$]^+$ Calcd for $C_{55}H_{44}ClOP_3Rh$ 951.1349; Found 951.1335; $[M - Cl]^+$ Calcd for $C_{55}H_{45}OP_3Rh$ 917.1738; Found 917.1703.

***In Situ* Characterization of Complex 5.** **2** (10 mg, 0.018 mmol) and $[RhH(PPh_3)_4]$ (21 mg, 0.018 mmol) were added into a NMR tube under N_2 atmosphere. The components were dissolved in C_6D_6 (0.6 mL) and then analyzed soon after. The NMR spectroscopic data were obtained at 280 K to reduce the rate of conversion from intermediate **5** to complex **3**. ^{1}H NMR (500 MHz, C_6D_6) = δ_H −8.58 (1 H, d (br), $^2J_{PH}$ = 90 Hz, Rh-*H*), 1.39 (1 H, d, $^3J_{HH}$ = 3.3 Hz, O*H*), 8.0−6.2 (43 H, m, Ar-*H*), 9.87 (1 H, s (br), C(OH)-*H*). ^{1}H−^{1}H COSY NMR shows strong correlation between signals at δ_H 9.87 and 1.39. The doublet at δ_H 1.39 is not resolved upon broadband ^{31}P decoupling. Selected ^{13}C NMR data (from HMBC/HSQC) = δ_C 69.3 (C), 147.4 (C). $^{31}P\{^1H\}$ NMR (202 MHz, C_6D_6) = δ_P 31.0 (d (br), $^1J_{RhP}$ = 131 Hz), 34.3 (d (br), $^1J_{RhP}$ = 170 Hz).

DOI: 10.1021/acs.organomet.7b00158
Organometallics 2017, 36, 1609−1617

***In Situ* Characterization of Complex 6.** To a sample of **3** prepared from **1** and $[RhH(PPh_3)_4]$ in toluene-d_8 (0.6 mL) as described above was applied a pressure of hydrogen gas (4 atm). The sample was then analyzed using VT-NMR spectroscopic experiments. Selected NMR spectroscopic data for **6** at 233 K: ^{1}H NMR (500 MHz, C_6D_6) = δ_H −6.8 (2 H, d (br), $^2J_{PH}$ = 140 Hz, Rh-*H*), 4.25 (1 H, d, $^4J_{PH}$ = 4.4 Hz, O*H*). ^{13}C NMR data (from HMBC) = δ_C 95.8 (1 C, dd, $^2J_{PC}$ = 95.2 Hz, $^1J_{RhC}$ = 28.6 Hz, Rh-C−OH). ^{31}P{^{1}H} NMR (202 MHz, C_6D_6) = δ_P 45.6 (d (br), $^1J_{RhP}$ = 86.5 Hz), 41.7 (dt, $^1J_{RhP}$ = 84.5 Hz, $^2J_{PP}$ = 14.9 Hz).

Preparation of Deuterium-Labeled Ligand 2a. A 1:1 mixture of D_2O/THF was added to **2** followed by evaporation to dryness. Approximately 81% deuteration of the hydroxyl position at 2.25 ppm was determined by ^{1}H NMR spectroscopy. ^{1}H NMR (400 MHz, C_6D_6) = δ_H 6.89 (td, *J* = 7.5, 1.4 Hz, 2H, Ar-*H*), 6.94−7.06 (m, 14H, Ar-*H*), 7.19−7.24 (m, 2H, Ar-*H*), 7.27−7.37 (m, 8H, Ar-*H*), 7.50−7.56 (m, 2H, Ar-*H*), 7.76 (t, *J* = 6.2 Hz, 1H, C(OH)-*H*). ^{31}P{^{1}H} NMR (162 MHz, C_6D_6) = δ_P −17.3 (s, 2 P).

Preparation of Deuterium-Labeled Ligand 2b. *Part A.* (2-Bromophenyl)diphenylphosphene (2.00 g, 5.9 mmol) was dissolved in diethyl ether (25 mL). The solution is then treated dropwise with *n*-BuLi in hexane (6 mL, 1.6 M, 9.6 mmol) at −78 °C and stirred for 30 min. Dimethylformamide-d_7 (3 mL, 38.6 mmol) was added thereafter at −78 °C. The mixture was then allowed to come to room temperature and was stirred overnight. Dilute aqueous HCl solution (20 mL) was added, and then the aldehyde product was extracted using DCM (3 × 30 mL). The combined extractions were dried with Na_2SO_4 and then evaporated. The crude product was then recrystallized using methanol to give *deutero* 2-(diphenylphosphino)-benzaldehyde (0.901 g, 52%).

Part B. (2-Bromophenyl)diphenylphosphine (0.423 g, 1.24 mmol) was dissolved in diethyl ether (10 mL) and treated with *n*-BuLi (2.9 mL, 1.6 M, 1.78 mmol) at 0 °C. The reaction mixture was stirred for 30 min; thereafter, *deutero* 2-(diphenylphosphino)benzaldehyde (0.519 g, 1.78 mmol) was added. The reaction mixture was then stirred for an additional hour. The mixture is then allowed to come to room temperature, and degassed dilute aqueous HCl solution was added. Then, the product was extracted with diethyl ether (3 × 20 mL). The solvent was removed under vacuum and the crude product was recrystallized using methanol to give ligand **2b** as a white solid (0.136 g, 20%). ^{1}H NMR (400 MHz, C_6D_6) = δ_H 2.25 (t, *J* = 1.4 Hz, 1H, O*H*), 6.89 (td, *J* = 7.5, 1.4 Hz, 2H, Ar-*H*), 6.94−7.09 (m, 14H, Ar-*H*), 7.18−7.24 (m, 2H, Ar-*H*), 7.26−7.37 (m, 8H, Ar-*H*), 7.49−7.56 (m, 2H, Ar-*H*). ^{31}P{^{1}H} NMR (162 MHz, C_6D_6) = δ_P −17.3 (s, 2 P).

■ ASSOCIATED CONTENT

Supporting Information

The Supporting Information is available free of charge on the ACS Publications website at DOI: 10.1021/acs.organomet.7b00158.

Experimental methods, formation and isolation details, NMR monitoring details and spectra, HRMS spectra, X-ray crystallography data, and DFT calculations (PDF)
Crystallographic information files for **3**, **4**, and **7** (CIF)
Cartesian coordinates for **4** (XYZ)

■ AUTHOR INFORMATION

Corresponding Authors

*E-mail: t.kraemer@hw.ac.uk.
*E-mail: rowan.young@nus.edu.sg.

ORCID

Simon Sung: 0000-0002-7864-7694
Stuart A. Macgregor: 0000-0003-3454-6776
Tobias Krämer: 0000-0001-5842-9553
Rowan D. Young: 0000-0001-7437-8944

Notes

The authors declare no competing financial interest.

■ ACKNOWLEDGMENTS

We thank the National University of Singapore and the Singapore Ministry of Education for financial support (WBS R-143-000-586-112 and R-143-000-666-114) and Heriot-Watt University for the award of a James Watt Scholarship.

■ REFERENCES

(1) (a) Birch, A. J.; Williamson, D. H. In *Organic Reactions*; John Wiley & Sons, Inc.: Hoboken, NJ, 2011. (b) de Vries, J. G.; Elsevier, C. J. *The Handbook of Homogeneous Hydrogenation*; Wiley-VCH: Weinheim, 2007.

(2) (a) Schrock, R. R.; Osborn, J. A. *J. Chem. Soc. D* **1970**, 567. (b) Malacea, R.; Poli, R.; Manoury, E. *Coord. Chem. Rev.* **2010**, *254*, 729. (c) Samec, J. S. M.; Bäckvall, J.-E.; Andersson, P. G.; Brandt, P. *Chem. Soc. Rev.* **2006**, *35*, 237. (d) Clapham, S. E.; Hadzovic, A.; Morris, R. H. *Coord. Chem. Rev.* **2004**, *248*, 2201. (e) Gregorio, G.; Pregaglia, G.; Ugo, R. *Inorg. Chim. Acta* **1969**, *3*, 89. (f) Abdur-Rashid, K.; Clapham, S. E.; Hadzovic, A.; Harvey, J. N.; Lough, A. J.; Morris, R. H. *J. Am. Chem. Soc.* **2002**, *124*, 15104. (g) Wigfield, D. C. *Tetrahedron* **1979**, *35*, 449.

(3) Related systems that partake in ligand-assisted ionic hydrogenations typically rely upon the ligand to deliver a protic hydrogen, while the metal hydride transfers to the electrophilic carbonyl position (i.e., the metal-hydride also acts as a nucleophile as in route **A**). See (a) Bullock, R. M. *Chem. - Eur. J.* **2004**, *10* (10), 2366. (b) Clapham, S. E.; Hadzovic, A.; Morris, R. H. *Coord. Chem. Rev.* **2004**, *248* (21−24), 2201. (c) Wang, D.; Astruc, D. *Chem. Rev.* **2015**, *115* (13), 6621.

(4) (a) Simpson, M. C.; Cole-Hamilton, D. J. *Coord. Chem. Rev.* **1996**, *155*, 163. (b) MacDougall, J. K.; Simpson, M. C.; Green, M. J.; Cole-Hamilton, D. J. J. *J. Chem. Soc., Dalton Trans.* **1996**, 1161. (c) Sola, M.; Ziegler, T. *Organometallics* **1996**, *15*, 2611. (d) Cheliatsidou, P.; White, D. F. S.; Slawin, A. M. Z.; Cole-Hamilton, D. J. *Dalton Trans.* **2008**, 2389. (e) MacDougall, J. K.; Simpson, M. C.; Green, M. J.; Cole-Hamilton, D. J. J. *J. Chem. Soc., Dalton Trans.* **1996**, 1161. (f) Fahey, D. R. *J. Am. Chem. Soc.* **1981**, *103*, 136. (g) Milstein, D. *J. Am. Chem. Soc.* **1986**, *108*, 3525.

(5) For examples, see (a) Peterson, E.; Khalimon, A. Y.; Simionescu, R.; Kuzmina, L. G.; Howard, J. A. K.; Nikonov, G. I. *J. Am. Chem. Soc.* **2009**, *131*, 908. (b) Sieffert, N.; Bühl, M. *J. Am. Chem. Soc.* **2010**, *132*, 8056. (c) Bosson, J.; Poater, A.; Cavallo, L.; Nolan, S. P. *J. Am. Chem. Soc.* **2010**, *132*, 13146. (d) Khalimon, A. Y.; Ignatov, S. K.; Simionescu, R.; Kuzmina, L. G.; Howard, J. A. K.; Nikonov, G. I. *Inorg. Chem.* **2012**, *51*, 754. (e) Wang, W.; Gu, P.; Wang, Y.; Wei, H. *Organometallics* **2014**, *33*, 847. (f) Iron, M. A.; Sundermann, A.; Martin, J. M. L. *J. Am. Chem. Soc.* **2003**, *125*, 11430.

(6) (a) Pruett, R. L. *Ann. N. Y. Acad. Sci.* **1977**, *295*, 239. (b) Feder, H. M.; Rathke, J. W. *Ann. N. Y. Acad. Sci.* **1980**, *333*, 45. (c) Fahey, D. R. *J. Am. Chem. Soc.* **1981**, *103*, 136. (d) Bradley, J. S. *J. Am. Chem. Soc.* **1979**, *101*, 7419. (e) Dombek, B. D. *J. Am. Chem. Soc.* **1980**, *102*, 6855. (f) Keim, W.; Berger, M.; Schlupp, J. *J. Catal.* **1980**, *61*, 359. (g) Daroda, R. J.; Blackborow, J. R.; Wilkinson, G. *J. Chem. Soc., Chem. Commun.* **1980**, 1098. (h) Daroda, R. J.; Blackborow, J. R.; Wilkinson, G. *J. Chem. Soc., Chem. Commun.* **1980**, *0*, 1101. (i) Paxson, T. E.; Reilly, C. A.; Holecek, D. R. *J. Chem. Soc., Chem. Commun.* **1981**, 618. (j) Knifton, J. F. *J. Chem. Soc., Chem. Commun.* **1981**, 188. (k) Backvall, J. E.; Akermark, B.; Ljunggren, S. O. *J. Am. Chem. Soc.* **1979**, *101*, 2411. (l) Roth, J. A.; Orchin, M. *J. Organomet. Chem.* **1979**, *172*, C27. (m) Sisak, A.; Sámpár-Szerencsés, E.; Galamb, V.; Németh, L.; Ungváry, F.; Pályi, G. *Organometallics* **1989**, *8*, 1096.

(7) (a) Vaughn, G. D.; Gladysz, J. A. *J. Am. Chem. Soc.* **1981**, *103* (18), 5608. (b) Garralda, M. A.; Hernández, R.; Ibarlucea, L.; Pinilla, E.; Torres, M. R.; Zarandona, M. *Organometallics* **2007**, *26*, 1031. (c) Van Voorhees, S. L.; Wayland, B. B. *Organometallics* **1985**, *4*, 1887. (d) Fu, X.; Basickes, L.; Wayland, B. B. *Chem. Commun.* **2003**, 520. (e) Fu, X.; Wayland, B. B. *J. Am. Chem. Soc.* **2005**, *127*, 16460.

DOI: 10.1021/acs.organomet.7b00158
Organometallics 2017, 36, 1609−1617

(f) Vaughn, G. D.; Strouse, C. E.; Gladysz, J. A. *J. Am. Chem. Soc.* **1986**, *108*, 1462. (g) Vaughn, G. D.; Gladysz, J. A. *J. Am. Chem. Soc.* **1986**, *108*, 1473. (h) Brockaart, G.; El Mail, R.; Garralda, M. A.; Hernández, R.; Ibarlucea, L.; Santos, J. I. *Inorg. Chim. Acta* **2002**, *338*, 249. (i) El Mail, R.; Garralda, M. A.; Hernández, R.; Ibarlucea, L.; Pinilla, E.; Torres, M. R. *Organometallics* **2000**, *19*, 5310.

(8) For current state-of-the-art, see (a) Nguyen, K. D.; Herkommer, D.; Krische, M. J. *J. Am. Chem. Soc.* **2016**, *138*, 14210. (b) Geary, L. M.; Glasspoole, B. W.; Kim, M. M.; Krische, M. J. *J. Am. Chem. Soc.* **2013**, *135*, 3796. (c) Patman, R. L.; Chaulagain, M. R.; Williams, V. M.; Krische, M. J. *J. Am. Chem. Soc.* **2009**, *131*, 2066.

(9) Jing, Q.; Sandoval, C. A.; Wang, Z.; Ding, K. *Eur. J. Org. Chem.* **2006**, *2006*, 3606.

(10) Nakamura, Y.; Yoshikai, N.; Ilies, L.; Nakamura, E. *Org. Lett.* **2012**, *14*, 3316.

(11) Saes, B. W. H.; Verhoeven, D. G. A.; Lutz, M.; Klein Gebbink, R. J. M.; Moret, M.-E. *Organometallics* **2015**, *34*, 2710.

(12) (a) Doyle, L. E.; Piers, W. E.; Borau-Garcia, J. *J. Am. Chem. Soc.* **2015**, *137*, 2187. (b) Doyle, L. E.; Piers, W. E.; Borau-Garcia, J.; Sgro, M. J.; Spasyuk, D. M. *Chem. Sci.* **2016**, *7*, 921.

(13) For examples, see (a) Bruce, M. I.; Hambley, T. W.; Snow, M. R.; Swincer, A. G. *J. Organomet. Chem.* **1982**, *235*, 105. (b) Akkerman, F. A.; Lentz, D. *Angew. Chem., Int. Ed.* **2007**, *46*, 4902. (c) Choi, J.-C.; Sarai, S.; Koizumi, T.; Osakada, K.; Yamamoto, T. *Organometallics* **1998**, *17* (10), 2037. (d) Nishihara, Y.; Yoda, C.; Itazaki, M.; Osakada, K. *Bull. Chem. Soc. Jpn.* **2005**, *78*, 1469. (d1) Bianchini, C.; Meli, A.; Peruzzini, M.; Vizza, F.; Frediani, P.; Ramirez, J. A. *Organometallics* **1990**, *9*, 226. (e) Tejel, C.; Geer, A. M.; Jiménez, S.; López, J. A.; Ciriano, M. A. *Organometallics* **2012**, *31*, 2895. (f) Carr, S. W.; Shaw, B. L.; Thornton-Pett, M. *J. Chem. Soc., Dalton Trans.* **1987**, 1763.

(14) (a) van der Boom, M. E.; Zubkov, T.; Shukla, A. D.; Rybtchinski, B.; Shimon, L. J. W.; Rozenberg, H.; Ben-David, Y.; Milstein, D. *Angew. Chem., Int. Ed.* **2004**, *43*, 5961. (b) Daugulis, O.; Brookhart, M. *Organometallics* **2004**, *23*, 527. (c) Pawley, R. J.; Huertos, M. A.; Lloyd-Jones, G. C.; Weller, A. S.; Willis, M. C. *Organometallics* **2012**, *31*, 5650.

(15) (a) Moxham, G. L.; Randell-Sly, H.; Brayshaw, S. K.; Weller, A. S.; Willis, M. C. *Chem. - Eur. J.* **2008**, *14*, 8383. (b) Arras, J.; Speth, H.; Mayer, H. A.; Wesemann, L. *Organometallics* **2015**, *34*, 3629. (c) Barthes, C.; Lepetit, C.; Canac, Y.; Duhayon, C.; Zargarian, D.; Chauvin, R. *Inorg. Chem.* **2013**, *52*, 48. (d) Lepetit, C.; Poater, J.; Alikhani, M. E.; Silvi, B.; Canac, Y.; Contreras-García, J.; Solà, M.; Chauvin, R. *Inorg. Chem.* **2015**, *54*, 2960. (e) Lesueur, W.; Solari, E.; Floriani, C.; Chiesi-Villa, A.; Rizzoli, C. *Inorg. Chem.* **1997**, *36*, 3354. (f) Logan, J. R.; Piers, W. E.; Borau-Garcia, J.; Spasyuk, D. M. *Organometallics* **2016**, *35*, 1279.

(16) Scherer, W.; Dunbar, A. C.; Barquera-Lozada, J. E.; Schmitz, D.; Eickerling, G.; Kratzert, D.; Stalke, D.; Lanza, A.; Macchi, P.; Casati, N. P. M.; Ebad-Allah, J.; Kuntscher, C. *Angew. Chem., Int. Ed.* **2015**, *54*, 2505.

(17) Kozuch, S.; Shaik, S. *Acc. Chem. Res.* **2011**, *44*, 101.

(18) Zhang, Y.; Lewis, J. C.; Bergman, R. G.; Ellman, J. A.; Oldfield, E. *Organometallics* **2006**, *25*, 3515.

(19) Goodman, J.; Grushin, V. V.; Larichev, R. B.; Macgregor, S. A.; Marshall, W. J.; Roe, D. C. *J. Am. Chem. Soc.* **2010**, *132*, 12013.

(20) (a) Minenkov, Y.; Occhipinti, G.; Jensen, V. R. *J. Phys. Chem. A* **2009**, *113*, 11833. (b) Zhao, Y.; Truhlar, D. G. *Org. Lett.* **2007**, *9*, 1967. (c) Sieffert, N.; Bühl, M. *Inorg. Chem.* **2009**, *48*, 4622. (d) McMullin, C. L.; Jover, J.; Harvey, J. N.; Fey, N. *Dalton Trans.* **2010**, *39*, 10833. (e) Ahlquist, M. S. G.; Norrby, P.-O. *Angew. Chem., Int. Ed.* **2011**, *50*, 11794.

(21) (a) Ahmad, N.; Levison, J. J.; Robinson, S. D.; Uttley, M. F.; Wonchoba, E. R.; Parshall, G. W. *Inorg. Synth.* **1990**, *28*, 81−83. (b) Jing, Q.; Sandoval, C. A.; Wang, Z.; Ding, K. *Eur. J. Org. Chem.* **2006**, *2006*, 3606−3616. (c) Nakamura, Y.; Yoshikai, N.; Ilies, L.; Nakamura, E. *Org. Lett.* **2012**, *14*, 3316−3319.

DOI: 10.1021/acs.organomet.7b00158
Organometallics 2017, 36, 1609−1617